Development and Implementation of a Trajectory Prediction Methodology

by

Clay Jackson Robertson

A thesis submitted to the Graduate Faculty of
Auburn University
in partial fulfillment of the
requirements for the Degree of
Master of Science

Auburn, Alabama
May 7, 2012

Keywords: Time Horizon, Trajectory Prediction, Kalman Filter

Approved by

Dr. Gilbert Crouse, Chair, Associate Professor of Aerospace Engineering
Dr. David Cicci, Professor of Aerospace Engineering
Dr. John Cochran, Professor and Head of Aerospace Engineering

Abstract

Operation of unmanned aircraft in the United States' National Airspace System (NAS) is currently severely restricted, primarily due to the need to ensure adequate separation between manned and unmanned aircraft (UA). A particular problem in conflict avoidance algorithm is estimating where conflicting traffic is likely to be in the future. While most air traffic spends a large percentage of its time in straight and level flight, maneuvers are still quite common and must be considered. Incorporating uncertainty in tracking algorithms is well established, but current methods primarily only consider uncertainty related to sensor errors and modeling errors. They do not consider the uncertainty of pilot decisions regarding maneuvers. The objective of this research is to quantify the level of uncertainty in aircraft position due to pilot maneuvers and develop methods for incorporating that information into tracking and conflict avoidance algorithms.

The uncertainty in position and velocity can arise from different sources such as sensor uncertainty, but a significant contributor is that the future behavior of non-cooperative aircraft is generally unknown. A pilot may maneuver for quite a number of different reasons. While aircraft on a cross-country trip will generally only make small course or altitude adjustments at various waypoints along their planned track, pilots that are just out "boring holes in the sky" or student pilots practicing various maneuvers may engage in fairly aggressive maneuvers unexpectedly. Thus it is helpful to quantify not only where a non-cooperative aircraft would be in the future given that it maintains its current velocity, but also where it could be if the pilot chooses to maneuver. In this study, time histories of aircraft tracks have been used to develop statistical models of aircraft maneuvers. Two sources of aircraft tracks have been used. Auburn University has a small fleet of flight training aircraft and

GPS tracking devices were placed in these aircraft and their movements were tracked over approximately six weeks. Since these aircraft are used almost exclusively for flight training they represent aircraft that are most likely to maneuver. Each GPS unit was packaged with a high capacity NiMH battery pack to allow the unit to operate for up to a week without recharge.

The second dataset was obtained from the FAA and includes tracks from aircraft operating over the contiguous United States. The Federal Aviation Administration (FAA) database include aircraft that are either operating under Instrument Flight Rules (IFR) or aircraft under Visual Flight Rules (VFR) but using radar flight following. IFR aircraft and VFR aircraft using flight following are typically traveling between two points so these aircraft would not be expected to execute many maneuvers enroute. These two dataset should provide a bound on the frequency of maneuvers.

A statistical approach to analyzing the data was used to describe error in the projection due to maneuvers off the projected course. The aircraft tracking data was analyzed to determine how accurately the position of an aircraft could be projected forward in time assuming the aircraft travels at a constant velocity. At each point in time, the aircrafts' position and velocity were estimated using Kalman filter and other straight projection techniques. This position and velocity was projected forward over various time horizons and compared to the aircrafts actual position at that projected time. By accumulating the occurrence of error from the expected projection point, the confidence in projection both along- track and cross-track could be calculated for private, IFR and VFR aircraft. Frequency and extent of deviations for cooperative and non-cooperative air traffic can be used in testing conflict avoidance algorithms for unmanned aircraft. Confidence intervals were developed for compliant and non-compliant aircraft in the NAS at various flight levels in terminal and non-terminal environments.

Acknowledgments

The author would like to acknowledge Dr. Gilbert Crouse for his guidance and support throughout this work. The author would also like to thank LTC Trey Kelley and Viva Austin at the US Army UAS Project Office in Hunstville, Alabama for the opportunity to investigate this problem and the Aerospace Engineering Department at Auburn University for its support and financial assistance. Finally, the author would like to bestow many thanks to his family and friends for their constant encouragement and unwavering support.

This work is dedicated to the author's parents, Nana J Robertson and Larry D Robertson and sister, Jourdan D Robertson, whose support, dedication, encouragement, humor, advice, inspiration, and love are never without appreciation and held dear.

Table of Contents

List of Figures

List of Tables

Chapter 1

Introduction

The purpose of this effort was to assist the Army in their Ground Based Sense and Avoid approach to maintaining separation between unmanned aircraft and other air traffic during free flight. Two separate collections of flight data were analyzed: radar tracks provided by the FAA of the national airspace system (NAS) and global positioning system (GPS) tracks from a flight training aircraft at the Auburn University Airport. The motions of the aircraft in each dataset were analyzed to determine how reliably their position and velocity could be projected forward in time. Sense and avoid efforts typically take current position and velocity estimates of air traffic and project them forward in time to determine if any conflicts may arise in the future between the other air traffic and the unmanned aircraft. If the other air traffic maintains its course, speed and altitude this works well, but often air traffic maneuvers for a variety of reasons so additional buffer space must be maintained when projected tracks forward. This task focuses on ascertaining how large a buffer is required for different types of air traffic and for different operational environments.

Chapter 2

Literature Review

Several aspects of position prediction using extended time horizons have been investigated. Important works exist in the literature related to the concept of aircraft sense and avoidance along with future state prediction. Much of the work in future state prediction and collision avoidance originated from efforts in the robotics community for path planning applications. The methods used by Elnagar is 2001 illustrated that by modeling the movement of a free path object with kinematic constraints, a Kalman filter can be used to process the signals from the measurement sensors and predicts the objects' future position [1]. Using a straight projection technique with a known velocity and heading and a short time horizon, collision probability with other moving or stationary objects could be predicted. A generic sampling technique for prediction of an aircraft when given course and heading was develped by Cale in 2001 [2]. The sampling process was developed from the perspective of the air traffic controller such that it anticipated the flight path of the aircraft for several different intervals using the current states and flight plan to enhance the projection. The quality of the projection was then determined by comparing the predicted position to the measured at the respective time horizon. This particular method is adopted by many prediction simulations with the accuracy increased with the addition of flight plan information, wind field models, target location and other information about the aircraft's environment. This method was enhanced by the use of boundary restrictions and multiple sensors. These efforts were extended by Barrios in 2011 to predict the position of a vehicle with multiple models to estimate collision probabilities [3]. Using a separate model for constant position, velocity, acceleration and jerk a comparison between each models prediction, using a Kalman filter,

against the measured future position determined the optimum model to use for each portion of the track.

Using the robotic community efforts as a platform, the aerospace industry adopted many of the methods of path prediction in the "sense and avoid" movement for unmanned aircraft (UA). The use of multiple models was implemented by Bar-Shalom in a switch filter that helped predict accelerations during maneuvers [4]. Employing a filter to switch between a constant velocity and constant acceleration model enabled the fading memory filter to determine the presence of a maneuver by an accumulation of increased covariance. Realizing the inability to predict maneuvers and the need to address the nonlinear nature of the system, an extended Kalman filter was implemented. The extended Kalman filter uses linearized system equations and introduces an update equation to produce results with the same order of magnitude in accuracy as the Kalman filter. An extended Kalman filter was used in Mao with a stochastic ordinary differential equation model to solve the flip ambiguity developed by range measurements for two cooperative unmanned aircraft on a third aircraft without GPS signal [5]. Using a priori information about the air vehicle's course and velocity as well as a specified time horizon, the extended Kalman filter provided additional information for the range measurement on where to look for the lost aircraft. The predictability characteristic of the extended Kalman filter was explored by Prévest [6] over varied time horizons. Using the constant acceleration approach, a motion model was used to project the future position of the aircraft and the quality of the projection was determined by the variance between the true and the prediction. The degradation of the prediction manifested as growing error between the predicted and measured position as the projected time increased, showing that conflict prediction was better with shorter time horizons. This same implementation of the motion model was used by Prévost again in 2008 with an extension to conflict avoidance [7]. By using the Federal Aviation Administration's (FAA) regulated separation distance of five nautical miles in the horizontal plane and 2000 feet in the vertical plane, time horizons were

projected to develop ellipsoidal shaped volumes in which the aircraft was projected to be. Given other cooperative aircraft with known position, a design space was developed in which the aircraft could travel safely. This simulation was enhanced by an end-game scenario in which the aircraft must travel through set waypoints as well as avoid projected trajectories from other cooperative aircraft sharing overlapping projected state geometries.

Given the need to measure and interpret predictability of an aircraft in free flight, various approaches to developing a metric of prediction probability have been made. A probabilistic approach to the conflict avoidance problem was addressed by Hu who moved to quantify safety in terms of the prescribed separation distance from other aircraft or prohibited airspace [8]. Using an aircraft's motion based on a stochastic differential equation model, Markov chains generated paths of greatest safety for aircraft to avoid conflict areas. The look-ahead time horizon, based on a flight plan and an end-game scenario, developed a series of planes that the Markov chains used to develop a path of least resistance for the aircraft. The level of conflict probability was then measured by the ability of the aircraft to avoid the conflict areas as well as make it to the target in a timely fashion. Another method of projection and avoidance used by Richards, termed "mixed-integer linear programming", modeled a design space based on fixed characteristics of the aircraft and conflict zones [9]. Designating the maximum turning radius and fixing the velocity of the aircraft, possible control inputs to maneuver around conflict zones, including conflicting aircraft, were processed through a cost function to minimize flight time while preserving the constrains imposed upon the system. The need for a metric was becoming more apparent such that analytical and numerical solutions to the conflict probability problem were developed. Paielli suggests that the conflict zones between the aircraft and the conflict region, aircraft-to-aircraft or aircraft-to-airspace, could be modeled as an ellipse and sphere, respectively [10]. It is difficult to formulate an analytical solution to the conflict probability based on the geometry of the problem. By changing the coordinate system from spherical to elliptical, the numerical solution could be

solved analytically to alleviate computational time and solve for the level of probability, or overlapping of geometries, for each engagement. Based on the findings of Paielli, Prandini later solved the conflict probability analytically without a coordinate change or complicated numerical solution [11]. This computationally more efficient approach produced a real time probabilistic interpretation to the predictability of the aircraft in free flight. By way of a Monte Carlo simulation, symmetric and streamline encounter situations demonstrated the effectiveness of the analytical solution by producing histograms of the separation distance.

Presenting the level of conflict and predictability in airspace has been the focus in the sense and avoid community. In projecting the position, using methods of conflict detection, the certainty of collision was measured by Al-Basman using a likelihood density approach [12]. The amount of aircraft and coincident trajectories in the environment designated the level of congestion which was ranked through selected levels of intensity. This produced contours of congestions, identifying hazardous airspace through the accumulation of aircraft in the area. The quality of a projection can be broken into its accuracy cross-track and along-track. Gong developed a methodology of determining the effectiveness of projections in both directions, producing Gaussian distributions of error for planar motion as well as three dimensional aircraft motion [13]. Using flight plans and disregarding flights that deviated from planned waypoints, the quality of a straight projection was presented in histograms, giving shape to the predictability of compliant aircraft in free flight.

Chapter 3

Estimating Future Position of Air Traffic

Determining whether two aircraft will be in conflict with each other in the future requires estimating where those aircraft will be in the future. There are obvious limitations to how precisely this can be done. The most significant limitation is that the future behavior of non-cooperative aircraft is generally unknown. A pilot may maneuver for quite a number of different reasons. While aircraft on a cross-country trip will generally only make small course or altitude adjustments at various waypoints along their planned track, pilots that are just out "boring holes in the sky" or student pilots practicing various maneuvers may engage in fairly aggressive maneuvers unexpectedly. Thus it would be helpful to be able to quantify not only where a non-cooperative aircraft would be in the future given that it maintains its current velocity, but also where it could be if the pilot chooses to maneuver. In this study, time histories of aircraft tracks have been used to develop statistical models of aircraft maneuvers. Two sources of aircraft tracks have been used.

3.1 National Airspace System Data

Seven days of data were acquired from the FAA through a freedom of information act request to be used for research. Figure 3.1 below shows all the tracks from this data set over a 24 hour period. The FAA database include aircraft that are either operating under Instrument Flight Rules (IFR) or aircraft under Visual Flight Rules (VFR) but using radar flight following. IFR aircraft and VFR aircraft using flight following are typically traveling between two points so these aircraft would not be expected to execute many maneuvers enroute.

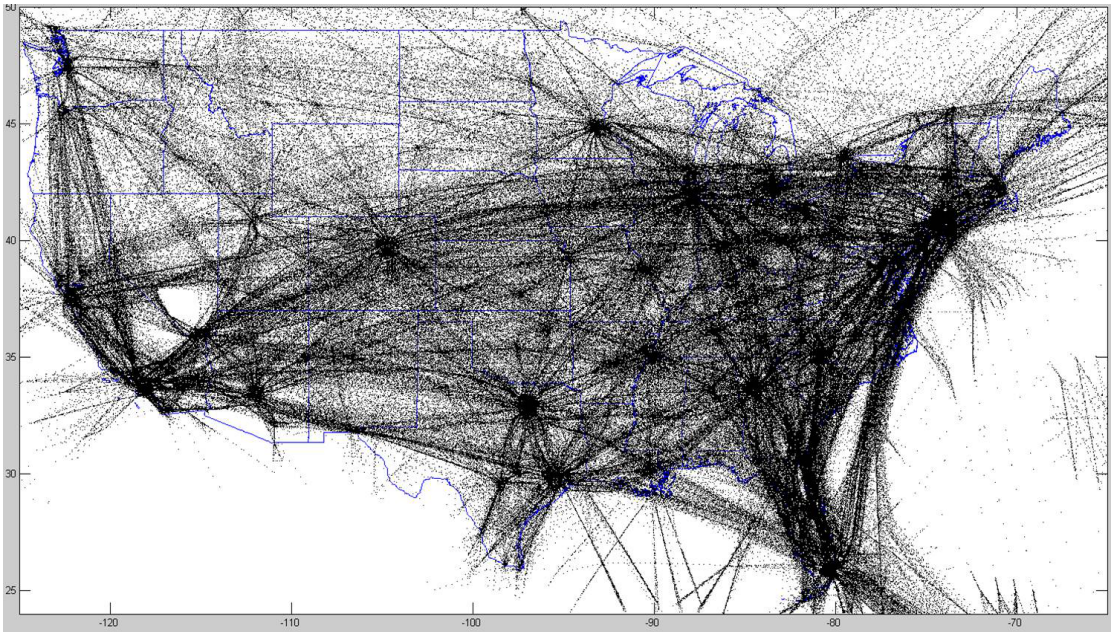

Figure 3.1: NAS data over the United States over a 24 hour period

3.2 Auburn University Personal Aircraft GPS Data

A second dataset was acquired using Auburn University's small fleet of flight training aircraft. GPS tracking devices were placed in these aircraft and their movements were tracked over approximately six weeks. Since these aircraft are used almost exclusively for flight training they represent aircraft that are most likely to maneuver. Each GPS unit was packaged with a high capacity NiMH battery pack to alow the unit to operate for us to a week without recharge as shown in Fig. 3.2a. The aircraft are mostly Cessna 172R models, a single engine high wing aircraft, pictured in Fig. 3.2b.

(a) GPS unit and NiMH battery pack (b) Auburn University Cessna 172R

Figure 3.2: Materials and Aircraft used in GPS track study

Figure 3.3 shows all of the tracks acquired over a six week period. Several long cross-country flights are obvious to Savannah, GA, Huntsville, AL, Rome, GA, Birmingham, AL and the Gulf Coast, but mostly the aircraft are operated within a relatively small area around Auburn, AL.

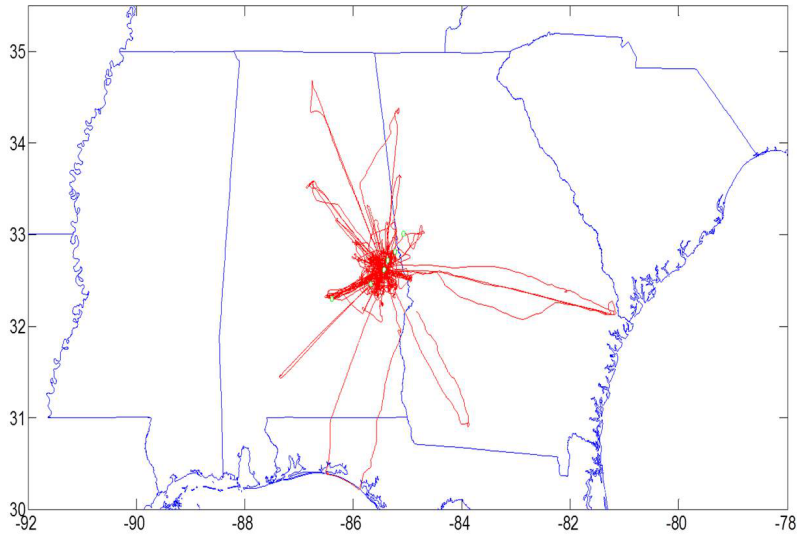

Figure 3.3: All GPS tracks from Auburn, AL

The FAA dataset and the AU fleet dataset should represent two ends of the maneuver spectrum. Aircraft traveling between two points such as most of those in the FAA dataset should behave very predictably whereas the flight training aircraft such as those in the AU fleet should behave much more erratically.

Chapter 4

Data Processing

To assess the uncertainty associated with pilot maneuvers, the aircraft tracks in both datasets were processed similarly. At each data point in the track, the airplane's position was projected forward in time assuming the velocity remained constant. The actual position at that future time was then extracted from the track and compared with the projected position. The statistics associated with this "error" between the projected and actual position were accumulated over the entire length of each aircraft's track and over the entire dataset of different aircraft tracks.

The FAA dataset provided documented flights of compliant aircraft over the course of a week across the contiguous United States. Geographical latitude and longitude, altitude, and ground speed were given in one minute increments for each aircraft, listed by tail number. Each flight was designated by its provided tail number and used according to the length of its radar track. If the selected time horizon exceeded the recorded flight time of the aircraft, the flight was not used in the error analysis.

4.1 Development of Histogram Error

To compare each measured flight with its projected, a system of analyzing the data statistically was developed. The objective was to have a way of organizing the error such that each flight, regardless of the aircraft type, could contribute to the description of the airspace it occupied.

A forward projection was used, given an initial position, course, and speed [2]. To overcome the induced error provided by a flat Earth assumption, this projection used rhumb

lines that accounted for the Earth's curvature rather than a projection into the XY-plane. A further description of rhumb lines is given in Appendix C. Given the projected location, the relative position and bearing were found between the projected position and the measured position at the projected time.

The process of accumulating the histograms is shown below in Fig. 4.1. In the top left of the figure, the first projection takes place based off prior knowledge of the velocity and bearing. Using the projected position and bearing as the origin and orientation of the grid, respectively, shown in the top right of the figure. Once the location on the grid is recorded, the next projection takes place and the process repeats, as seen in the bottom left of the figure. The error locations were accumulated and saved with each time step, developing occurrences in each two dimensional error bin.

Each location on the X-axis of the grid describes the error cross-track of the projected location, while the Y-axis describes the error along-track, providing a two dimensional description of the projected error. Accumulating these points creates a statistical description of the aircraft at various projection lengths. To allow comparisons between aircraft of differing speeds, each projected error was normalized by the aircraft's instantaneous speed such that the error of a fast aircraft could be compared to that of a slower one. The result is an error unit expressed in seconds.

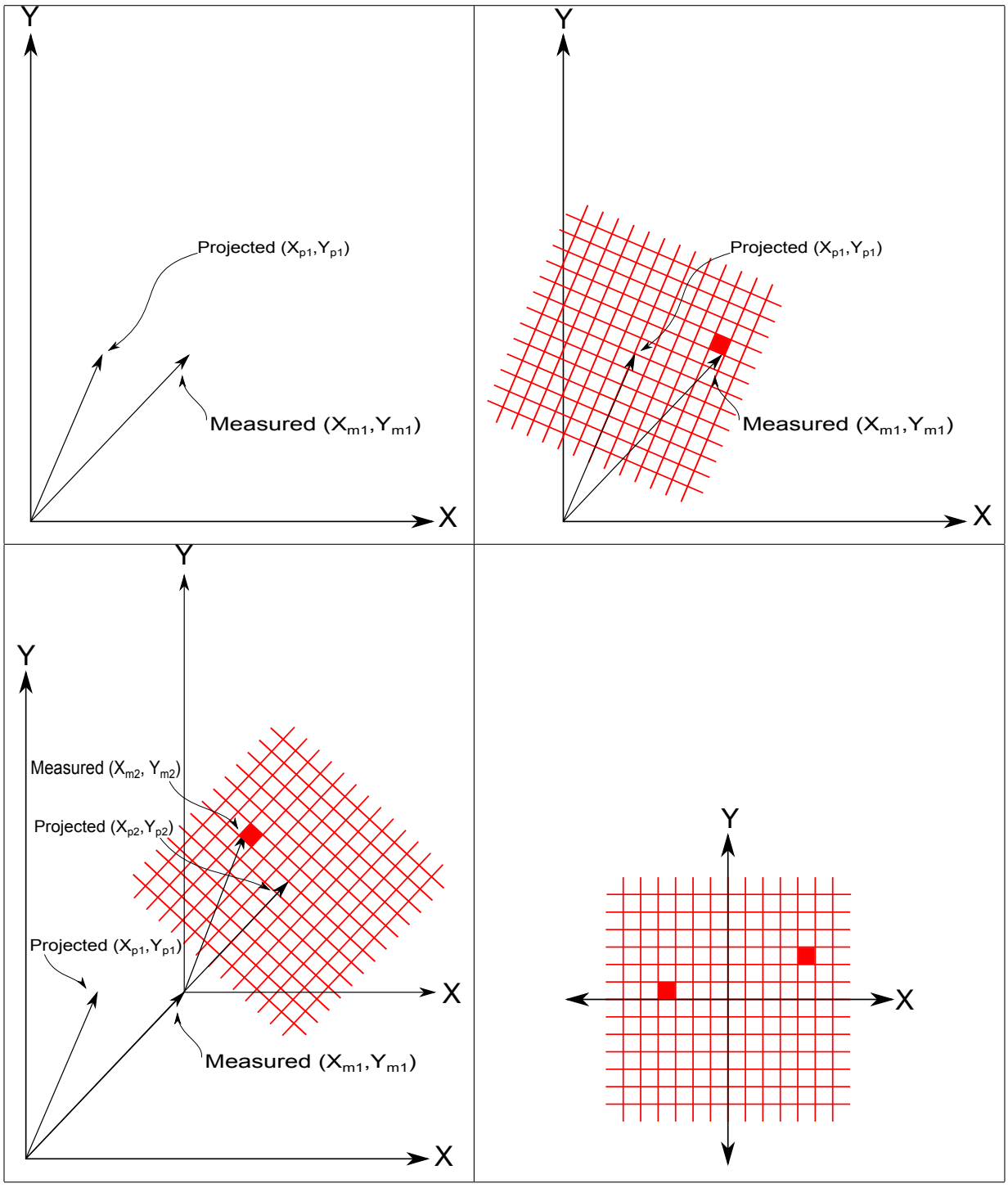

Figure 4.1: Progression of histogram error development

4.2 Development of Altitude Comparison

In order to help determine the activity in different regions of airspace, the analysis was repeated for different altitude ranges. Using the same FAA radar data, the airspace was split into three altitude regions: below 10,000 ft, between 10,000 ft and 18,000 ft, and above 18,000 ft. These altitude ranges correspond to certain operating restrictions associate with the NAS. Below 10,000 ft aircraft are restricted from operating faster than 250 kts IAS. Above 18,000 ft is considered Class A airspace and all aircraft must operate under Instrument Flight Rules. Aircraft tracks that transitioned between the different altitude regions were split into segments so that the portions in each altitude range were treated appropriately.

4.3 The Kalman Filter

The range and range-rate observations received from satellites by the GPS units arrive with noise in the signal. This noise, developed through the measurement and model receiving the measurements, must be filtered to develop the best measurement derived from the signal. A well-known mathematical approach, developed by R.E. Kalman, for sequentially processing observations of a linear dynamic system can be used to separate noise from the observations in a recursive manor at each discrete time step. The set of recursive equations was developed in 1960 by Kalman and is known as the Kalman filter [14]. The GPS units use a Kalman filter to develop position and rate from the satellite signals. Observations used to develop the statistical model have uncertainties from satellite loss or signal degradation, as well as noise developed from the GPS unit's Kalman filter.

The Kalman filter produces an optimal estimate of a system's state. The state dynamics must be linear, therefore the current state, $\mathbf{x}(t)$, can be expressed as a linear function of the previous state, $\mathbf{x}(t - \Delta t)$. Also, the observation process must be linear such that the observations, $\mathbf{z}(t)$, are a linear function of the current state, $\mathbf{x}(t)$. Kalman assumed that

the state dynamics are perturbed by random excitation, $w(t)$, and the measurements are corrupted by random noise, $v(t)$. Given these assumptions the state dynamics assume the form shown in Eq.(4.1)

$$\dot{\mathbf{x}}(t) = \mathbf{F}\mathbf{x}(t) + \mathbf{w}(t) \tag{4.1}$$

where $\mathbf{F}$ is a constant state matrix and $\mathbf{w}(t)$ is a vector of zero-mean Gaussian random variables. At intervals, the state of the system is observed through Eq.(4.2)

$$\mathbf{z}(t) = \mathbf{H}\mathbf{x}(t) + \mathbf{v}(t) \tag{4.2}$$

where $\mathbf{z}(t)$ represents the observations or measurements. $\mathbf{H}$ is a matrix which maps the states to the observations and $\mathbf{v}(t)$ is a vector of zero-mean Gaussian random variables.

The Kalman filter algorithm proceeds using the following steps. First the state and covariance matrix are projected forward in time using Eqs.(4.3) and (4.4).

$$\hat{\mathbf{x}}_k^- = \mathbf{\Phi}_k \hat{\mathbf{x}}_{k-1} \tag{4.3}$$

$$\mathbf{P}_k^- = \mathbf{\Phi}_k \mathbf{P}_{k-1} \mathbf{\Phi}_k^T + \mathbf{Q}_k \tag{4.4}$$

Next the Kalman gain, $\mathbf{K}_k$, is calculated in Eq.(4.5) and a corrected estimate of the current state is determined in Eq.(4.6), incorporating the new measurements. The covariance is then updated in Eq.(4.7) using the Kalman gain.

$$\mathbf{K}_k = \mathbf{P}_k^- \mathbf{H}_k^T \left[\mathbf{H}_k \mathbf{P}_k^- \mathbf{H}_k^T + \mathbf{R}_k \right]^{-1} \tag{4.5}$$

$$\hat{\mathbf{x}}_k = \hat{\mathbf{x}}_k^- + \mathbf{K}_k \left[\mathbf{z}_k - \mathbf{H}_k \hat{\mathbf{x}}_k^- \right] \tag{4.6}$$

$$\mathbf{P}_k = \left[\mathbf{I} - \mathbf{K}_k \mathbf{H}_k \right] \mathbf{P}_k^- \tag{4.7}$$

Above in Eq.(4.3), $\mathbf{\Phi}$ is defined as the transition matrix for the state matrix H.

$$\mathbf{\Phi} = e^{\mathbf{H}\Delta t} \tag{4.8}$$

In Eq.(4.3) through (4.7), $\hat{\mathbf{x}}_k^-$ is the *a priori* state estimate at k and the *a posteriori* state estimate is $\hat{\mathbf{x}}_k$. $\mathbf{P}_k^-$ and $\mathbf{P}_k$ are the *a priori* and *a posteriori* estimated error covariance at k, respectively. The time update equations in (4.3) and (4.4) serve as the predictor equations while the measurement update equations in Eqs.(4.5) through (4.7) serve as the corrector equations in this predictor-corrector algorithm.

The state space model of the aircraft's kinematic motion is seen below in Eqs.(4.9) and (4.11). Equation (4.9) presents a constant velocity case for the model, assuming zero change in the acceleration of the aircraft. With this model, the range predictions over the specified time horizons were more accurate since the weight on the acceleration from the filter was neglected. Because of the straight projection provided by this filter, maneuvers were modeled as noise and prediction during these maneuvers resulted in a reduction in the quality of the projection. Equation (4.11) represents a constant acceleration model of the aircraft. Because of the higher Kalman gain needed to adjust for unexpected maneuvers, the constant acceleration model suffers in range prediction while providing more accurate projections for maneuvering aircraft.

$$\mathbf{\Phi} = \begin{bmatrix} 1 & 0 & \Delta t & 0 \\ 0 & 1 & 0 & \Delta t \\ 0 & 0 & 1 & 0 \\ 0 & 0 & 0 & 1 \end{bmatrix} \tag{4.9}$$

where,

$$\mathbf{x} = \begin{bmatrix} x & y & v_x & v_y \end{bmatrix}^T \tag{4.10}$$

$$\mathbf{\Phi} = \begin{bmatrix} 1 & 0 & \Delta t & 0 & \frac{1}{2}\Delta t^2 & 0 \\ 0 & 1 & 0 & \Delta t & 0 & \frac{1}{2}\Delta t^2 \\ 0 & 0 & 1 & 0 & \Delta t & 0 \\ 0 & 0 & 0 & 1 & 0 & \Delta t \\ 0 & 0 & 0 & 0 & 1 & 0 \\ 0 & 0 & 0 & 0 & 0 & 1 \end{bmatrix} \tag{4.11}$$

where,

$$\mathbf{x} = \begin{bmatrix} x & y & v_x & v_y & a_x & a_y \end{bmatrix}^T \tag{4.12}$$

To account for error in the model, noise was added to the system in the form of a process noise to create an artificial floor for the covariance convergence. Because of the large number of measurements over long tracks, the covariance approaches zero, reducing the Kalman gain such that corrections to the state becomes ineffective. The addition of process noise increases the weight placed on measurements at each time step and reduces the reliance on previous information[15] [16].

For both the constant velocity and constant acceleration models, the process noise was selected to reduce the error between the actual tracks and the projected future positions. Using the distance error between the state at each time horizon and the measured state for all GPS tracks as the a cost function, the diagonals of the process noise matrix were determined using a MATLAB numerical minimization function ga(). This function is a genetic algorithm optimization routine provided in MATLAB used here to optimize the process noise variables. The diagonals of the process noise matrix were optimized for each of the following datasets: all tracks with airports, all tracks without airports, selected tracks with airports, and selected

tracks without airports.

$$\mathbf{Q}(t) = \begin{bmatrix} q_1 & 0 & 0 & 0 \\ 0 & q_1 & 0 & 0 \\ 0 & 0 & q_2 & 0 \\ 0 & 0 & 0 & q_2 \end{bmatrix} \tag{4.13}$$

$$\mathbf{Q}(t) = \begin{bmatrix} q_1 & 0 & 0 & 0 & 0 & 0 \\ 0 & q_1 & 0 & 0 & 0 & 0 \\ 0 & 0 & q_2 & 0 & 0 & 0 \\ 0 & 0 & 0 & q_2 & 0 & 0 \\ 0 & 0 & 0 & 0 & q_3 & 0 \\ 0 & 0 & 0 & 0 & 0 & q_3 \end{bmatrix} \tag{4.14}$$

The covariance matrix updates at each time step. The initial position of the aircraft is unknown to the filter, therefore the diagonals of the covariance matrix were initially given high values to allow the filter to rely primarily on the measured position. The cross covariance terms were set to zero because of the initially unknown correlation between each element of the matrix. Eqs. (4.15) and (4.16) present the structure of the covariance matrices for each model of the filter.

$$\mathbf{P} = \begin{bmatrix} \sigma_{xx}^2 & \sigma_{xy} & \sigma_{xv_x} & \sigma_{xv_y} \\ \sigma_{yx} & \sigma_{yy}^2 & \sigma_{yv_x} & \sigma_{yv_y} \\ \sigma_{v_x x} & \sigma_{v_x y} & \sigma_{v_x v_x}^2 & \sigma_{v_x v_y} \\ \sigma_{v_y x} & \sigma_{v_y y} & \sigma_{v_y v_x} & \sigma_{v_y v_y}^2 \end{bmatrix} \tag{4.15}$$

$$\mathbf{P} = \begin{bmatrix} \sigma_{xx}^2 & \sigma_{xy} & \sigma_{xv_x} & \sigma_{xv_y} & \sigma_{xa_x} & \sigma_{xa_y} \\ \sigma_{yx} & \sigma_{yy}^2 & \sigma_{yv_x} & \sigma_{yv_y} & \sigma_{ya_x} & \sigma_{ya_y} \\ \sigma_{v_xx} & \sigma_{v_xy} & \sigma_{v_xv_x}^2 & \sigma_{v_xv_y} & \sigma_{v_xa_x} & \sigma_{v_xa_y} \\ \sigma_{v_yx} & \sigma_{v_yy} & \sigma_{v_yv_x} & \sigma_{v_yv_y}^2 & \sigma_{v_ya_x} & \sigma_{v_ya_y} \\ \sigma_{a_xx} & \sigma_{a_xy} & \sigma_{a_xv_x} & \sigma_{a_xv_y} & \sigma_{a_xa_x}^2 & \sigma_{a_xa_y} \\ \sigma_{a_yx} & \sigma_{a_yy} & \sigma_{a_yv_x} & \sigma_{a_yv_y} & \sigma_{a_ya_x} & \sigma_{a_ya_y}^2 \end{bmatrix} \tag{4.16}$$

The measurement error matrix is shown in Eq. (4.17). The GPS unit utilizes a differential global positioning system with an accuracy up to 10 meters. Therefore the standard deviation of the error for the GPS unit is presented in the measurement error matrix as 100 m^2. The measurement matrices for the constant velocity and constant acceleration filters are given in Eqs. (4.18) and (4.19), respectively.

$$\mathbf{R} = \begin{bmatrix} 10^2 & 0 \\ 0 & 10^2 \end{bmatrix} \tag{4.17}$$

$$\mathbf{H} = \begin{bmatrix} 1 & 0 & 0 & 0 \\ 0 & 1 & 0 & 0 \end{bmatrix} \tag{4.18}$$

$$\mathbf{H} = \begin{bmatrix} 1 & 0 & 0 & 0 & 0 & 0 \\ 0 & 1 & 0 & 0 & 0 & 0 \end{bmatrix} \tag{4.19}$$

4.4 Other Projection Techniques

Other projection techniques were explored to verify the quality of the projection methods. Using the measured signal from the GPS units, the data was projected forward over the time horizon using two other prediction techniques.

As described in Appendix C, rhumbline's can be used to project to a future position given the course and velocity of the vehicle over the time horizon. Similar to the Kalman filter method for a constant velocity model, the rhumbline projection assumes a constant velocity and course over the time horizon in the projection. Rhumbline's lend themselves to this type of projection because of their course of constant bearing towards the destination.

A second constant velocity technique used was to convert the spherical latitude and longitude coordinates into the Cartesian coordinats. This process reduced the complexity of the project, but was only valid for short distances do to the flat Earth assumption needed to make the conversion possible. With all flights being centralized around the Auburn University Airport, the flat Earth assumption does not cause the projections to diverge as they would for a cross-country track.

Lastly, a moving average of the data was taken to smooth the error caused by jumps in sample time. Due to lose of satellite signal the sample rate varies, causing the projection error to increase with longer gaps in sample time. To reduce this effect on the quality of the projection, a moving average with a window of five seconds diminished the accumulation of error using a straight projection from the last known velocity and course.

Chapter 5

Results

5.1 National Airspace System Radar Tracks

Several different methods of presenting the results will be used. Figure 5.1 shows results from all aircraft tracks for the three different altitude ranges plus a summary of all altitudes when the position is projected three minutes into the future. The two dimensional histogram is presented as a colored contour plot. The X-axis represents cross-track error and the Y-axis represents along-track error. The contour lines represent confidence intervals. The outside of the colored portion is the 99% confidence region. The red star in the image is the location of the aircraft prior to projecting the position forward in time. These graphs demonstrate the expected trends. The graph for above 18,000 ft (lower left of Fig. 5.1) shows that the actual positions are always in front of the previous position. The largest hump in the probability density function is straight ahead at the previous speed. There are some "wings" to the distribution indicating that some aircraft turn left or right, but no aircraft turn completely around. The upper two graphs, representing lower that 10,000 ft on the left and 10,000 ft to 18,000 ft on the right, indicate more maneuvers. The "wings" on the distribution now wrap around the previous spot marked by the star. That indicates some aircraft have turned completely around and are traveling in the opposite direction during the projection interval.

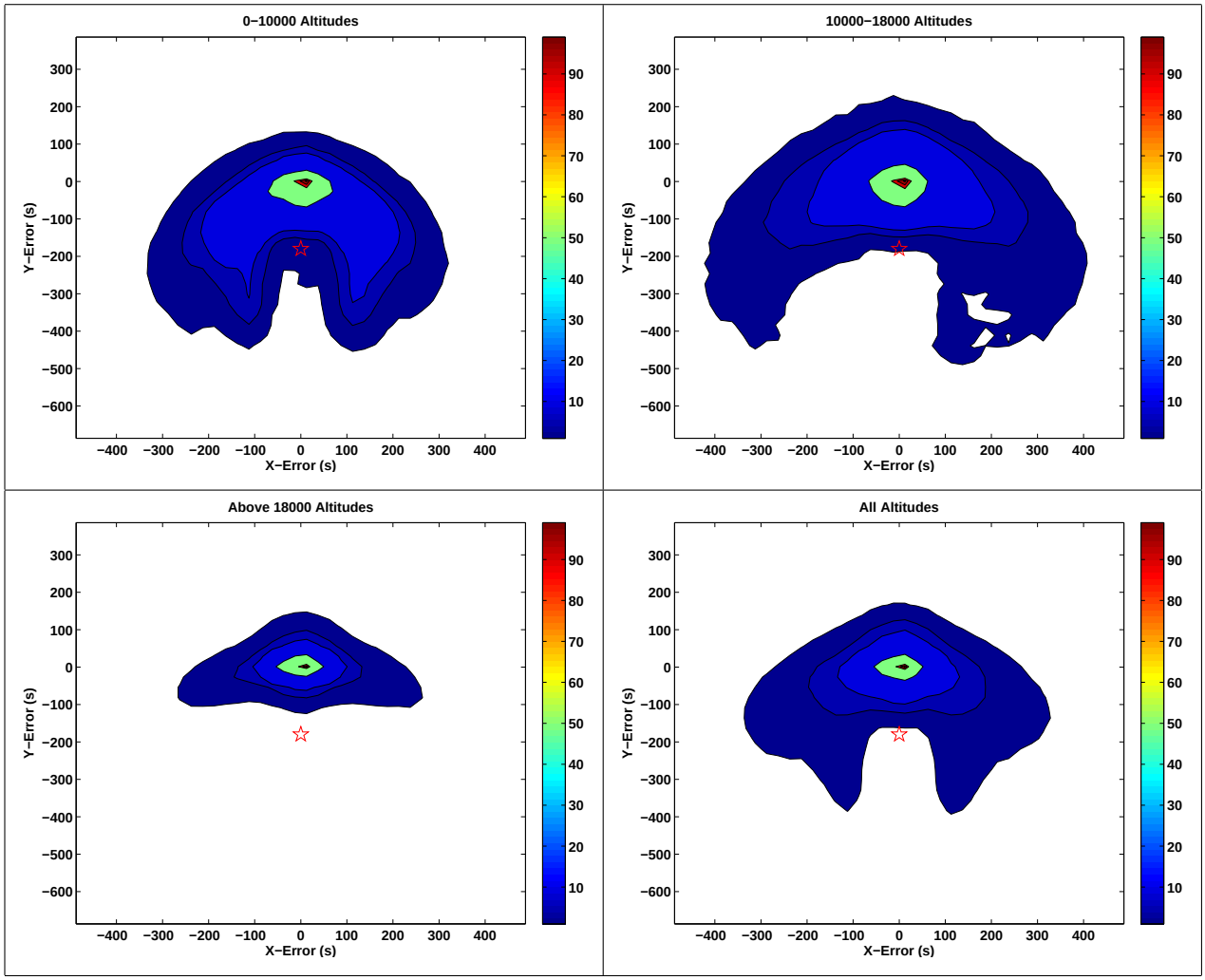

Figure 5.1: All tracks, 3 minute projection, difference in projection to measured histograms

The next figure, Fig. 5.2, shows the same presentation and same altitude ranges, but for a projection 10 minutes into the future. Note that the scales are considerably larger than the previous figure and wrapping around the previous position is evident. As with Fig. 5.1, the predictability of the aircraft increases as the altitude increases. If the projections were perfect, the probability density function would be a spike at the origin. Obviously that is unlikely, but the more of the probability density function that lies ahead of the original position, the more the aircraft could be described as predictable. In the graph for above

18,000 ft, even at 10 minutes of projection, the bulk of the error lies in the direction of the vehicle's path.

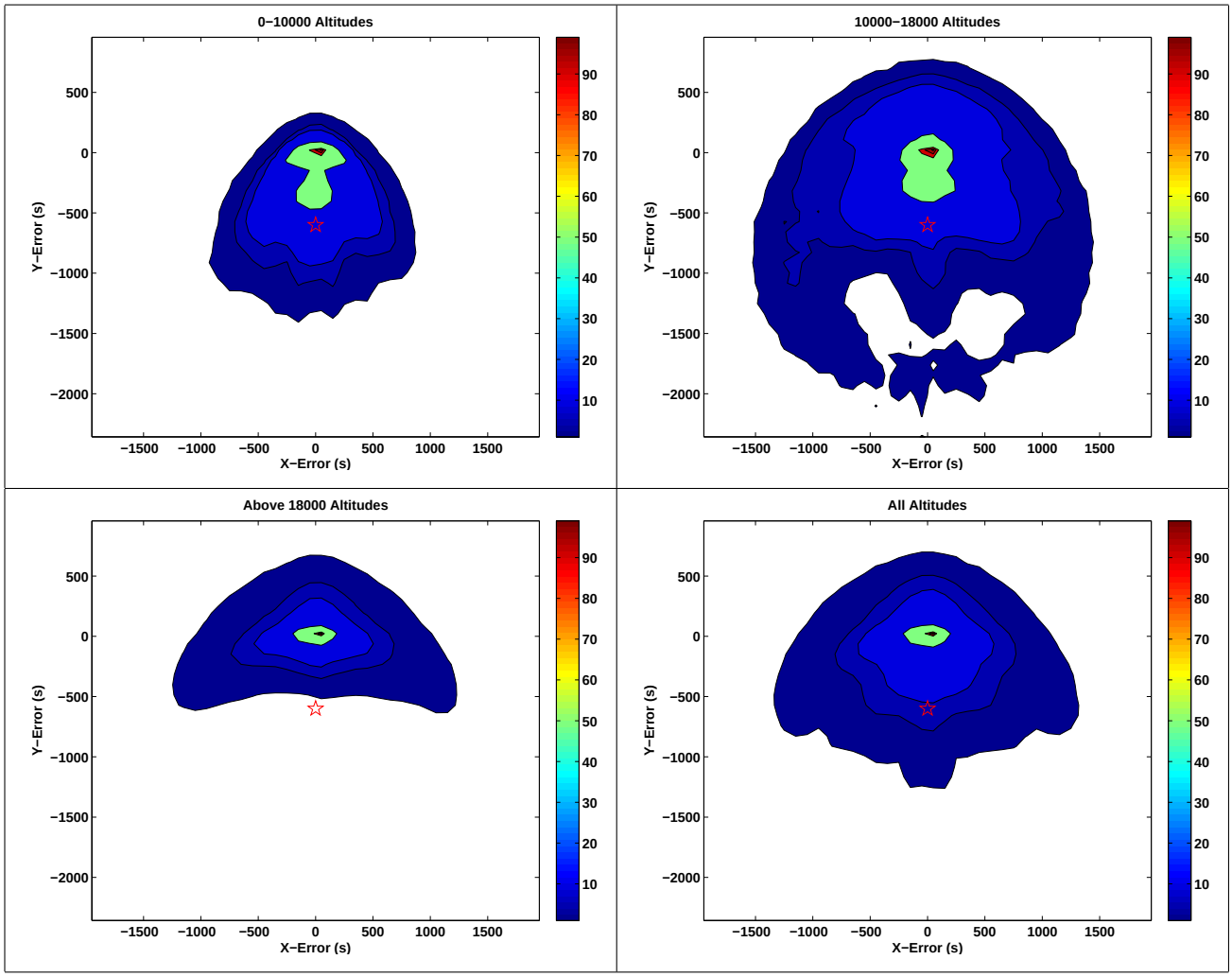

Figure 5.2: All tracks, 10 minute projection, difference in projection to measured histograms

The next two figures show the motion of the aircraft in the same altitude plane. We can also look at changes in altitude. Figure 5.3 below compares altitude changes with a three minute projection for the four different altitude ranges. In the all altitude case (lower right) and the above 18,000 ft case (lower left) both show large peaks centered at zero error. That indicates that aircraft above 18,000 ft rarely change their altitude. Below 18,000 ft however,

there are differing results. There is a large peak at zero error, but there are also very strong peaks away from zero. The 10,000 ft to 18,000 ft range is a transitional range. It is above the altitude most small, single engine aircraft fly and below the flight levels (18,000 ft) where transports operate. Consequently, much of the traffic in that region is either climbing to the flight levels or descending from the flight levels. That explains the large peaks at zero error at off to the sides showing climbs and descents. The same holds true for below 10,000 ft where many of the aircraft are involved in terminal operations (takeoff, landing and approach).

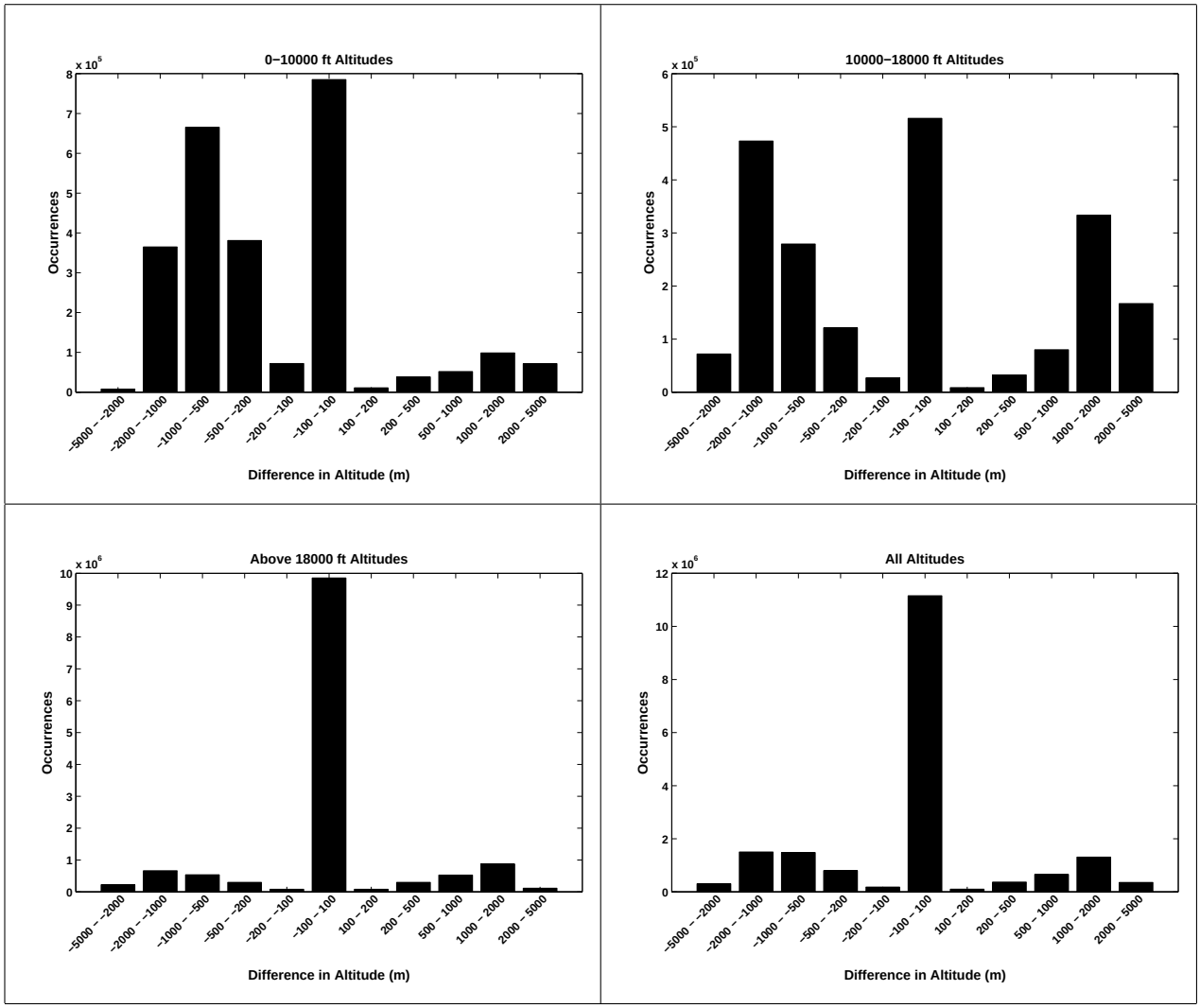

Figure 5.3: Difference in altitude, all tracks, 3 minute projection

Figure 5.4 shows changes in speed over the ground over a three minute projection. As with altitude changes, the tracks are most predictable at higher altitude and the variability increases in the lower altitude ranges. The distribution is obviously not Gaussian at less than 10,000 ft and between 10,000 ft to 18,000 ft. The plot showing flights less than 10,000 ft shows a distinct hump for the -25%–10% speed range. This may correspond to aircrafts slowing down for approach and landing.

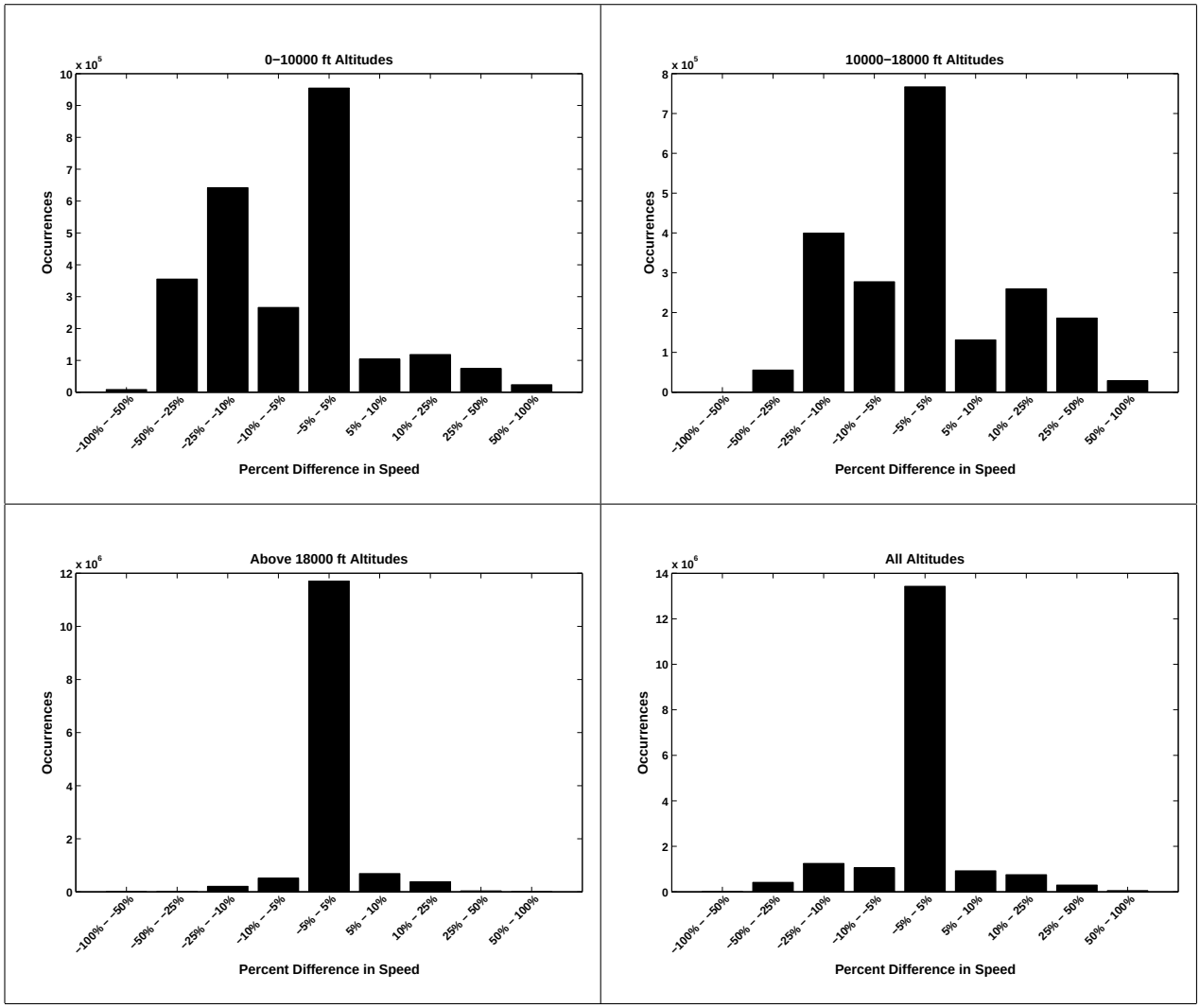

Figure 5.4: Percent difference in speed, all tracks, 3 minute projection

With a five minute projection, the differences in bearing at low altitudes are very high as shown in Fig. 5.5. At high altitudes the distribution is a very strong peak and appears to be Gaussian, but at lower altitudes the distribution is much more spread. Below 10,000 ft, the distribution shows clear peaks left and right of zero error. These peaks are also evident for 10,000 ft to 18,000 ft, but definitely less pronounced. It is not clear what these peaks relate to.

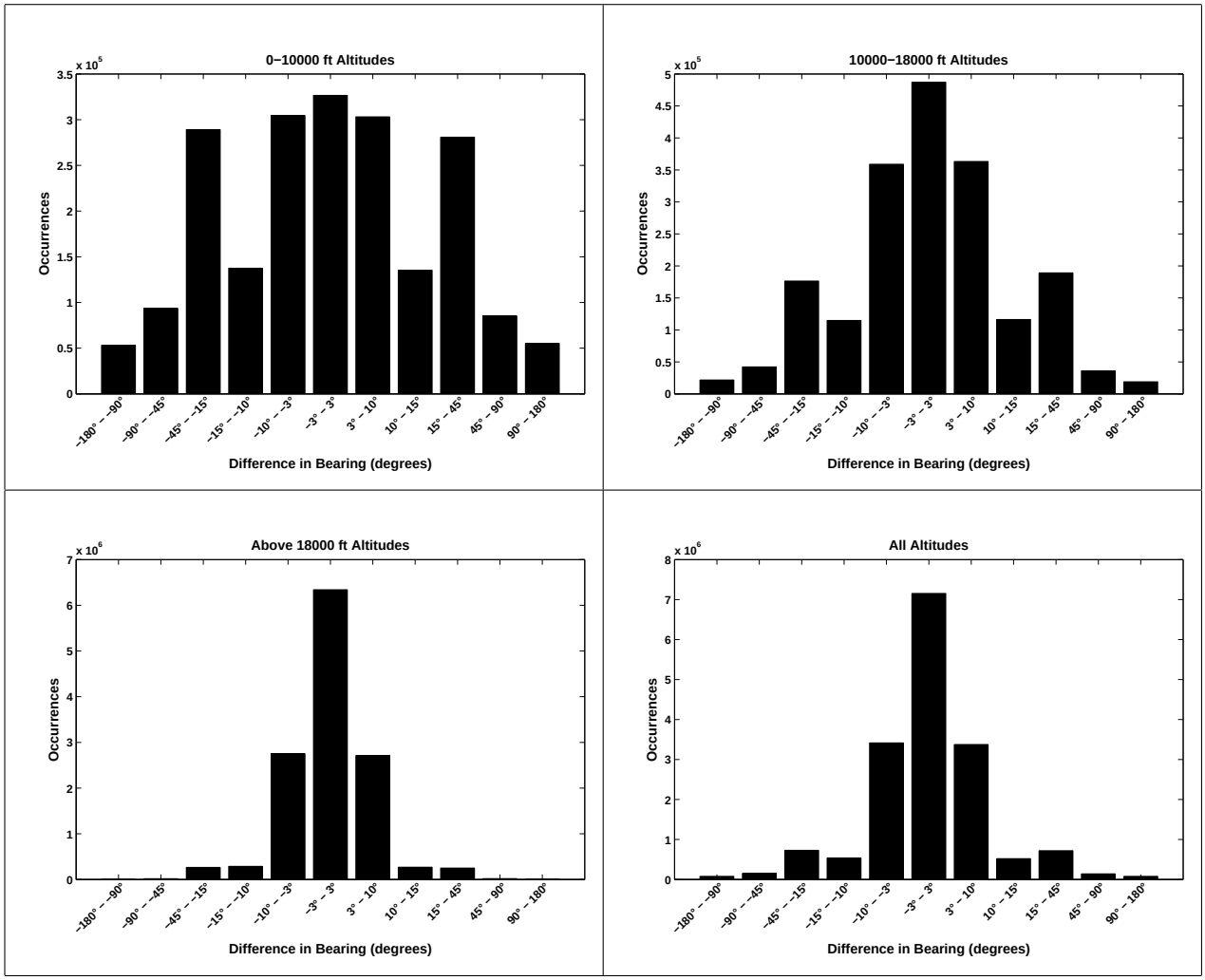

Figure 5.5: Difference in bearing, all tracks, 5 minute projection

A slightly different way of looking at the probability density functions is through a three dimensional histogram bar chart. These graphs are somewhat more difficult to read quantitatively, but they provide a clear qualitative picture of the statistical distribution. Figure 5.6 below shows the characteristics of air traffic around Fort Campbell in Kentucky. The segments of any air traffic that passed within a 50 km radius around Fort Campbell were included in these plots. As home to the 101st Airborne Division, the area around Fort Campbell sees significant military air traffic. These plots show data for a one minute

projection in time. As expected, the data show a tighter distribution at higher altitudes than at low altitudes. At low altitudes, a number of peaks are seen around the central peak. This is probably due to the low sample size of this local data. Note that the central peak on the less than 10,000 ft chart is around 40 occurrences compared to a peak of around 800 occurrences above 18,000 ft.

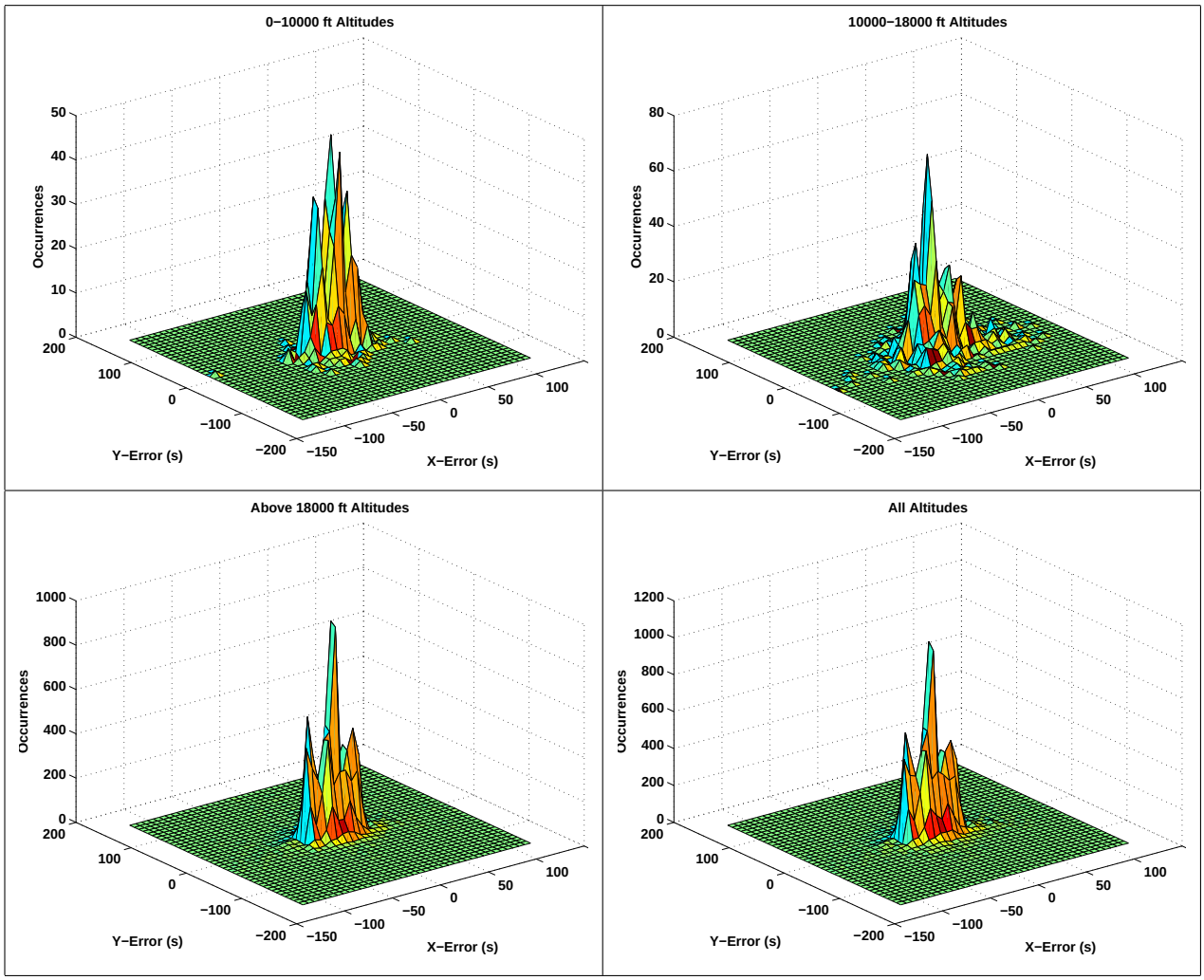

Figure 5.6: Fort Campbell, 50 km radius, 1 minute projection, difference in projection to measured three dimensional histograms

The bar histograms below in Fig. 5.7 show the differences in altitude for air traffic around Fort Campbell. This is again a one minute projection in time. Here the altitude is predictable as expected above 18,000 ft and also very predictable below 10,000 ft. More variation is seen in the 10,000 to 18,000 ft range, but as seen before, that is most likely due to aircraft transitioning through those altitudes.

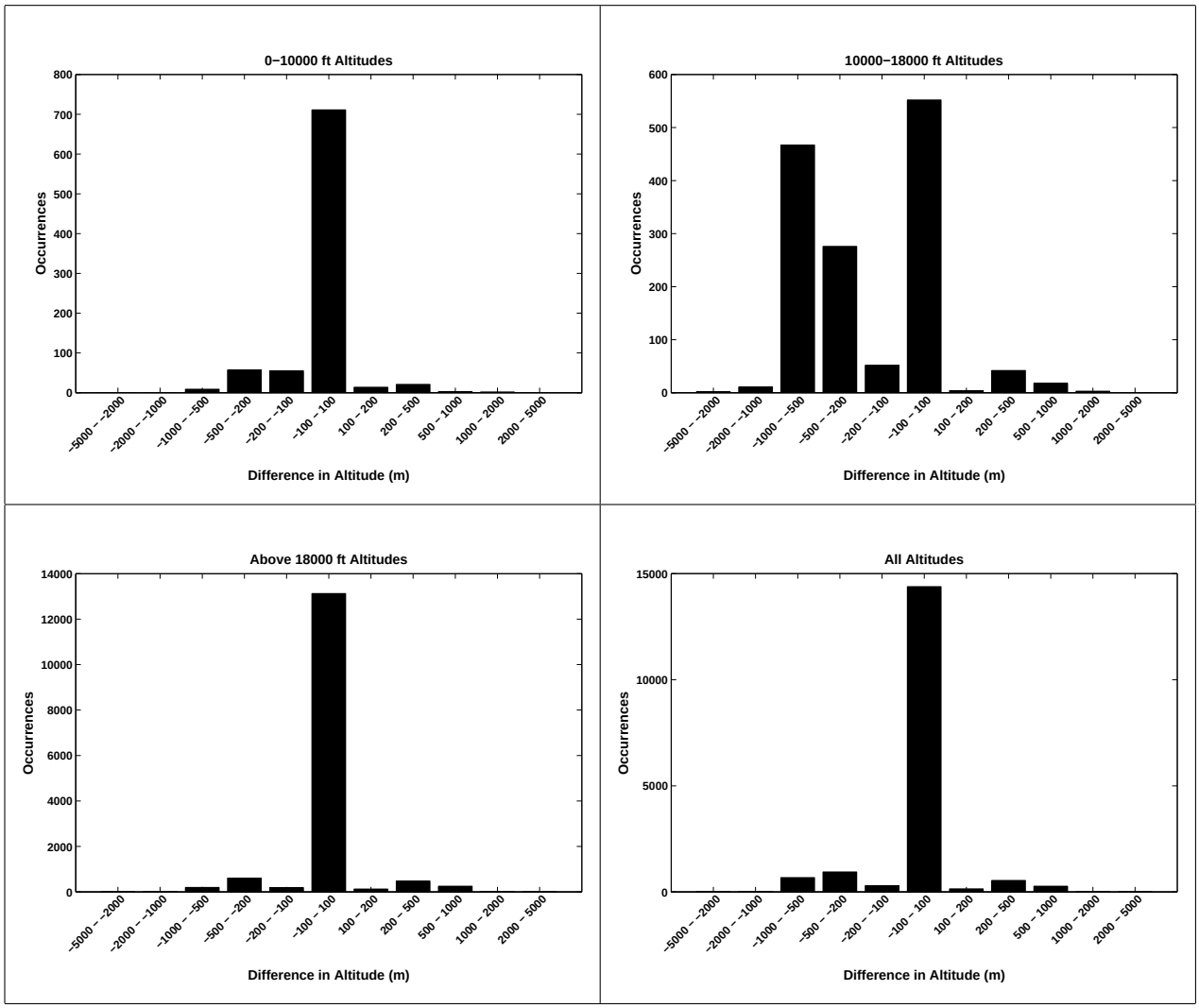

Figure 5.7: Fort Campbell, 50 km radius, 1 minute projection, difference in altitude

Figure 5.8 shows the accuracy of the bearing estimates for a one minute projection. There is a strong central peak even at low altitudes, but the distribution is distinctly non Gaussian and it spreads across the large bearing swath. In the flight levels (above 18,000 ft), the distribution returns to looking more Gaussian.

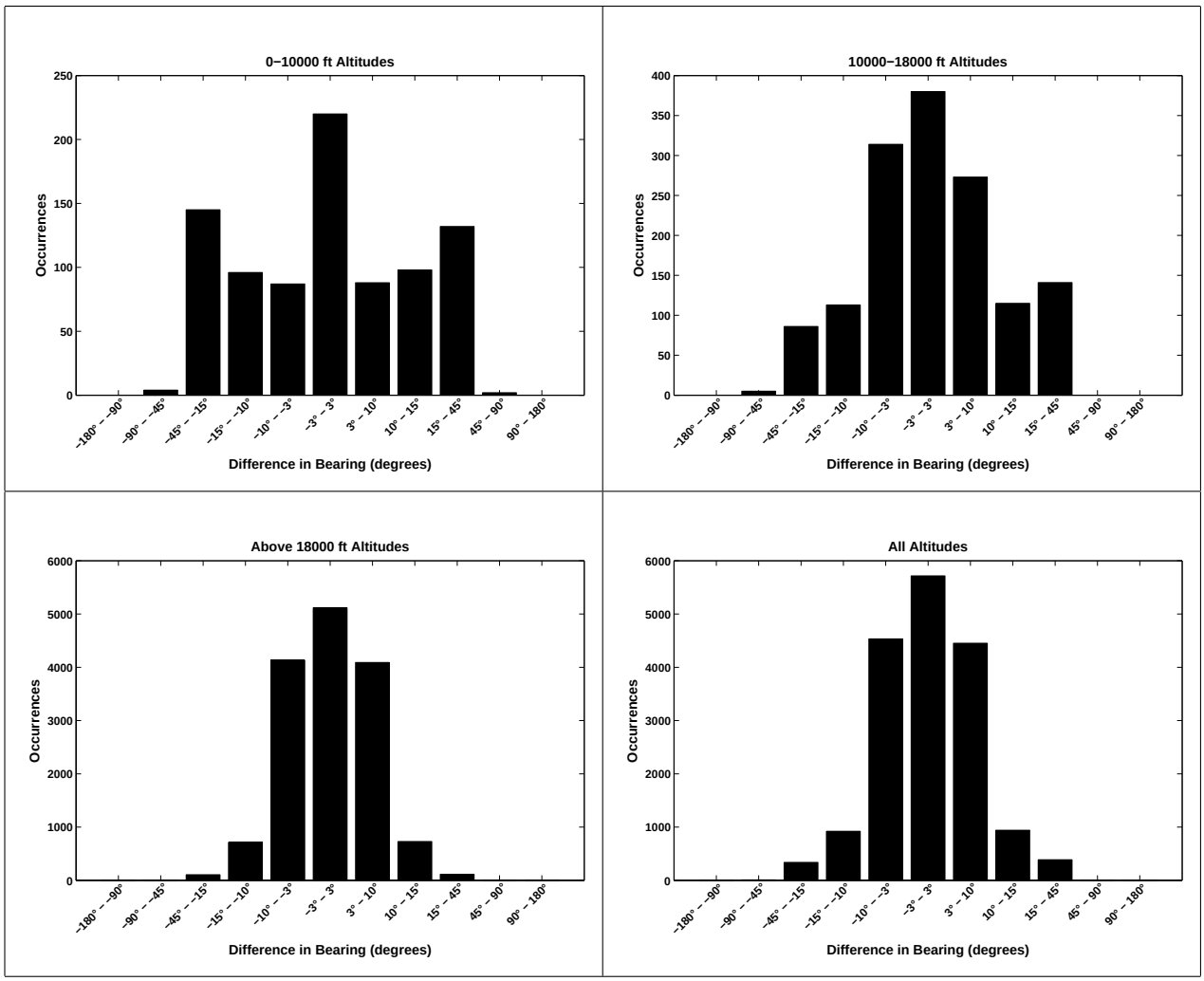

Figure 5.8: Fort Campbell, 50 km radius, 1 minute projection, difference in bearing

The next two figures compare the traffic around Fort Campbell, Kentucky and Las Cruces, New Mexico. Las Cruces in Fig. 5.9, was selected because while it is lightly populated and hence would not normally see high amounts of air traffic, restricted areas in the area

funnel air traffic passing through the region into a narrow section nearby. Consequently, the air traffic should reflect a significant amount of aircraft just passing through. This hypothesis is borne out in the data. Fort Campbell in Fig. 5.10, shows that because of its terminal nature, it is less predictable at all altitude ranges than Las Cruces. More error points lie in front of the original position for Las Cruces than Fort Campbell yet both share common error trends at the 10,000 to 18,000 feet ranges. At 10,000 to 18,000 ft altitudes, the Las Cruces region is more concentrated around the zero error point than Fort Campbell, as expected.

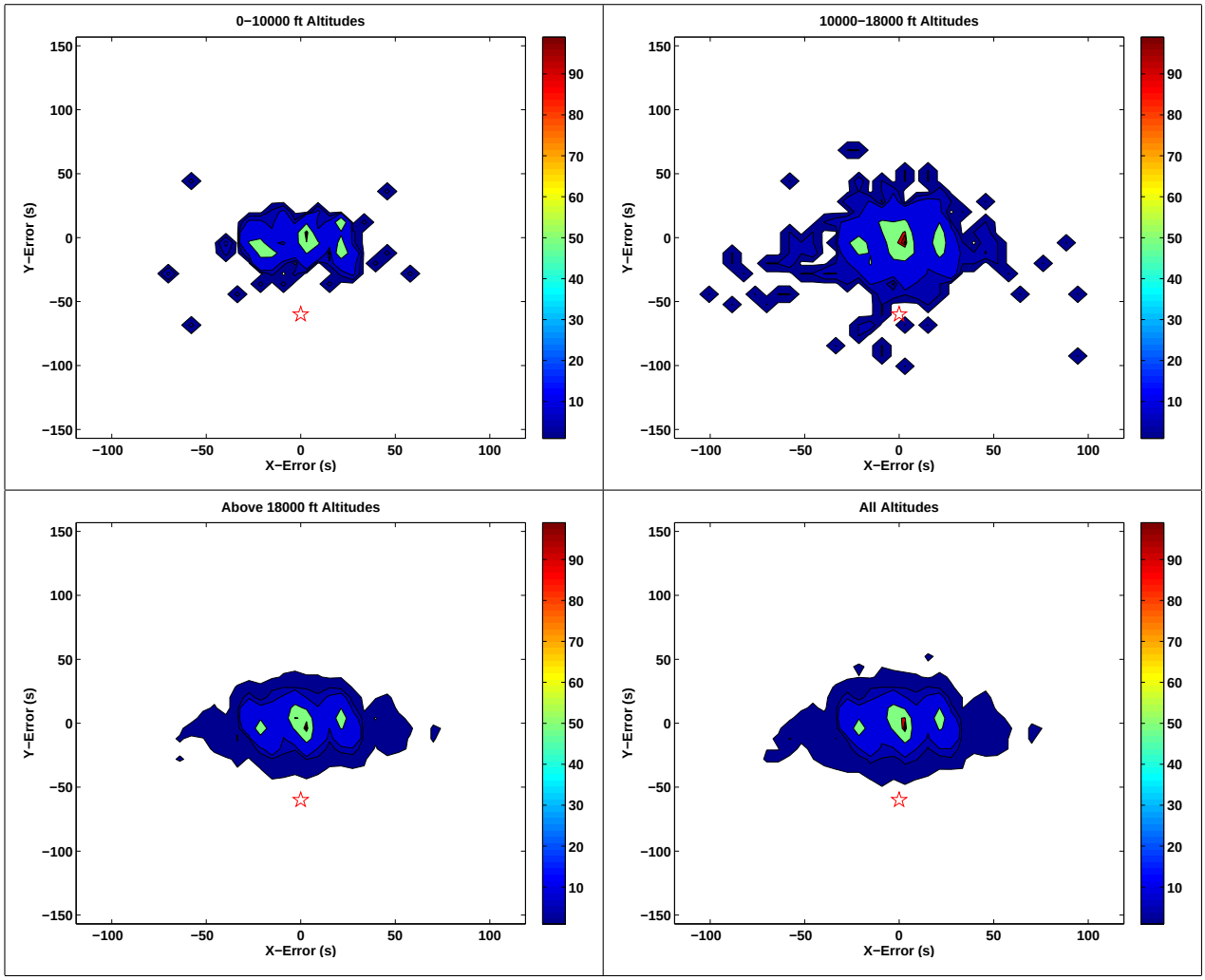

Figure 5.9: Las Cruces, 50 km radius, 1 minute projection, difference in projection to measured histograms

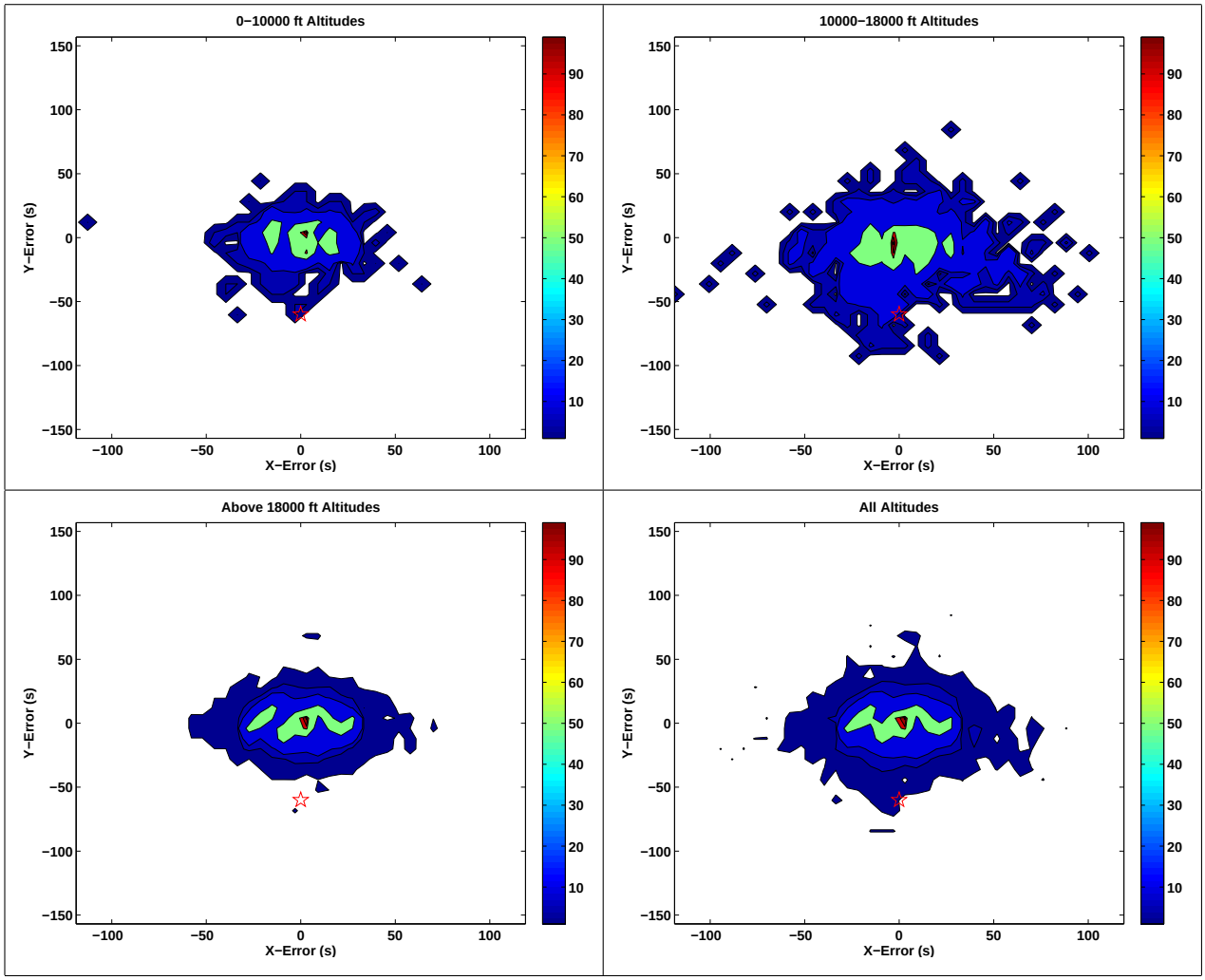

Figure 5.10: Fort Campbell, 50 km radius, 1 minute projection, difference in projection to measured histograms

If we expand the radius around Fort Campbell and Las Cruces to 250 km the trends continue approximately the same. Figures 5.11 and 5.12 show a one minute projection for both the areas. As noted before, the density functions for Las Cruces are slightly more compact and are more in front of the original position instead of spreading behind the original position point.

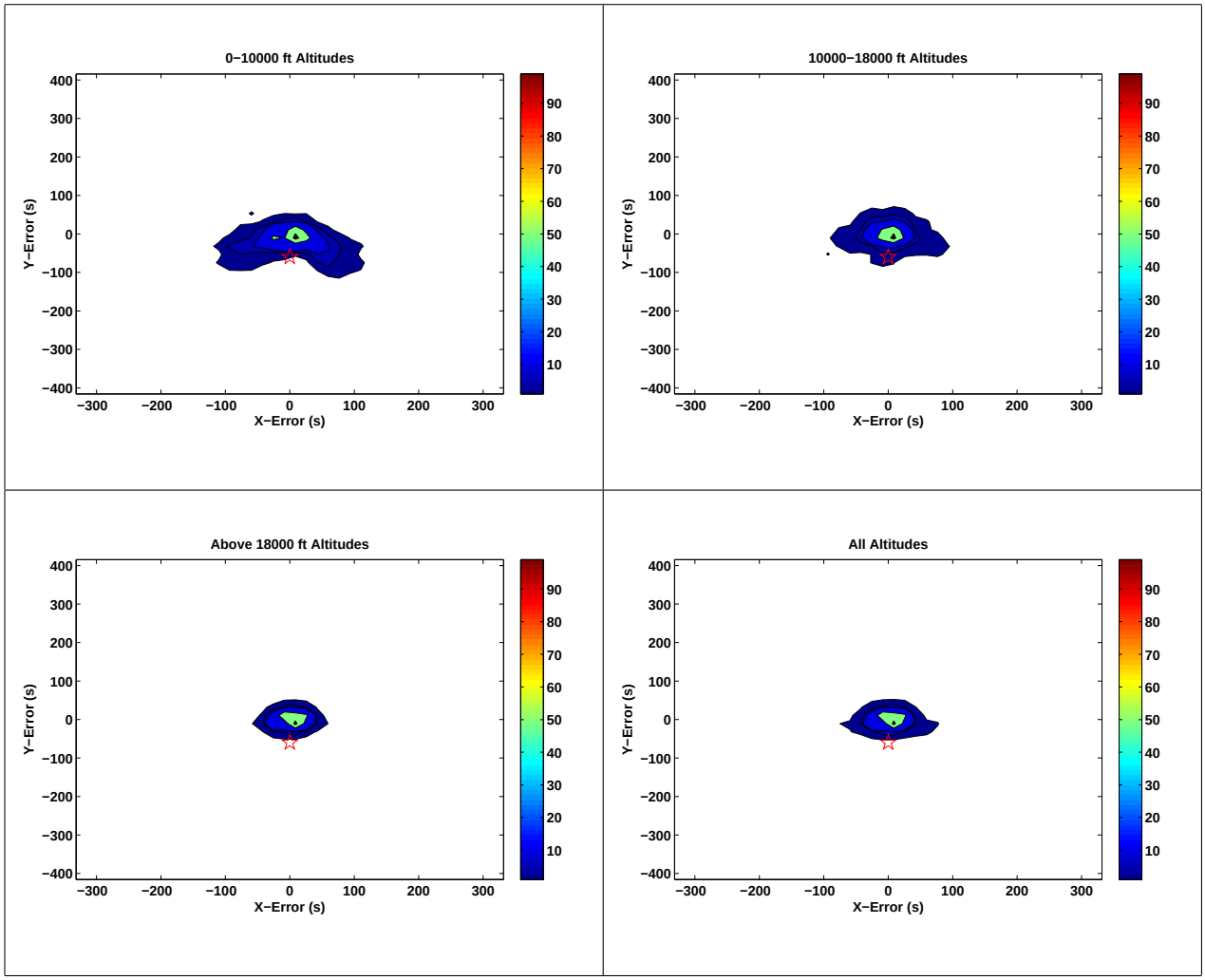

Figure 5.11: Las Cruces, 250 km radius, 1 minute projection, difference in projection to measured histograms

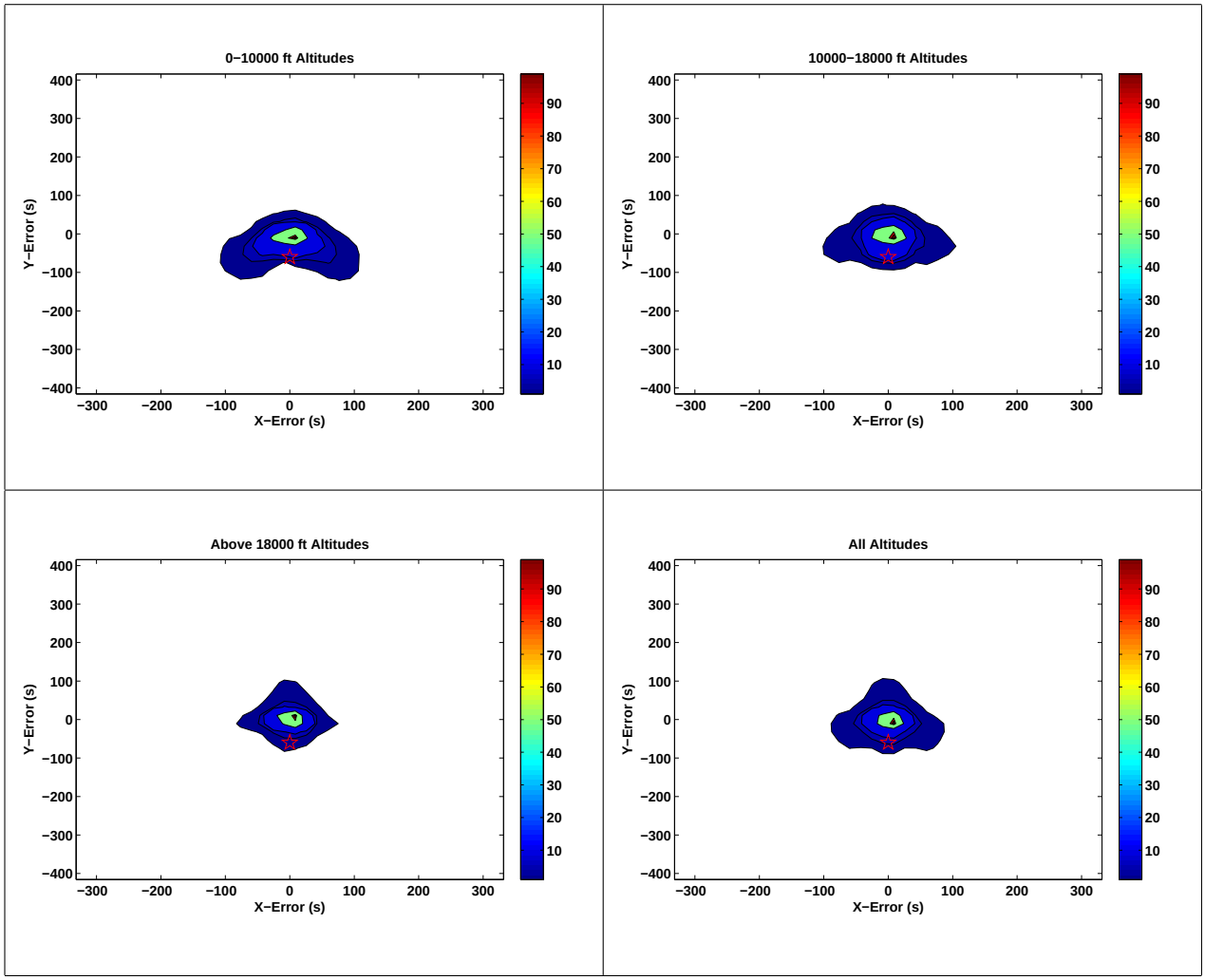

Figure 5.12: Fort Campbell, 250 km radius, 1 minute projection, difference in projection to measured histograms

Increasing the projection from one minute to five minutes changes the plots significantly but not the overall character. Both the Las Cruces (Fig. 5.13) and Fort Campbell (Fig. 5.14) data show more predictable flying at above 18,000 ft. Las Cruces tracks are more compact at high altitude than Fort Campbell.

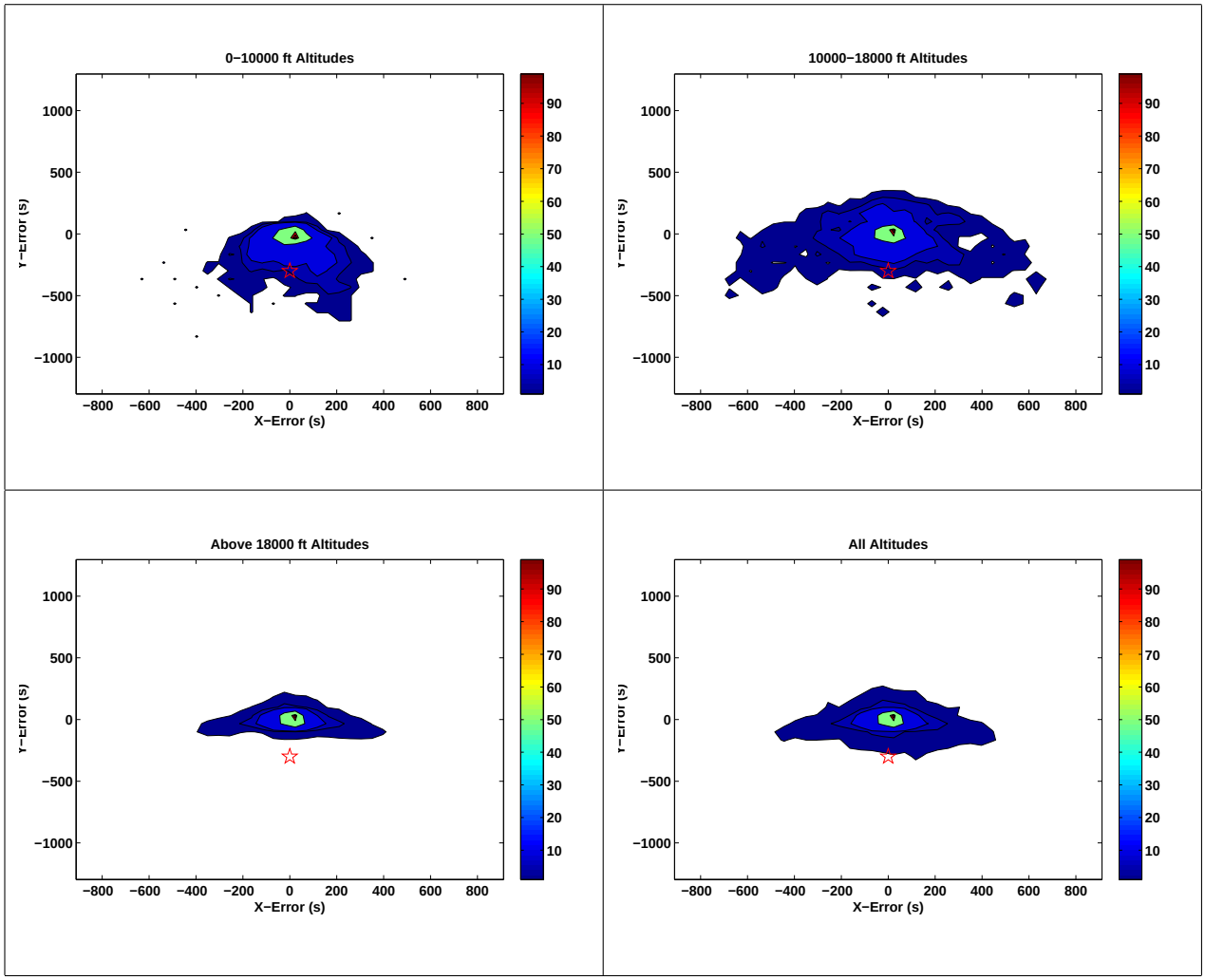

Figure 5.13: Las Cruces, 250 km radius, 5 minute projection, difference in projection to measured histograms

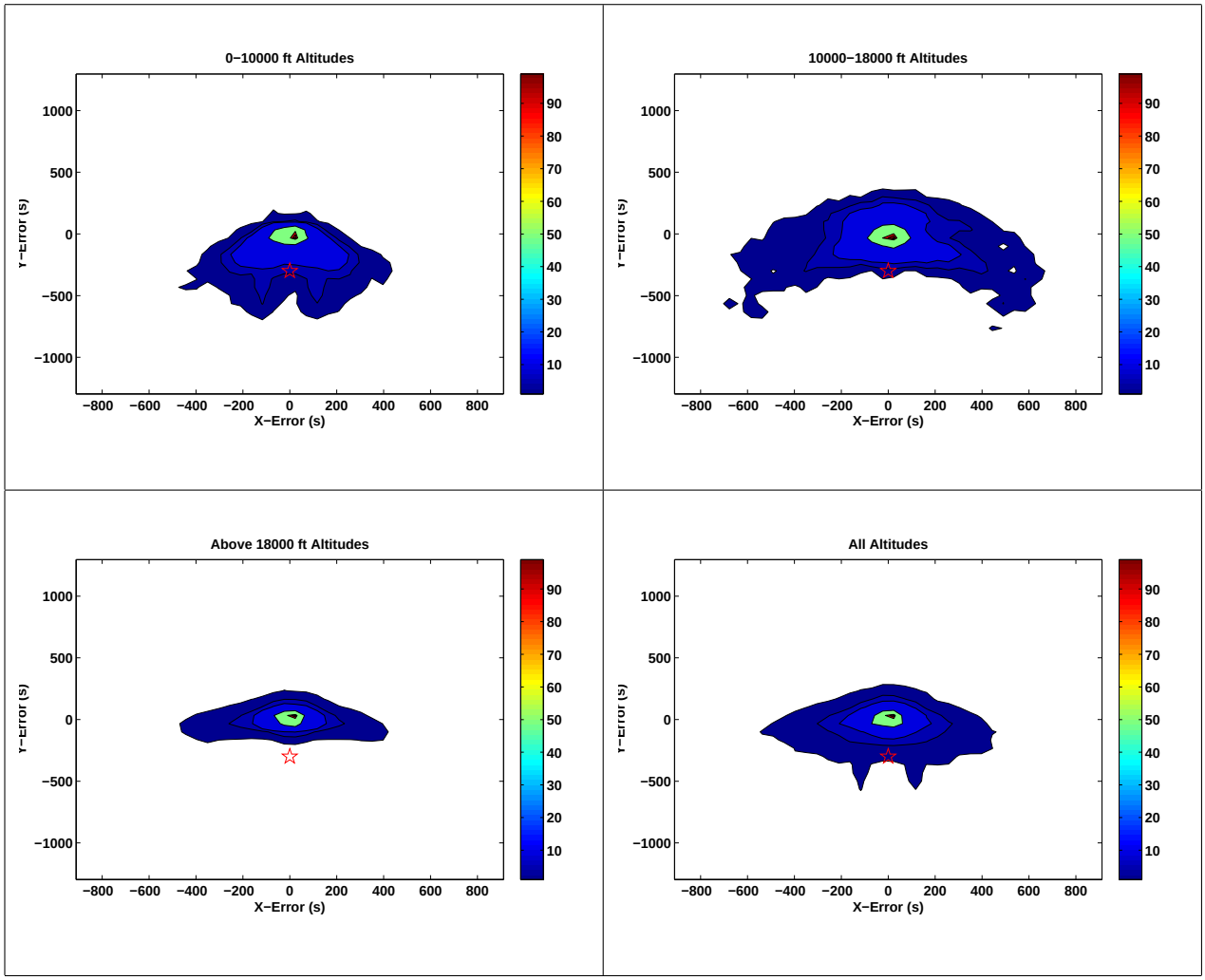

Figure 5.14: Fort Campbell, 250 km radius, 5 minute projection, difference in projection to measured histograms

In order to put these results to use, some metrics have been derived from the data. By sorting the data and finding percentiles within the data, some conclusions can be drawn. The next sets of tables show the confidence intervals for various parameters and altitude ranges. Tables 5.1 through 5.4 show the altitude confidence intervals. Using Table 5.1 for example, one could say that an aircraft will stay within 732 m over one minute 95% of the time, or within 3,139 m over five minutes 99% of the time.

Table 5.1: Altitude Confidence, All Tracks, 0-10000 ft Altitudes

	Confidence (m)			
Projection Time	0.75	0.90	0.95	0.99
1 Minute	335	549	732	1067
3 Minute	914	1341	1737	2438
5 Minute	1433	1920	2286	3139
10 Minute	2499	3292	3749	4602

Table 5.2: Altitude Confidence, All Tracks, 10000-18000 ft Altitudes

	Confidence (m)			
Projection Time	0.75	0.90	0.95	0.99
1 Minute	549	732	823	1067
3 Minute	1585	2042	2316	2865
5 Minute	2530	3200	3597	4359
10 Minute	4237	5243	5852	6858

Table 5.3: Altitude Confidence, All Tracks, Above 18000 ft Altitudes

	Confidence (m)			
Projection Time	0.75	0.90	0.95	0.99
1 Minute	30	427	610	853
3 Minute	274	1280	1676	2347
5 Minute	610	2042	2682	3658
10 Minute	1219	3749	4877	6431

Table 5.4: Altitude Confidence, All Tracks, All Altitudes

	Confidence (m)			
Projection Time	0.75	0.90	0.95	0.99
1 Minute	274	518	671	945
3 Minute	762	1463	1860	2469
5 Minute	1188	2316	2896	3810
10 Minute	2134	4084	4999	6462

Tables 5.5 through 5.8 may be a more reasonable metric, the expected error in bearing (or more precisely heading). This data clearly indicate the aircraft become more predictable at higher altitudes. At 20,000 ft for example, an aircraft will maintain bearing within about 20 degrees for 10 minutes with 95% confidence.

Table 5.5: Bearing Confidence, All Tracks, 0-10000 ft Altitudes

	Confidence (degrees)			
Projection Time	0.75	0.90	0.95	0.99
1 Minute	22.4	41.9	61.7	96.5
3 Minute	25.1	58.2	88.6	133.2
5 Minute	26.5	58.2	92.2	148.3
10 Minute	21.4	40.7	60.7	141.5

Table 5.6: Bearing Confidence, All Tracks, 10000-18000 ft Altitudes

	Confidence (degrees)			
Projection Time	0.75	0.90	0.95	0.99
1 Minute	12.6	21.4	29.8	58.8
3 Minute	12.8	26.3	40.9	94.0
5 Minute	15.1	31.9	52.3	125.2
10 Minute	16.9	34.2	56.8	137.2

Table 5.7: Bearing Confidence, All Tracks, Above 18000 ft Altitudes

	Confidence (degrees)			
Projection Time	0.75	0.90	0.95	0.99
1 Minute	7.6	10.3	12.7	21.9
3 Minute	5.5	8.6	11.9	26.1
5 Minute	5.5	9.2	13.8	30.5
10 Minute	6.3	11.9	18.2	41.0

Table 5.8: Bearing Confidence, All Tracks, All Altitudes

	Confidence (degrees)			
Projection Time	0.75	0.90	0.95	0.99
1 Minute	9.3	16.8	24.9	62.0
3 Minute	7.2	15.4	27.4	82.2
5 Minute	7.3	16.6	28.8	86.8
10 Minute	8.0	17.3	27.5	70.3

Table 5.9: Distance Confidence, All Tracks, 0-10000 ft Altitudes

	Confidence (%)			
Projection Time	0.75	0.90	0.95	0.99
1 Minute	25.6	48.0	64.8	104.6
3 Minute	22.5	42.2	65.4	143.7
5 Minute	29.8	62.9	121.8	305.0
10 Minute	47.2	94.8	166.8	507.5

Table 5.10: Distance Confidence, All Tracks, 10000-18000 ft Altitudes

	Confidence (%)			
Projection Time	0.75	0.90	0.95	0.99
1 Minute	18.9	35.8	51.4	82.1
3 Minute	15.8	23.7	29.2	47.1
5 Minute	19.4	27.9	34.2	60.3
10 Minute	27.2	38.3	47.6	118.4

Table 5.11: Distance Confidence, All Tracks, Above 18000 ft Altitudes

	Confidence (%)			
Projection Time	0.75	0.90	0.95	0.99
1 Minute	8.9	13.8	18.0	35.8
3 Minute	5.1	8.6	11.6	19.0
5 Minute	4.7	8.6	11.9	20.5
10 Minute	4.9	10.6	16.4	30.7

Table 5.12: Distance Confidence, All Tracks, All Altitudes

	Confidence (%)			
Projection Time	0.75	0.90	0.95	0.99
1 Minute	11.7	21.7	34.5	71.2
3 Minute	7.3	15.2	23.0	55.6
5 Minute	7.3	17.1	26.9	84.7
10 Minute	7.7	22.8	35.7	107.2

These confidence bounds could be used to develop metrics for a sense and avoid system. A compilation of all the plots made from the FAA radar data have been attached as Appendix A.

5.2 Private Aircraft GPS Tracks

Similar processing was done to the data gathered from the Auburn University flight training aircraft. This data wil be presented in histogram form with one minute, three minute, and five minute projections. In Fig. 5.15 below show the probability density function for a one minute projection in time using a constant velocity Kalman filter. The left figure shows data including the full aircraft track while the figure on the right shows data where portions of the tracks where the aircraft is operating in a traffic pattern reduces the number of maneuvers and the wrap around effect (where the track is going in the opposite direction of the projected position) is reduced.

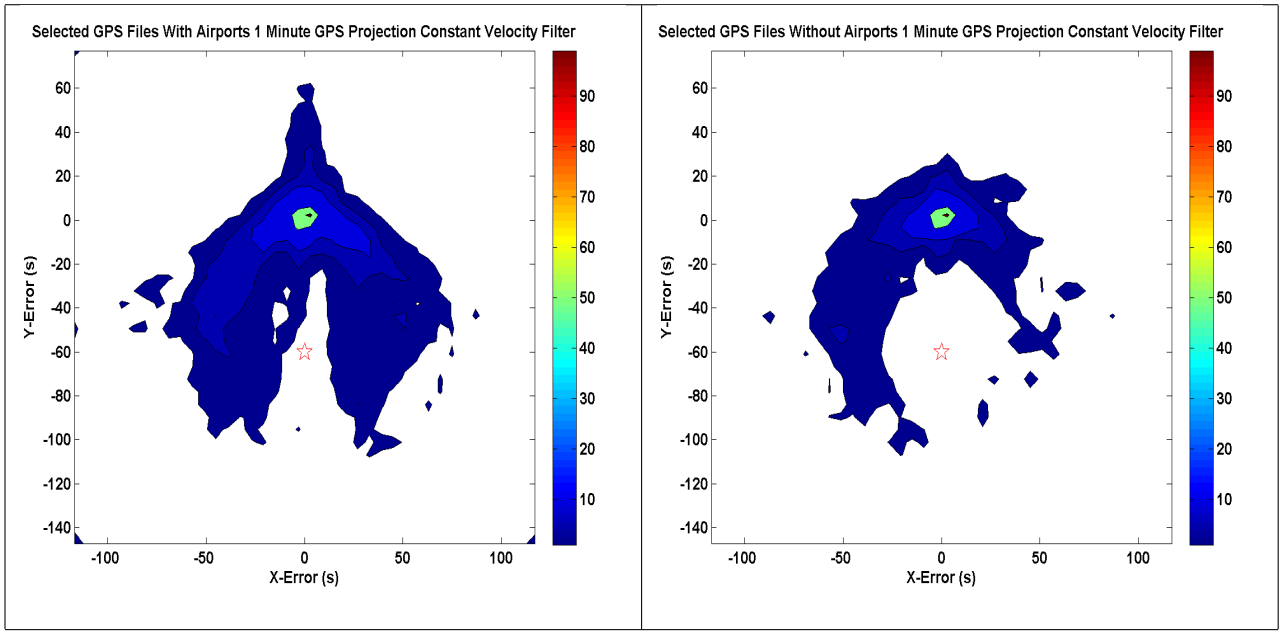

Figure 5.15: Selected GPS files with and without airports, 1 minute GPS projection using a constant velocity filter

Figure 5.16 show results for both a constant velocity Kalman filter (on the left) and a constant acceleration filter (on the right). Both of the figures have had the airport regions removed. The constant acceleration model on the right does a slightly better job of predicting the future positions and has a smaller spread. However, the constant acceleration model shows more along-track variation than the constant velocity filter (note the projection of the blue area forward from the peak and backward behind the peak).

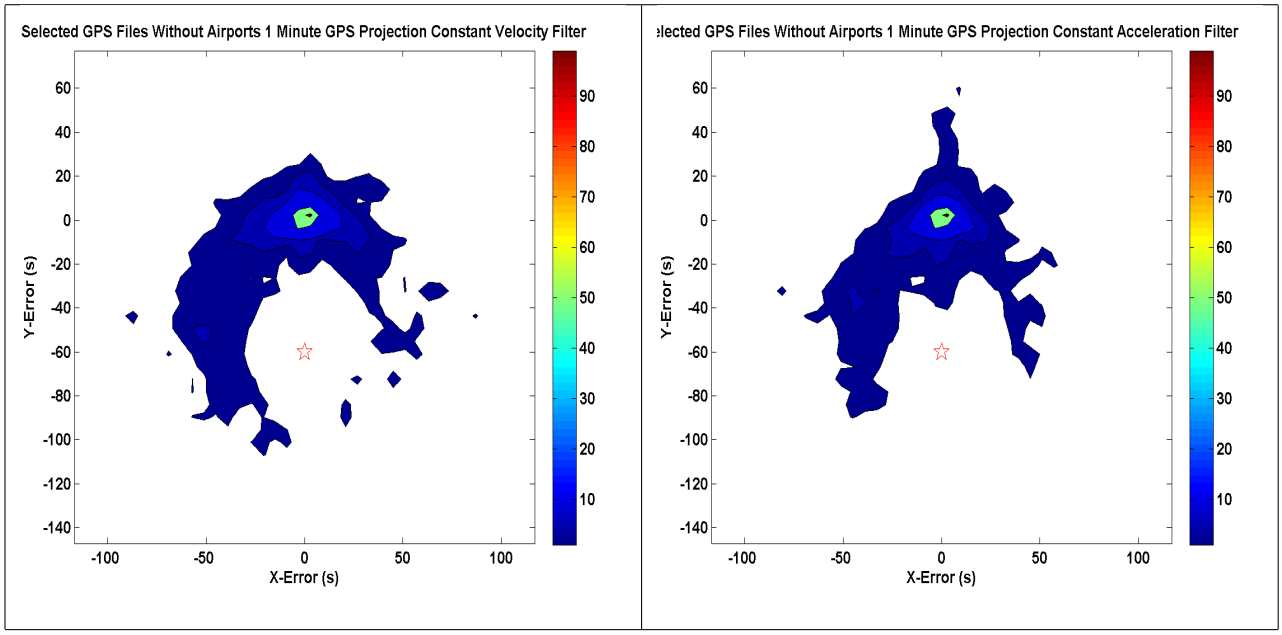

Figure 5.16: Selected GPS files with and without airports, 1 minute GPS projection using a constant velocity filter

A simple approach to calculating the velocity is to do a backwards difference between the positions at one point in time and a previous point in time. The left hand figure in 5.17 was prepared using this approach. The right-hand figure was computed using the GPS velocity at each time step. Very little difference can be noted between the two plots. The lower figure is the set shows results using a moving average of the GPS velocity. These results very closely model the other two methods.

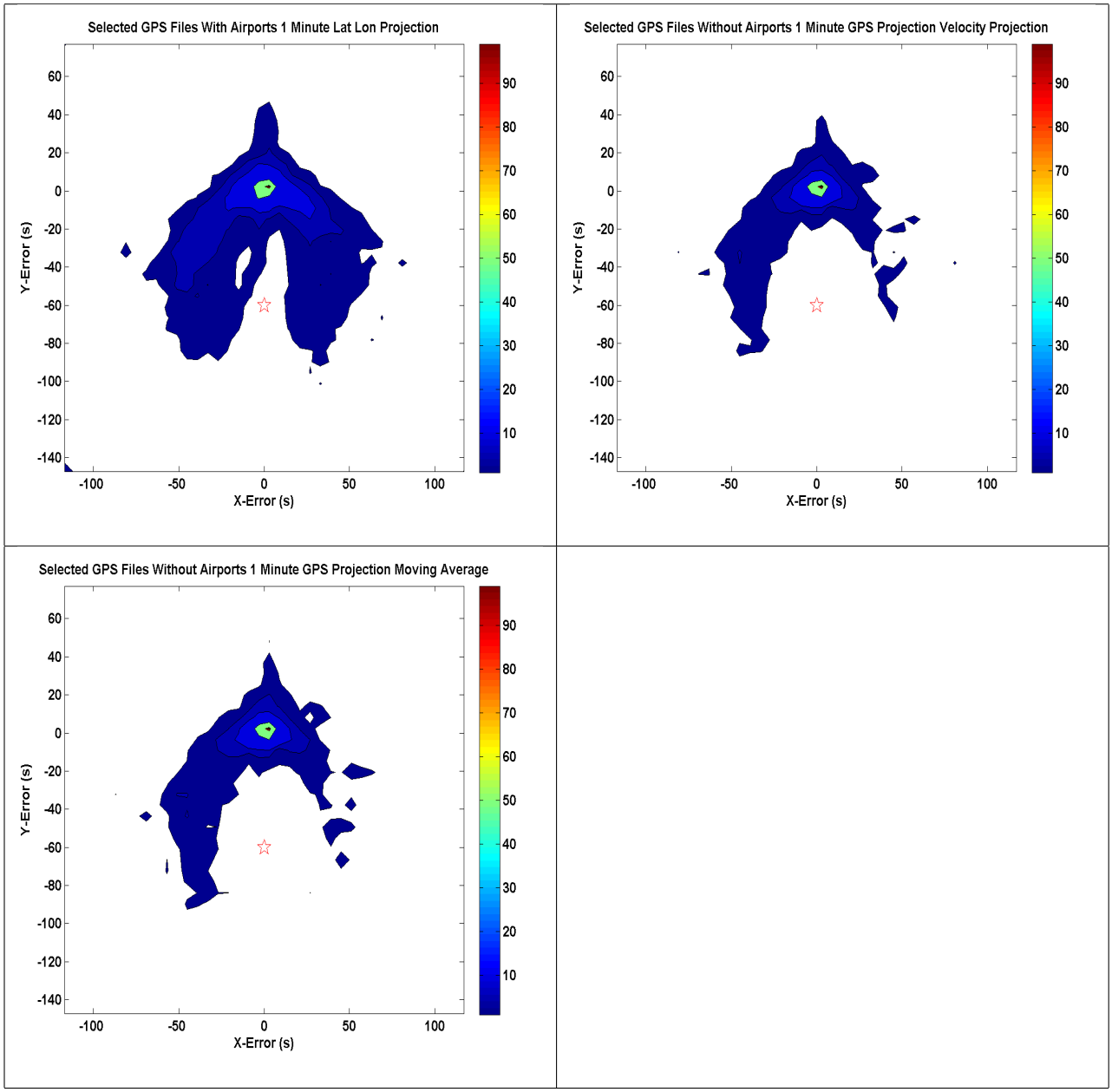

Figure 5.17: Selected GPS files with and without airports, 1 minute GPS projection using a constant velocity filter

Comparing all the different velocity estimation techniques shows that the Kalman filters have a tendency to under predict the wraparound effect by over predicting the distance but the density of the error is larger while the other projection techniques under predict the

change in bearing. The constant acceleration filter better predicts the distance, depicted in the figure by a more consistent radius about the initial point than the constant velocity Kalman filter.

Figure 5.18 shows the effect of different projection times on the results. All of the figures have had airport traffic patterns removed. One interesting feature of all of the plots is an apparent tendency to turn to the left more often than the right. That may be a behavioral issue since student pilots may be more comfortable turning toward the side where they are sitting when doing various maneuvers. The figures clearly indicate the increased uncertainty as the projection time increases.

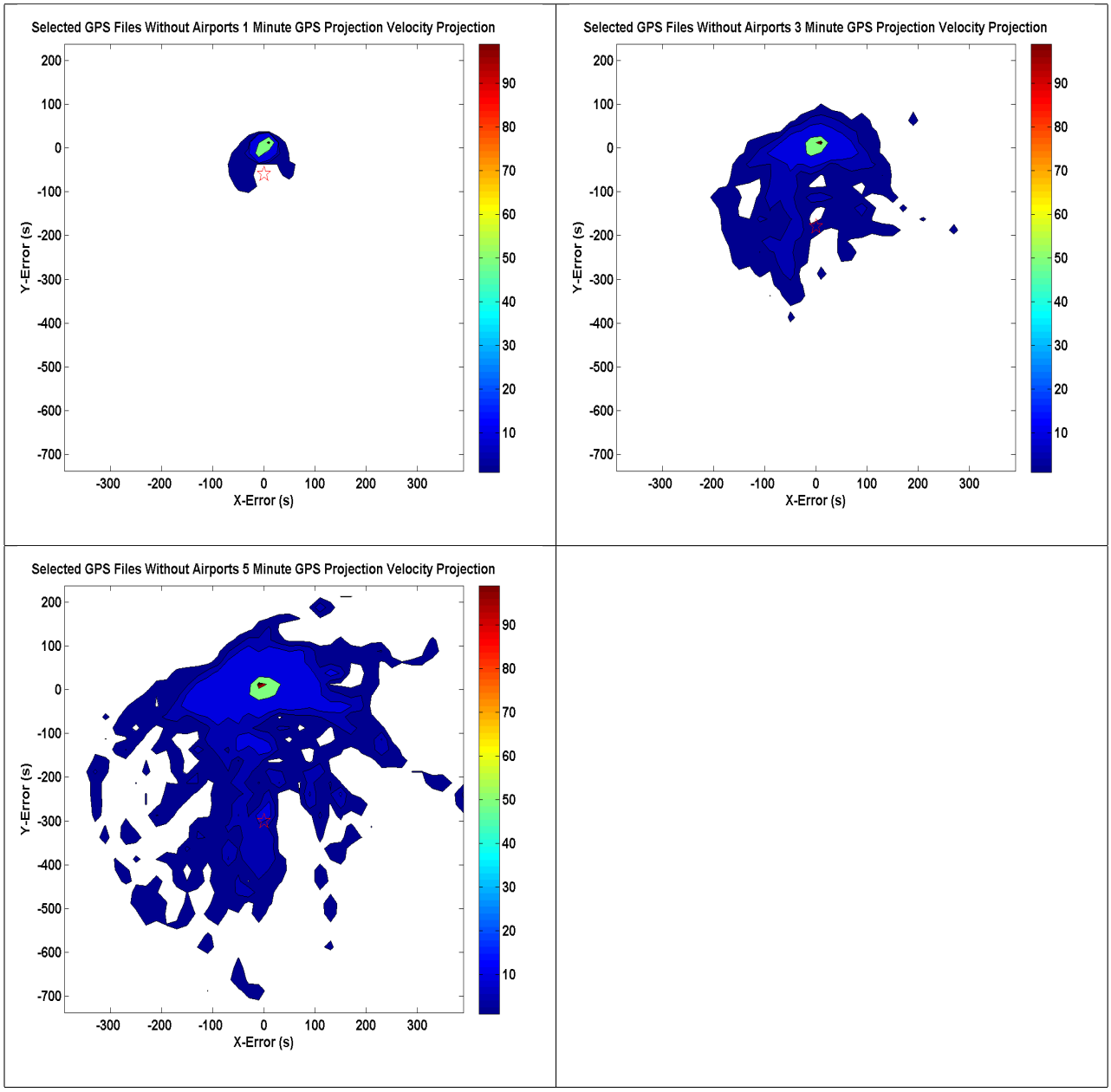

Figure 5.18: Selected GPS files with and without airports, 1 minute GPS projection using a constant velocity filter

Appendix B contains a compilation of all the GPS data results.

5.3 Comparison of Projection Techniques

Each of the projection techniques showed to have both strengths and weaknesses during all stages of the flight. As expected by the different Kalman filter models, the constant velocity model projected distance better than predicting a maneuver while the constant acceleration model projected changes in bearing better than changes in distance. Looking at the cross-track and along-track error the projection quality of each filter was analyzed to provide information on the filter type needed to predict future position under various flight conditions.

Taking a look at one track recorded by the GPS units in Fig. 5.19, the straight flight can be separated from the maneuvering portions to analyze how the filters perform on each segment. Each segment consist of 30 minutes of flight time. The performance of the constant velocity Kalman filter (CVF), the constant acceleration Kalman filter (CAF), GPS projection (GPS), and the moving average projection (MA) were analyzed using bar plots to show the error cross-track and along-track of the projection.

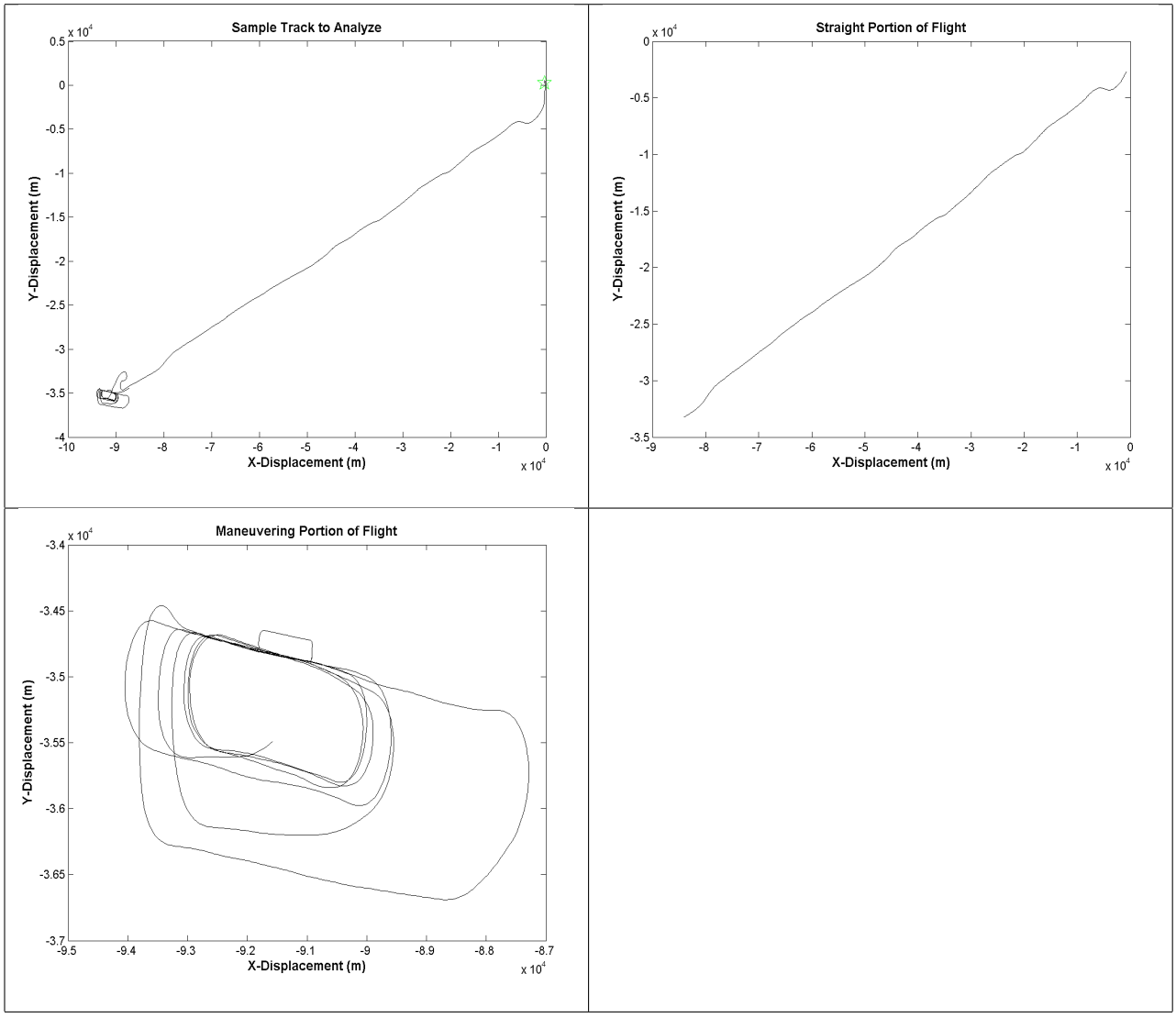

Figure 5.19: Single GPS flight analyzed, breaking the flight into two parts: straight flight and maneuvering flight

Analyzing the straight portion of the track first, the ability of each filter in straight flight is characterized by its projection error cross-track (Fig. 5.20) and along-track (Fig. 5.21).

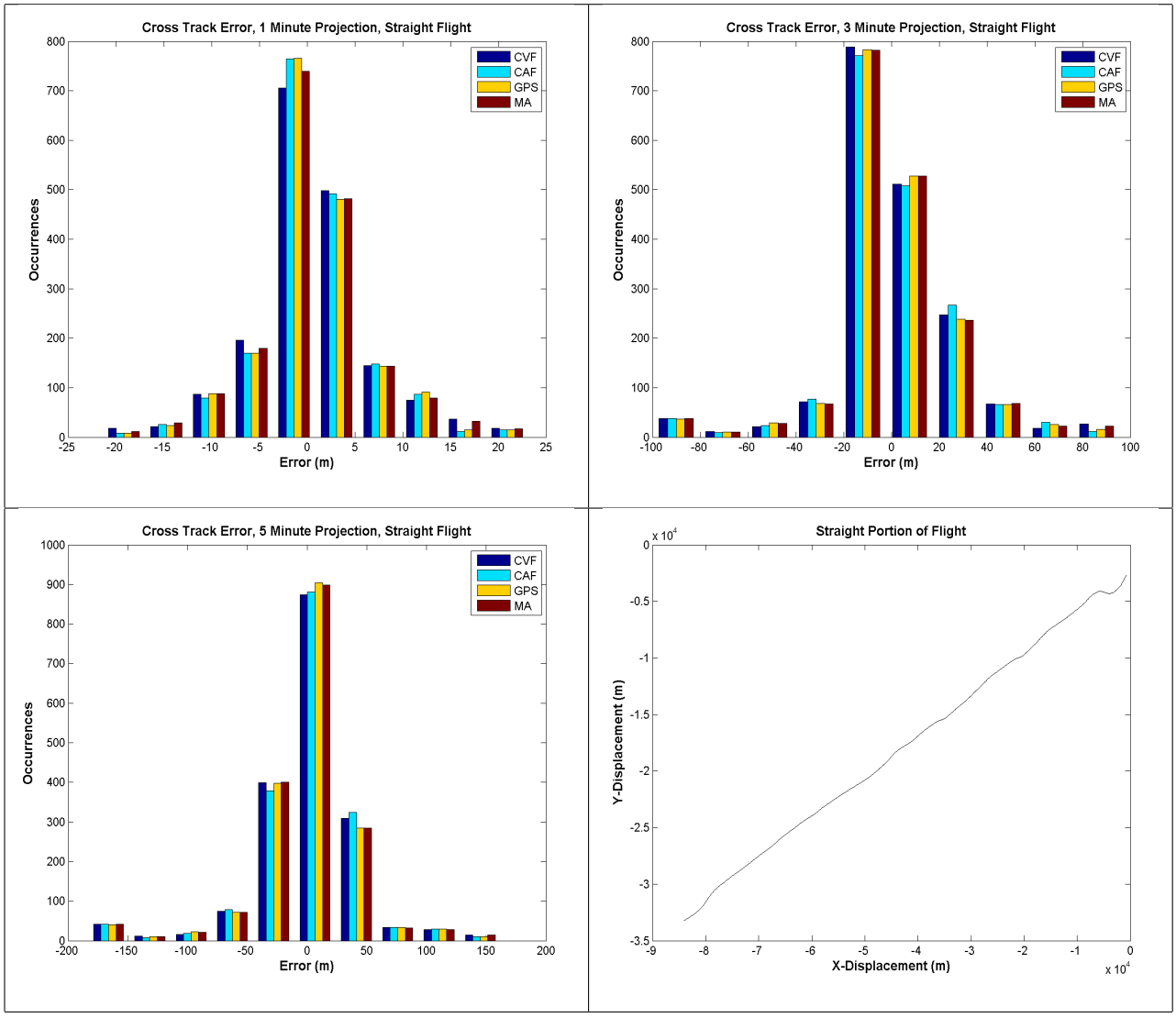

Figure 5.20: Cross track error for straight portion of the track using constant velocity Kalman filter (CVF), constant acceleration Kalman filter (CAV), GPS straight projection (GPS), and a moving average filter (MA)

The cross-track analysis in Fig. 5.20 shows that the error has a Gaussian distribution. Both the constant velocity and constant acceleration Kalman filter perform equally well in predicting corrections in the straight portion of the flight. The error grows with an extended time horizon but a better prediction in cross-track projection is shown in the

constant acceleration case as the projection time grows. The straight GPS projection using course and velocity shows greater error than the moving average. The smoothing of the measurement with the five second moving average window decreases the effect of velocity jumps in the measurements and predicts maneuvers better in predominately straight flight.

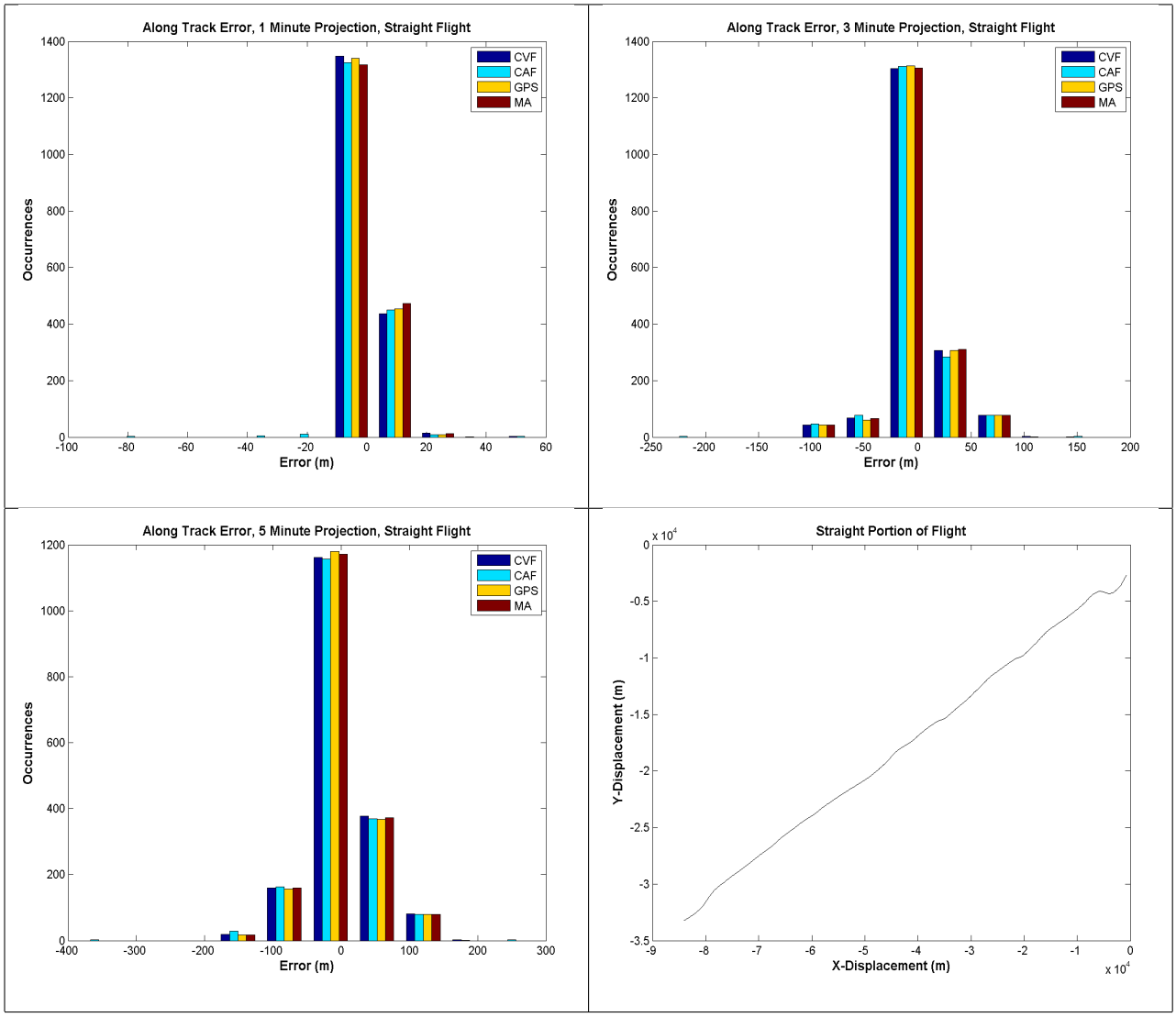

Figure 5.21: Along track error for straight portion of the track using constant velocity Kalman filter (CVF), constant acceleration Kalman filter (CAV), GPS straight projection (GPS), and a moving average filter (MA)

The along-track error in Fig. 5.21 is centered around zero for straight flight as expected, with a majority of the error due to underestimating the distance. For the one minute projection, the constant acceleration Kalman filter under predicts the displacement more often then the constant velocity Kalman filter. Both the GPS projection and the moving average tend to over predict the displacement more than the Kalman filters. In the case of the three and five minute projections, the distribution is Gaussian, giving the straight portion of flight a higher predictability in the along-track projection.

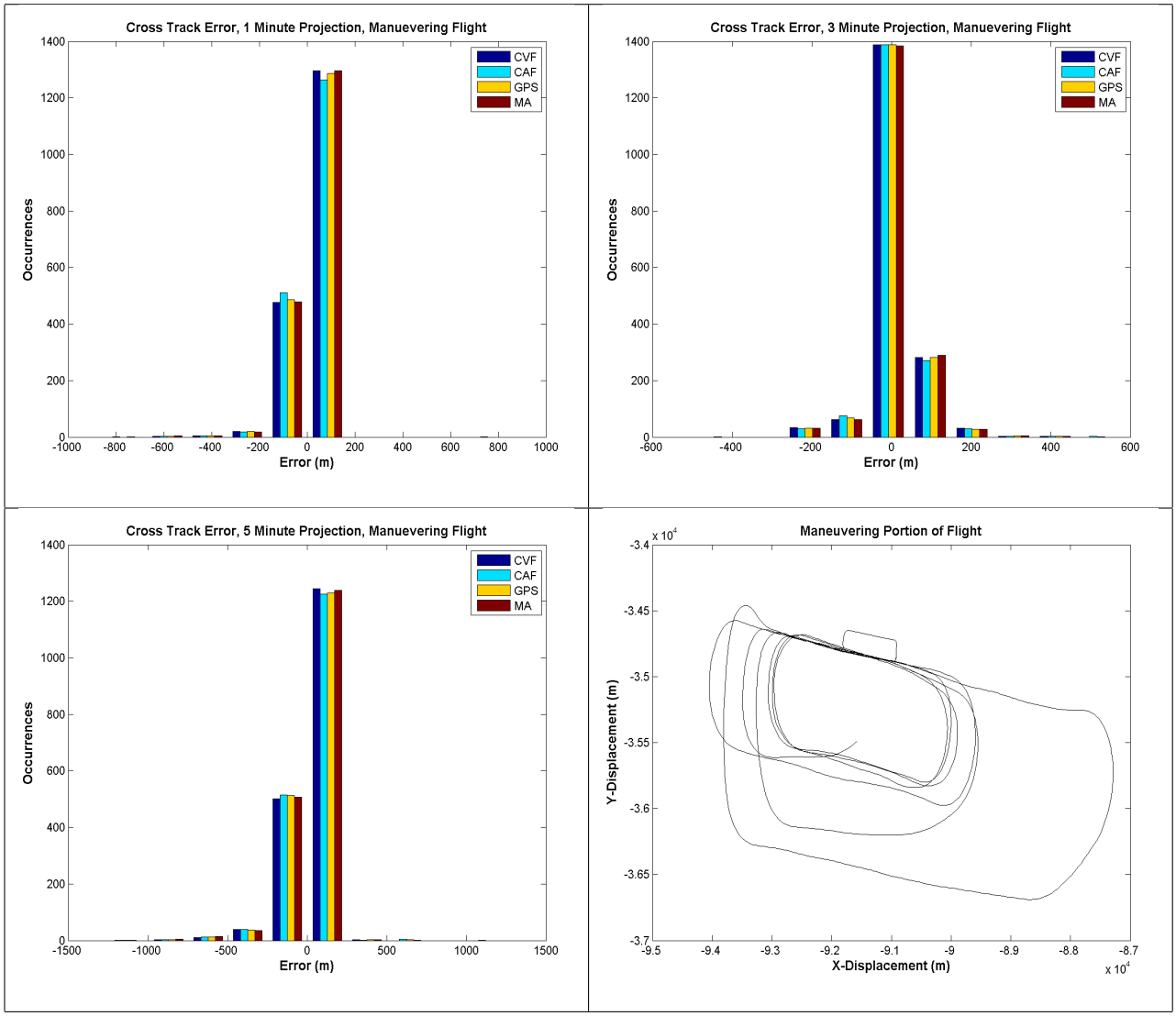

Figure 5.22: Cross track error for maneuvering portion of the track using constant velocity Kalman filter (CVF), constant acceleration Kalman filter (CAV), GPS straight projection (GPS), and a moving average filter (MA)

In maneuvering flight shown in Fig. 5.22, the range in error grows to several times the error distribution for straight flight in the cross-track case. A majority of the maneuvering error lies to the right of the zero error region, mainly because the turns performed by the aircraft in this situation are left-hand turns. The projection sends the estimated position

beyond the turn and under predicts the cross-track position. The constant acceleration Kalman filter holds more error around the zero region than the constant velocity Kalman filter, showing that the acceleration model more accurately predicts maneuvers. The GPS and moving average projections have a Gaussian distribution about the origin of error, more often over predicting the cross-track position, under estimating the magnitude of the maneuvers.

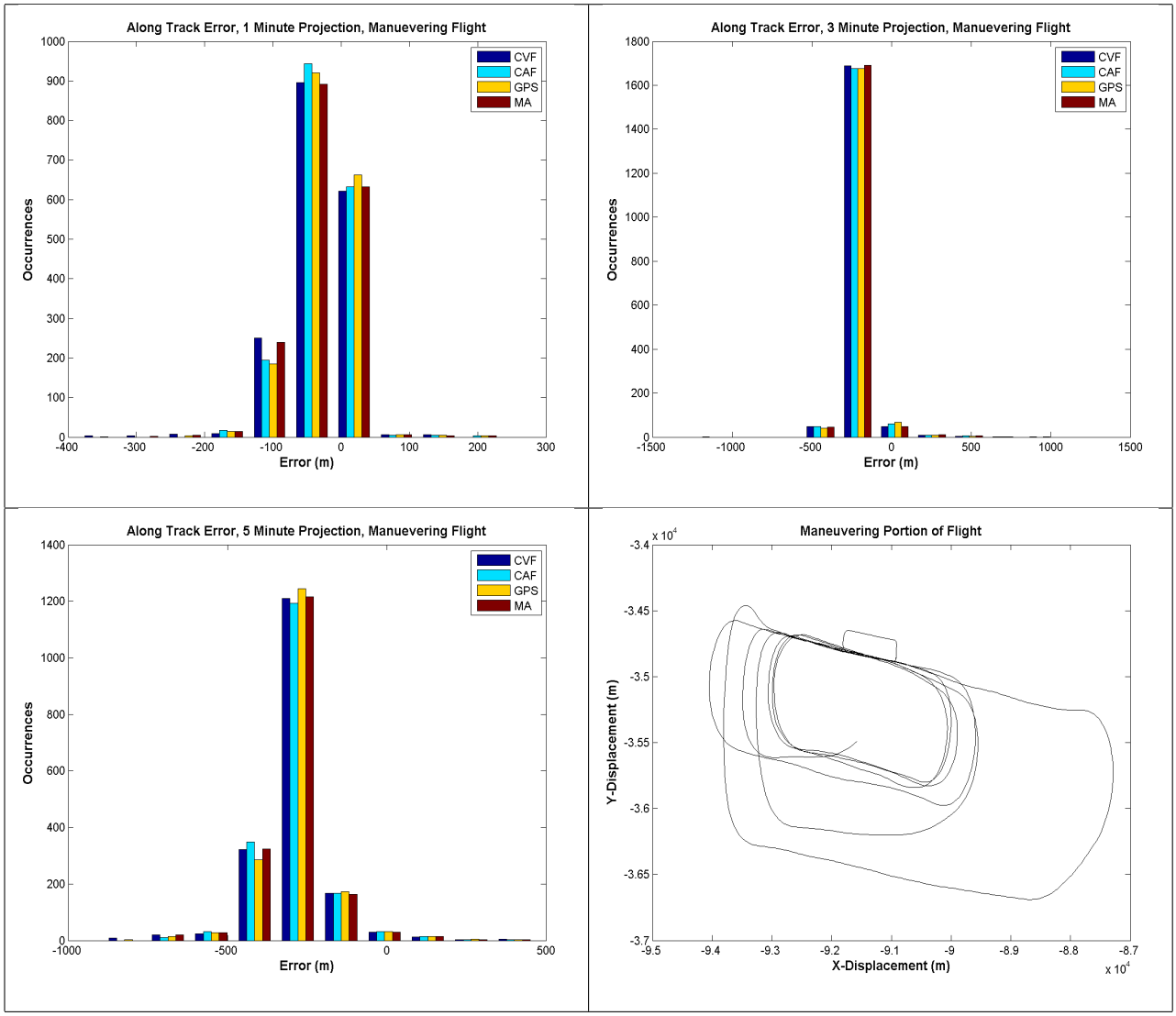

Figure 5.23: Along track error for maneuvering portion of the track using constant velocity Kalman filter (CVF), constant acceleration Kalman filter (CAV), GPS straight projection (GPS), and a moving average filter (MA)

For the maneuvering portion of the flight along-track shown in Fig. 5.23, the error distributions are Gaussian but not about the origin of error. Each projection technique under predicts the projection but constant acceleration Kalman filter retains more error near

the peak of the distribution while the constant velocity Kalman filter has more occurrences away from the origin of the Gaussian distribution.

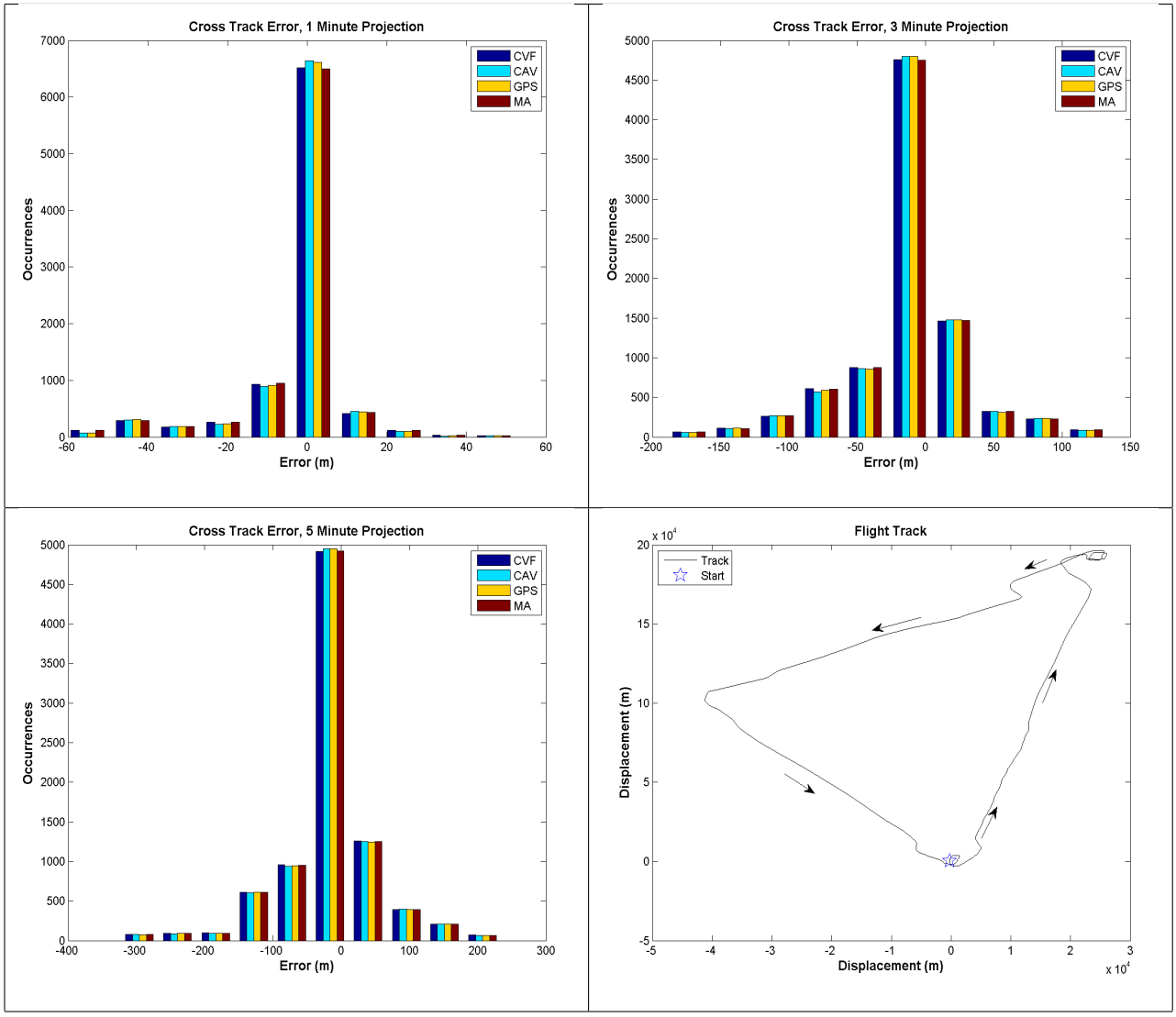

Figure 5.24: Cross track error for all GPS tracks using constant velocity Kalman filter (CVF), constant acceleration Kalman filter (CAV), GPS straight projection (GPS), and a moving average filter (MA)

A full flight is presented in Fig. 5.24. Again, the majority of the maneuvers are left-hand turns, developing growing error to the right of the origin because the projection sends

the predicted position beyond the left-hand turn. For each time horizon, the distribution is Gaussian and the range of error grows with the projection time. Little can be determined about the quality of projection for each projection method in the cross-track error given that the data has both straight and maneuvering flight patterns.

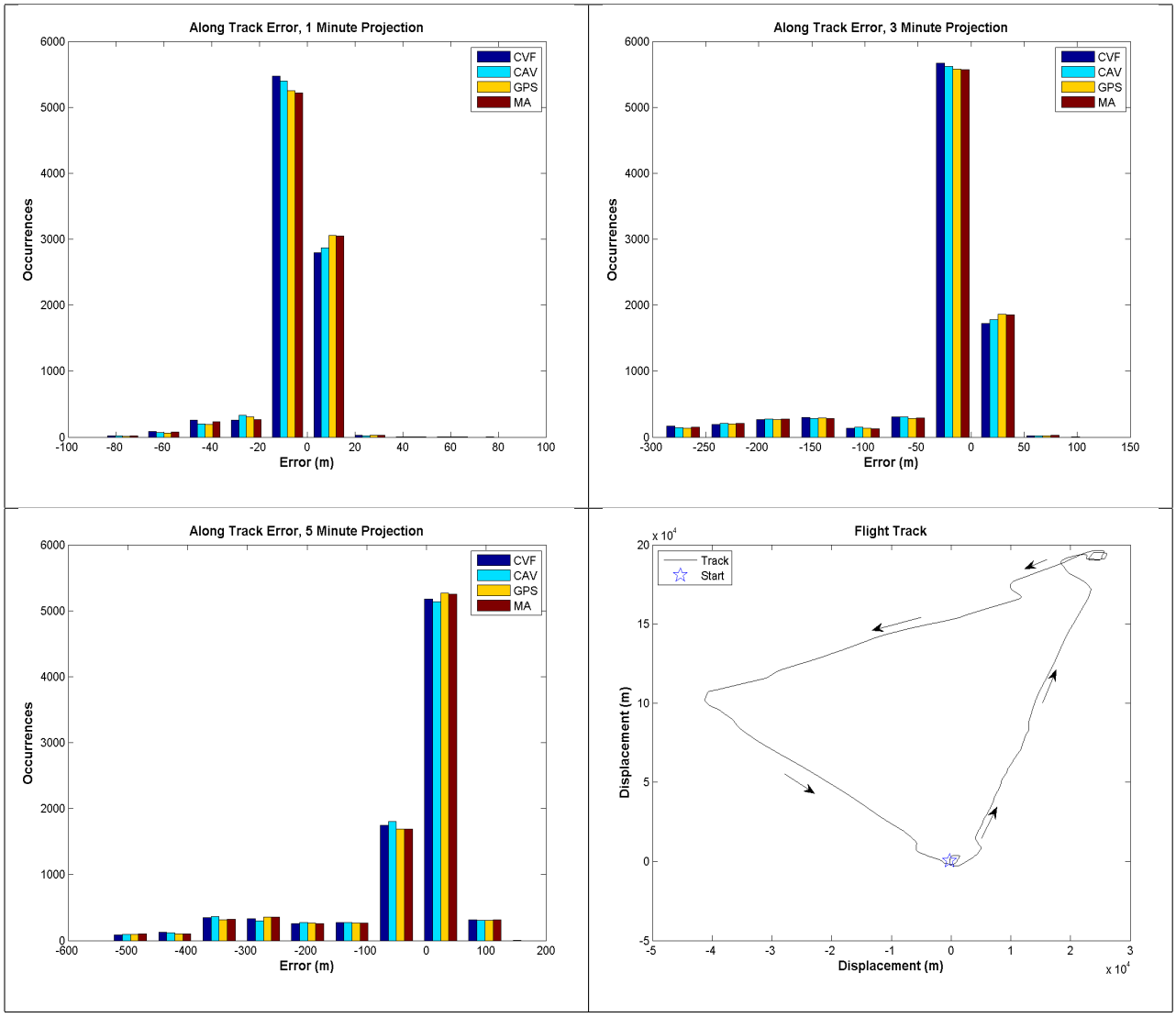

Figure 5.25: Along track error for all GPS tracks using constant velocity Kalman filter (CVF), constant acceleration Kalman filter (CAV), GPS straight projection (GPS), and a moving average filter (MA)

Figure 5.25 shows the along-track error distribution for a full flight. With the combination of straight and maneuvering segments of flight, the projections under predict the displacement along the track. The along-track error is reduced using a the constant velocity Kalman filter while the cross-track error is reduced using the constant acceleration Kalman filter. The GPS projection has shown to perform as well as the moving average technique yet the moving average controls velocity jumps inherent in the GPS units.

In the case of the NAS data with commercial IFR and VFR flights, the tracks pass through predetermined waypoints selected in such a way to reduce aerial conflict and reduce transit time. Given their straight line nature between their departure and arrival airports, their predictability increases. A more difficult case for predicting future position is the non-compliant aircraft flying without flight plans, tracked only by radar or GPS units. Shown in sections 5.1 and 5.2, the predictability of an commercial aircraft above 18,000 ft is much higher than the predictability of a private pilot training around small airports while commerical aircraft in a terminal environment at lower altitudes develop the same predictability characteristics as non-compliant aircraft. Although highly unpredictably, personal non-compliant aircraft can be tracked with measurable accuracy given the right models and the ability to detect possible maneuvers. Recognizing maneuvers through basic changes in bearing and velocity help determine the model to use and by possibly switching between models, a higher accuracy in displacement and bearing change could be achieved.

Chapter 6

Conclusion

The ability to predict an aircraft's future position based on prior knowledge of the states was found to be dependent on the aircraft's environment. In the case of compliant aircraft sampled in the NAS dataset over a week's time, the confidence in the quality of the projection varied by altitude levels and whether the aircraft was in a terminal or transit environment. At lower altitudes, aircraft performed many maneuvers either in preparation to land or when leaving the airport, making the performance of the projections less reliable. At altitudes ranging from 10,000 to 18,000 ft, aircraft become more predictable than the lower altitude range. This altitude region served as a transitional environment for commercial aircraft. The change in rate of altitude across the region suggest that aircraft are either beginning their approach or gaining altitude to enter the cruise portion of their flight. At altitudes above 18,000 ft, the projection error reduced and the confidence intervals of the projection produced greater predictability. At each altitude level, a level of certainty in aircraft prediction helped define the flight environment. These confidence intervals characterize the aircraft's motion at various altitudes and can be used to validate simulations for unmanned aircraft.

The more challenging task of predicting future position of non-compliant aircraft developed an understanding of the performance of different projection techniques under different flight conditions. The constant velocity Kalman filter projection more accurately predicted the displacement along the projection as well as reduced the projection error with small maneuvers. For more aggressive maneuvers, a constant acceleration Kalman filter predicted the change in course with less error than the constant velocity Kalman filter yet lacked the along-track performance that the constant velocity Kalman filter displayed. Using the

Kalman filters helped mimic the filter used by the GPS units and reduced the error inherent in a straight velocity projection. An improvement in reducing the effects of satellite loss and jumps in instantaneous velocity was incorporating a moving average. By smoothing the data, the discontinuities in velocity due to inconsistent time steps became less effective on the projection and reduced the error between the projected and observed position.

Looking at the projection success for both compliant and non-compliant aircraft demonstrated the erratic nature of training aircraft at low altitudes. In the hopes of developing models to simulate private pilot activity, combinations of filtering types and projection techniques will have to be utilized to adapt to the various flight environments and trajectories seen in a single track.

Chapter 7

Future Work

With unmanned aircraft entering the NAS, adequate sense and avoid technology is still needed to reduce aerial conflicts and open the skies to both manned and unmanned vehicles. Through individual analysis of each projection technique under different flight conditions and environments, the need to alternate between projection types and filtering techniques is apparent. In straight and level flight, the constant velocity Kalman filter is very capable yet during maneuvers its performance suffers. By switching between a constant velocity and constant acceleration filter when entering and exiting a maneuver, the prediction performance of the projection improves while keeping the computational cost at a minimum. Bar-Shalom demonstrated the ability of a switch filter when applied to a simulated track consisting of straight and maneuvering portions [4]. Also, much success has been seen in the application of the unscented Kalman filter to the vehicle tracking problem. Due to the highly non-linear nature of the system given the unpredictable changes in course and presence of non-Gaussian noise, the unscented Kalman filter has been used in many tracking applications and path planning models. Another approach to better predicting the future position of aircraft is incorporating more information about the environment into the model. Flight plans, restricted areas, weather conditions, and other information can be applied to the model to notify senors where to look for an aircraft. This approach, used for ground vehicle path planning, divides the airspace into possible regions of interest. The probability of sensing another vehicle or object would then be increased when the sampled environment is reduced.

Bibliography

[1] Elnagar, A., "Prediction of Moving Objects in Dynamic Environments Using Kalman Filters," *Proceedings of 2001 IEEE International Symposium on Computational Intelligence in Robotics and Automation, July 29 - August 1, 2001, Banff, Alberta, Canada*, Banff, Alberta, Canada, 2001, pp. 414–419.

[2] Cale, M., Liu, S., Oaks, R., Paglione, M., Ryan, H., and Summerill, S., "A Generic Sampling Technique for Measuring Aircraft Trajectory Prediction Accuracy," *Proceedings of 4th USA\EUROPE Air Traffic Management R & D Seminar, December 3rd-7th, 2001*, 2001.

[3] Barrios, C. and Motai, Y., "Improving Estimation of Vehicle's Trajectory Using the Latest Global Positioning System with Kalman Filtering," *IEEE Transactions on Instrumentation and Measurement*, Vol. 60, No. 12, Dec. 2011, pp. 3747–3755.

[4] Bar-Shalom, Y. and Birmiwal, K., "Variable Dimension Filter for Maneuvering Target Tracking," *IEEE Transactions on Aerospace and Electronic Systems*, Vol. 18, No. 5, Sept. 1982, pp. 621–628.

[5] Mao, G., Drake, S., and Anderson, B., "Design of a Extended Kalman Filter for UAV Localization," *IEEE Information, Decision and Control*, 2007, pp. 224–229.

[6] Prévost, C., Desbiens, A., and Gagnon, E., "Extended Kalman Filter for State Estimation and Trajectory Prediction of a Moving Object Detected by an Unmanned Aerial Vehicle," *Proceedings of the 2007 American Control Conference, Marriot Marquis Hotel at Times Square, New York City, USA, July 11-13, 2007*, New York City, USA, 2007, pp. 1805–1810.

[7] Prévost, C., Desbiens, A., Gagnon, E., and Hodouin, D., "UAV Optimal Cooperative Target Tracking and Collision Avoidance of Moving Objects," *Proceedings of the 17th World Congress, IFAC, Seoul, Korea, July 2008*, International Federation of Automatic Control, Seoul, Korea, pp. 5724–5729.

[8] Hu, J., Prandini, M., and Sastry, S., "Probabilistic Safety Analysis in Three Dimensional Aircraft Flight," *Proceedings of the 42nd IEEE, Conference on Decision and Control, Maui, Hawaii USA, December 2003*, HI, USA, 2003, pp. 5335–5340.

[9] Richards, A. and How, J. P., "Aircraft trajectory planning with collision avoidance using mixed integer linear programming," *American Control Conference (ACC)*, Vol. 3, 2002, pp. 1936–1941 vol.3.

[10] Paielli, R. and Erzberger, H., "Conflict Probability Estimation for Free Flight," *National Aeronautics and Space Administration*, Oct. 1996.

[11] Prandini, M., Hu, J., Lygeros, J., and Sastry, S., "A Probabilistic Approach to Aircraft Conflict Detection," *IEEE Transactions on Intelligent Transportation Systems*, Vol. 1, No. 4, Dec. 2000, pp. 199–220.

[12] AL-Basman, M. and Hu, J., "An Approach to Air Traffic Density Estimation and Its Application in Aircraft Trajectory Planning," *Proceedings of 24th Chinese Conference on Decision and Control, Taiyuan, China, May 23-25, 2012*, May 2012.

[13] Gong, C. and McNally, D., "A Methodology for Automated Trajectory Prediction Analysis," *AIAA Guidance, Navigation, and Control Conference and Exhibit, 16-19 August 2004, Providence, Rhode Island*, 2004.

[14] Kalman, R., "A New Approach to Linear Filtering and Prediction Problems," *Journal of Basic Engineering*, Vol. D, No. 82, 1960, pp. 34–45.

[15] Tapley, B., Schutz, B., and Born, G., *Statistical Orbit Determination*, Elsevier Academic Press, 2004.

[16] Crassidis, J. and Junkins, J., *Optimal Estimation of Dynamic Systems*, Chapman and Hall, 2004.

[17] MathWorks, "Great Circles, Rhumb Lines, and Small Circles," `http://www.mathworks.com/help/toolbox/map/f5-7173.html#f5-7179`, September 2011.

Appendices

List of Appendix A Figures

List of Appendix A Tables

Appendix A

National Airspace System Radar Tracks

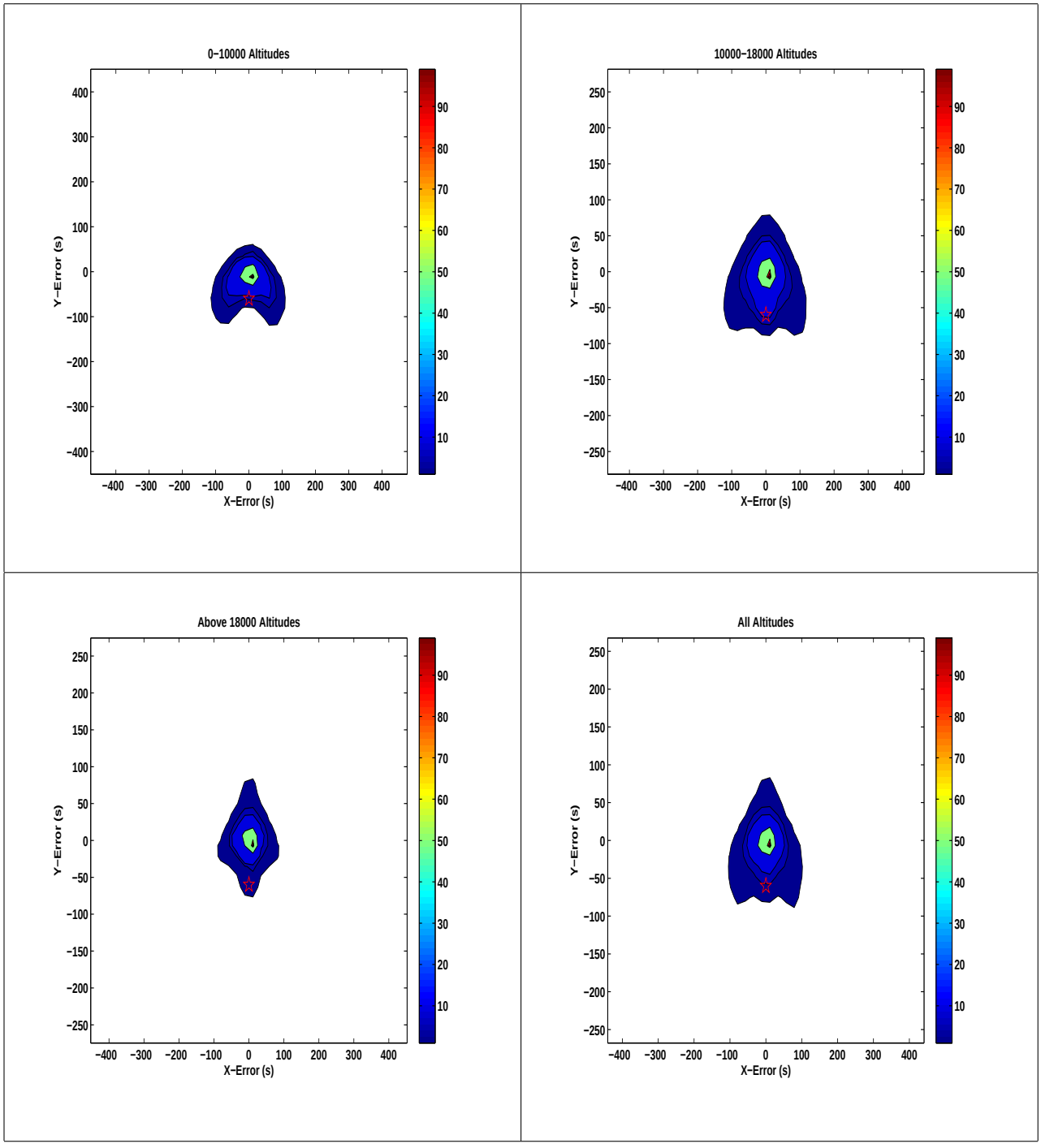

Figure A.1: All tracks, 1 minute projection, difference in projection to measured histograms

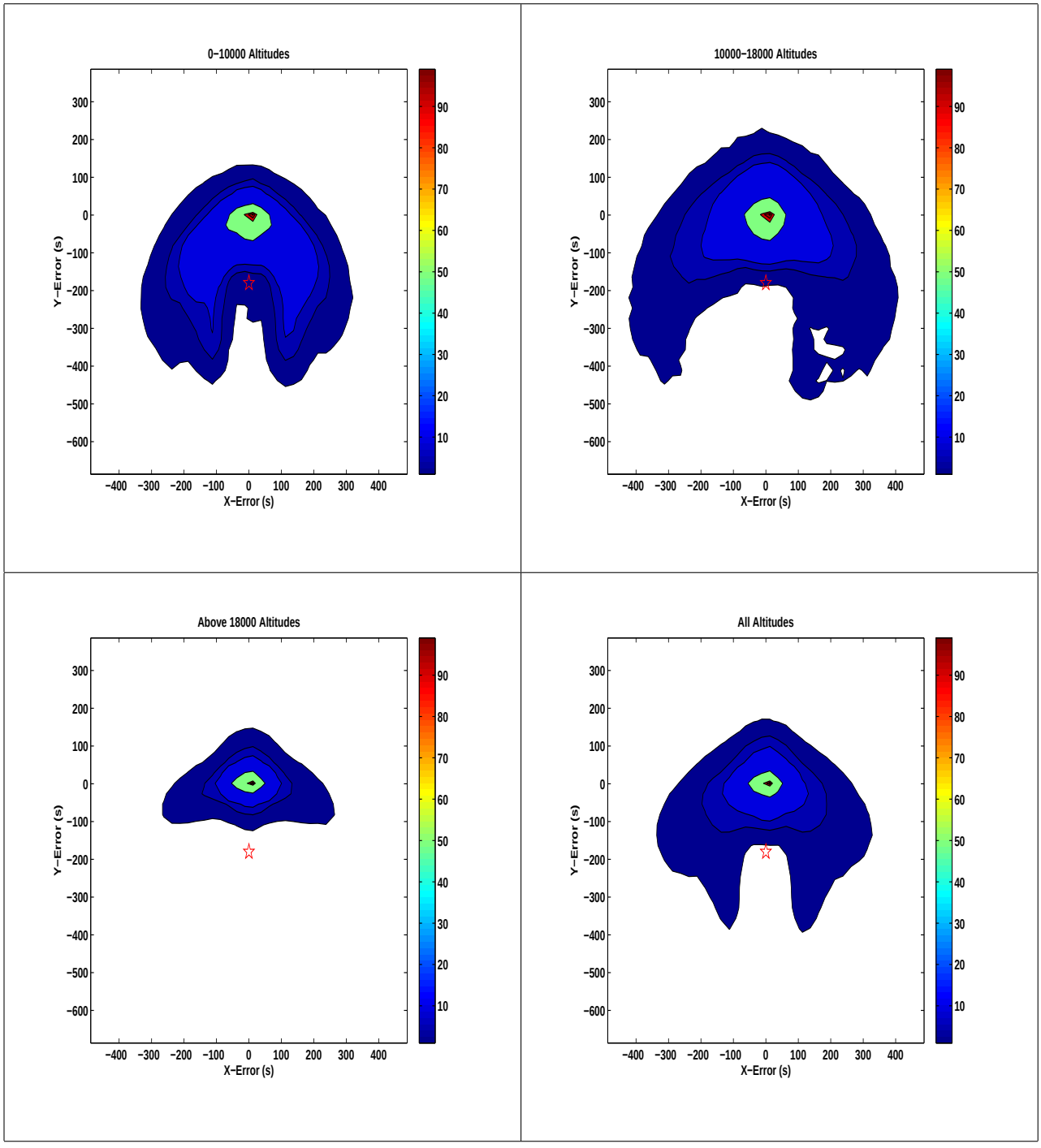

Figure A.2: All tracks, 3 minute projection, difference in projection to measured histograms

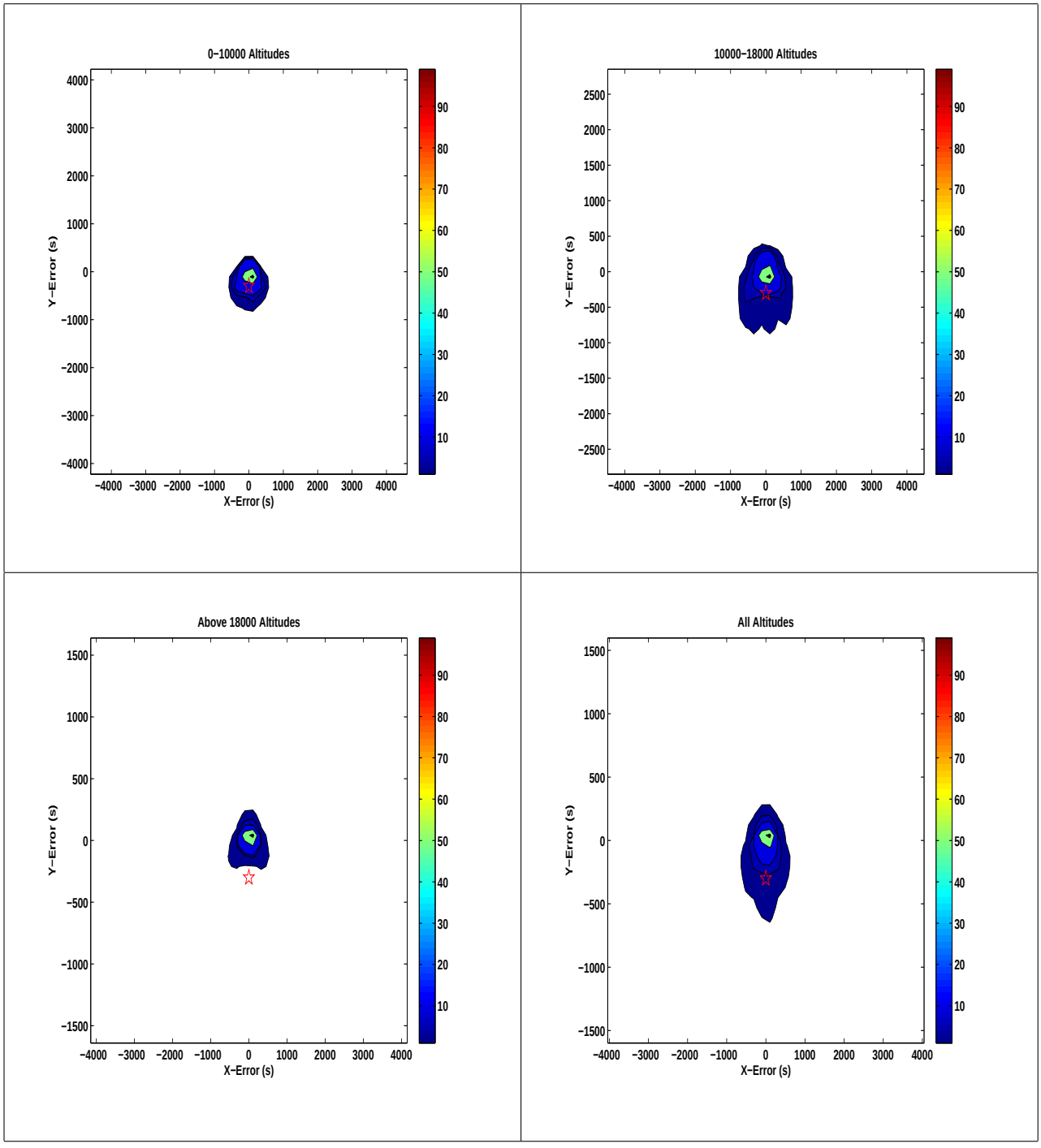

Figure A.3: All tracks, 5 minute projection, difference in projection to measured histograms

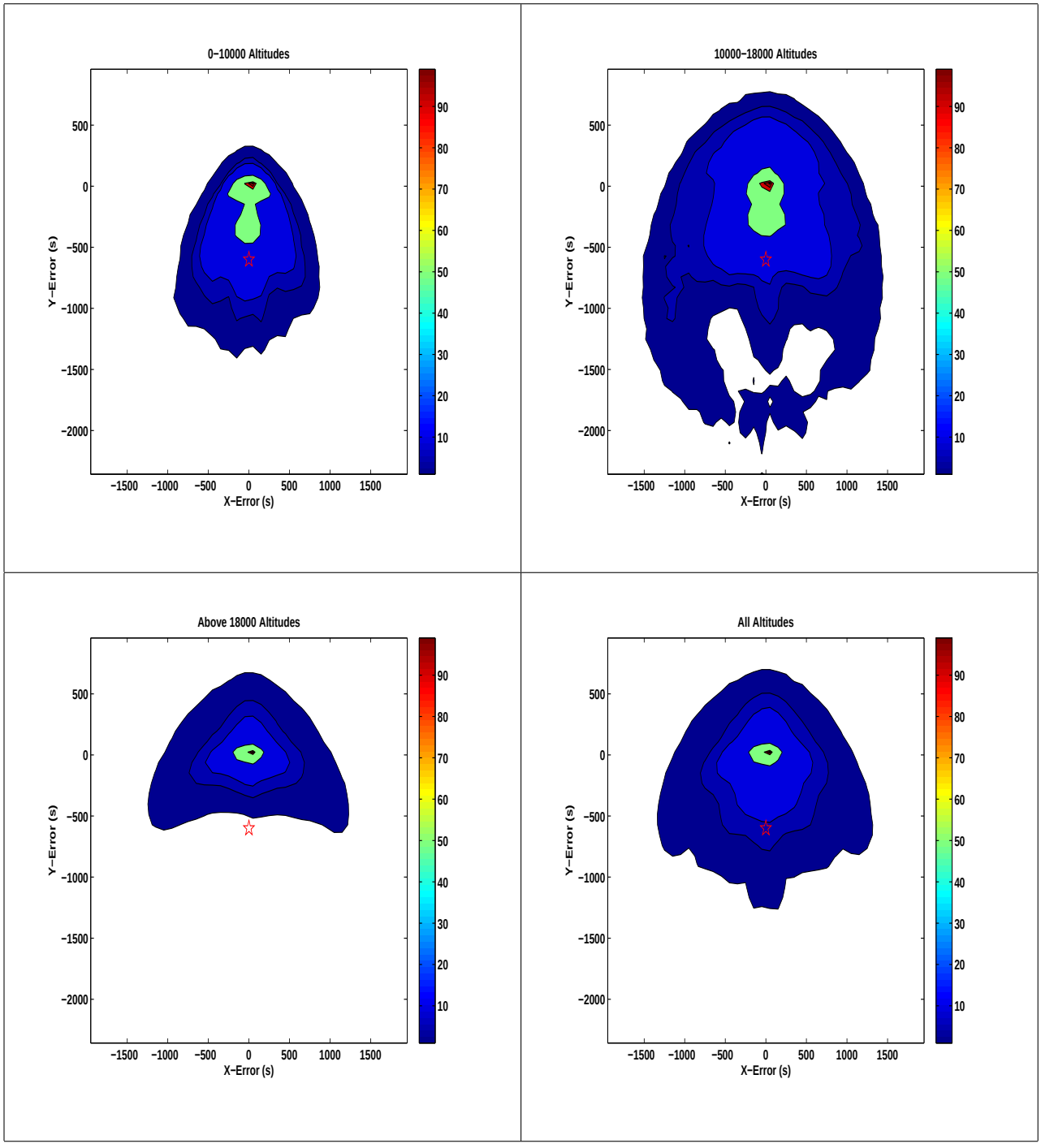

Figure A.4: All tracks, 10 minute projection, difference in projection to measured histograms

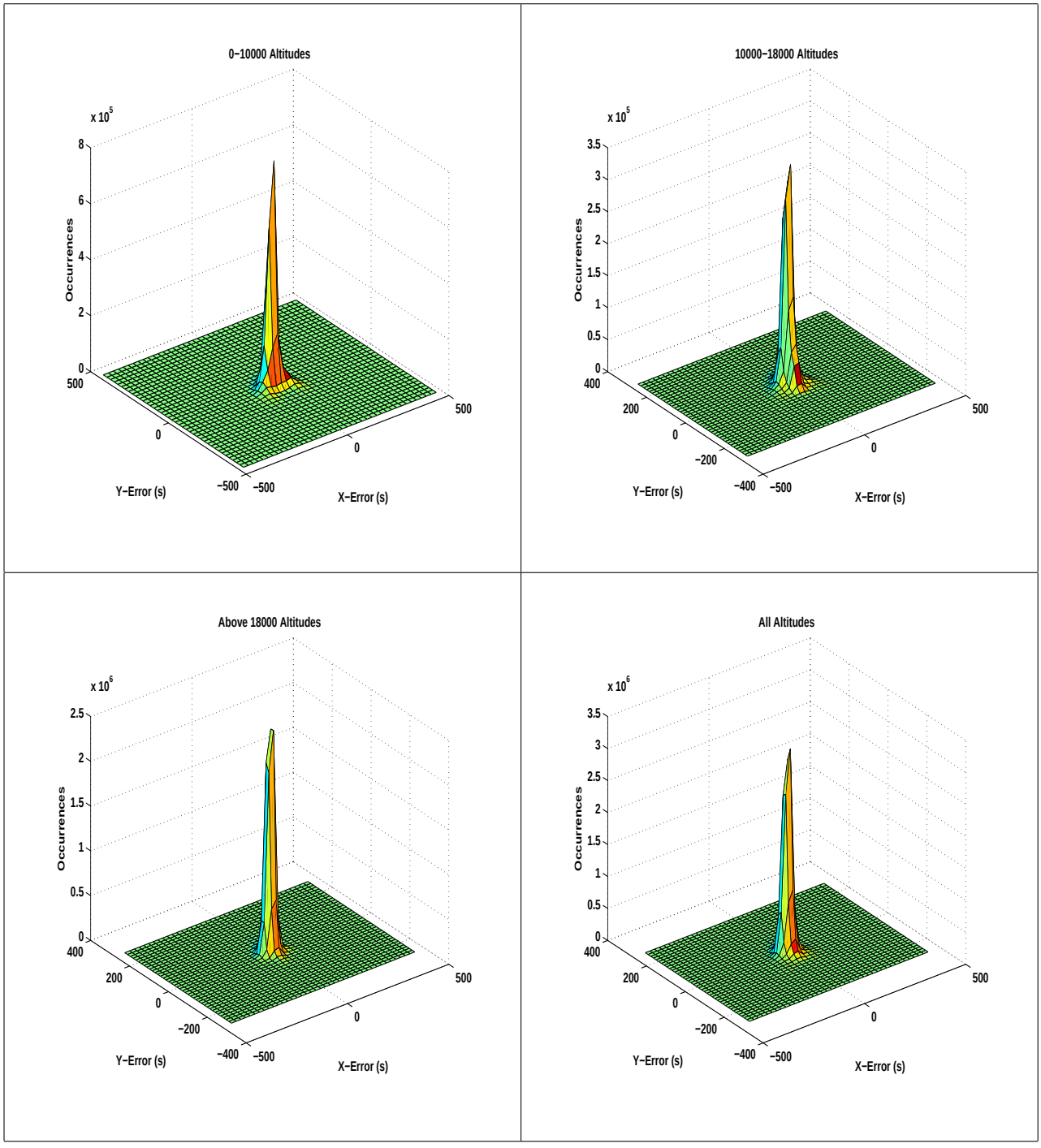

Figure A.5: All tracks, 1 minute projection, difference in projection to measured three dimensional histograms

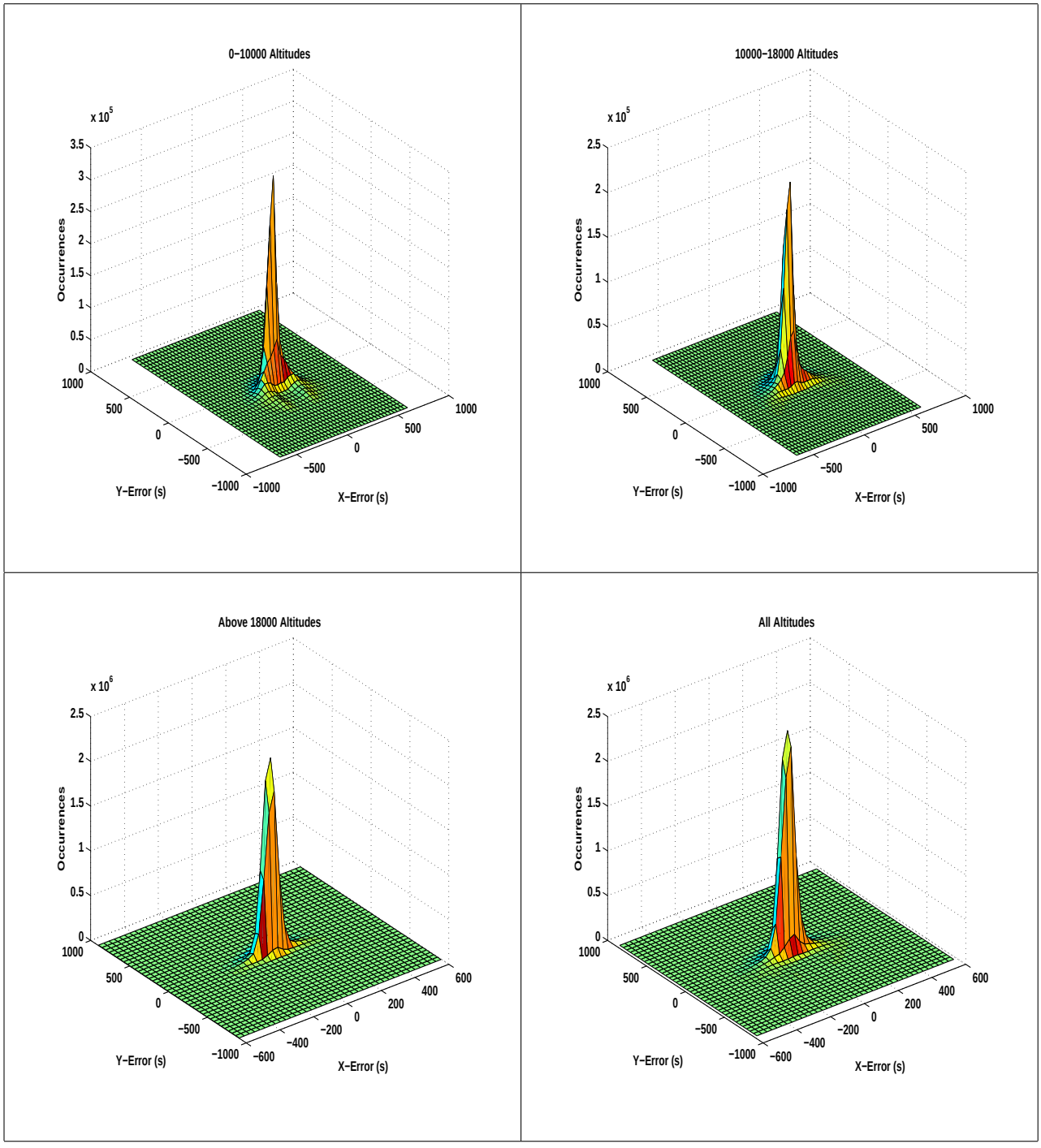

Figure A.6: All tracks, 3 minute projection, difference in projection to measured three dimensional histograms

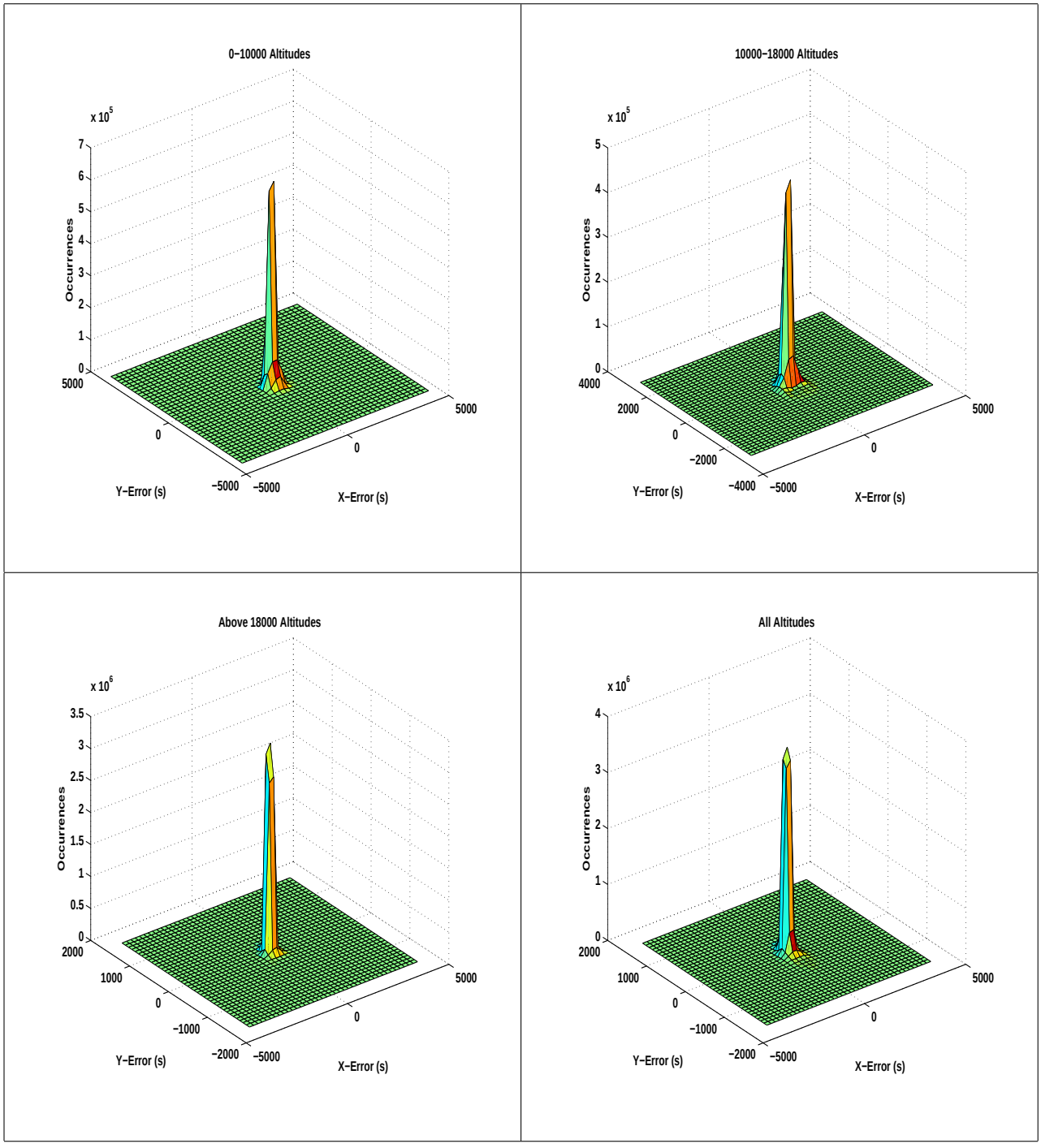

Figure A.7: All tracks, 5 minute projection, difference in projection to measured three dimensional histograms

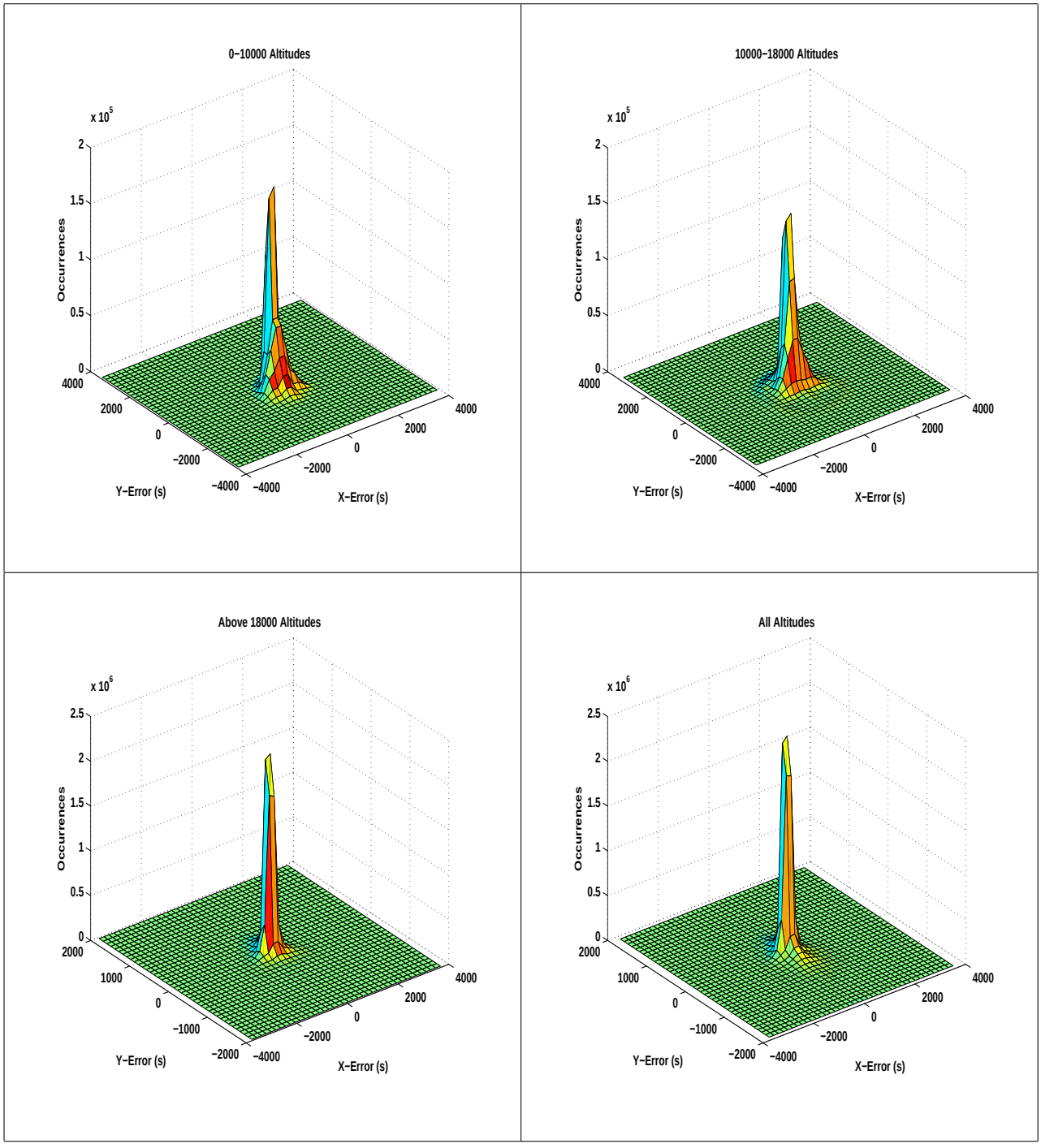

Figure A.8: All tracks, 10 minute projection, difference in projection to measured three dimensional histograms

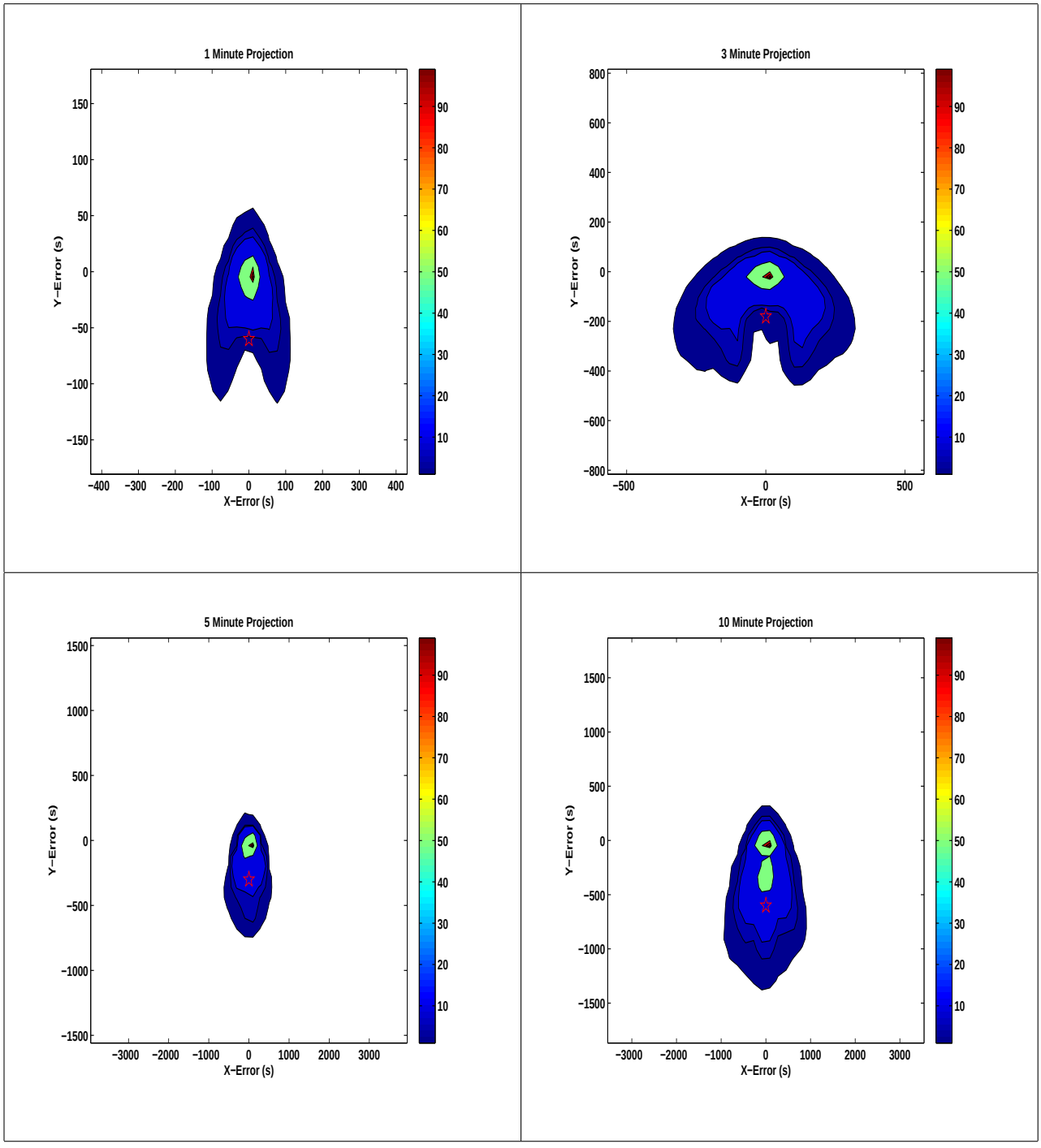

Figure A.9: All tracks, 0-10000 ft altitudes, difference in projection to measured histograms

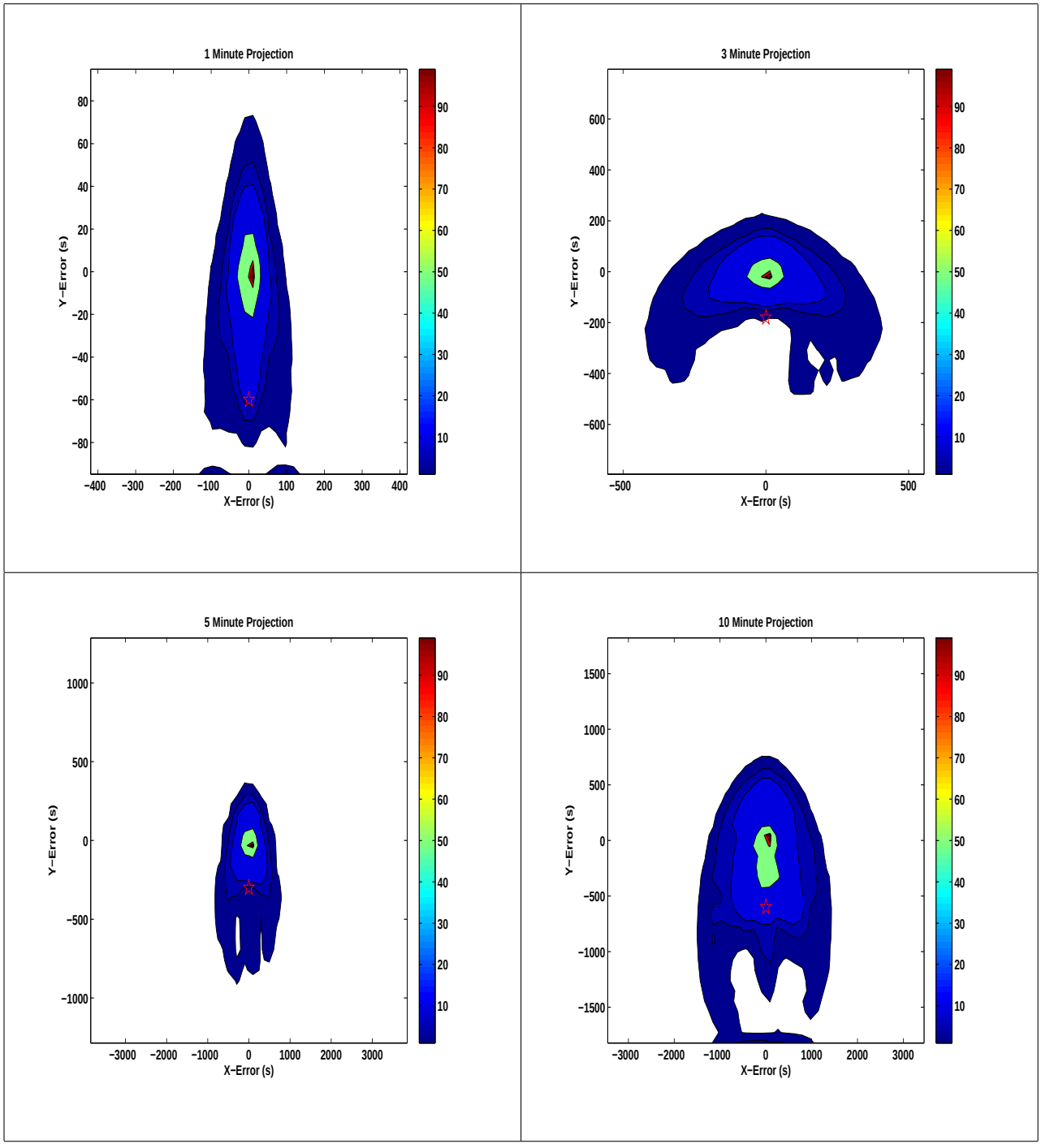

Figure A.10: All tracks, 10000-18000 ft altitudes, difference in projection to measured histograms

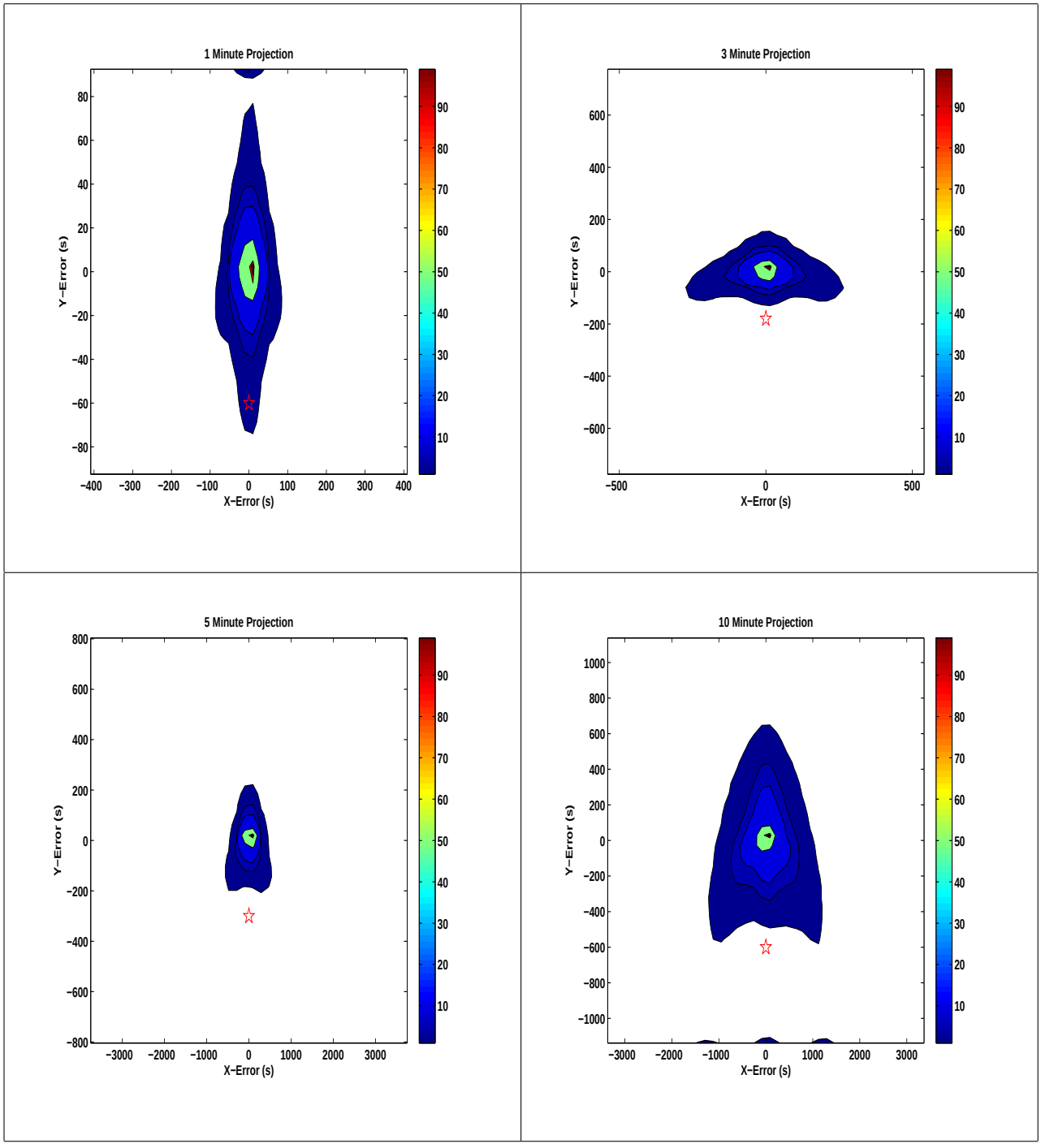

Figure A.11: All tracks, Above 18000 ft altitudes, difference in projection to measured histograms

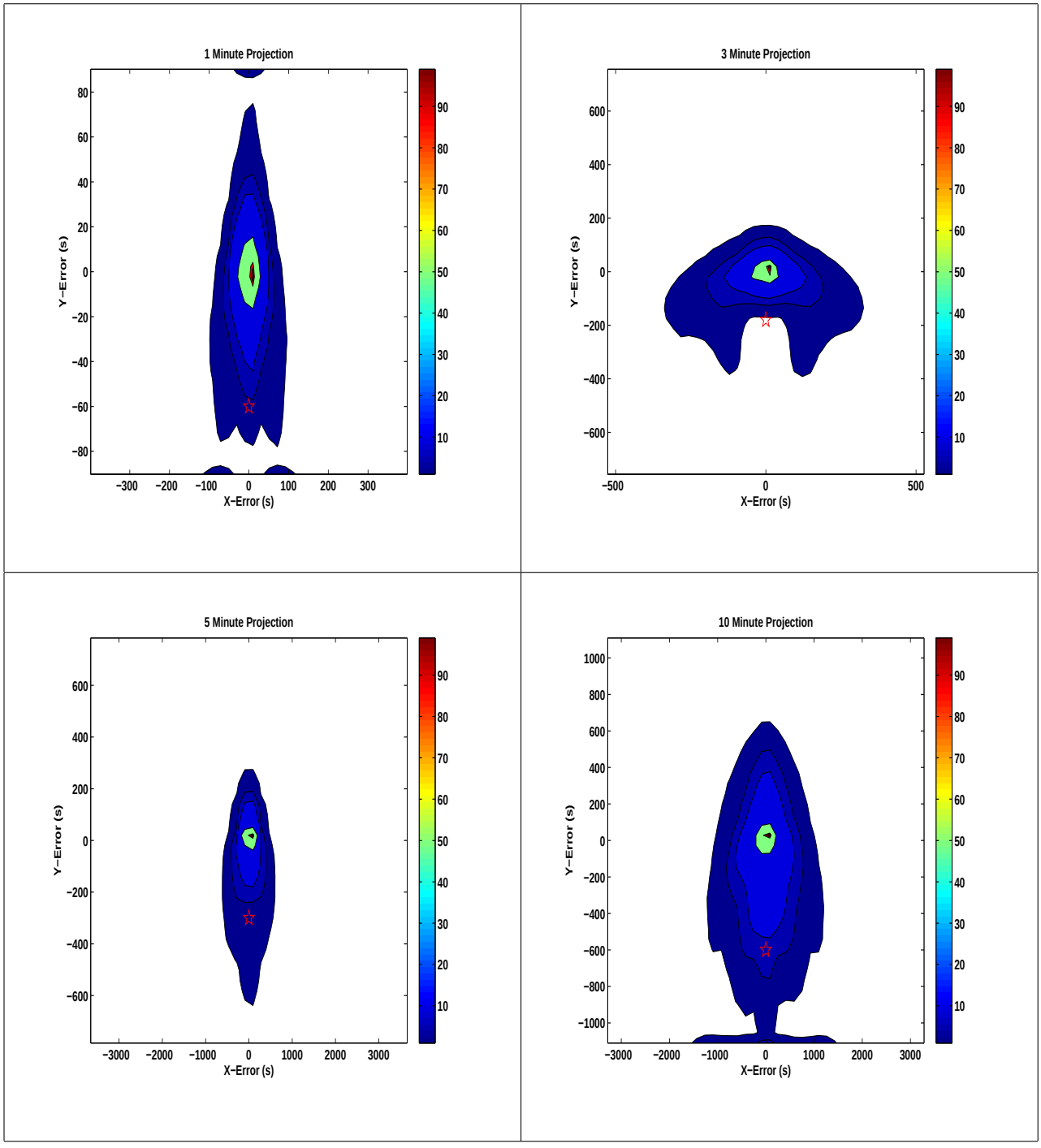

Figure A.12: All tracks, All Altitudes, difference in projection to measured histograms

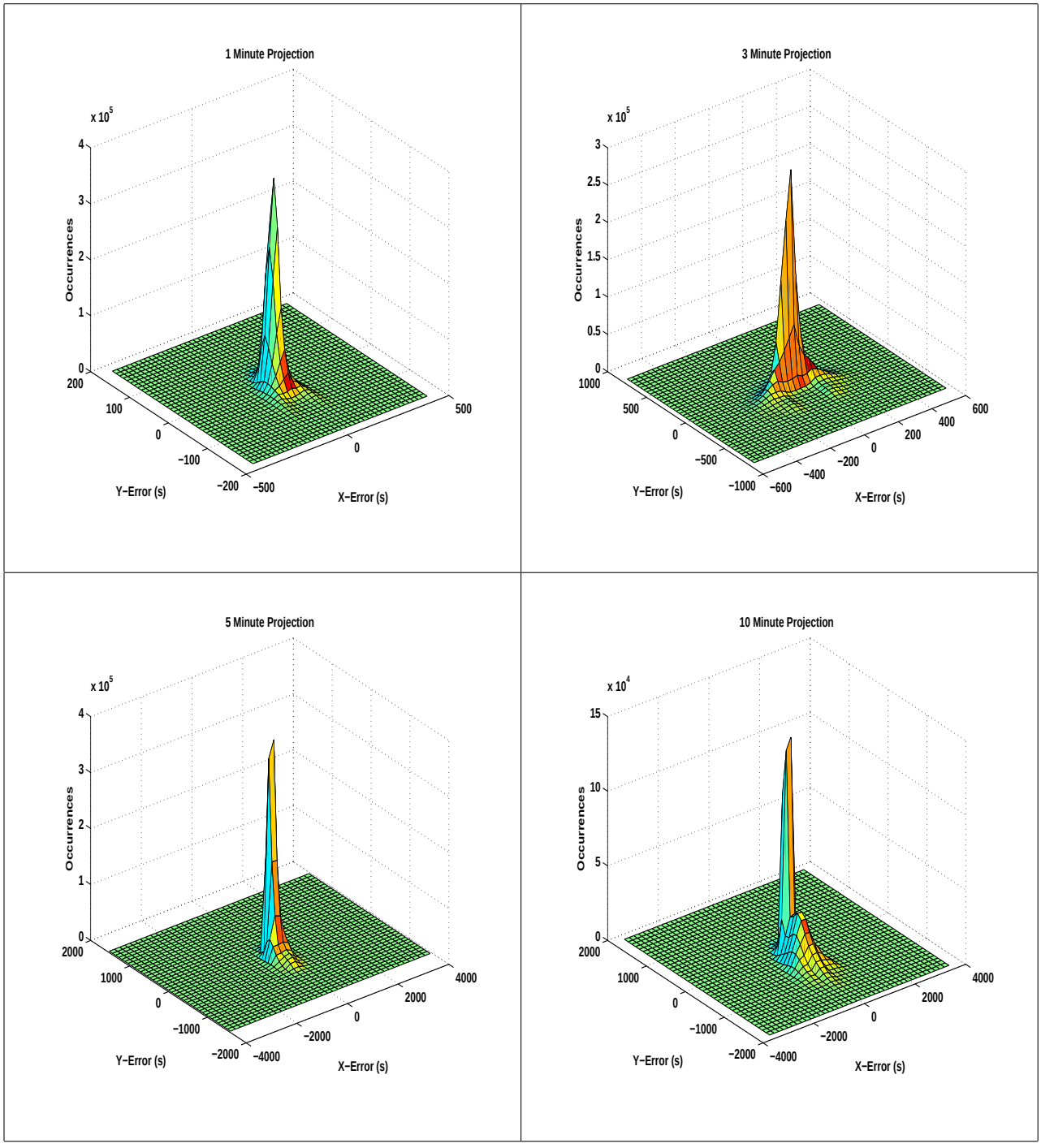

Figure A.13: All tracks, 0-10000 ft altitudes, difference in projection to measured three dimensional histograms

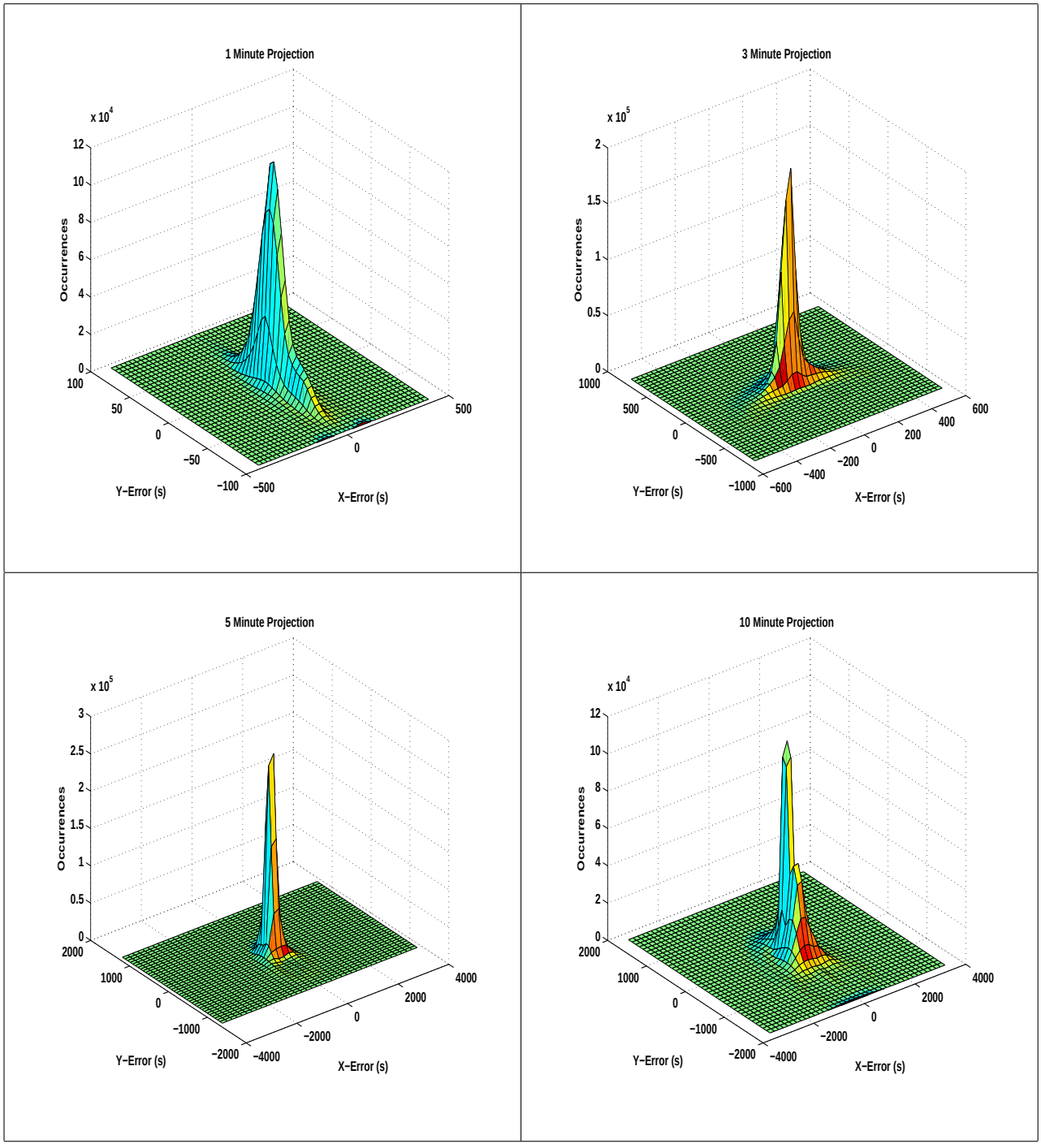

Figure A.14: All tracks, 10000-18000 ft altitudes, difference in projection to measured three dimensional histograms

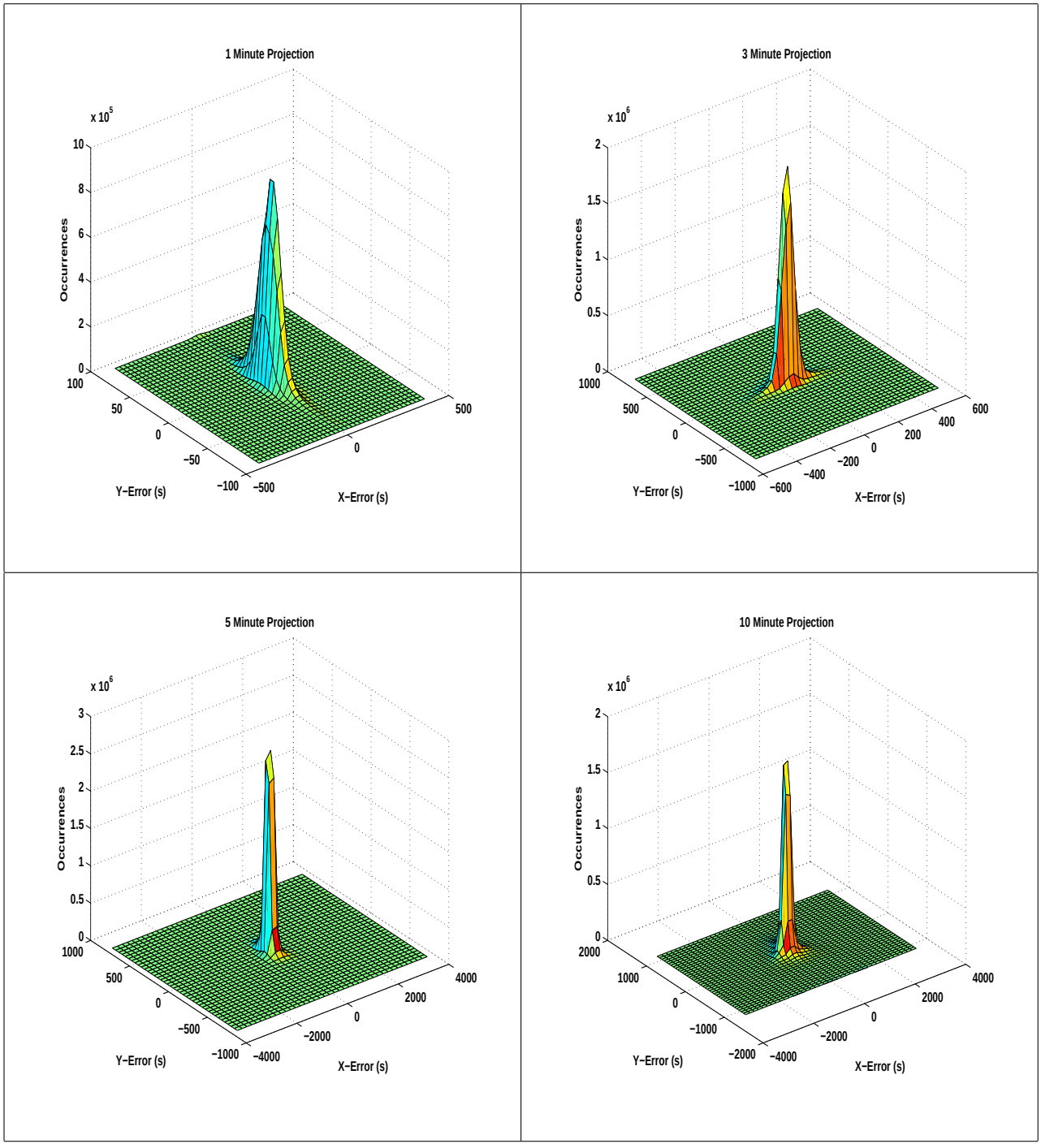

Figure A.15: All tracks, Above 18000 ft altitudes, difference in projection to measured three dimensional histograms

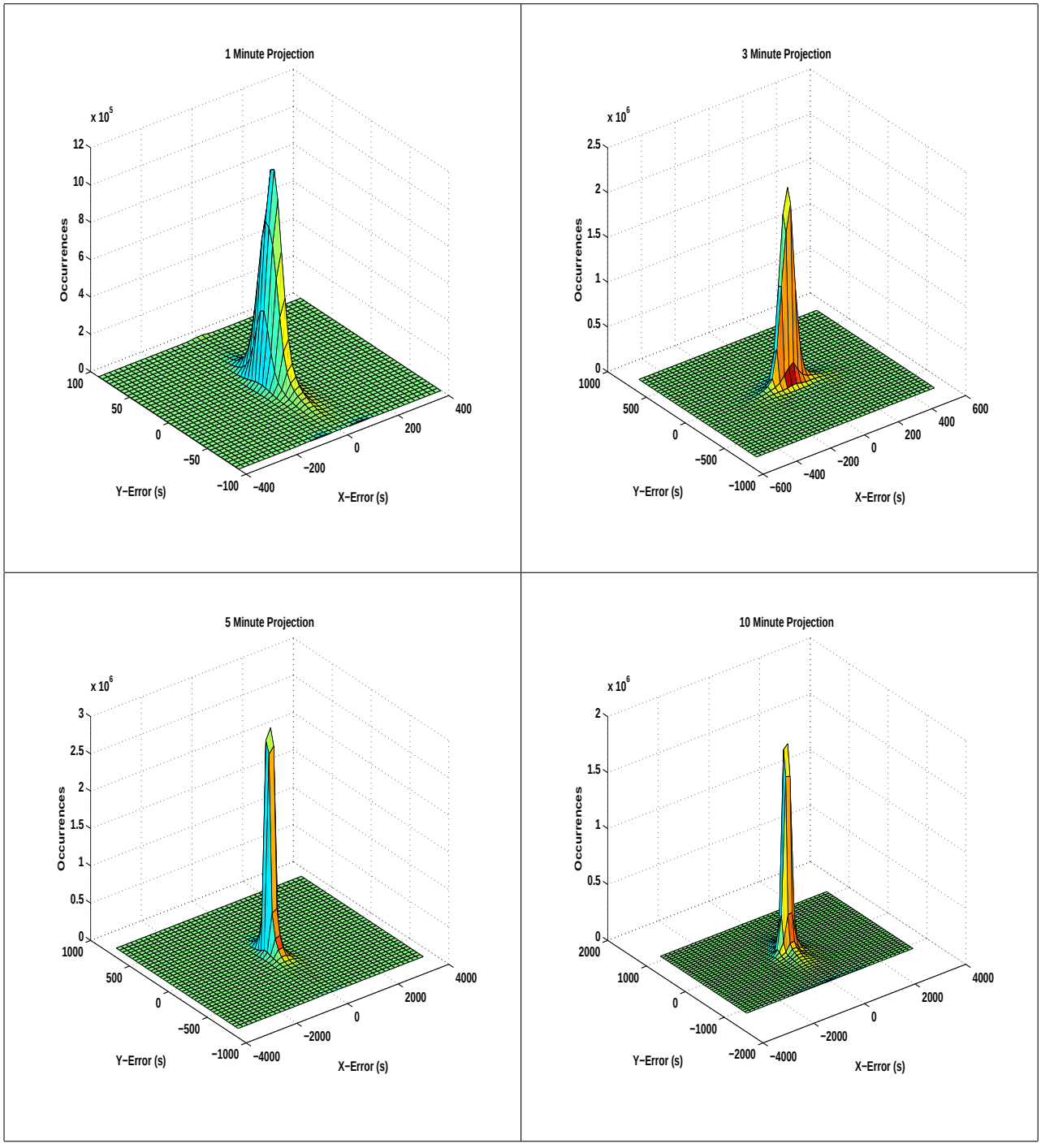

Figure A.16: All tracks, All Altitudes, difference in projection to measured three dimensional histograms

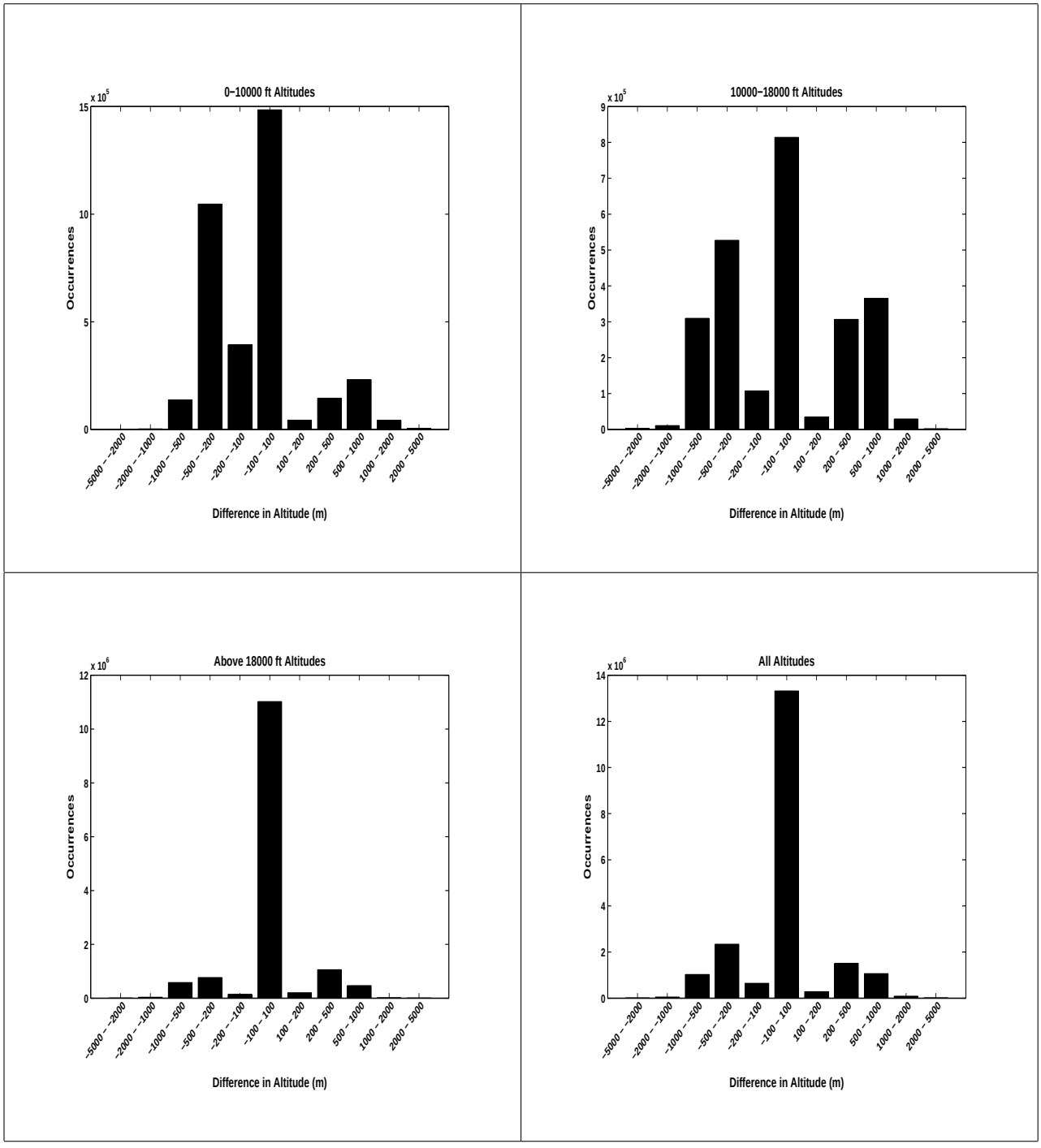

Figure A.17: Difference in altitude, all tracks, 1 minute projection

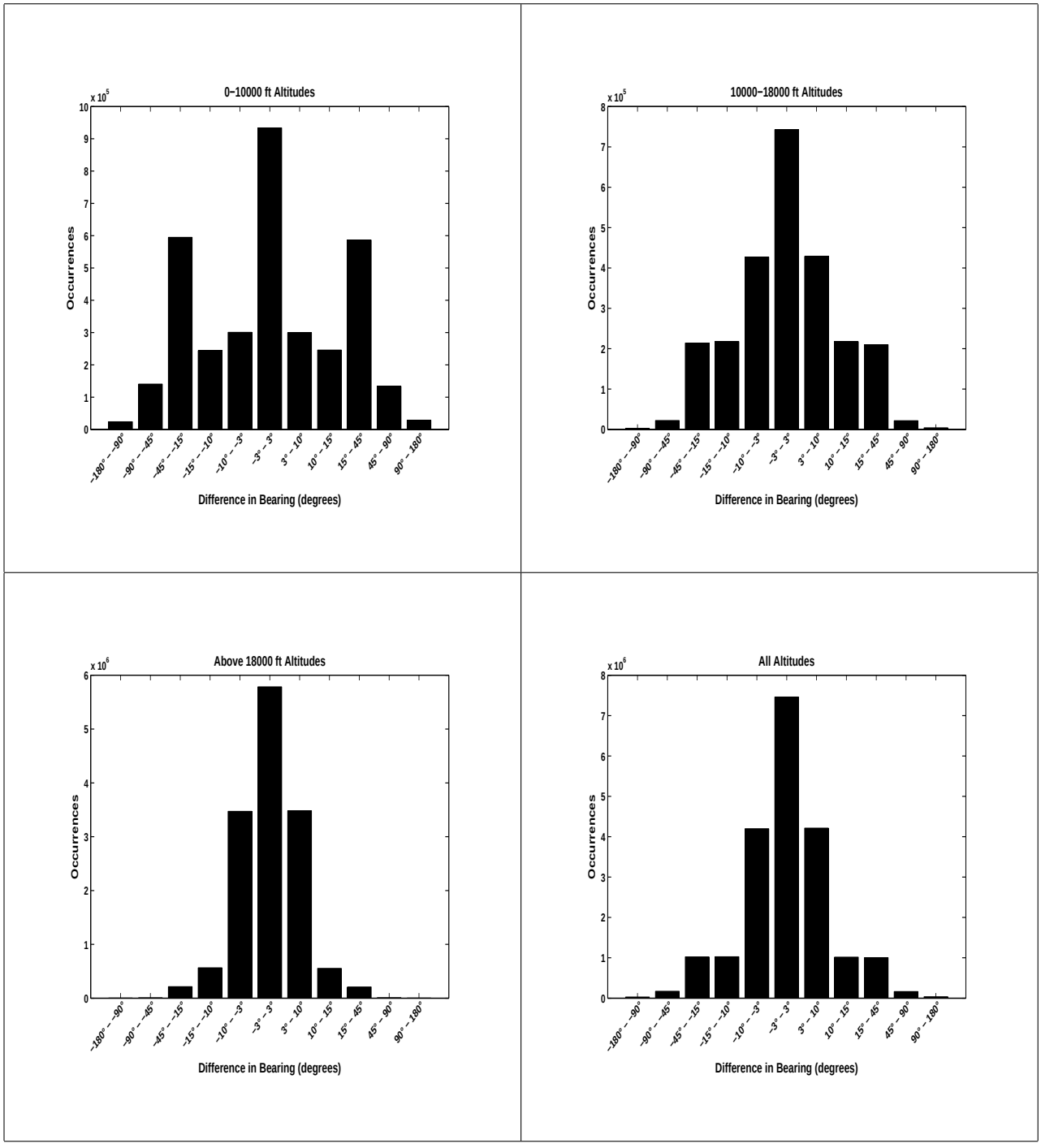

Figure A.18: Difference in bearing, all tracks, 1 minute projection

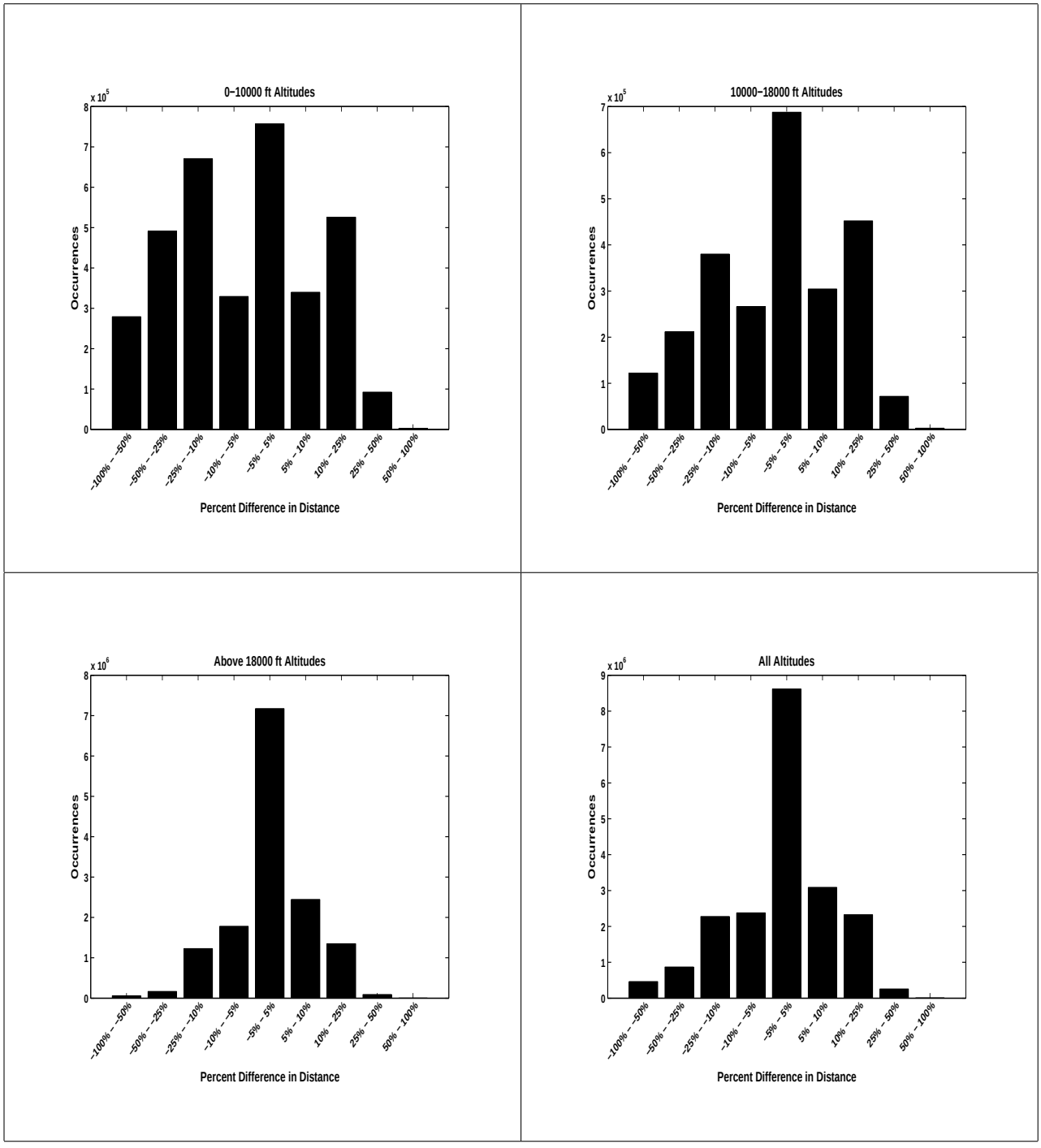

Figure A.19: Percent difference in distance, all tracks, 1 minute projection

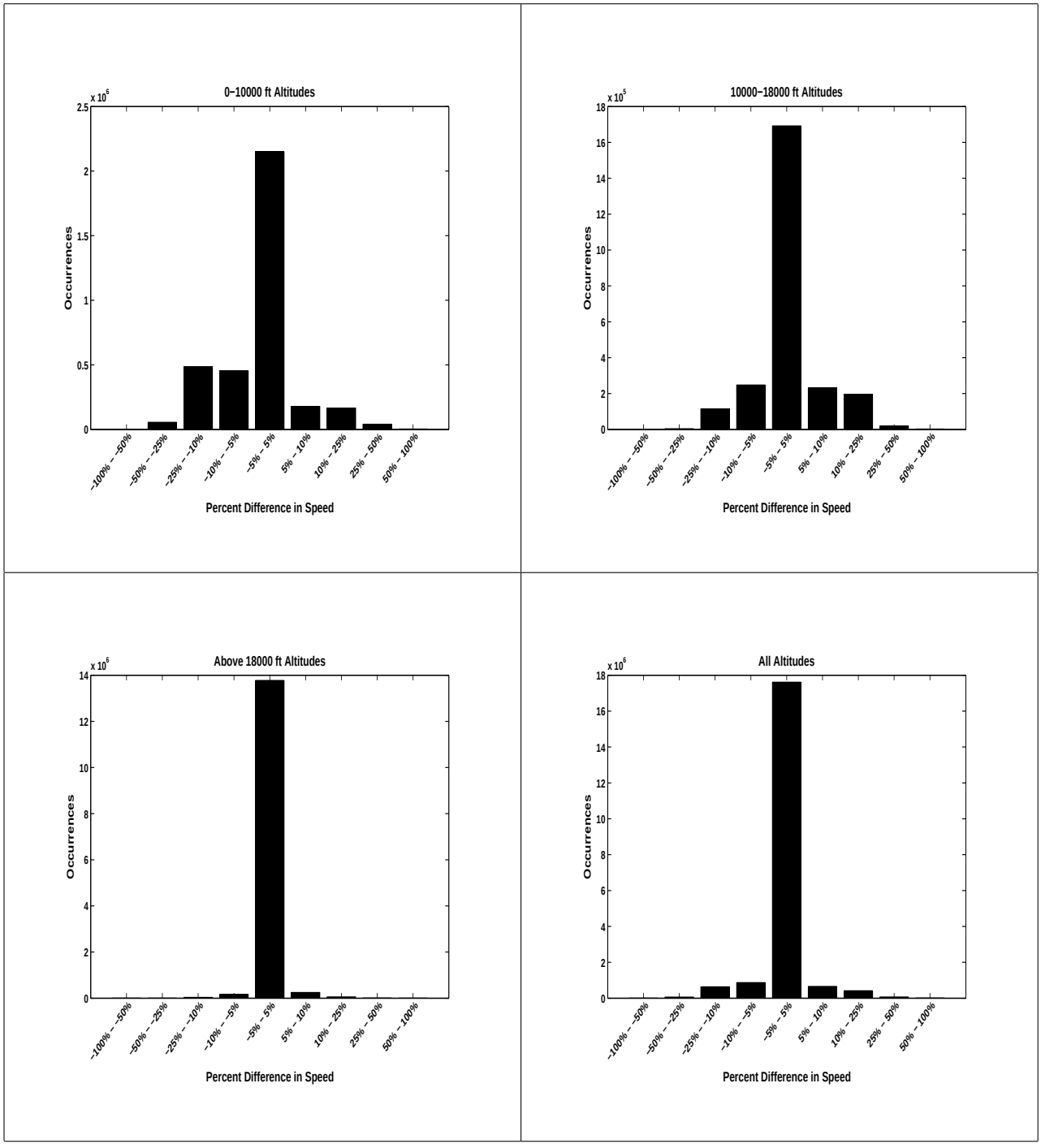

Figure A.20: Percent difference in speed, all tracks, 1 minute projection

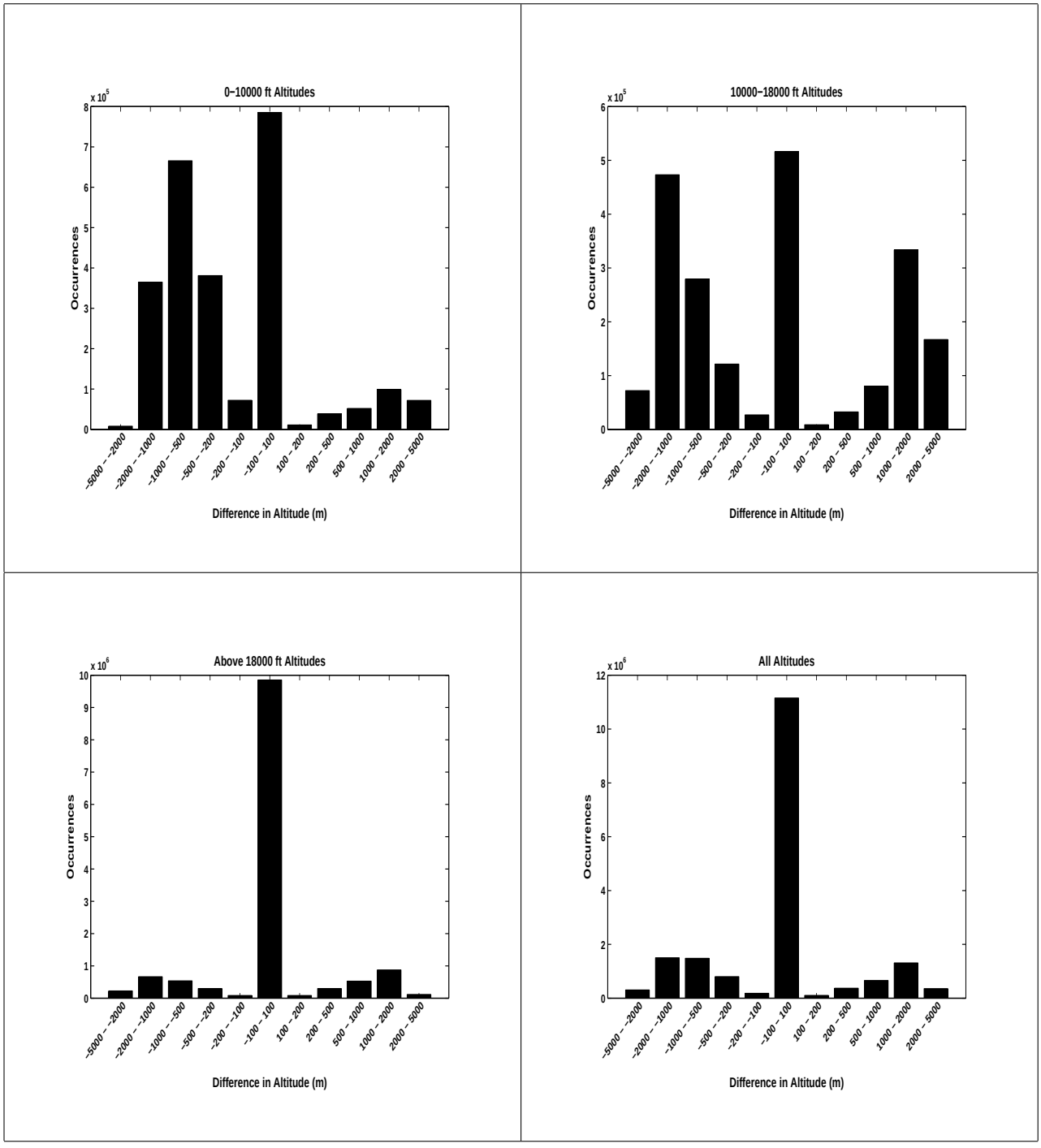

Figure A.21: Difference in altitude, all tracks, 3 minute projection

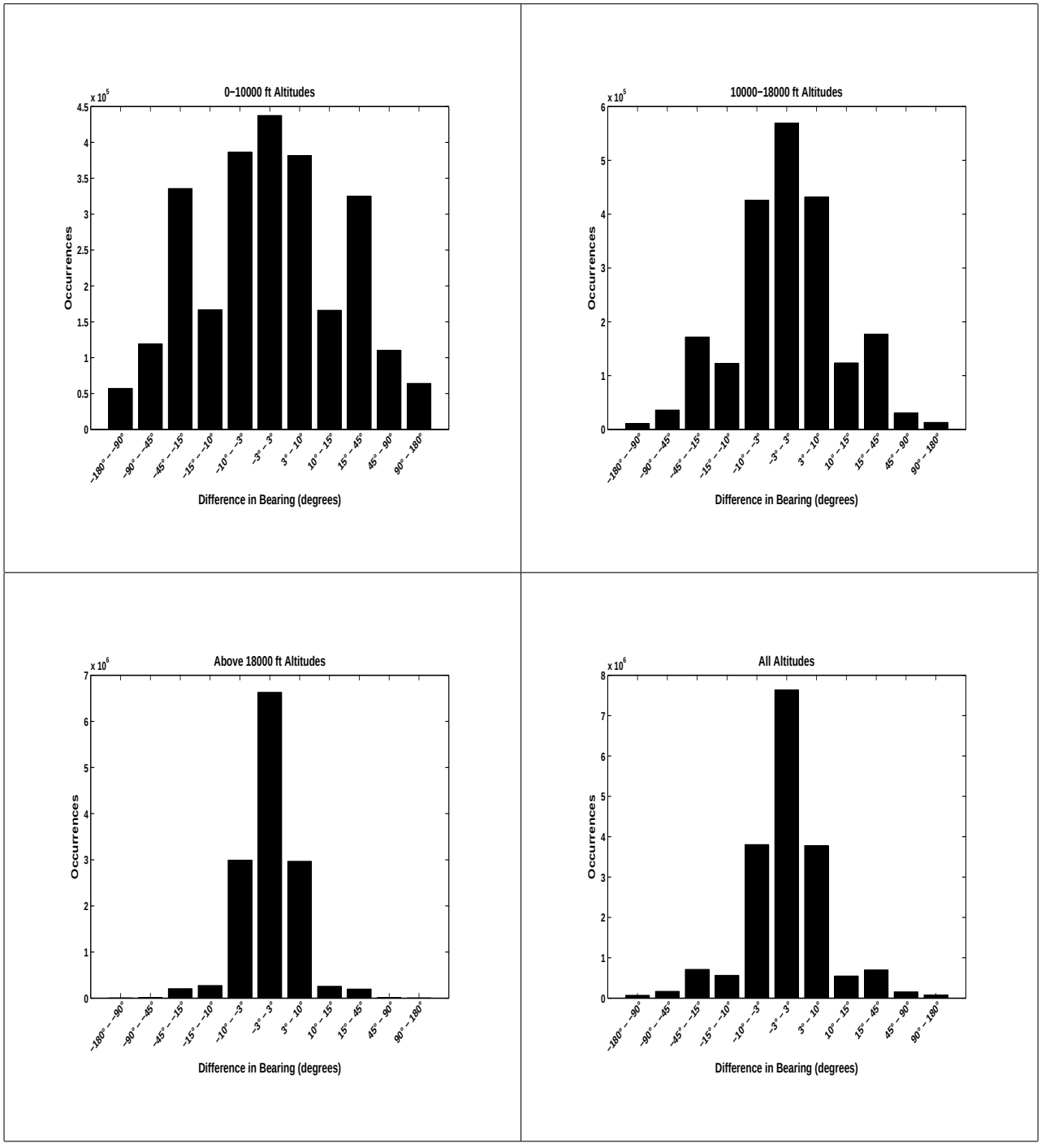

Figure A.22: Difference in bearing, all tracks, 3 minute projection

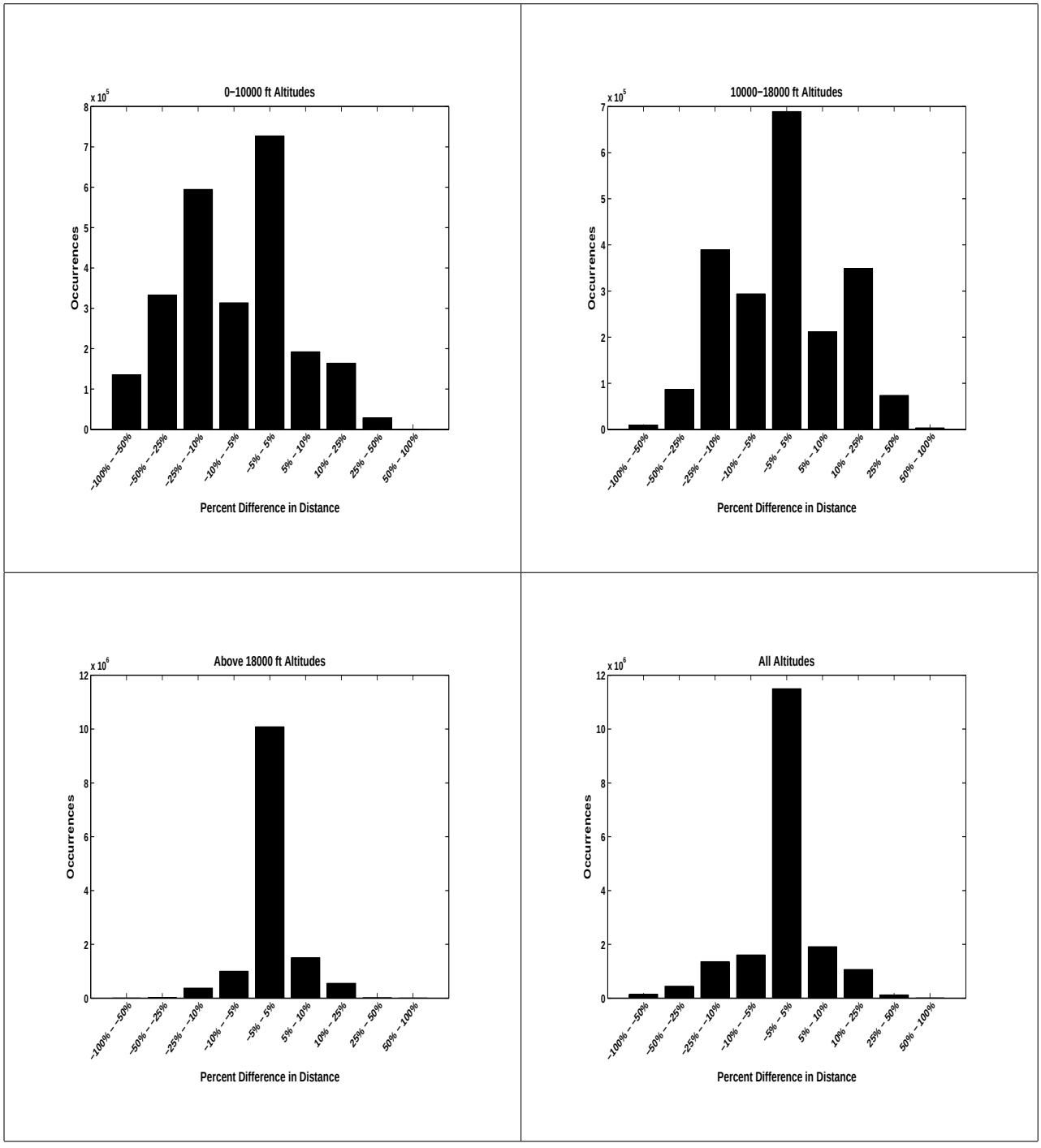

Figure A.23: Percent difference in distance, all tracks, 3 minute projection

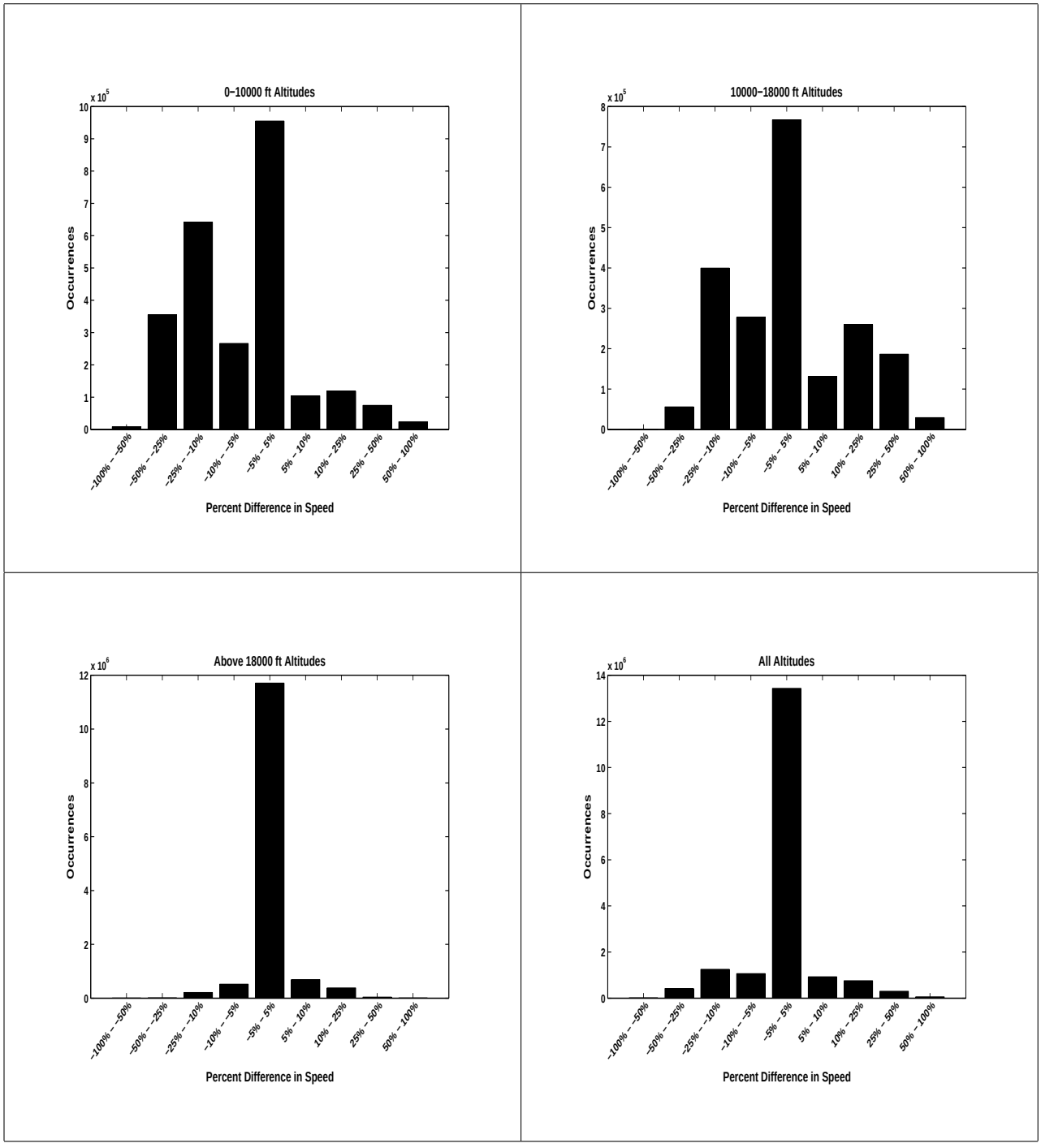

Figure A.24: Percent difference in speed, all tracks, 3 minute projection

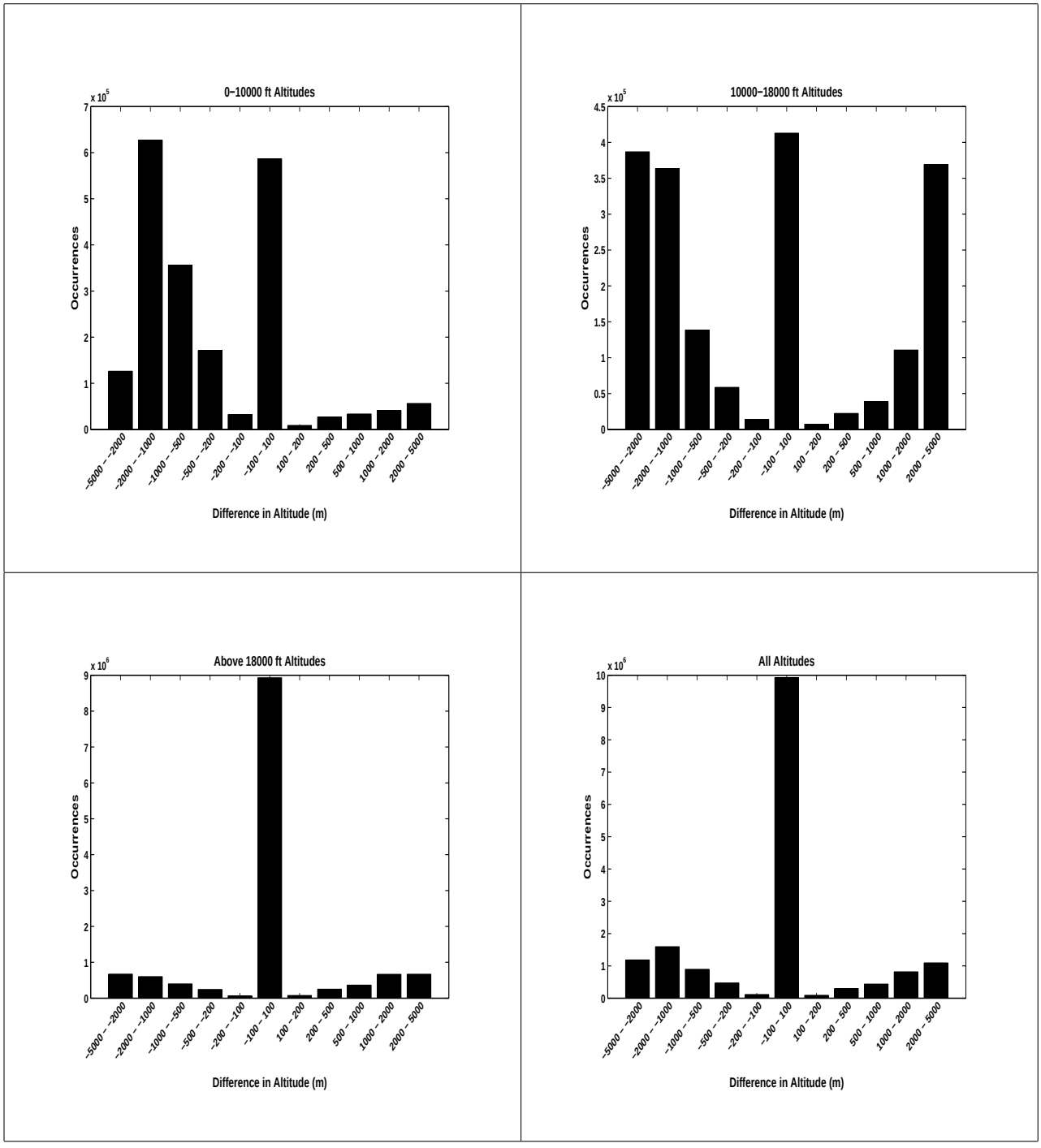

Figure A.25: Difference in altitude, all tracks, 5 minute projection

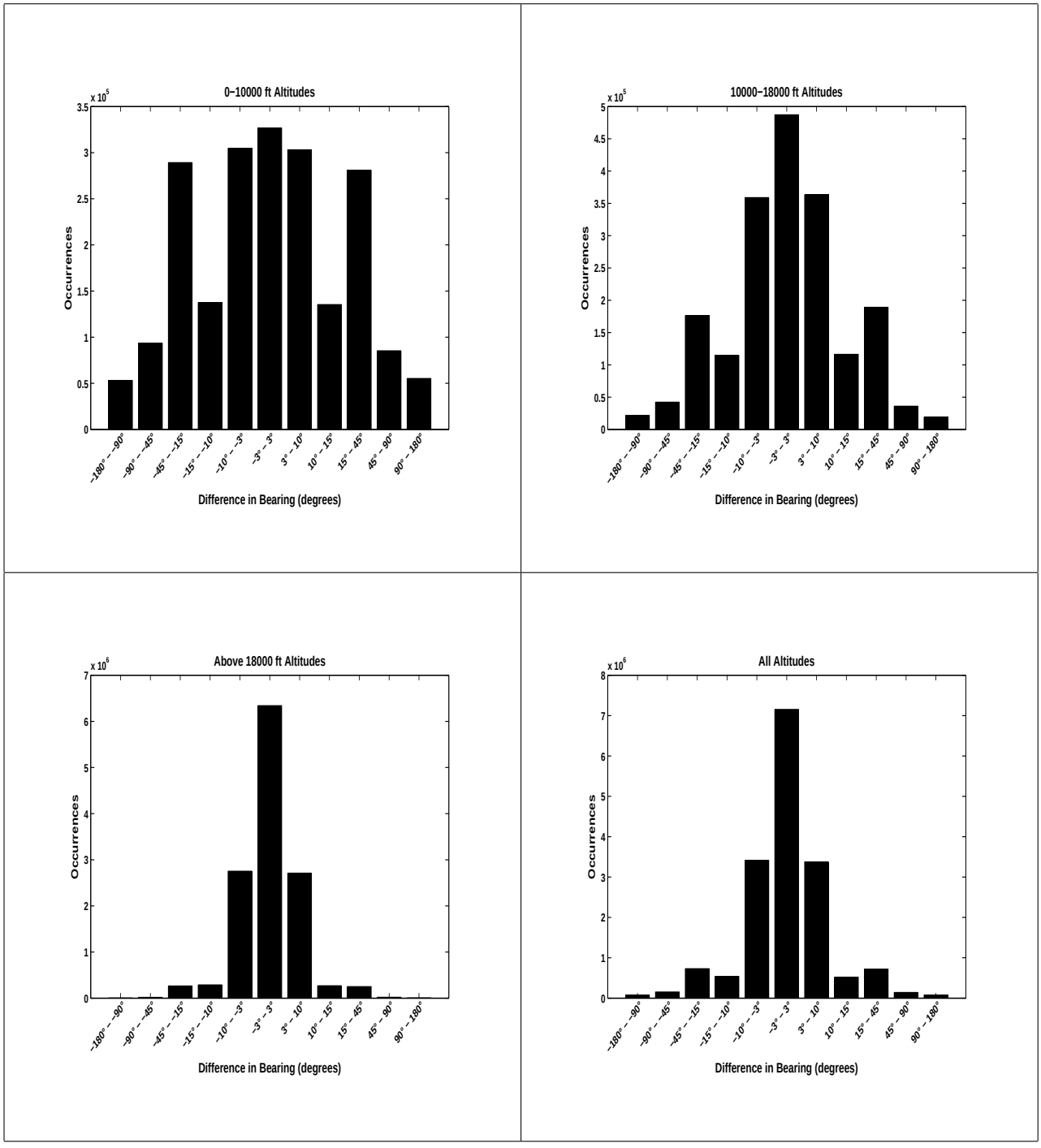

Figure A.26: Difference in bearing, all tracks, 5 minute projection

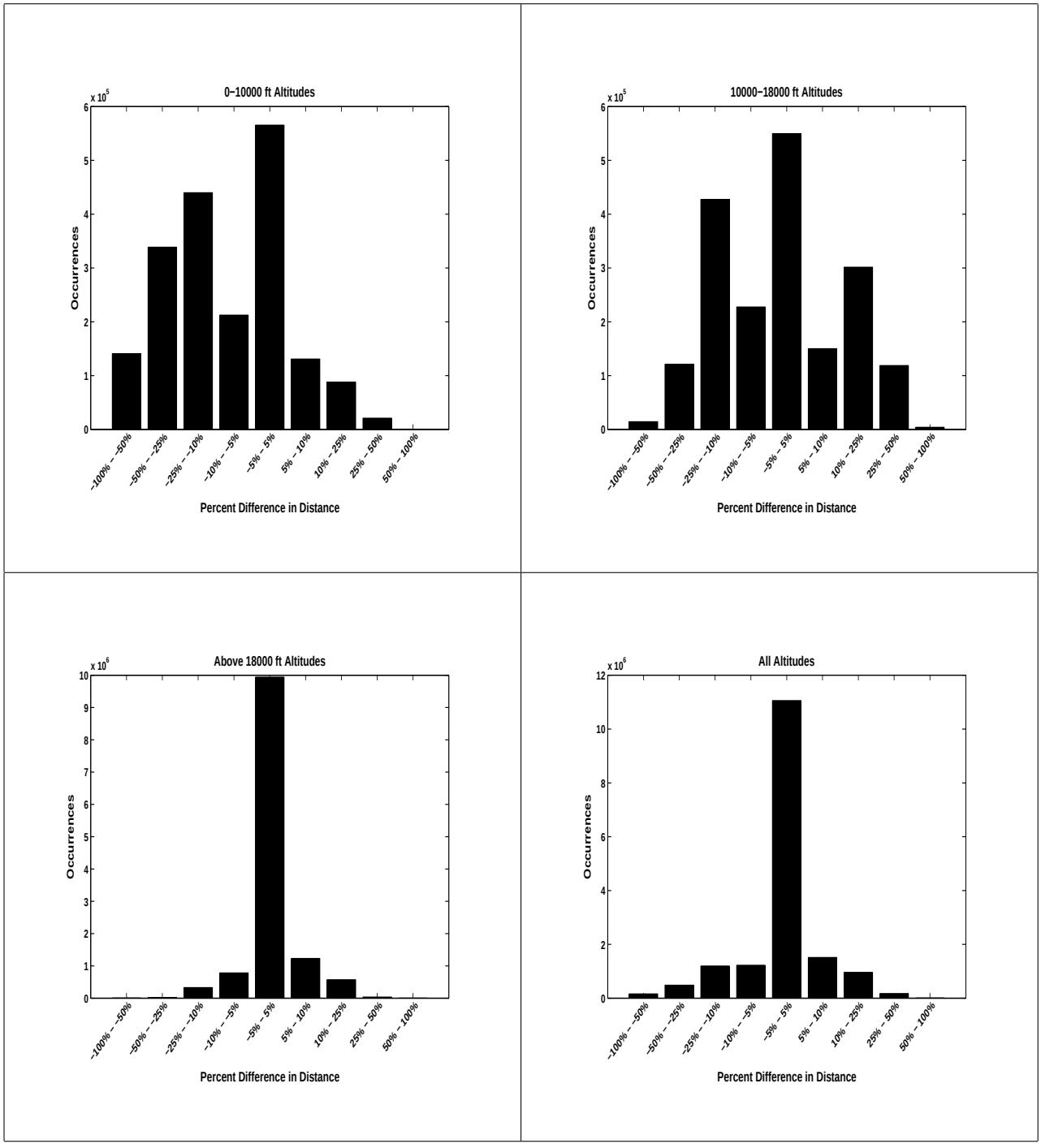

Figure A.27: Percent difference in distance, all tracks, 5 minute projection

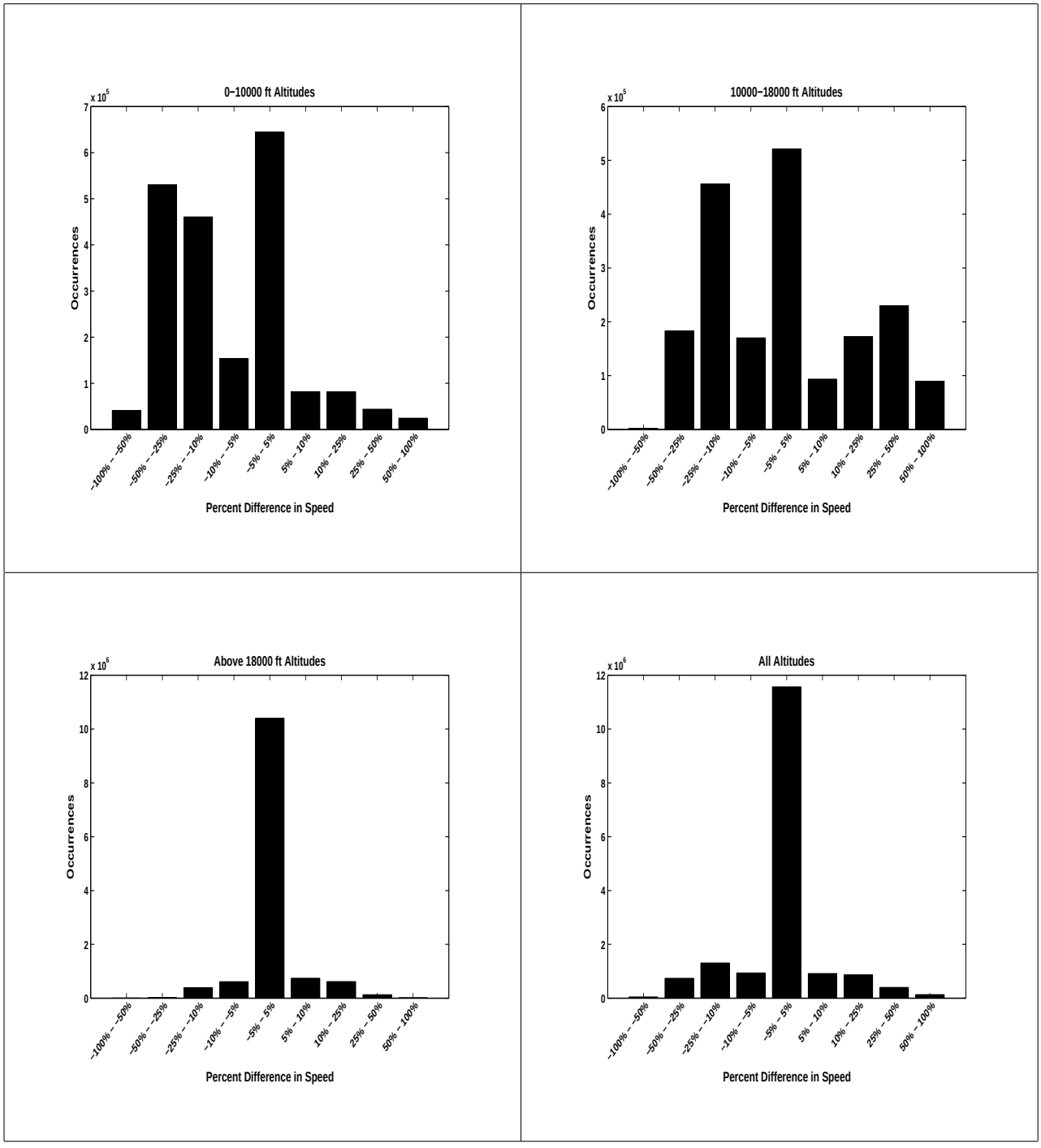

Figure A.28: Percent difference in speed, all tracks, 5 minute projection

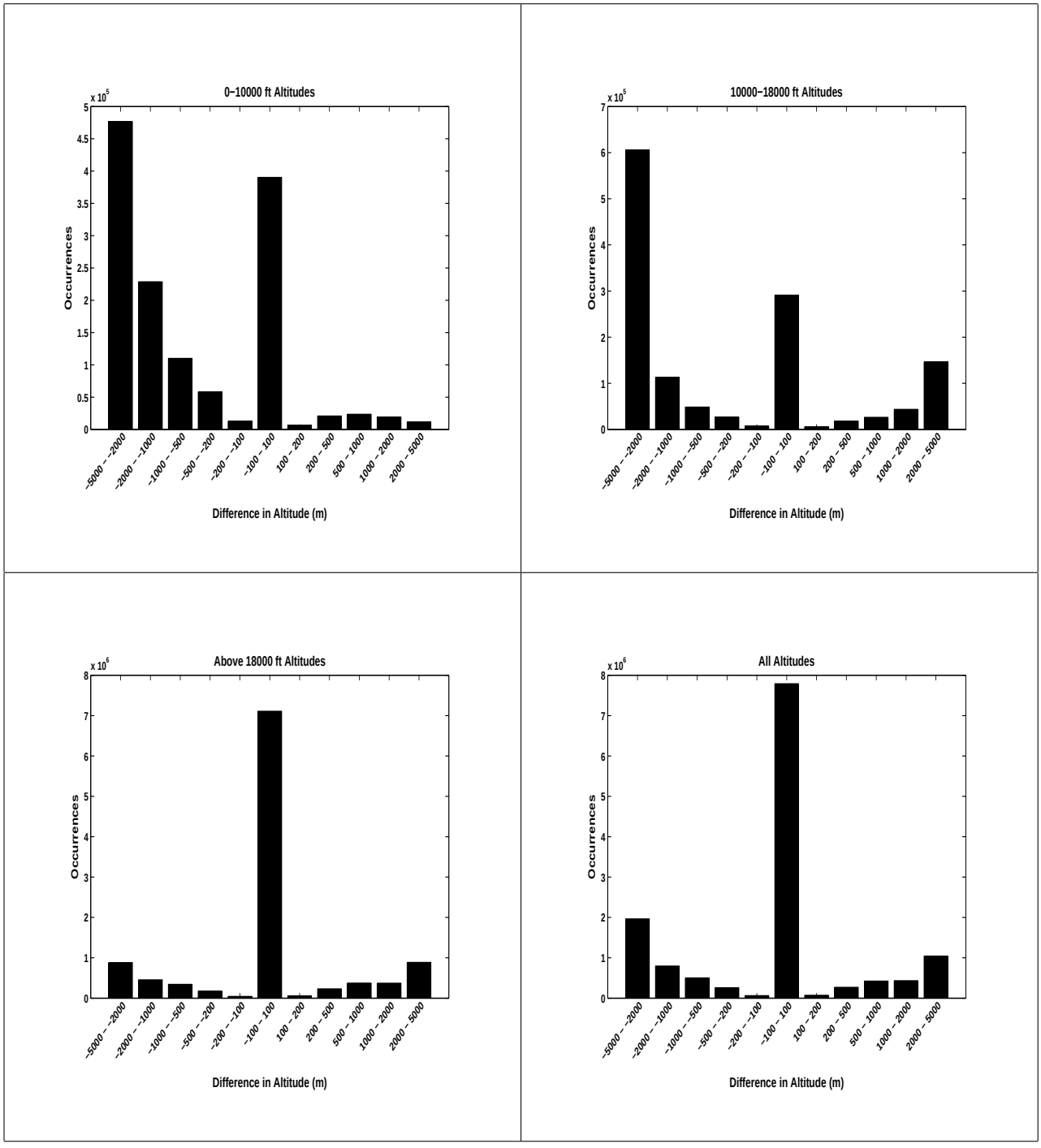

Figure A.29: Difference in altitude, all tracks, 10 minute projection

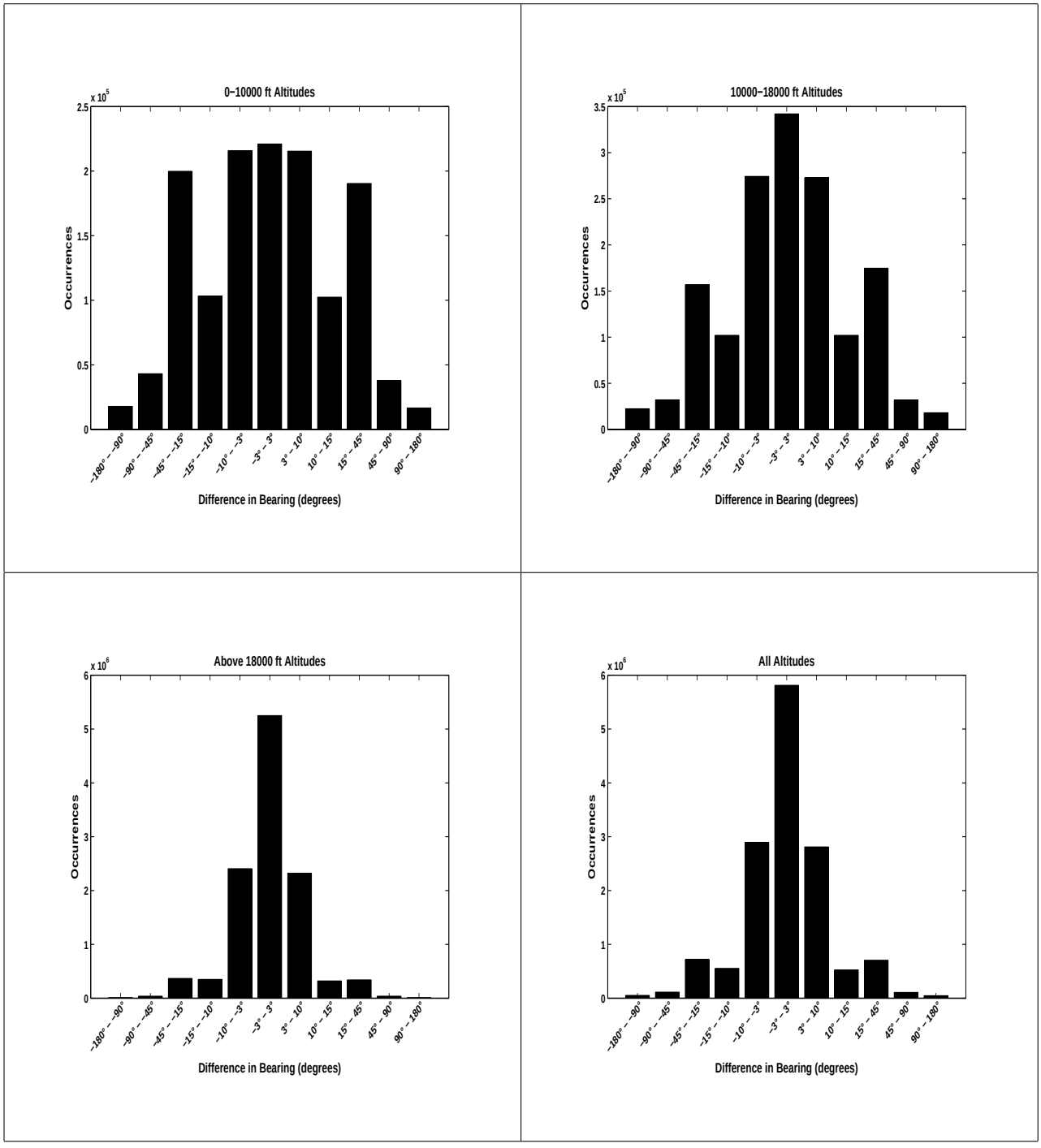

Figure A.30: Difference in bearing, all tracks, 10 minute projection

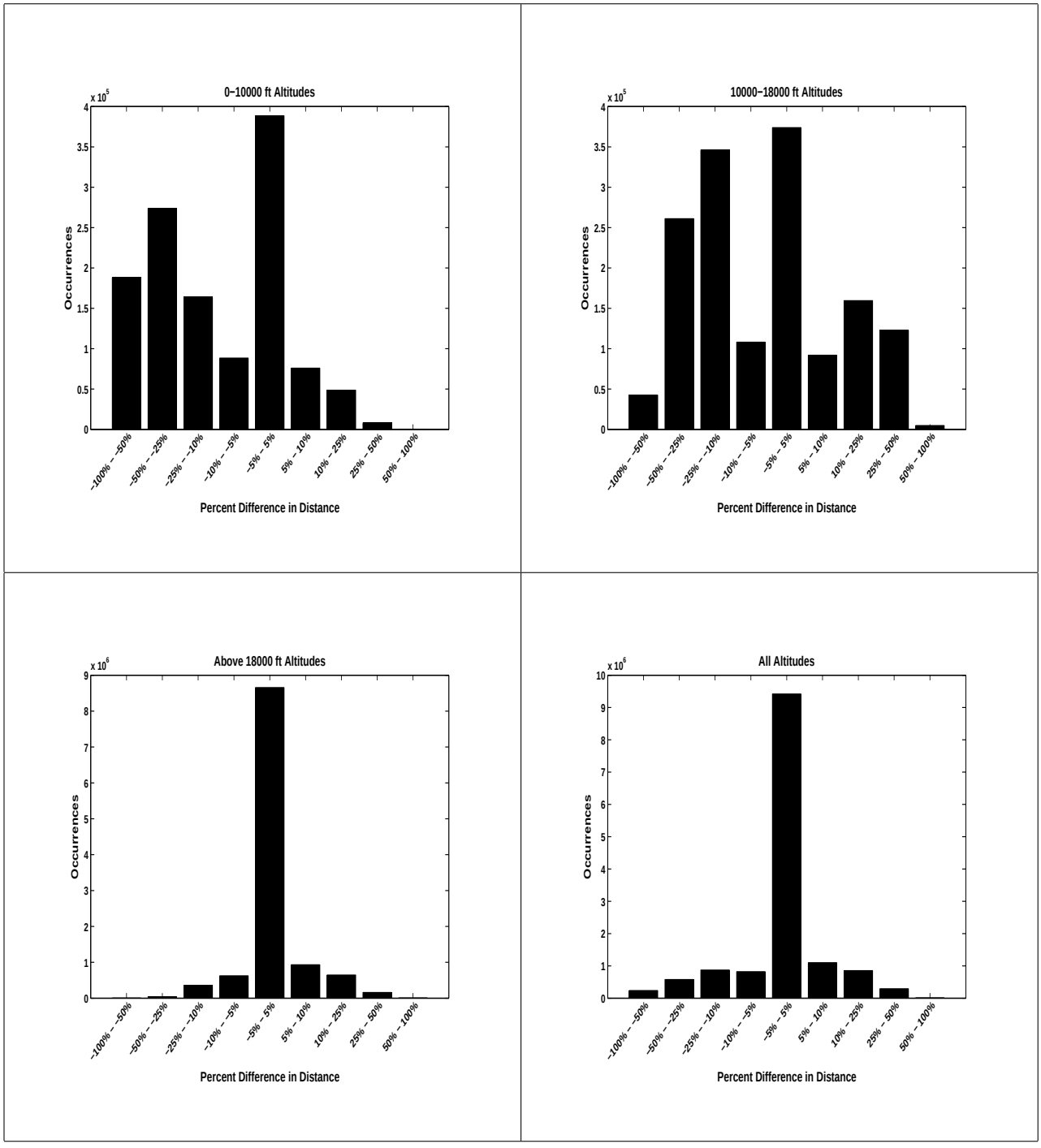

Figure A.31: Percent difference in distance, all tracks, 10 minute projection

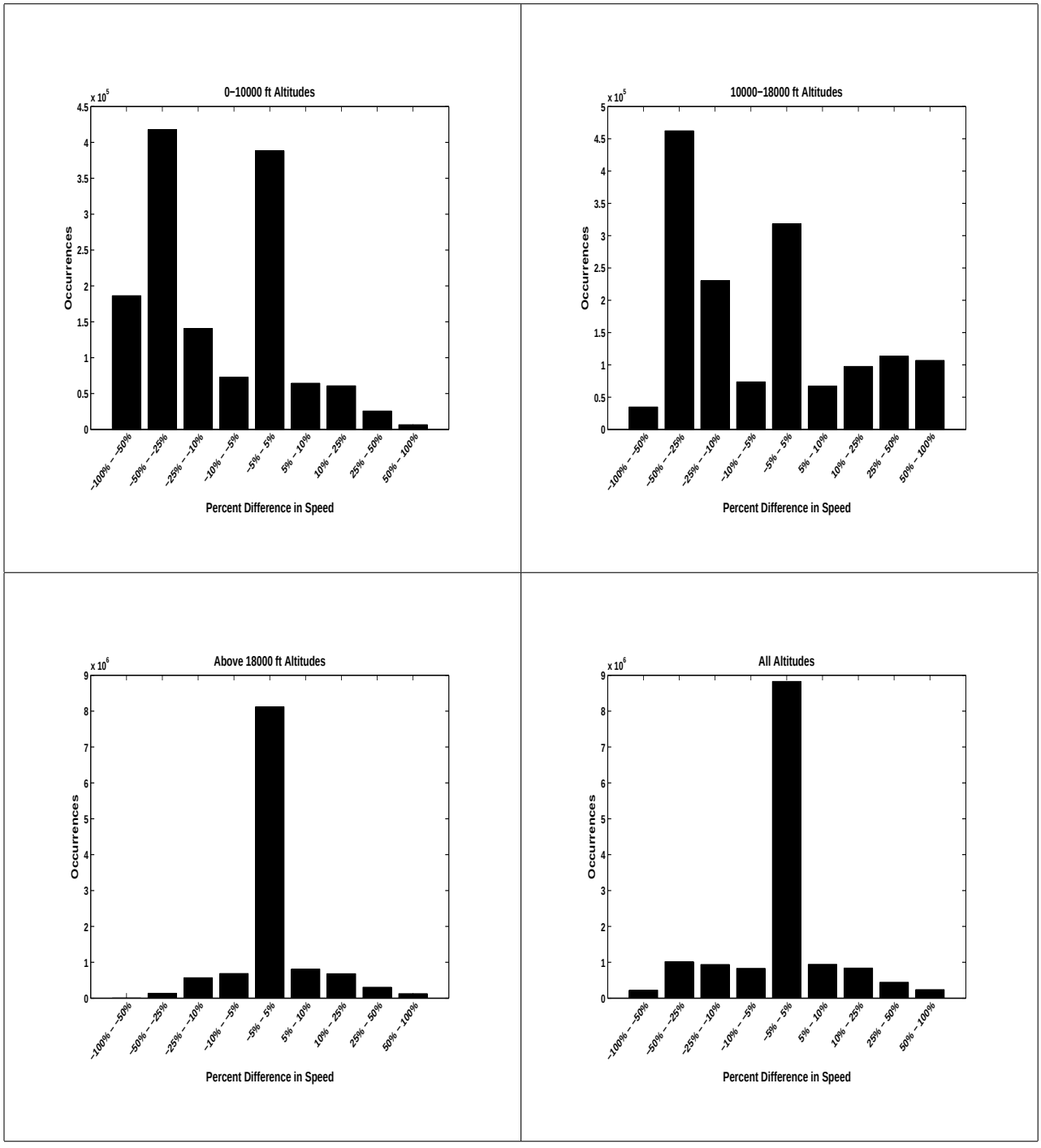

Figure A.32: Percent difference in speed, all tracks, 10 minute projection

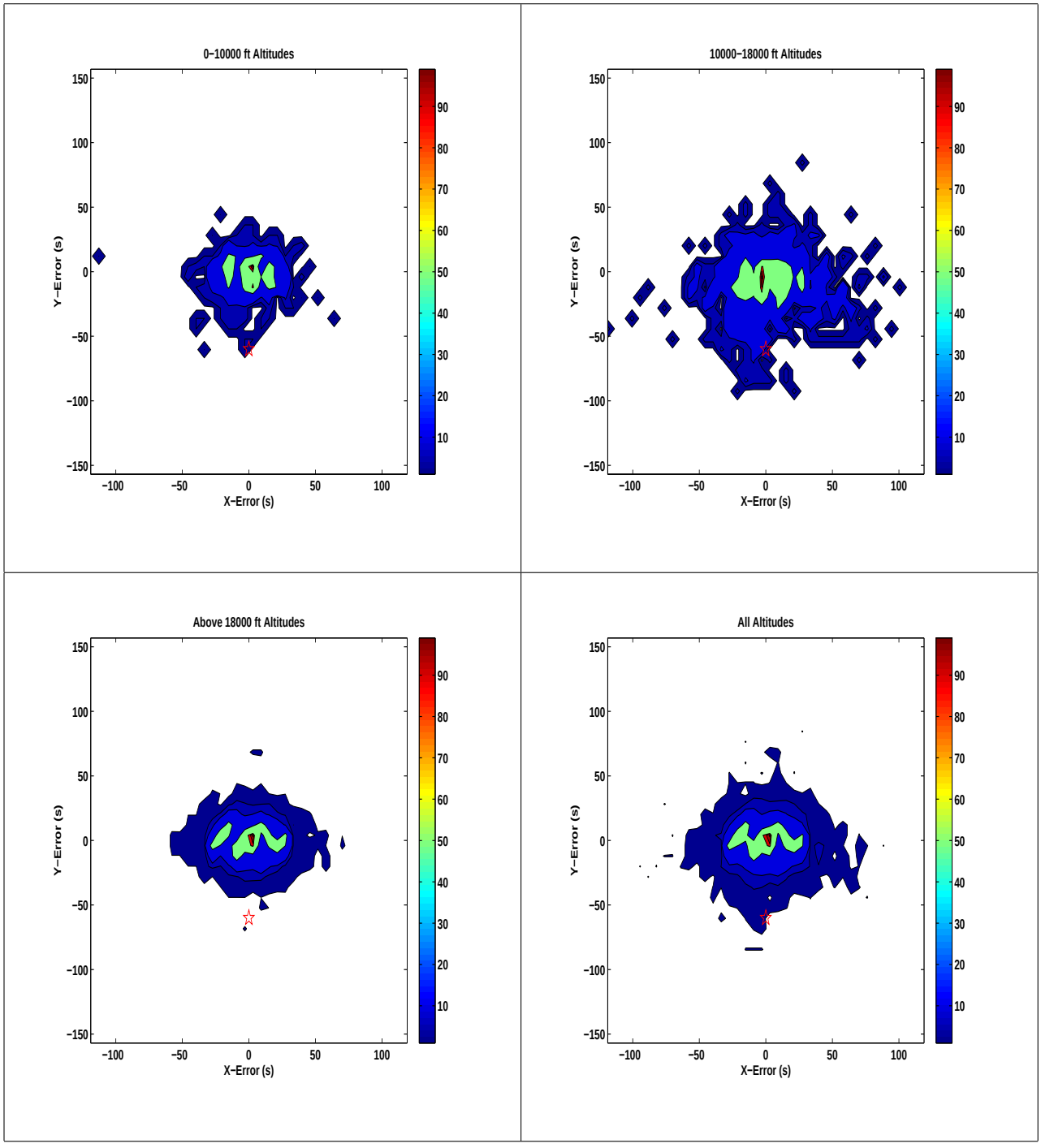

Figure A.33: Fort Campbell, 50 km radius, 1 minute projection, difference in projection to measured histograms

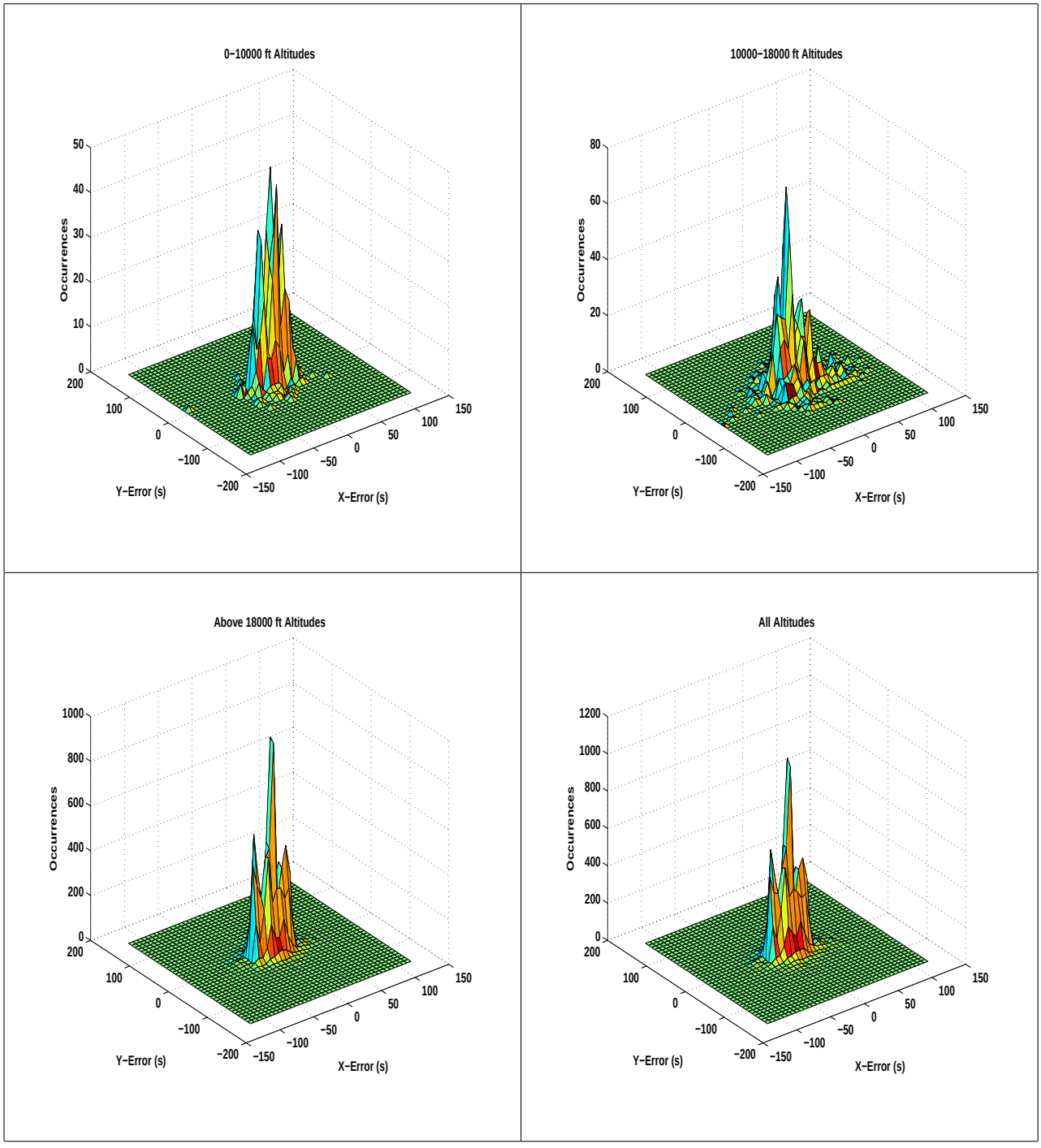

Figure A.34: Fort Campbell, 50 km radius, 1 minute projection, difference in projection to measured three dimensional histograms

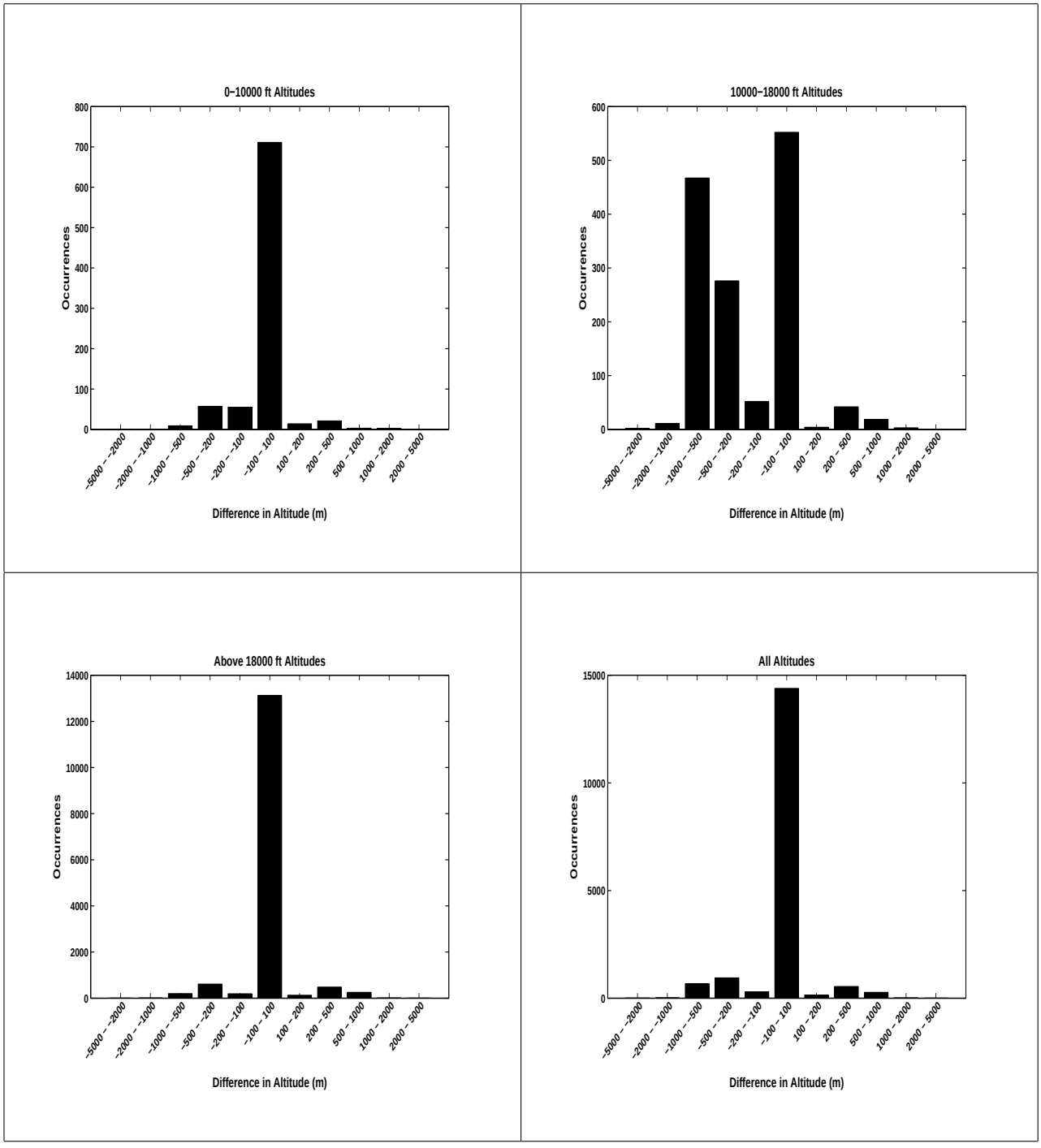

Figure A.35: Fort Campbell, 50 km radius, 1 minute projection, difference in altitude

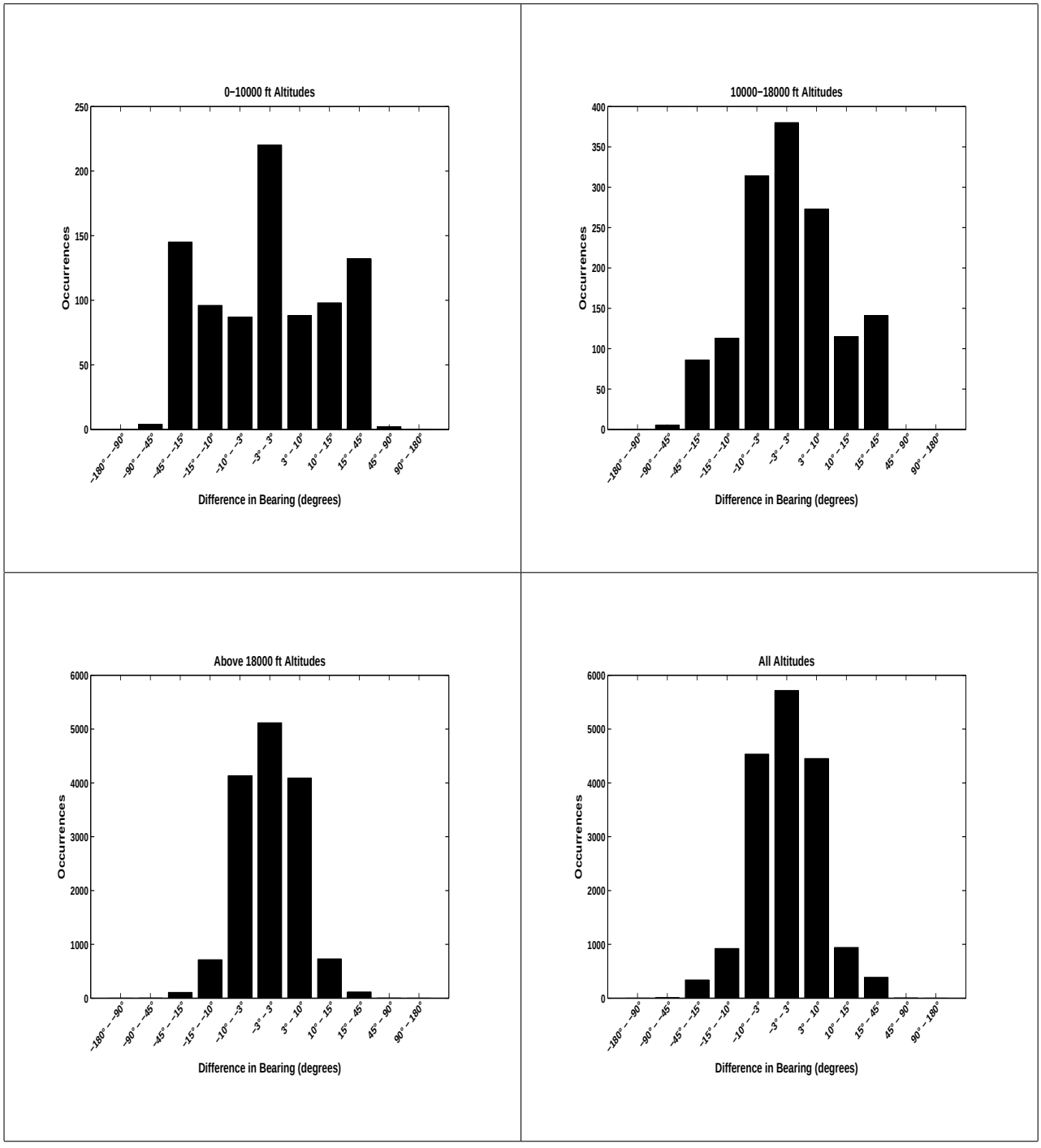

Figure A.36: Fort Campbell, 50 km radius, 1 minute projection, difference in bearing

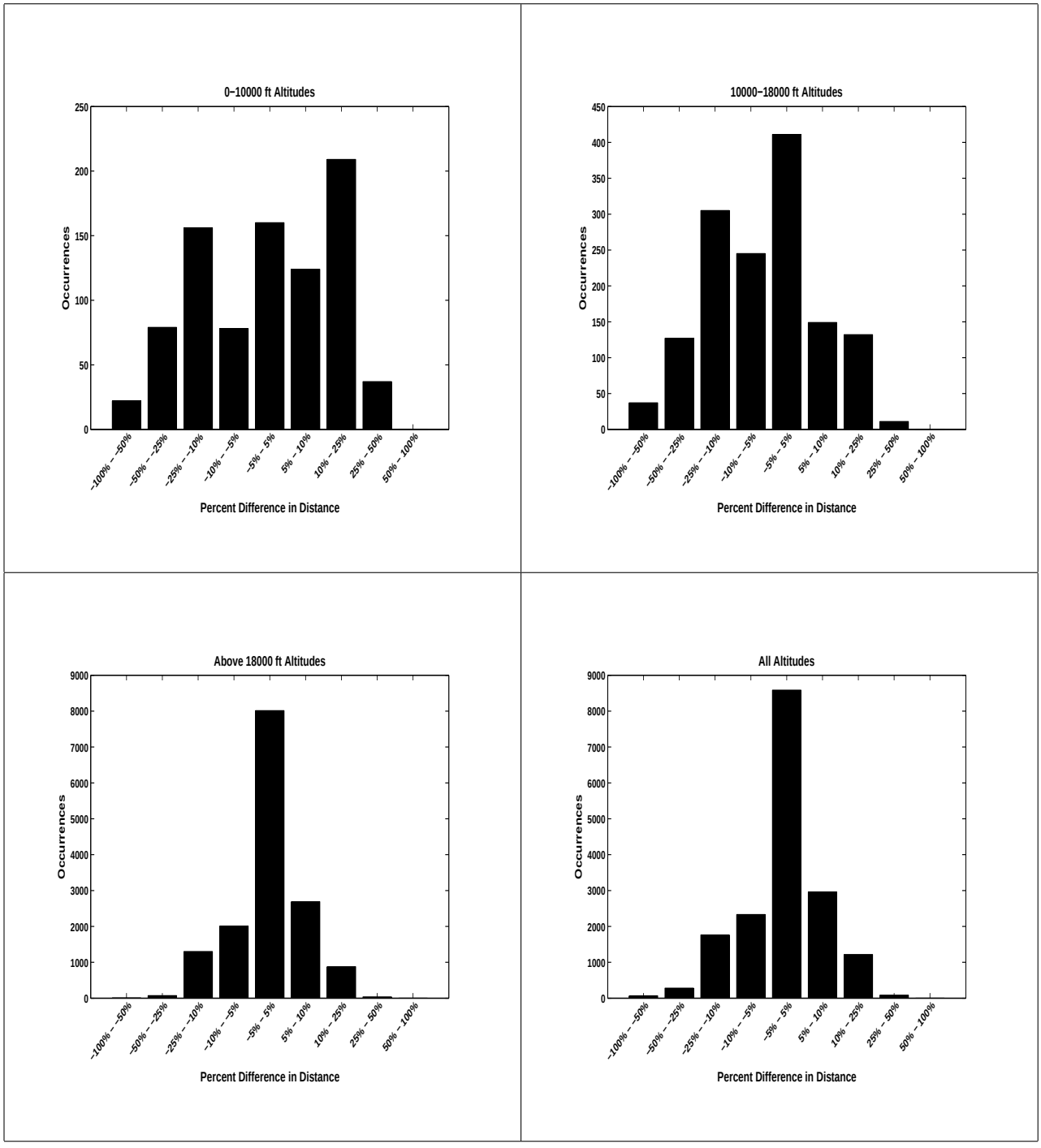

Figure A.37: Fort Campbell, 50 km radius, 1 minute projection, percent difference in distance

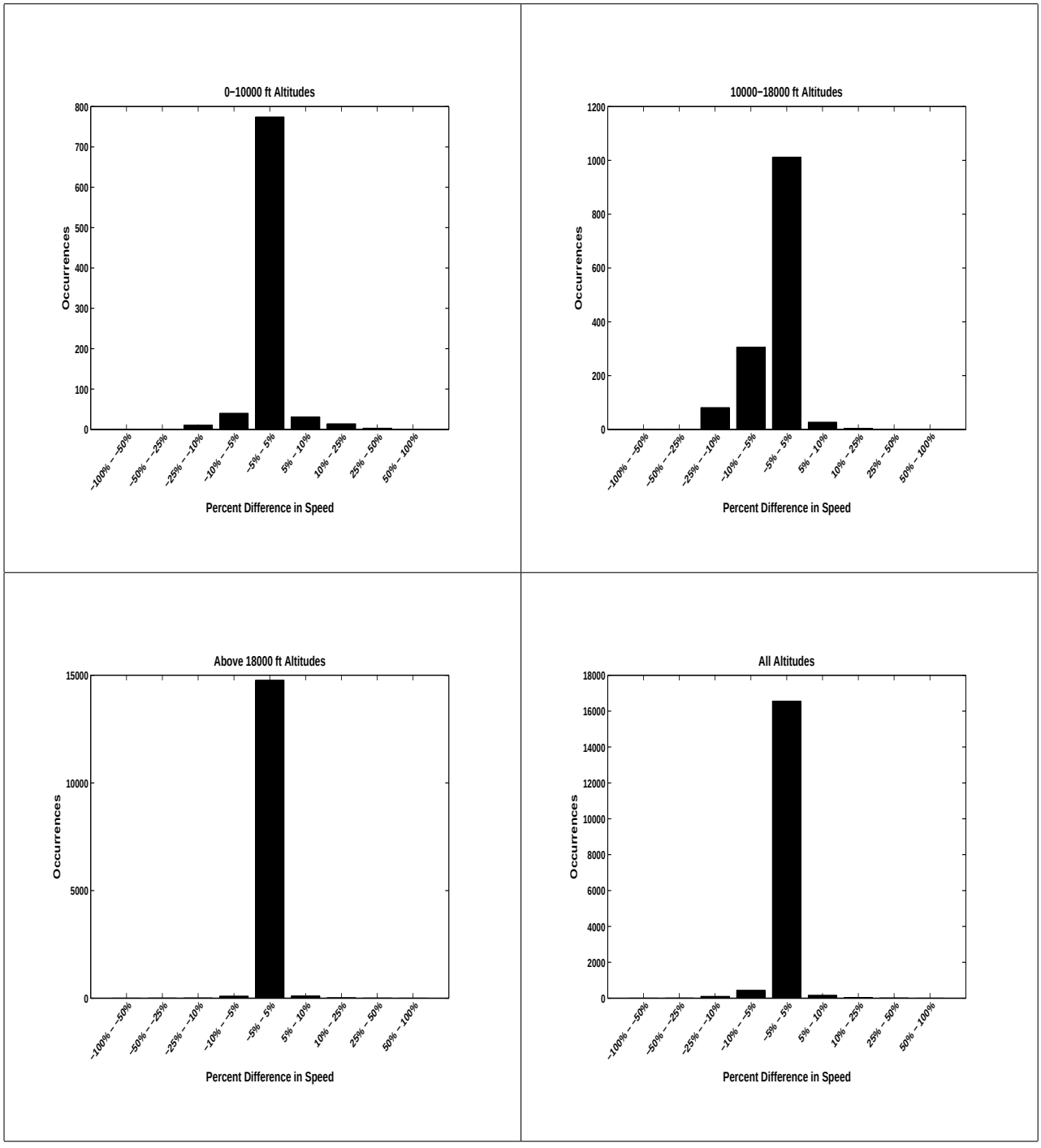

Figure A.38: Fort Campbell, 50 km radius, 1 minute projection, percent difference in speed

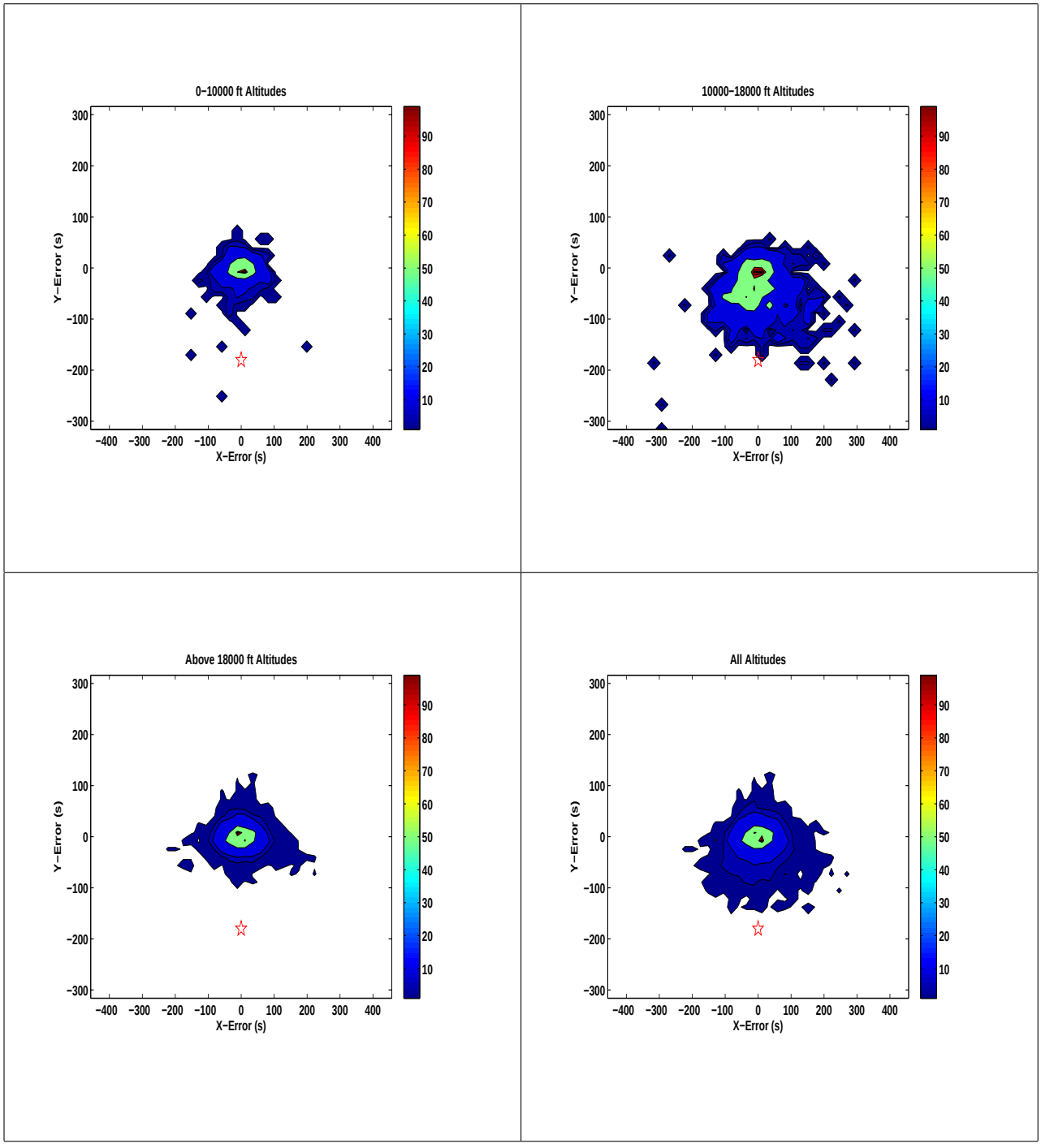

Figure A.39: Fort Campbell, 50 km radius, 3 minute projection, difference in projection to measured histograms

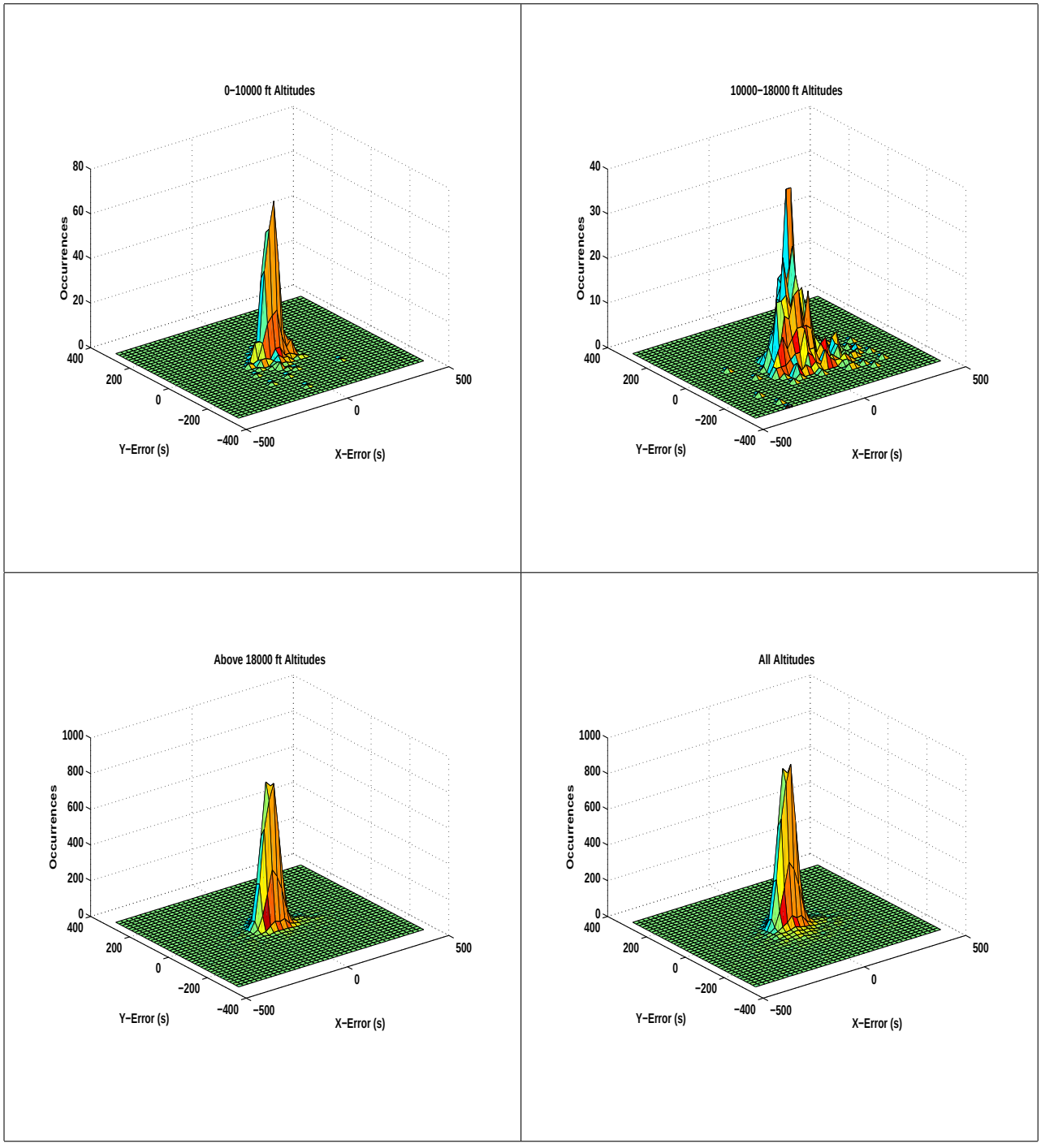

Figure A.40: Fort Campbell, 50 km radius, 3 minute projection, difference in projection to measured three dimensional histograms

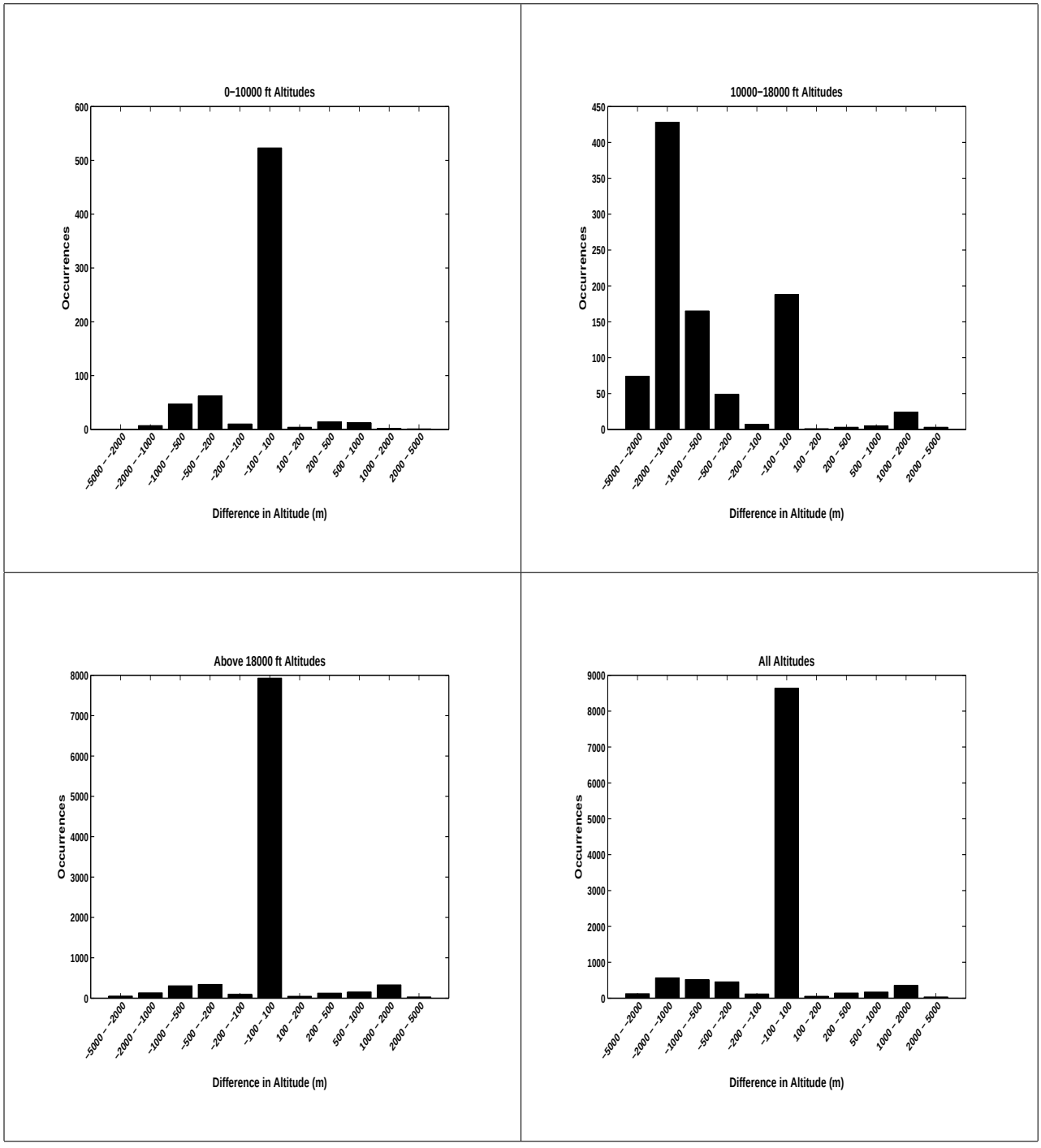

Figure A.41: Fort Campbell, 50 km radius, 3 minute projection, difference in altitude

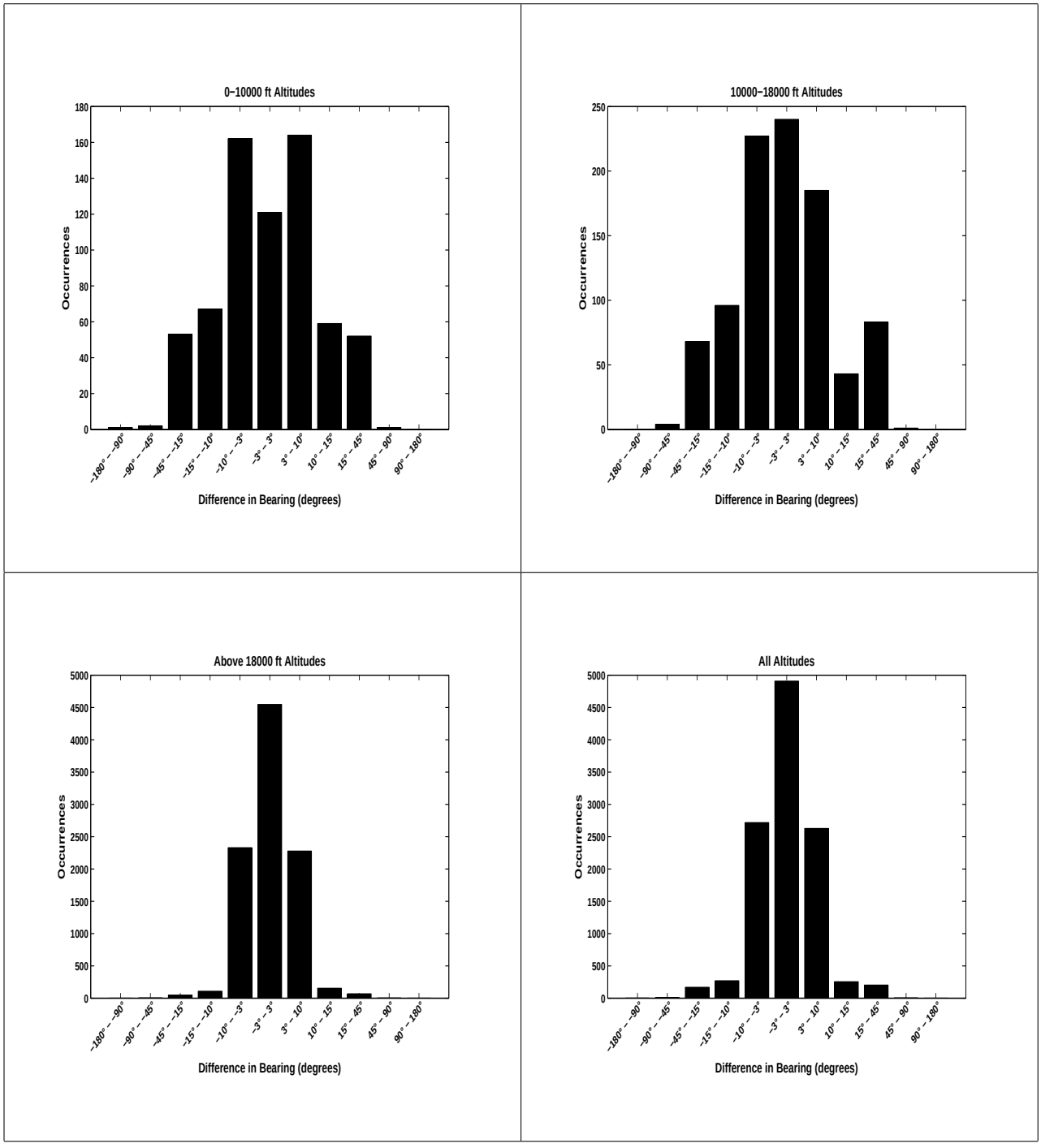

Figure A.42: Fort Campbell, 50 km radius, 3 minute projection, difference in bearing

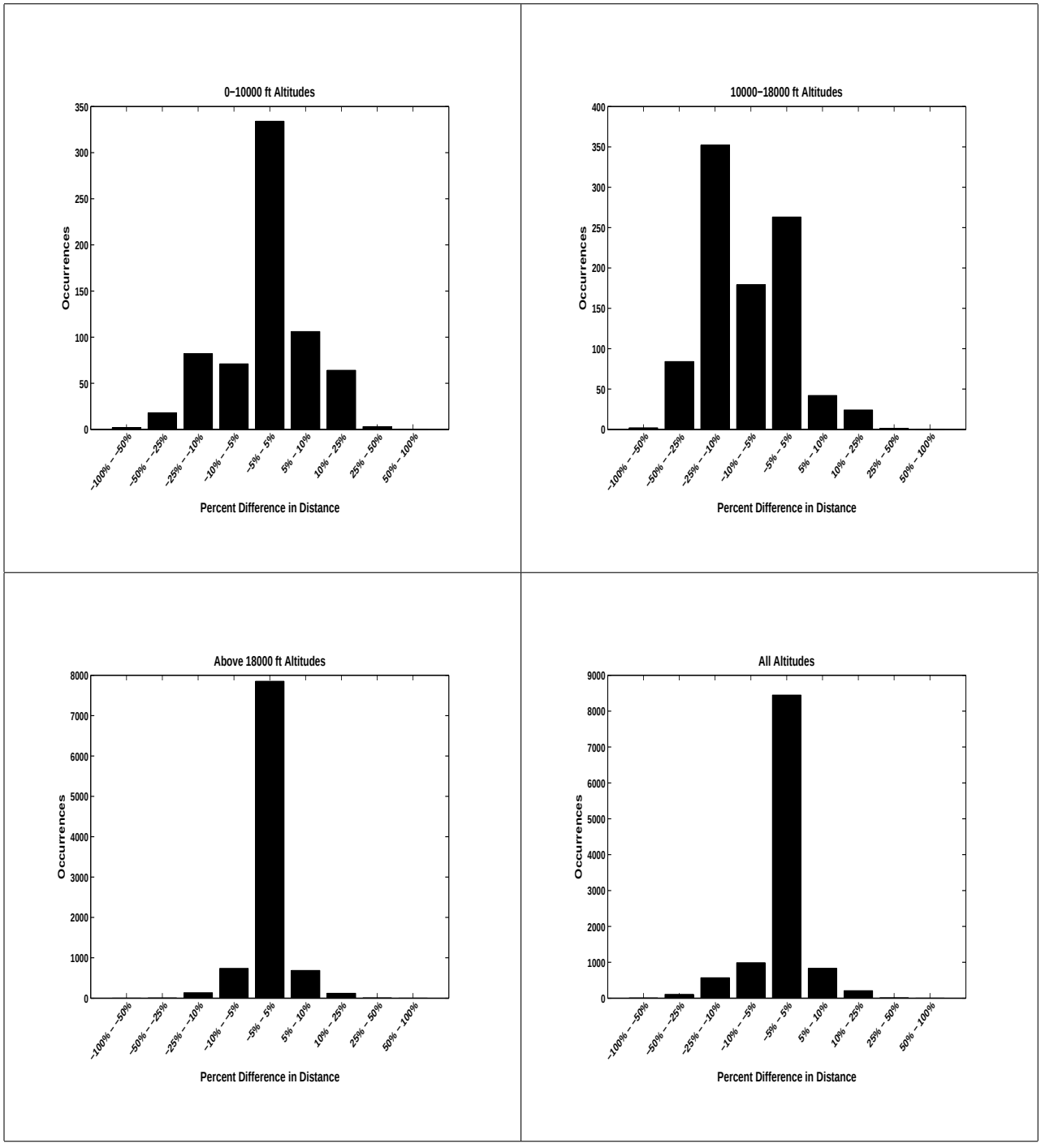

Figure A.43: Fort Campbell, 50 km radius, 3 minute projection, percent difference in distance

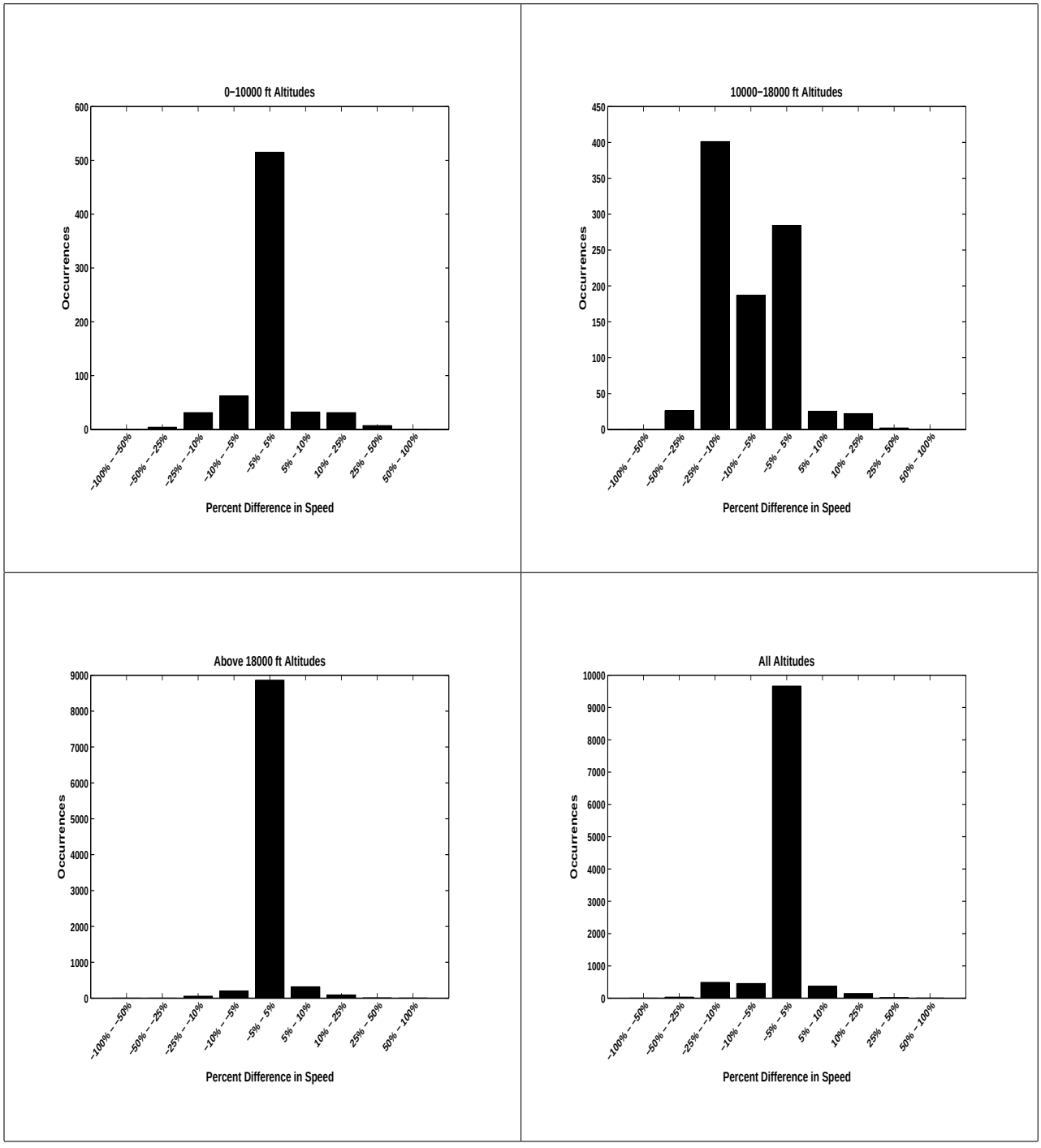

Figure A.44: Fort Campbell, 50 km radius, 3 minute projection, percent difference in speed

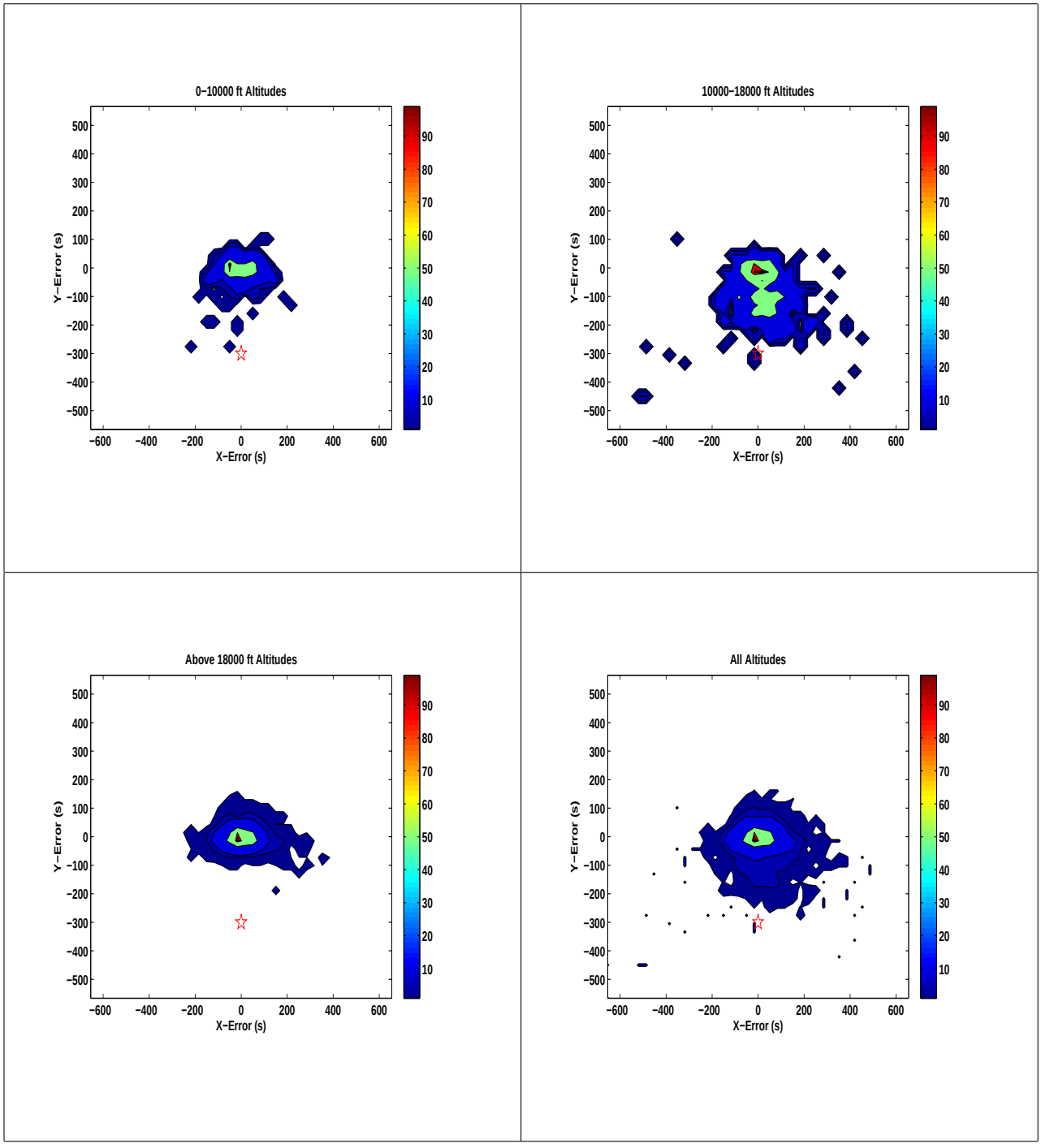

Figure A.45: Fort Campbell, 50 km radius, 5 minute projection, difference in projection to measured histograms

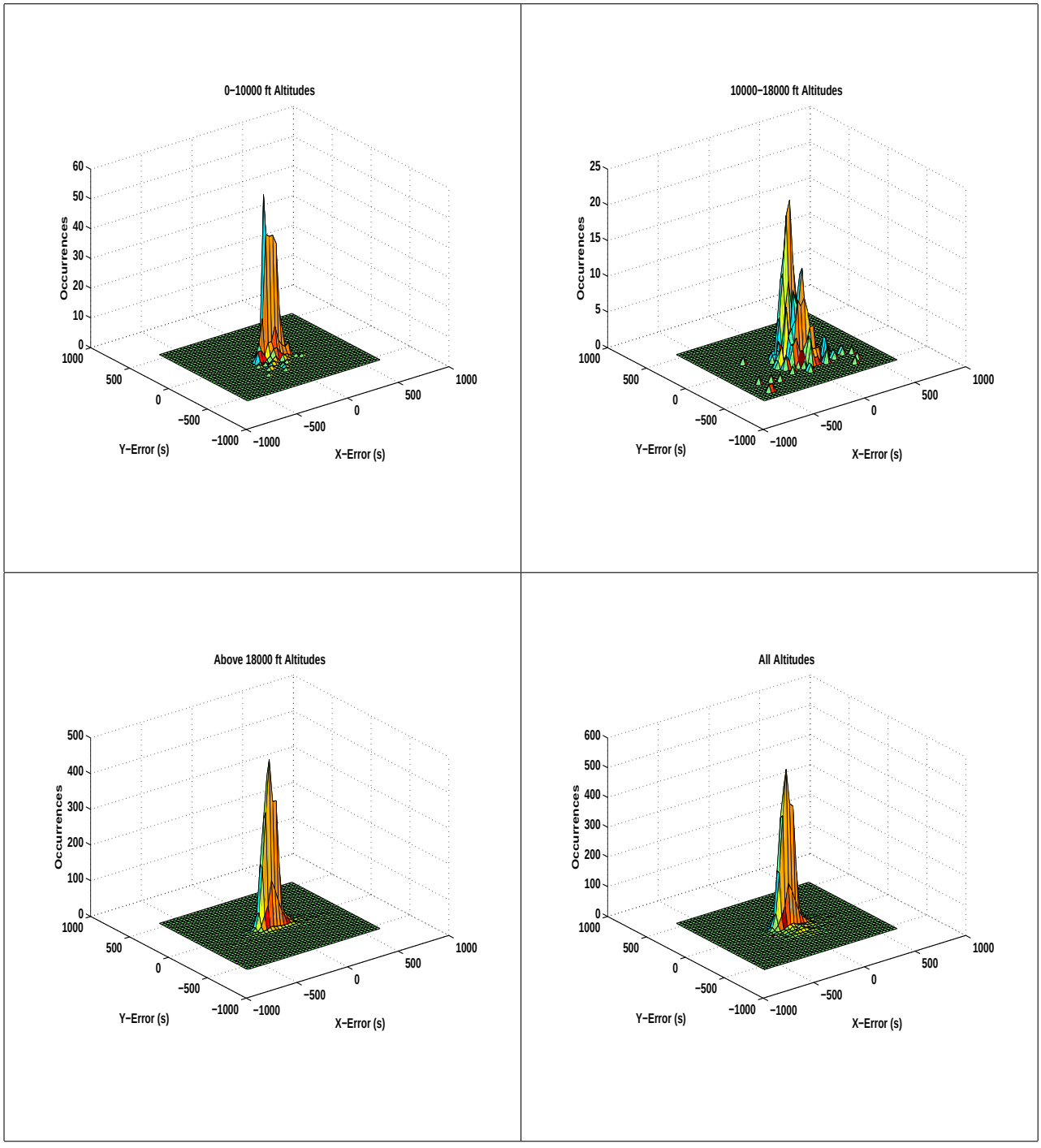

Figure A.46: Fort Campbell, 50 km radius, 5 minute projection, difference in projection to measured three dimensional histograms

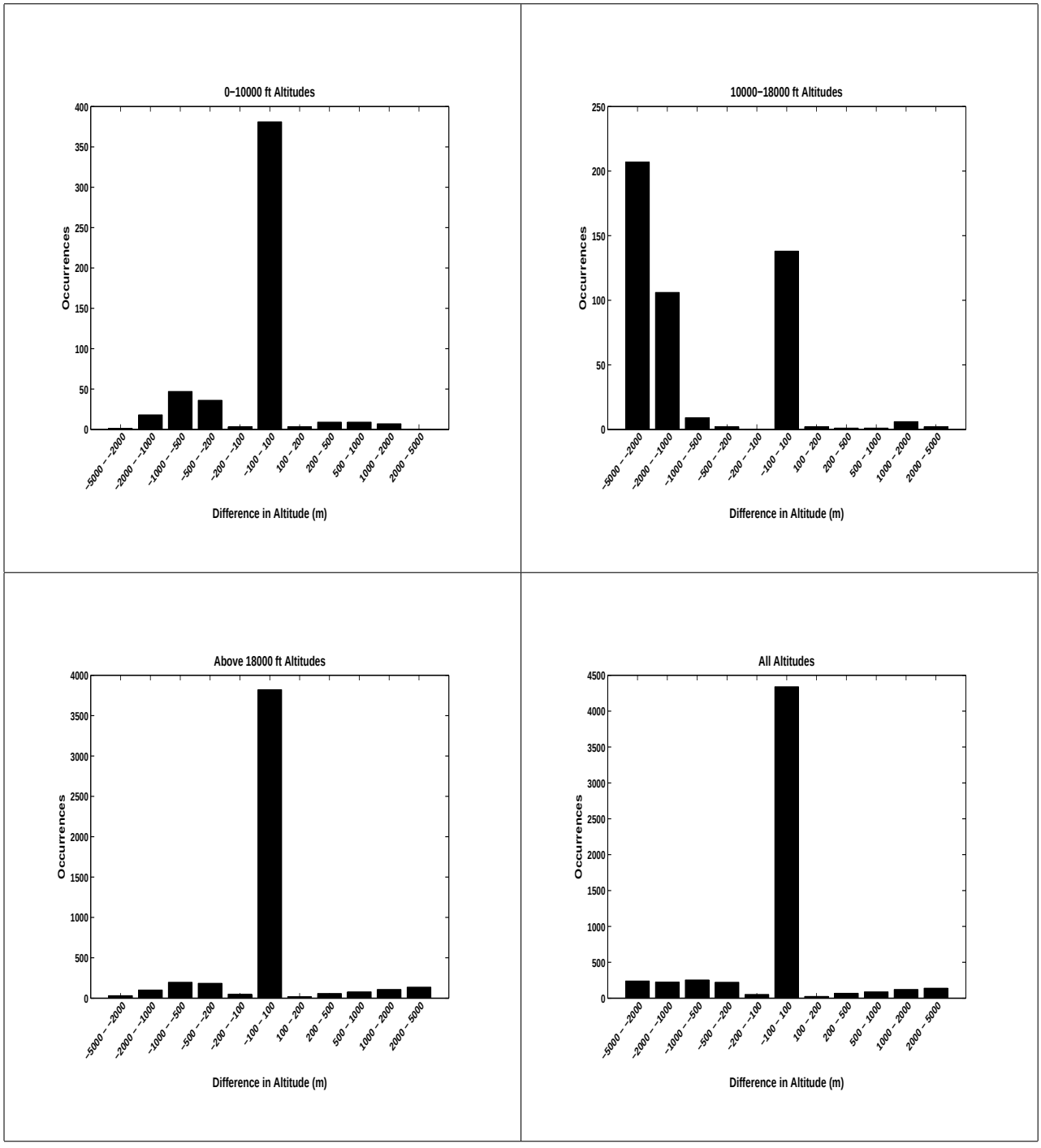

Figure A.47: Fort Campbell, 50 km radius, 5 minute projection, difference in altitude

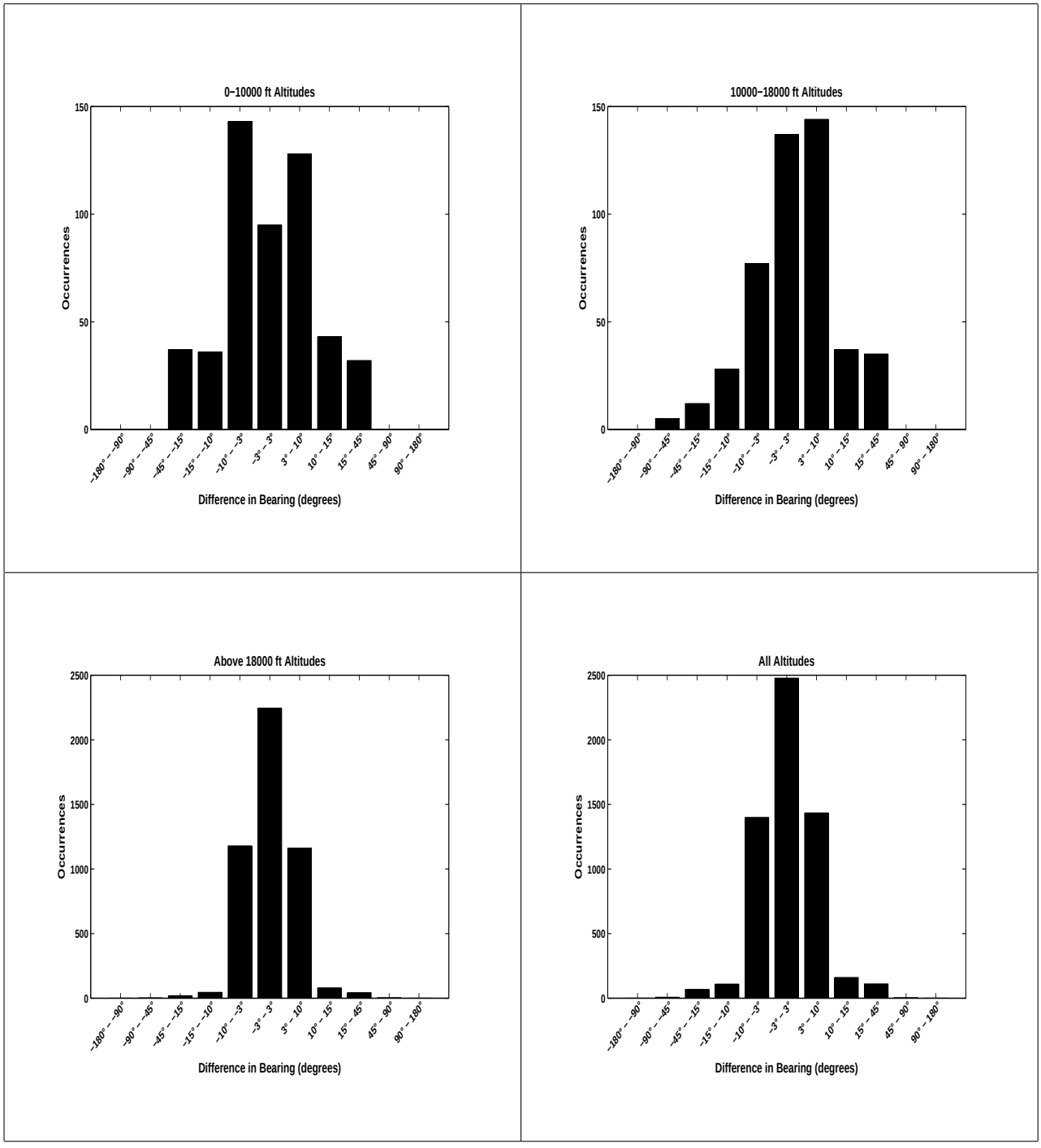

Figure A.48: Fort Campbell, 50 km radius, 5 minute projection, difference in bearing

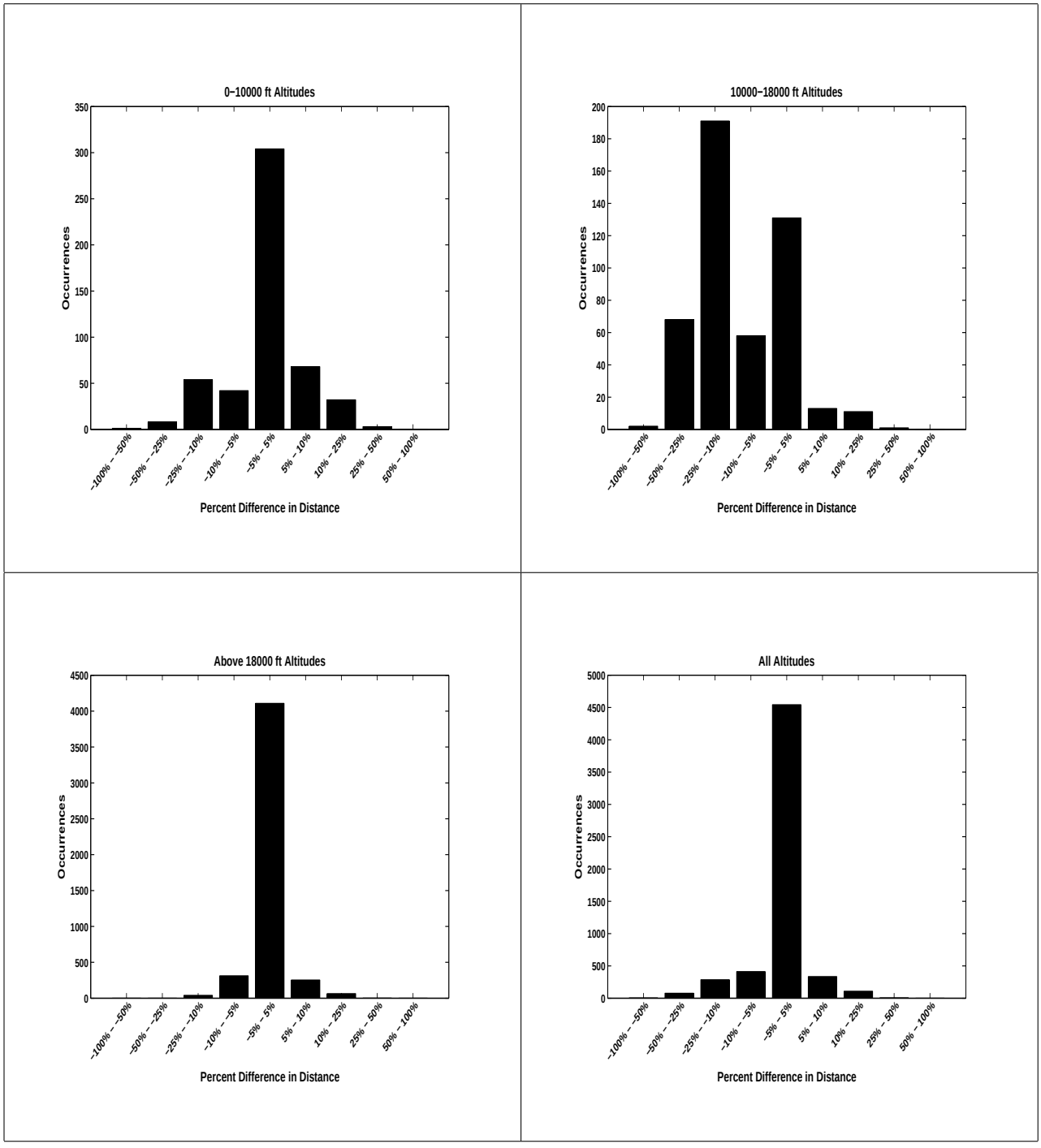

Figure A.49: Fort Campbell, 50 km radius, 5 minute projection, percent difference in distance

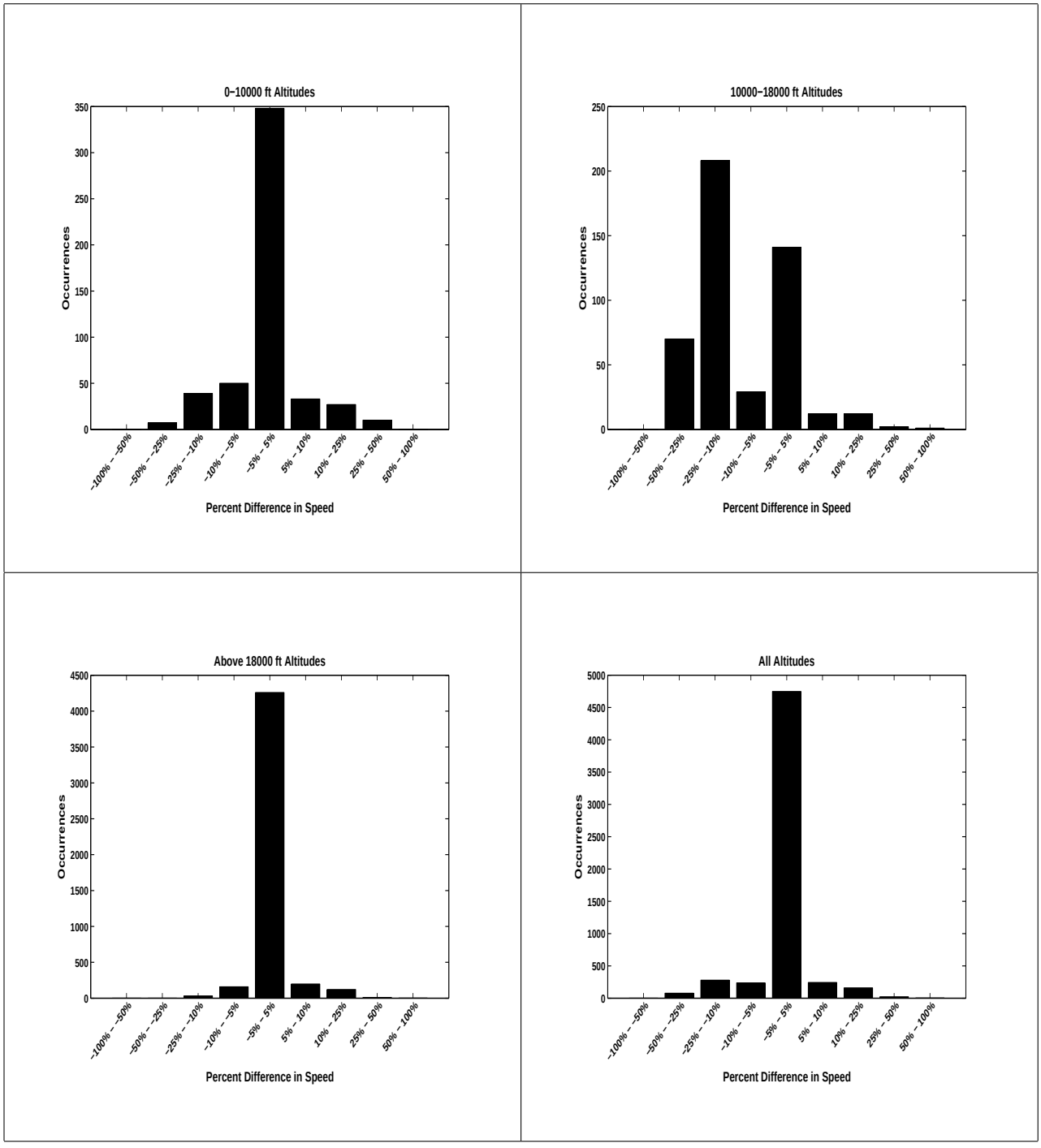

Figure A.50: Fort Campbell, 50 km radius, 5 minute projection, percent difference in speed

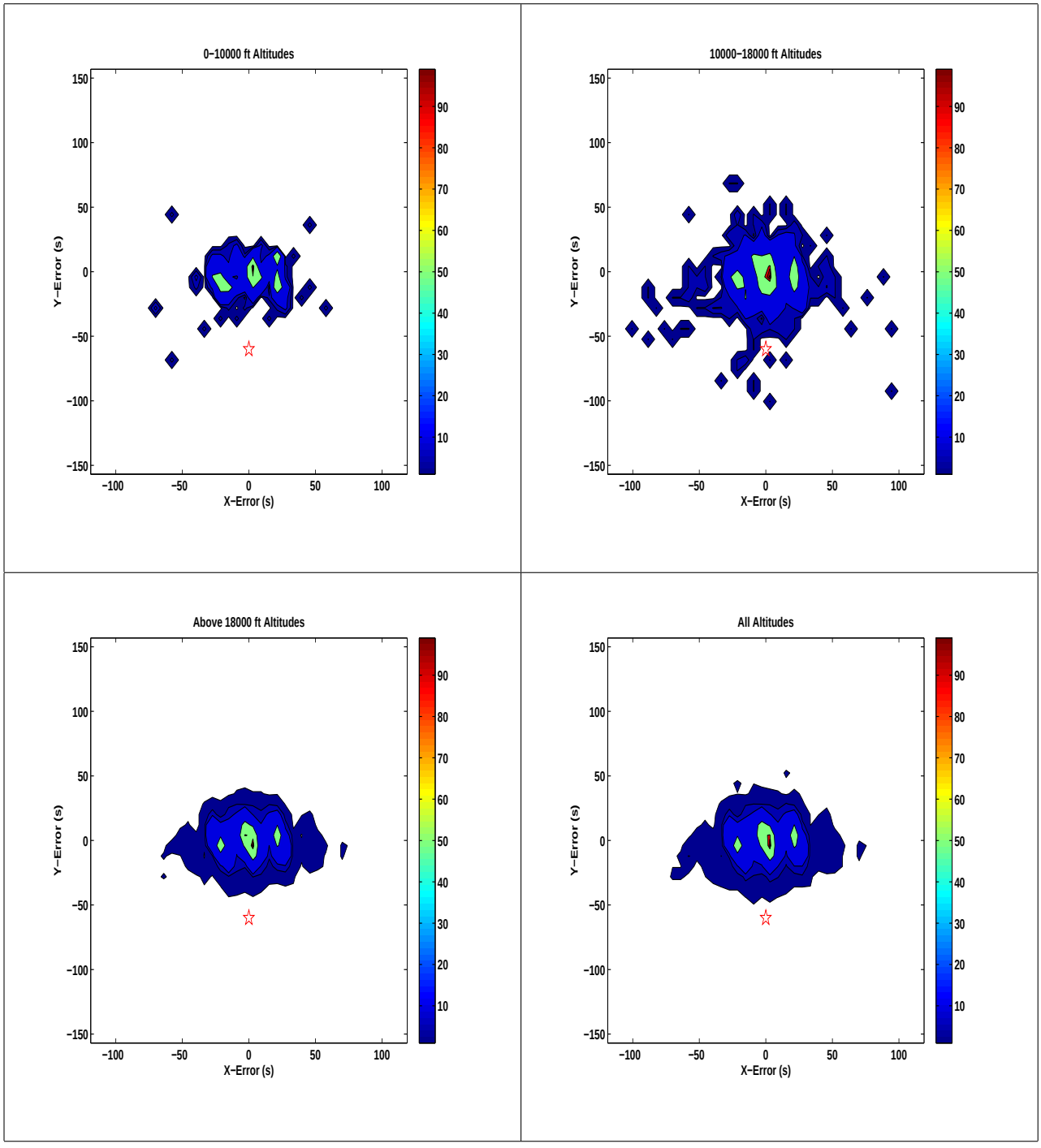

Figure A.51: Las Cruces, 50 km radius, 1 minute projection, difference in projection to measured histograms

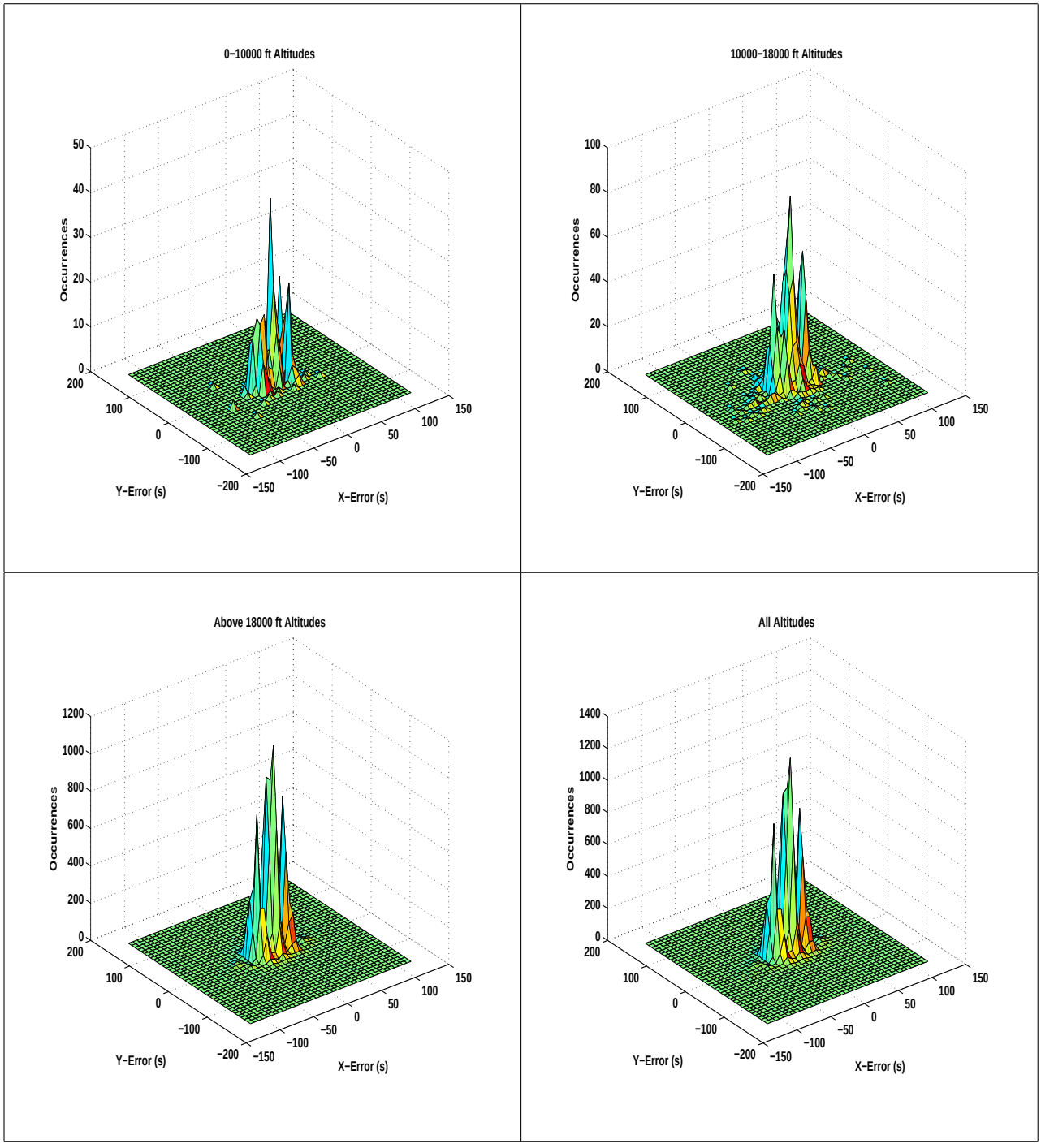

Figure A.52: Las Cruces, 50 km radius, 1 minute projection, difference in projection to measured three dimensional histograms

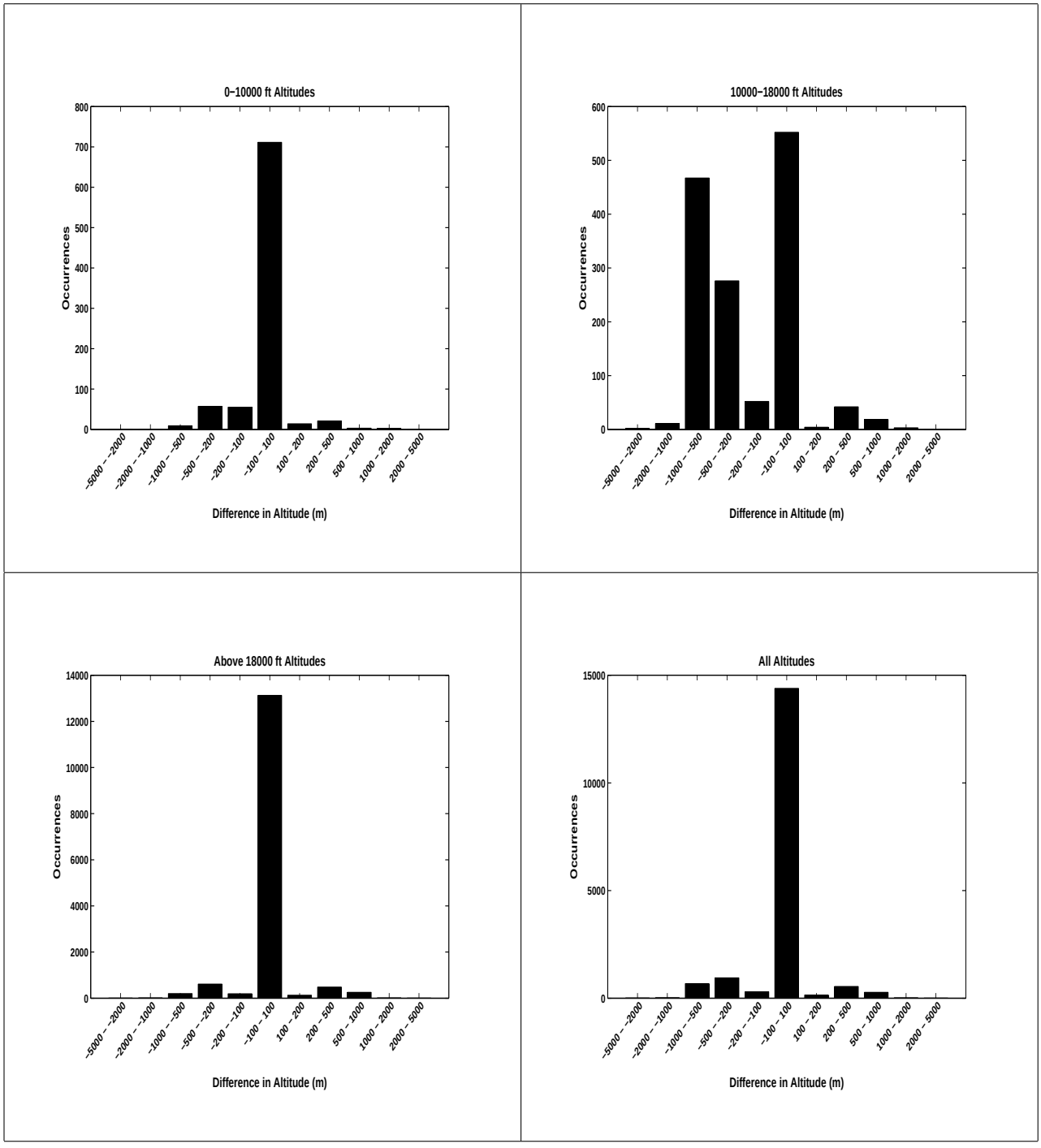

Figure A.53: Las Cruces, 50 km radius, 1 minute projection, difference in altitude

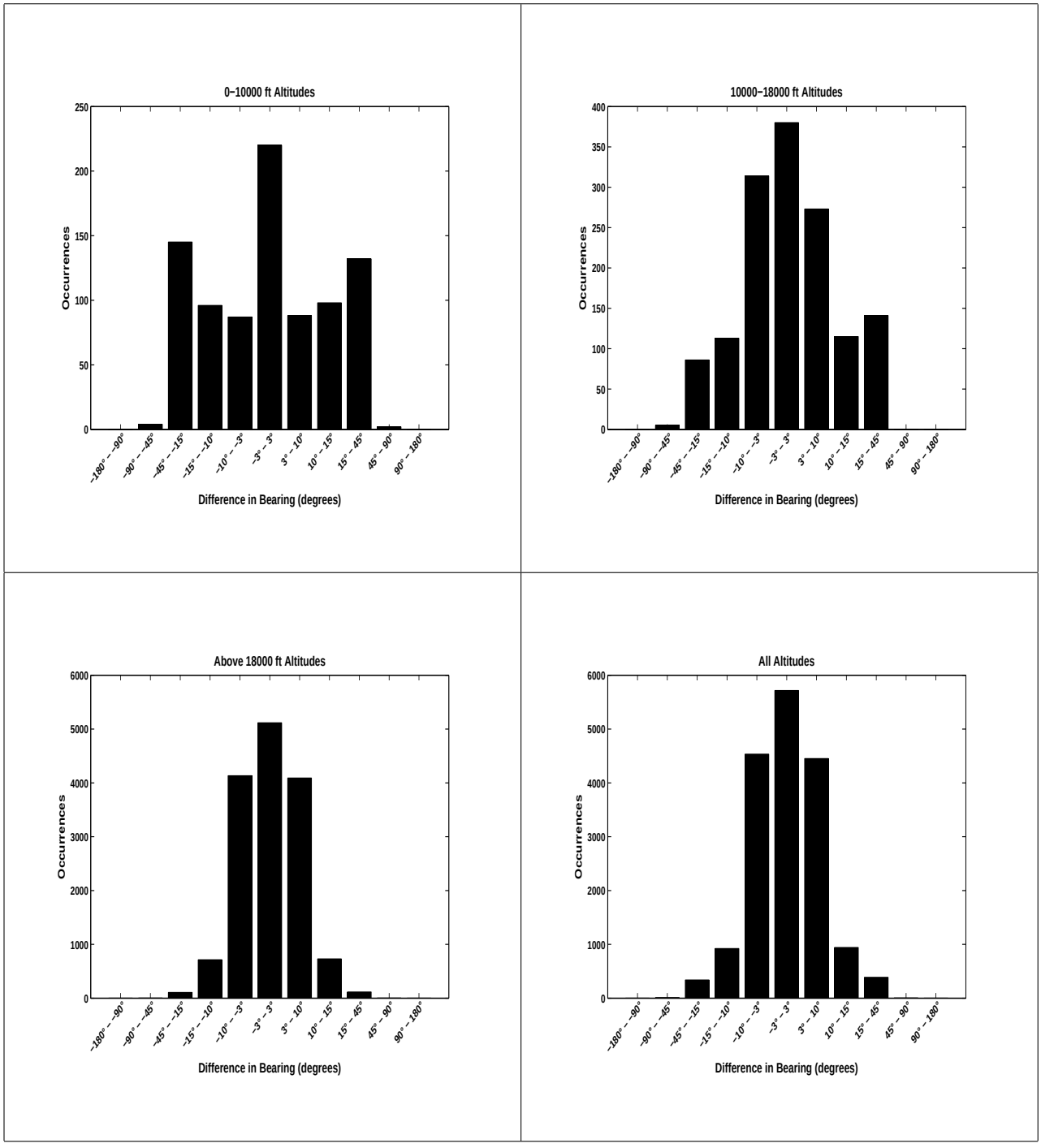

Figure A.54: Las Cruces, 50 km radius, 1 minute projection, difference in bearing

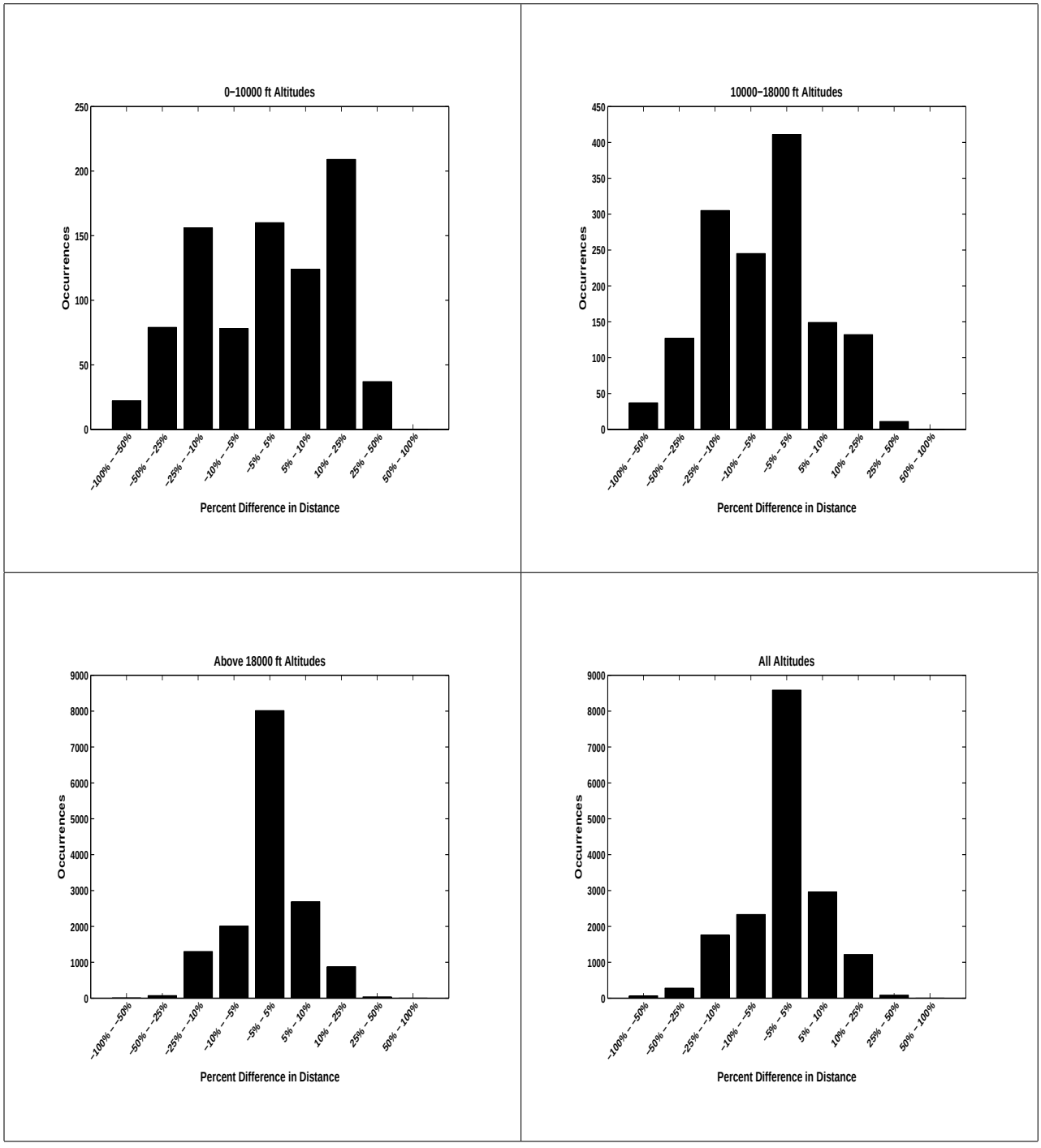

Figure A.55: Las Cruces, 50 km radius, 1 minute projection, percent difference in distance

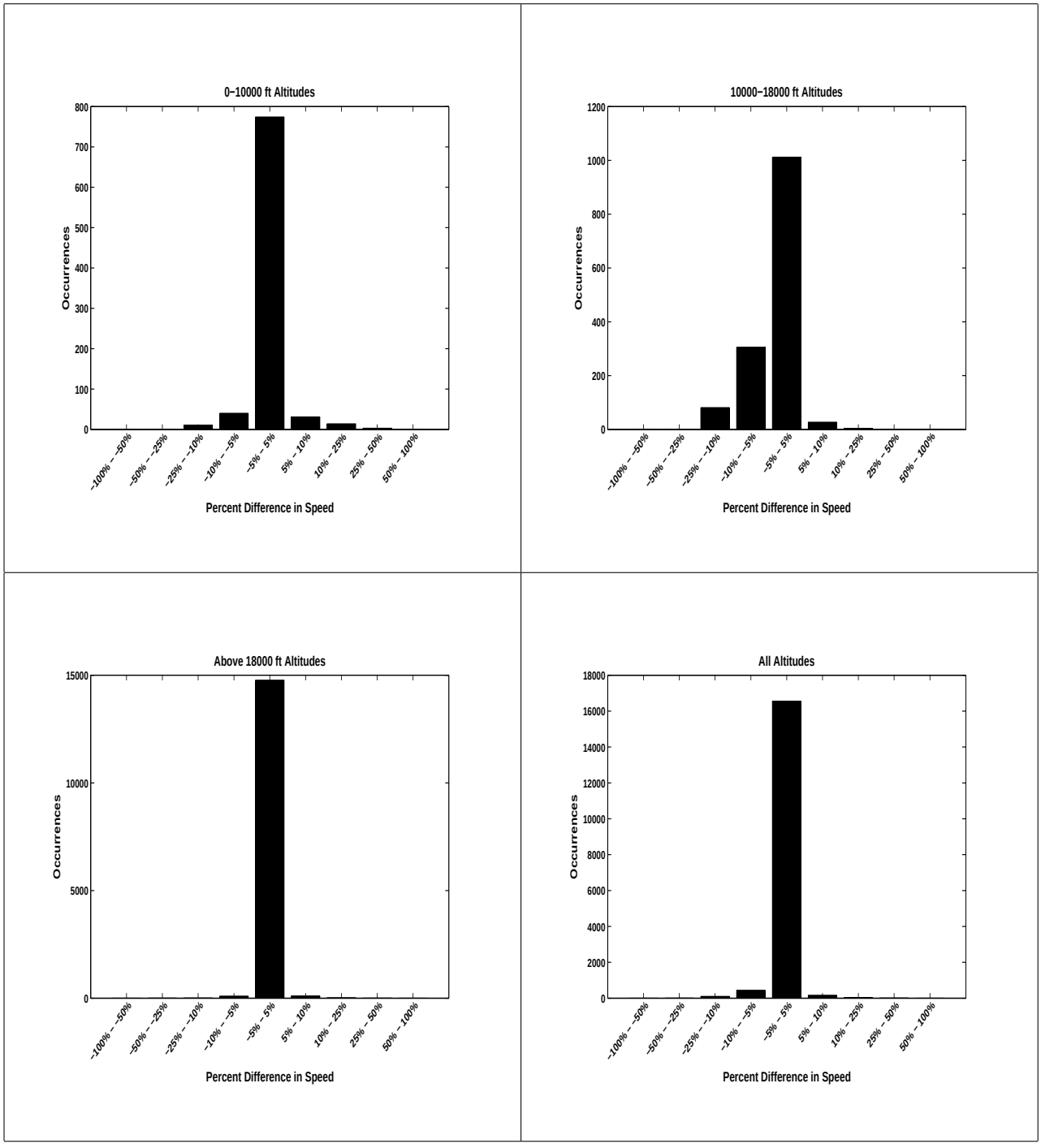

Figure A.56: Las Cruces, 50 km radius, 1 minute projection, percent difference in speed

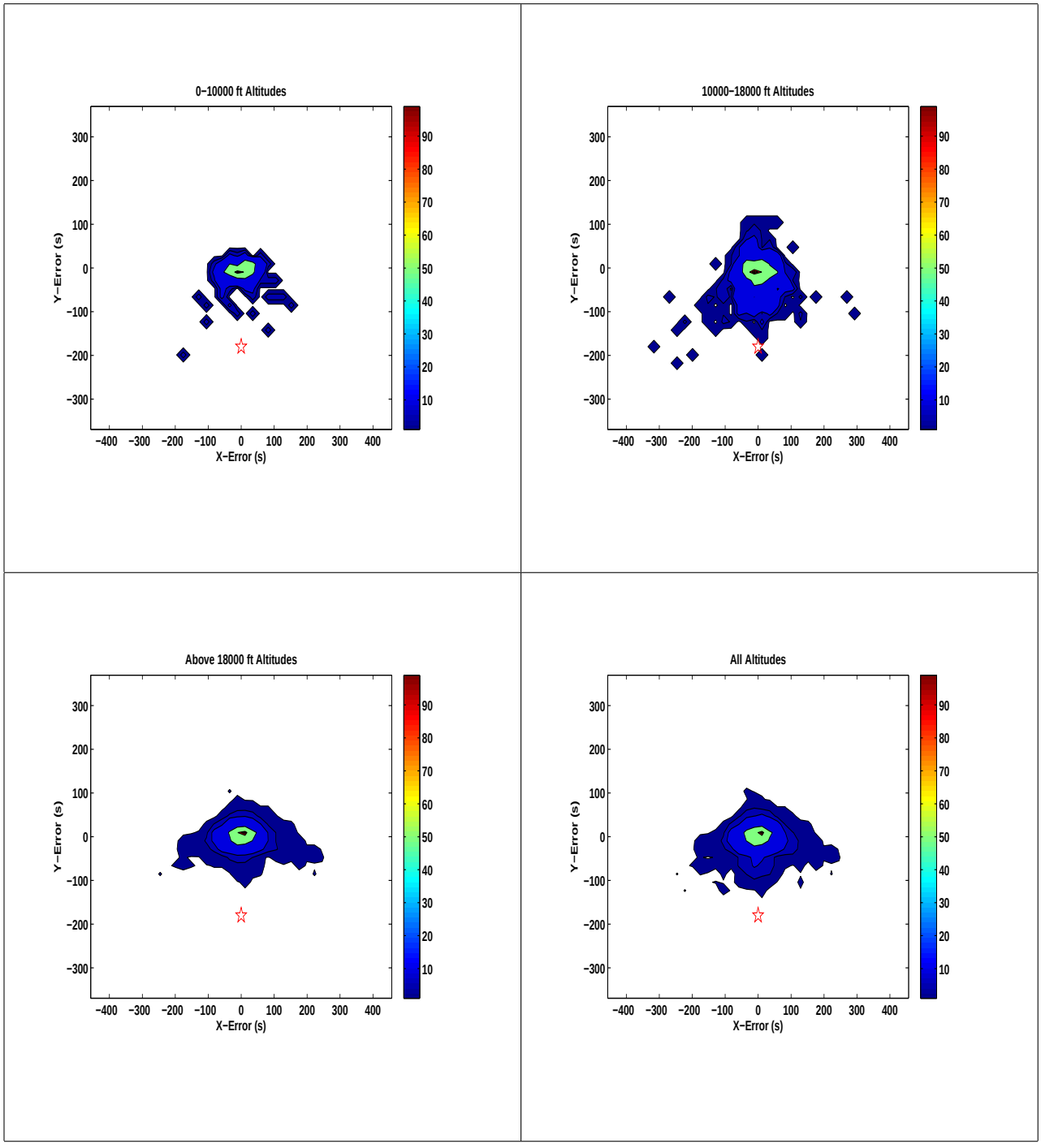

Figure A.57: Las Cruces, 50 km radius, 3 minute projection, difference in projection to measured histograms

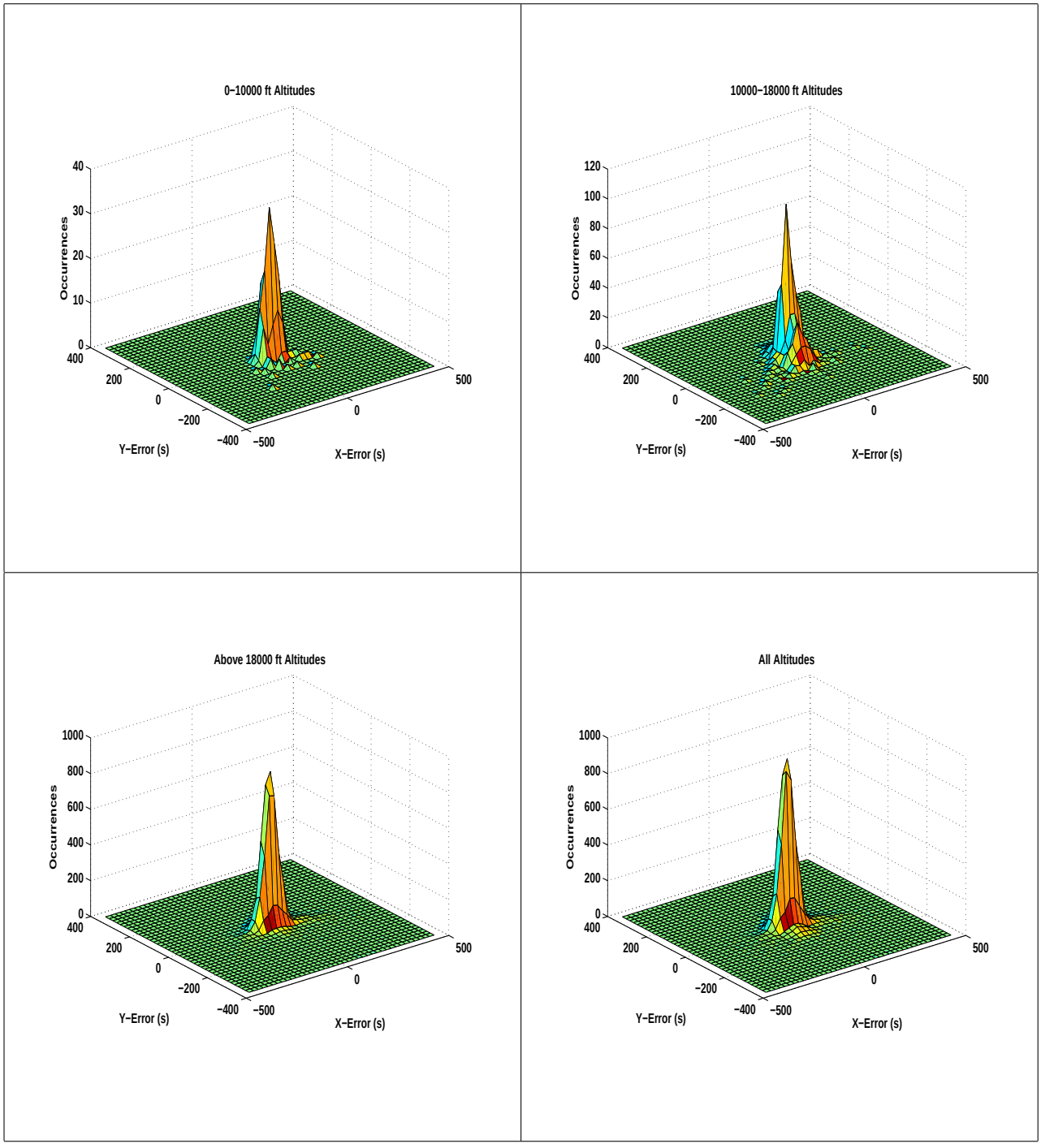

Figure A.58: Las Cruces, 50 km radius, 3 minute projection, difference in projection to measured three dimensional histograms

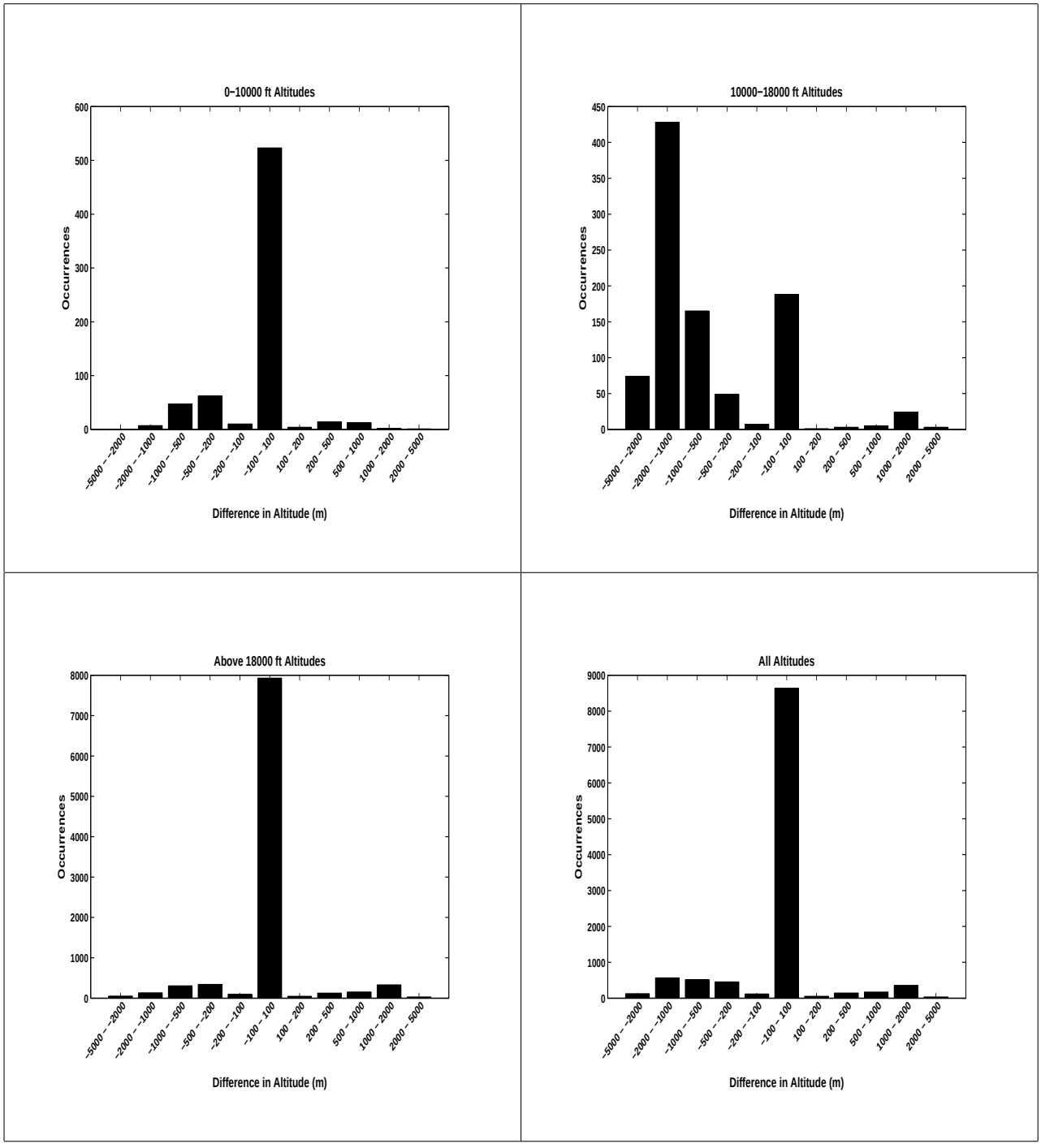

Figure A.59: Las Cruces, 50 km radius, 3 minute projection, difference in altitude

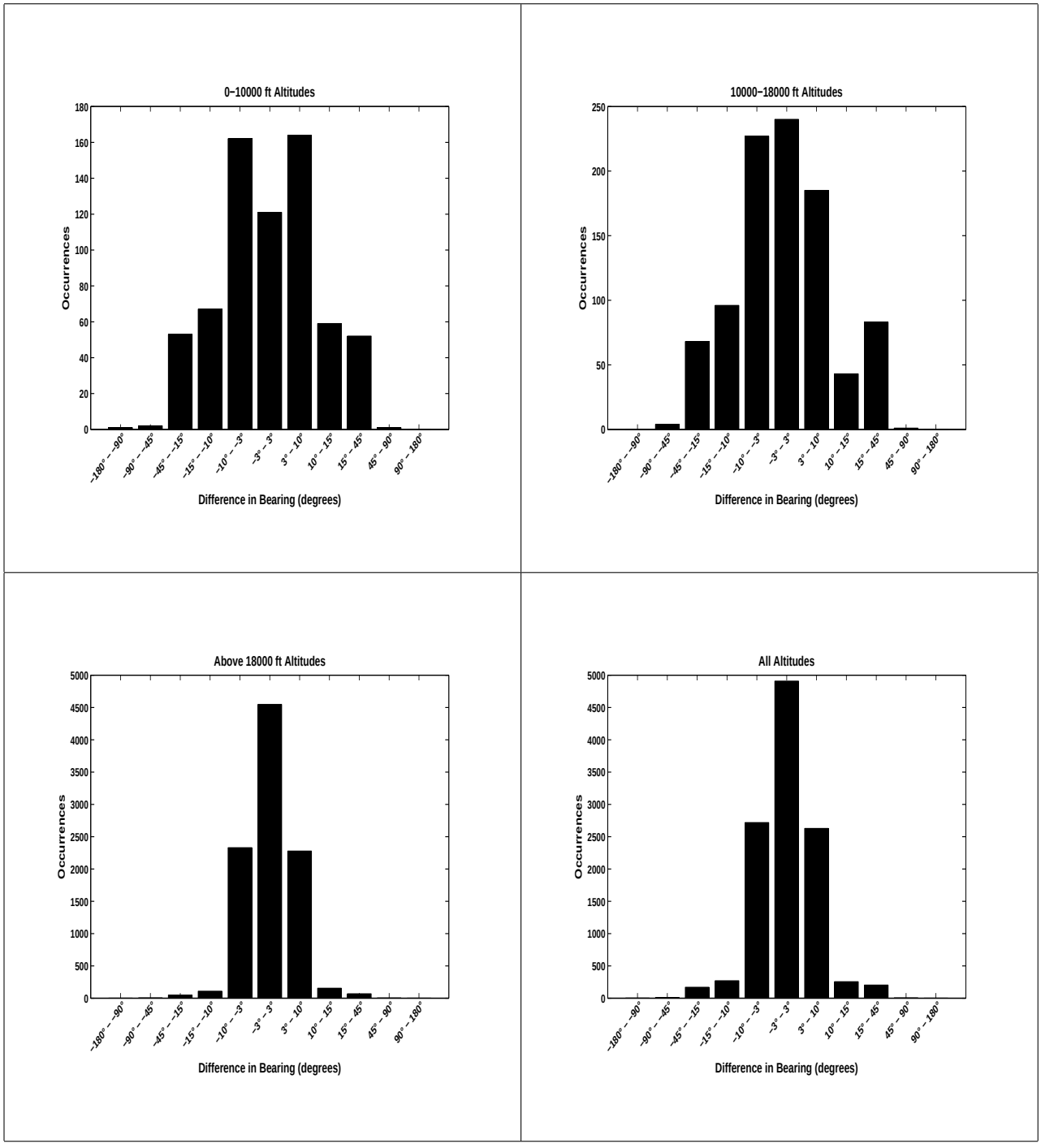

Figure A.60: Las Cruces, 50 km radius, 3 minute projection, difference in bearing

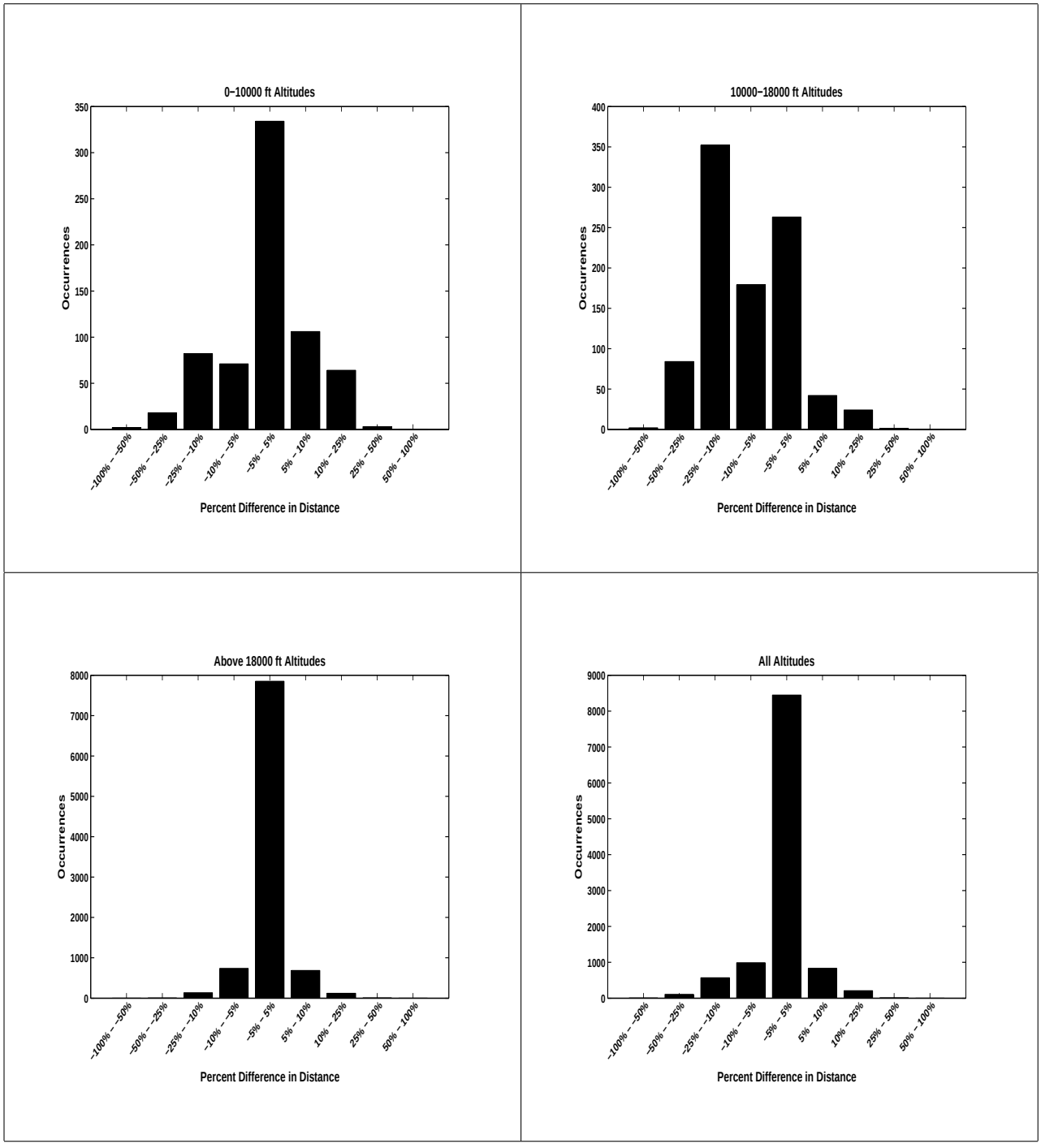

Figure A.61: Las Cruces, 50 km radius, 3 minute projection, percent difference in distance

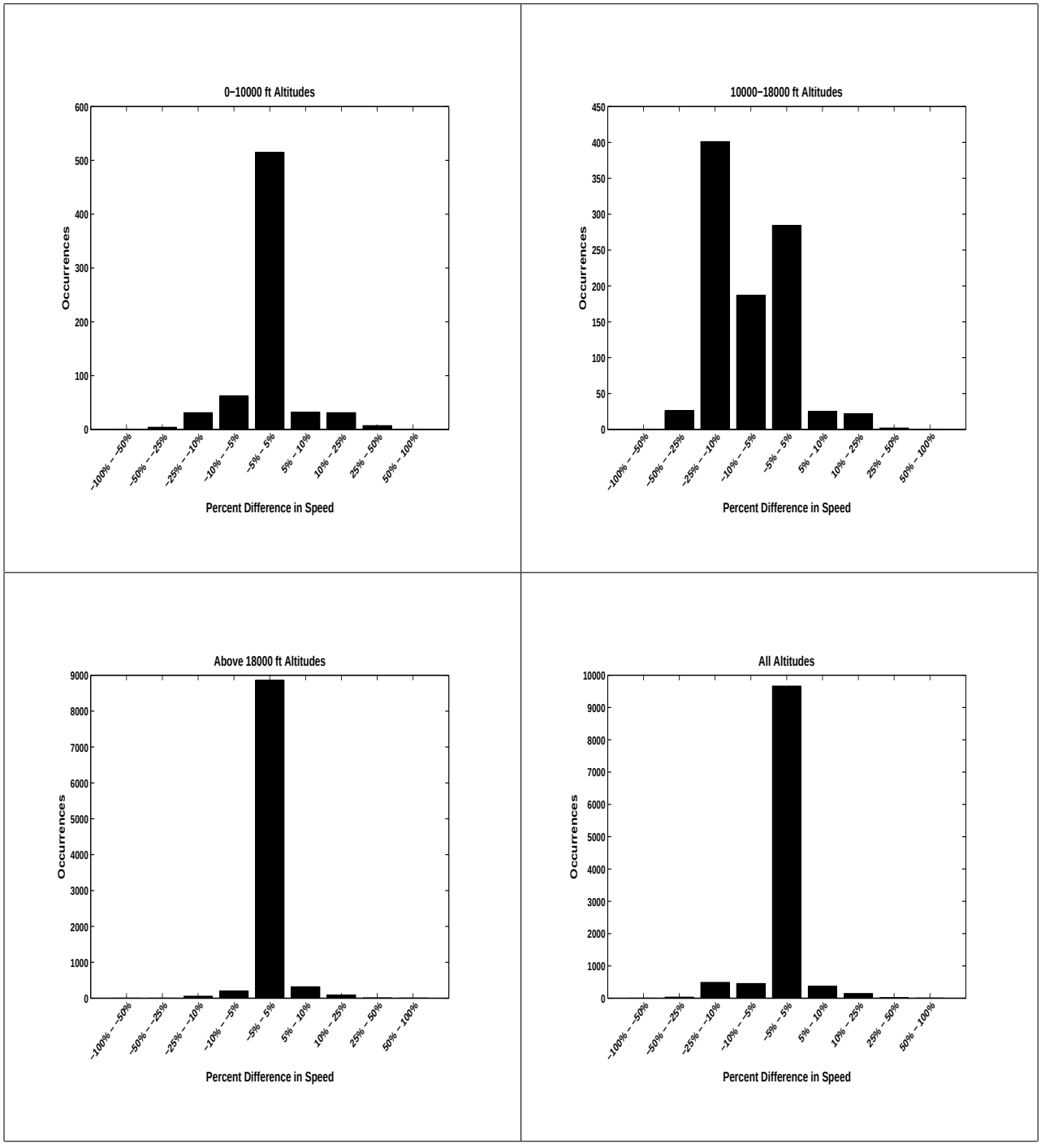

Figure A.62: Las Cruces, 50 km radius, 3 minute projection, percent difference in speed

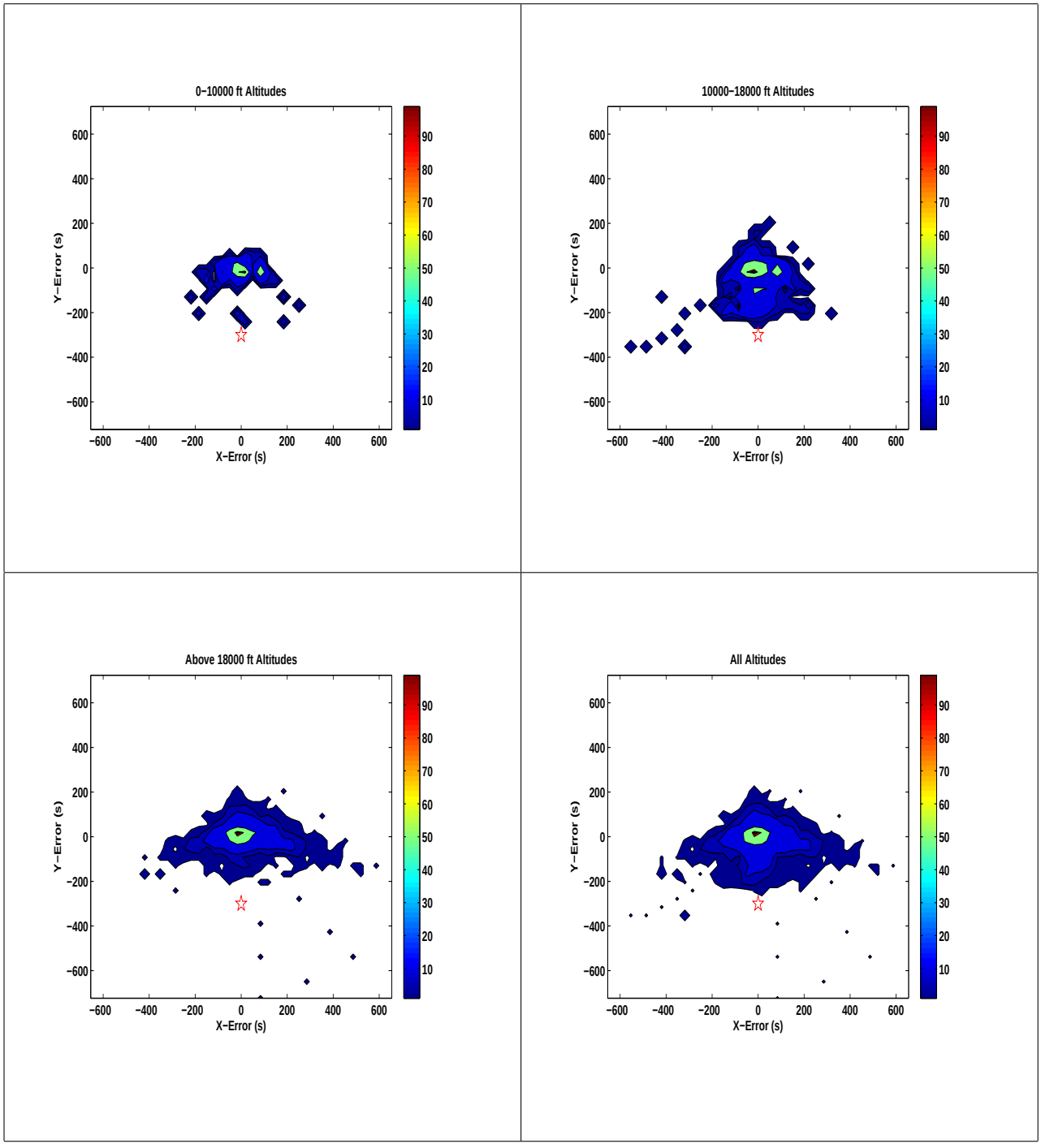

Figure A.63: Las Cruces, 50 km radius, 5 minute projection, difference in projection to measured histograms

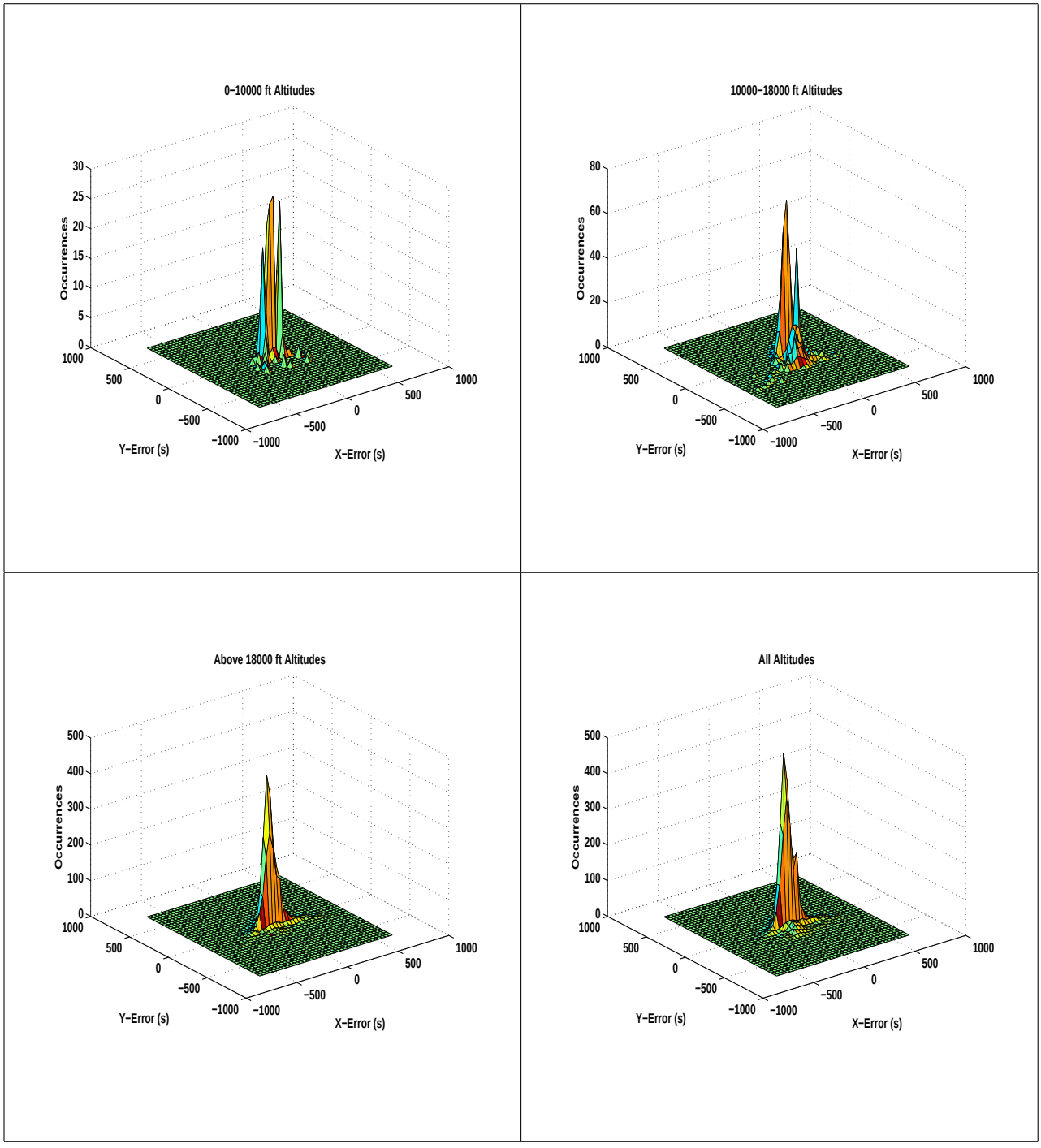

Figure A.64: Las Cruces, 50 km radius, 5 minute projection, difference in projection to measured three dimensional histograms

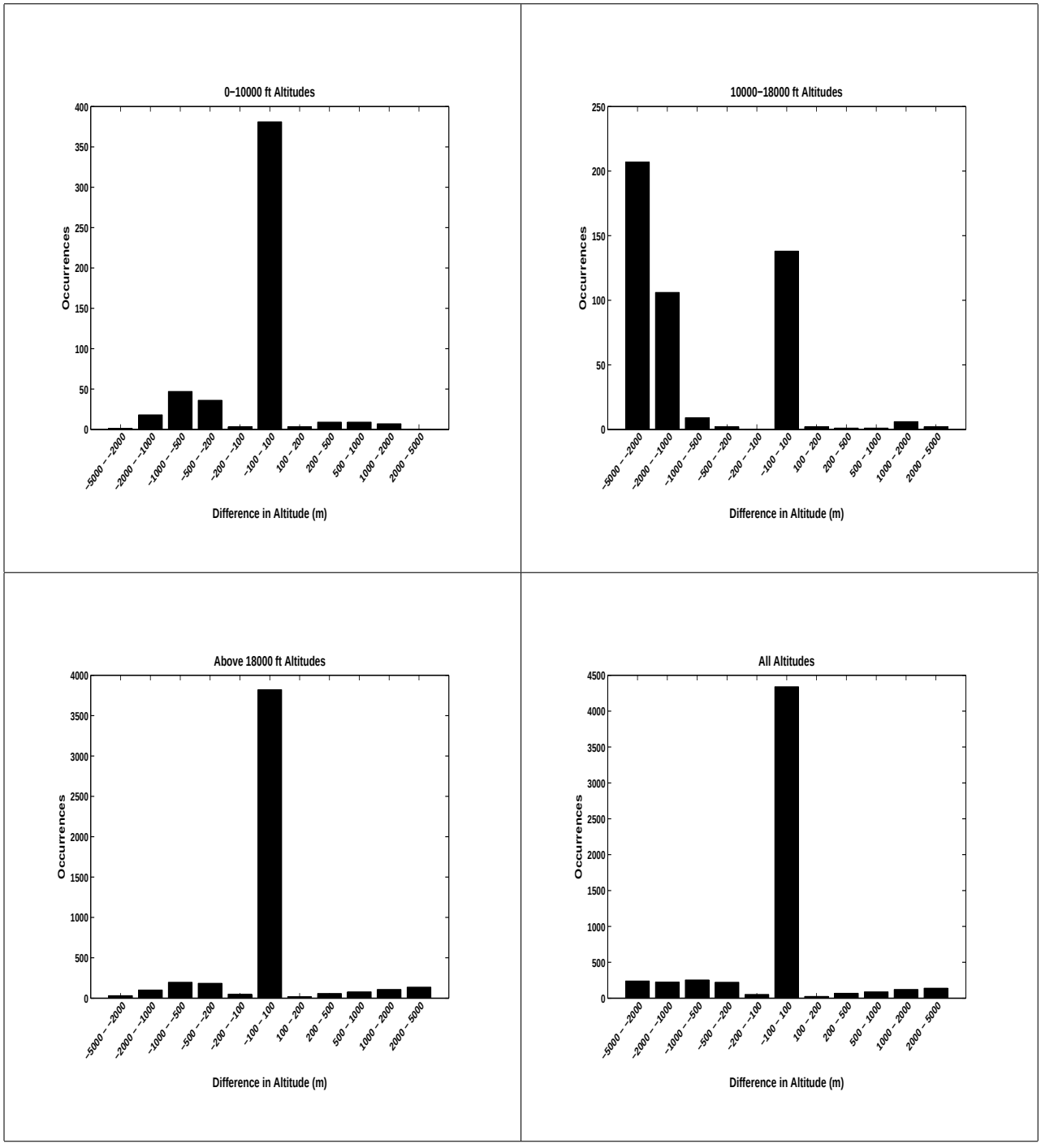

Figure A.65: Las Cruces, 50 km radius, 5 minute projection, difference in altitude

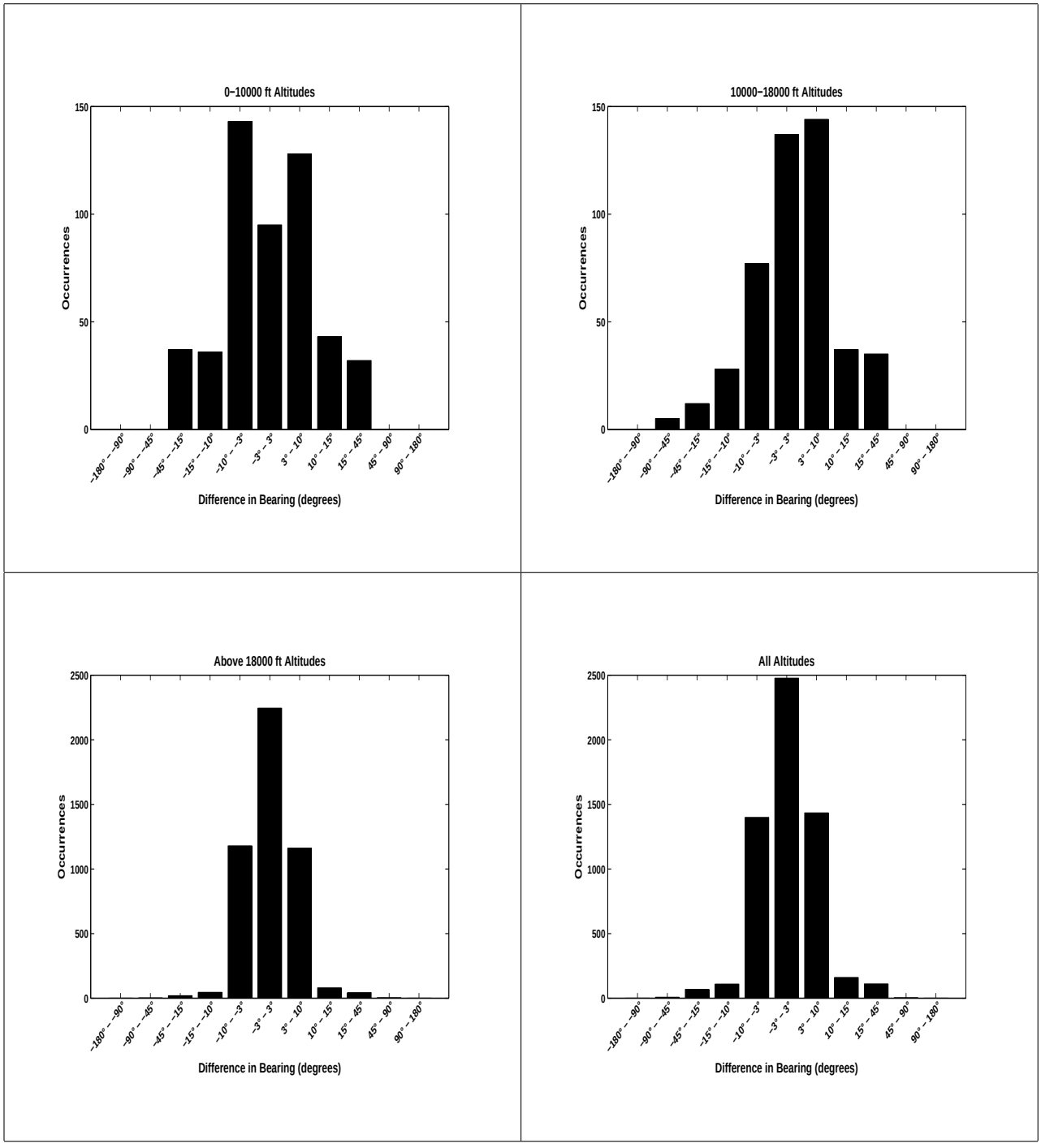

Figure A.66: Las Cruces, 50 km radius, 5 minute projection, difference in bearing

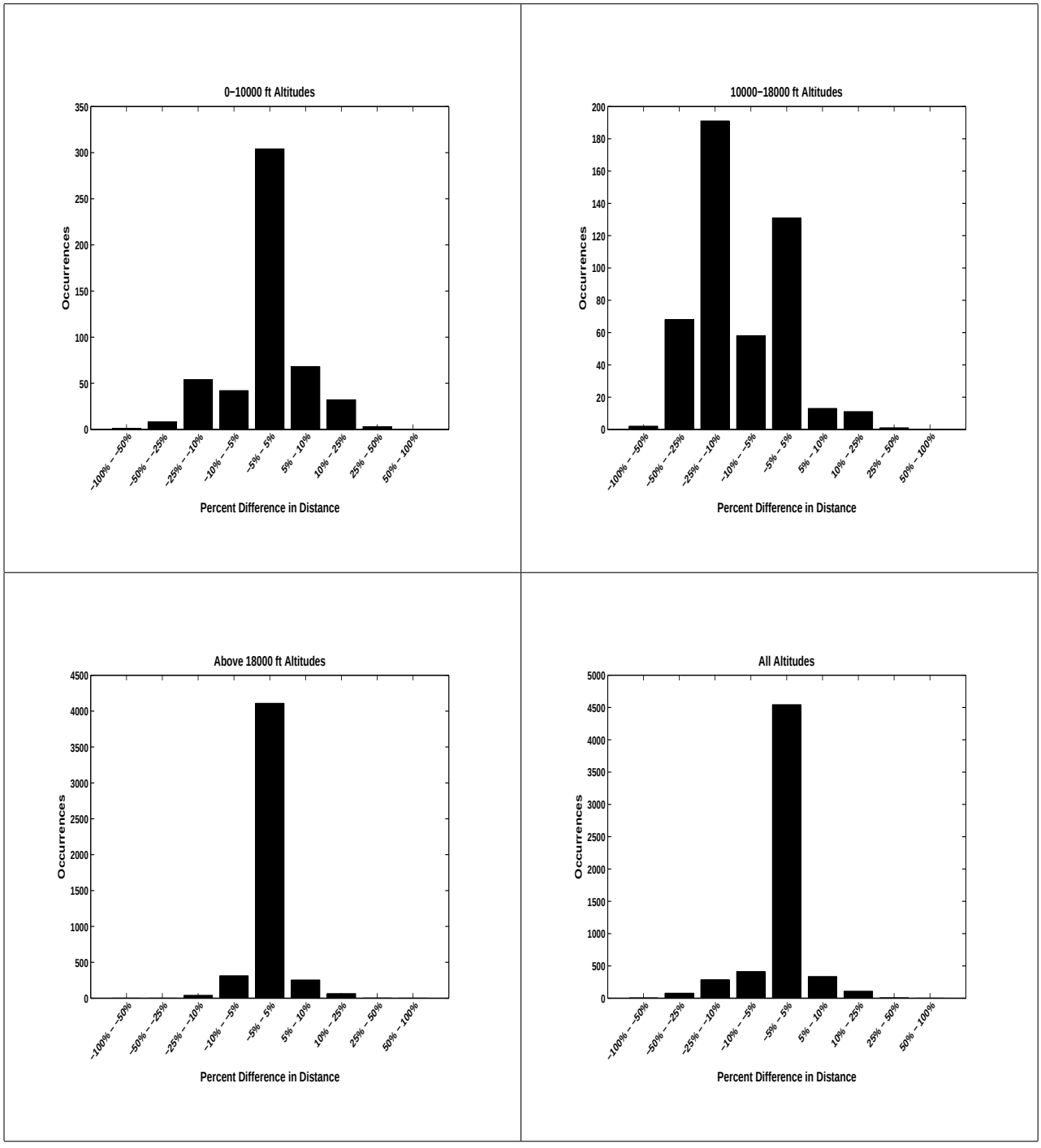

Figure A.67: Las Cruces, 50 km radius, 5 minute projection, percent difference in distance

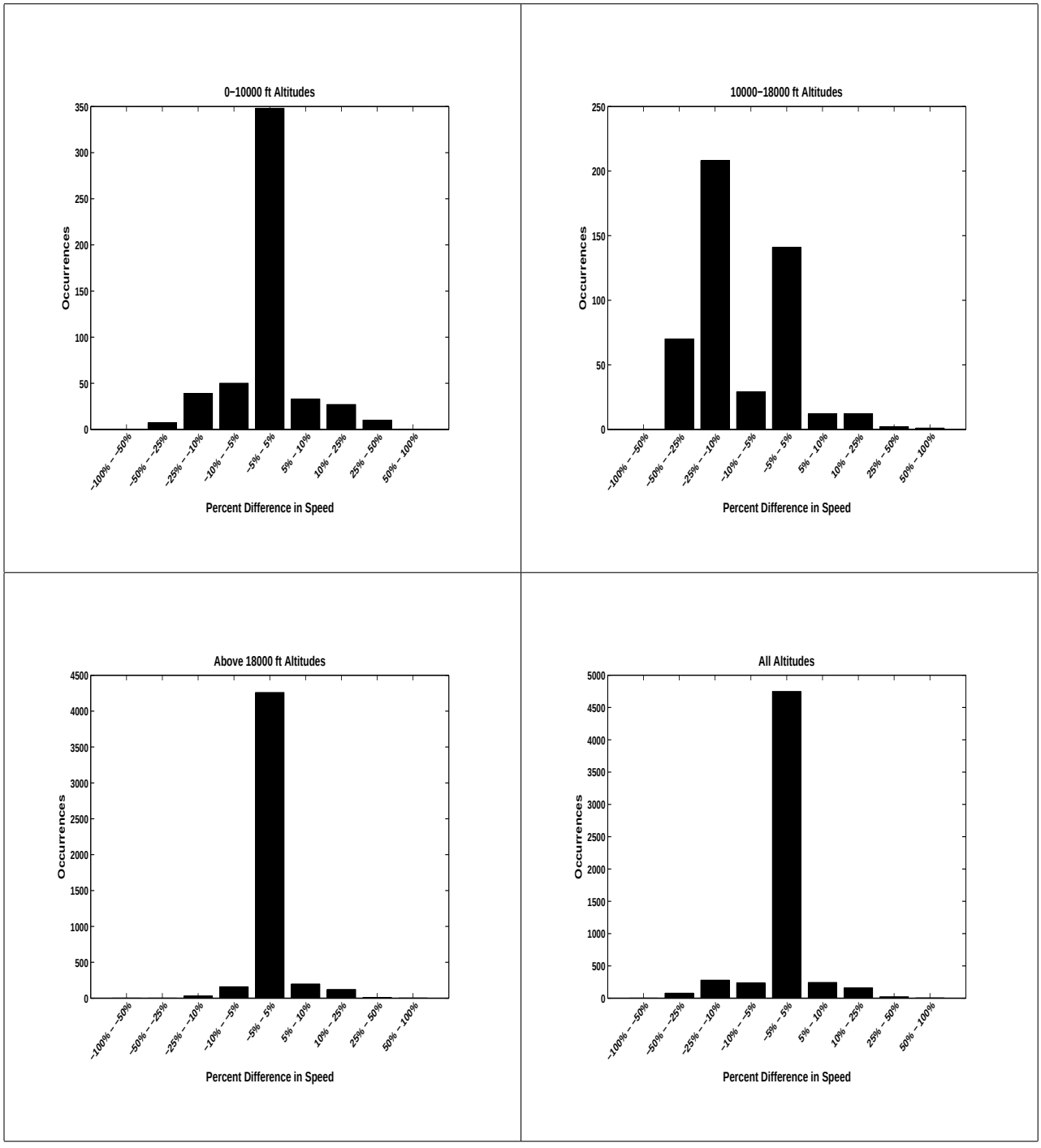

Figure A.68: Las Cruces, 50 km radius, 5 minute projection, percent difference in speed

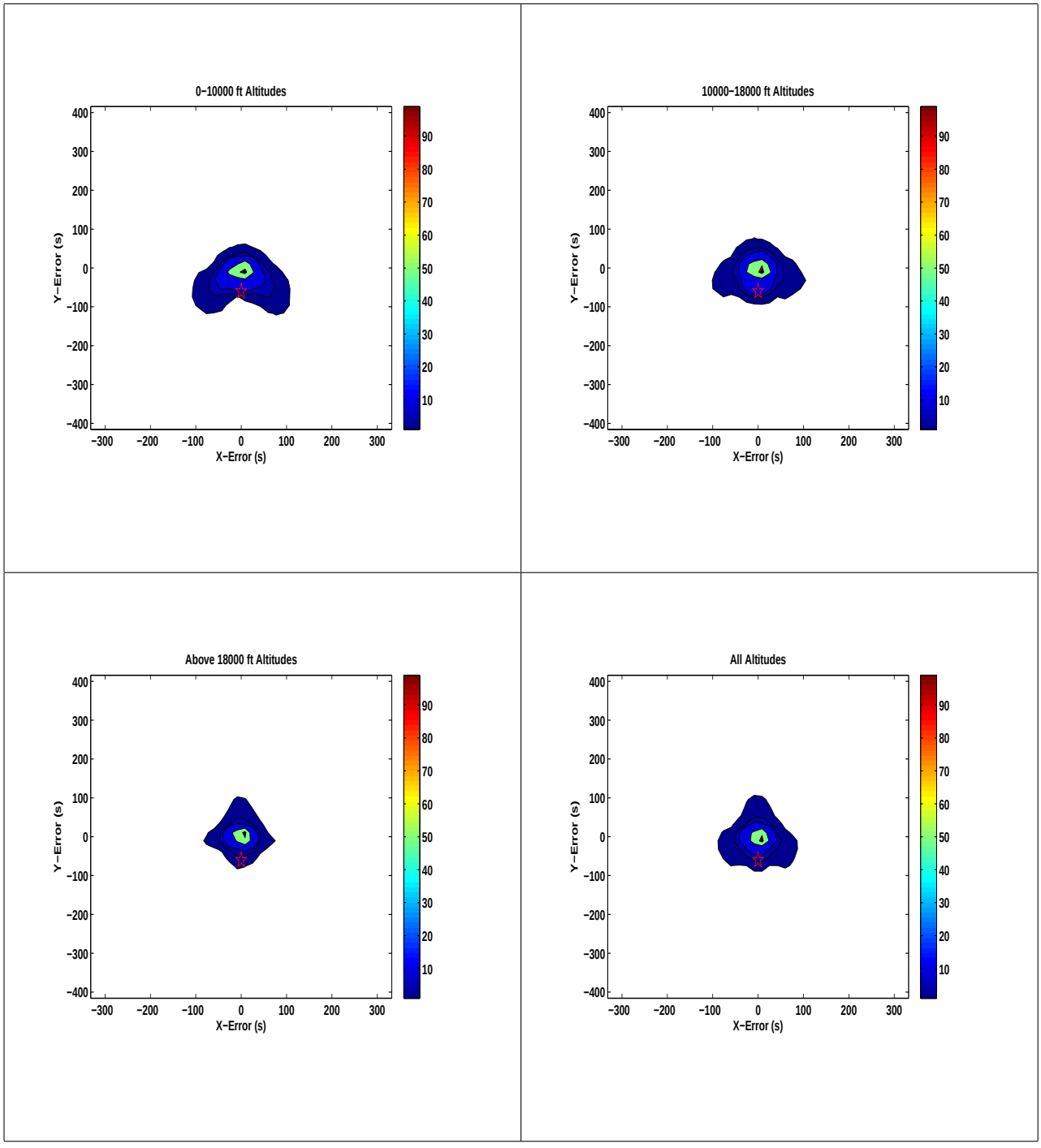

Figure A.69: Fort Campbell, 250 km radius, 1 minute projection, difference in projection to measured histograms

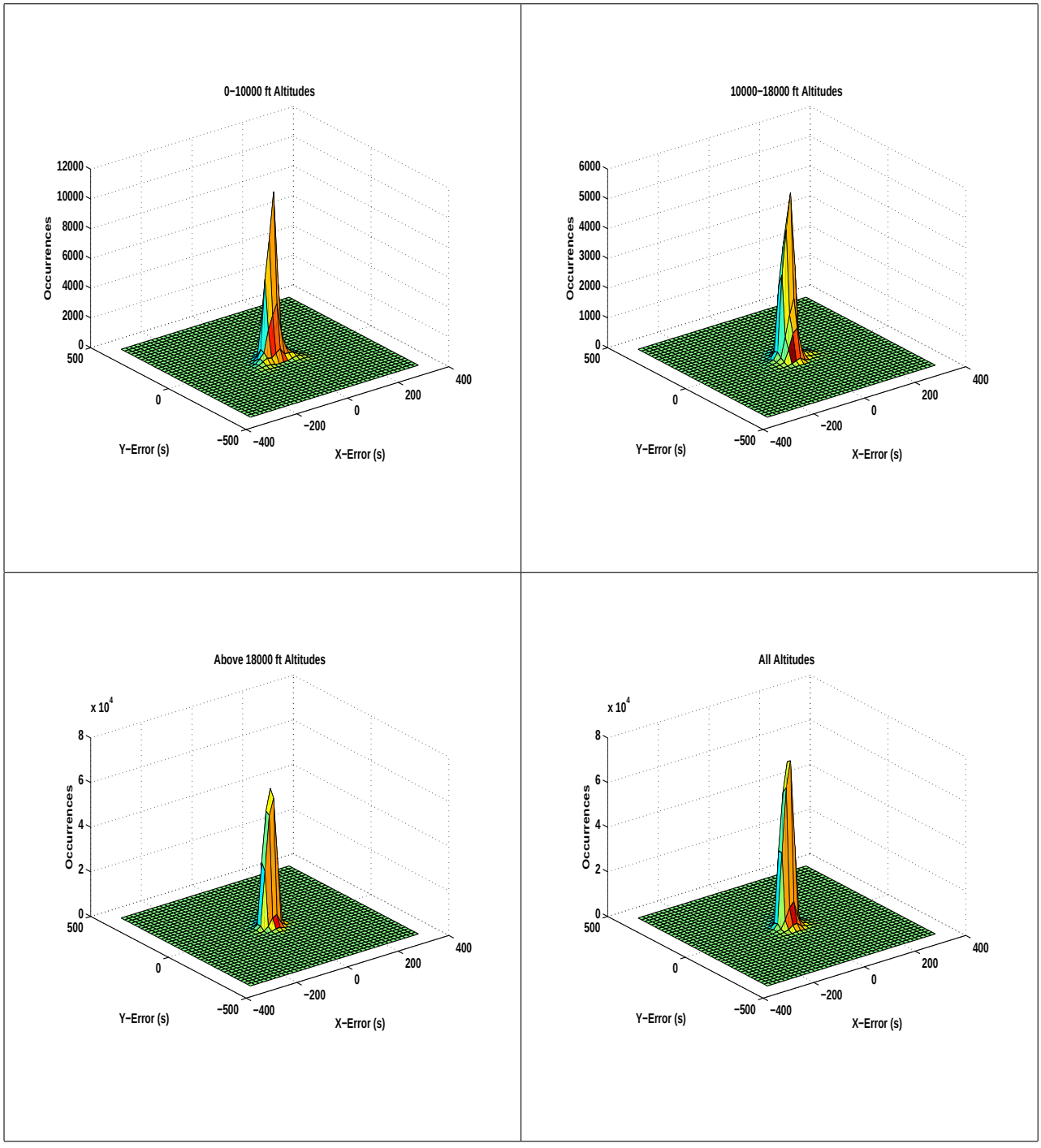

Figure A.70: Fort Campbell, 250 km radius, 1 minute projection, difference in projection to measured three dimensional histograms

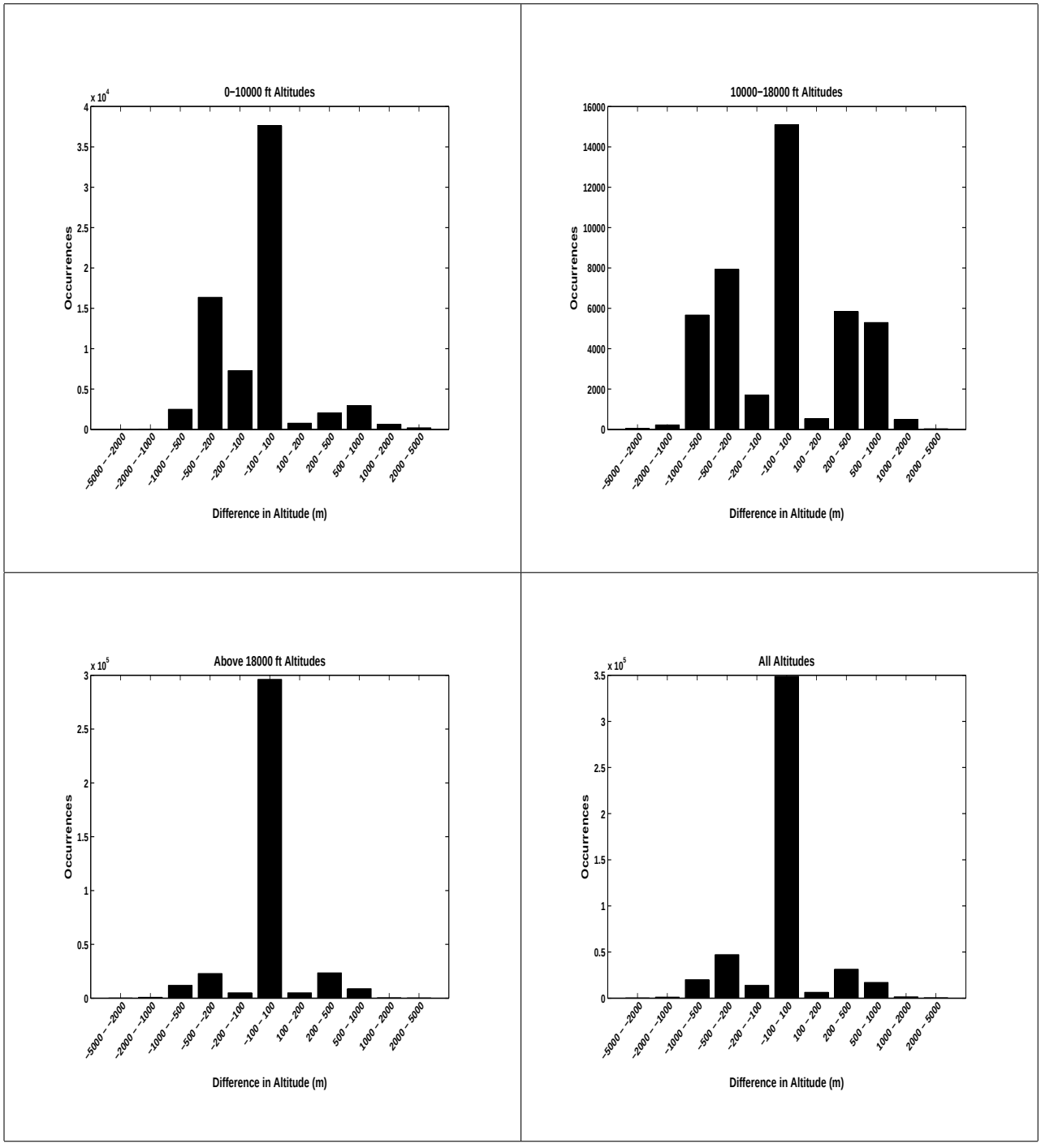

Figure A.71: Fort Campbell, 250 km radius, 1 minute projection, difference in altitude

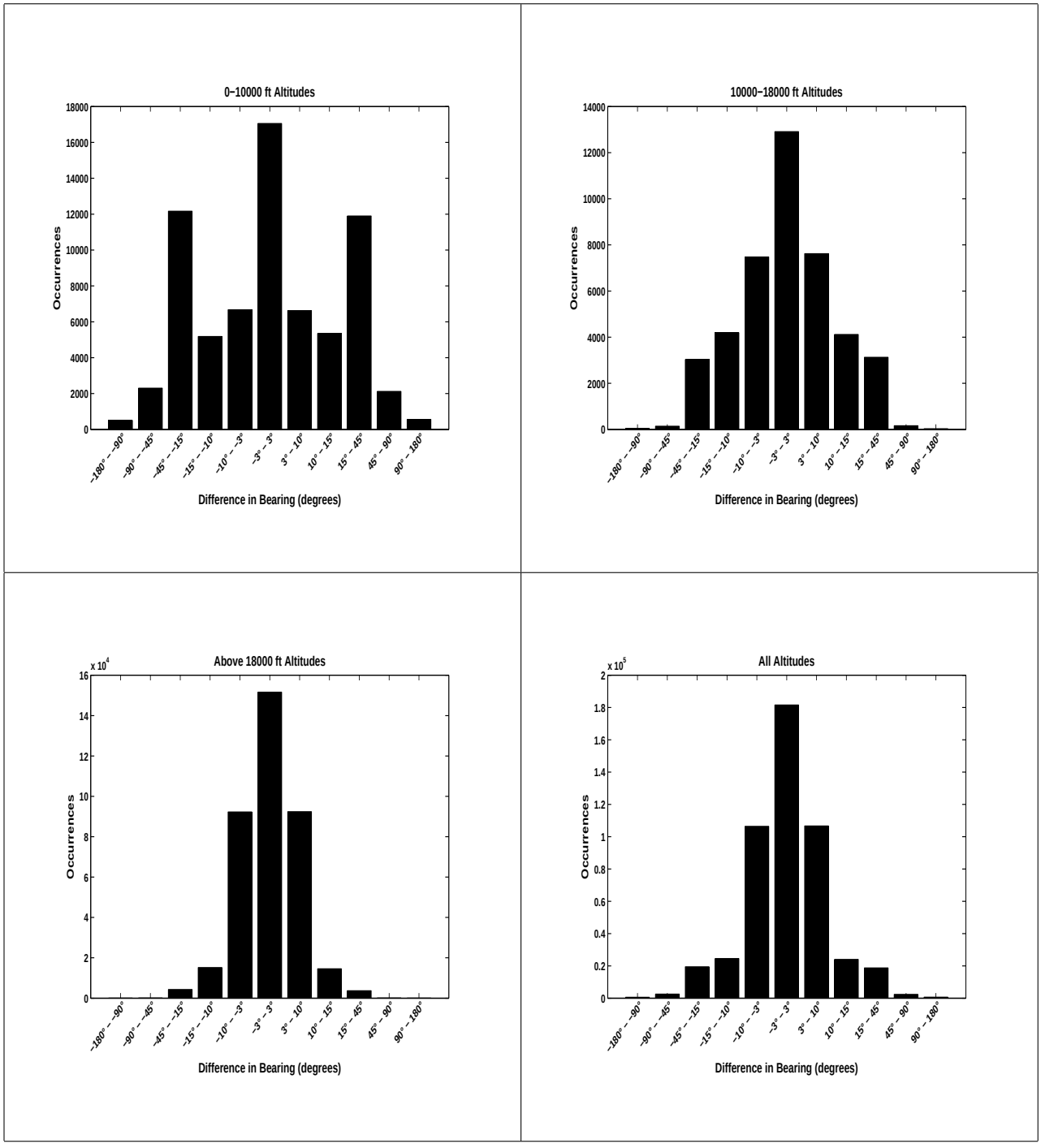

Figure A.72: Fort Campbell, 250 km radius, 1 minute projection, difference in bearing

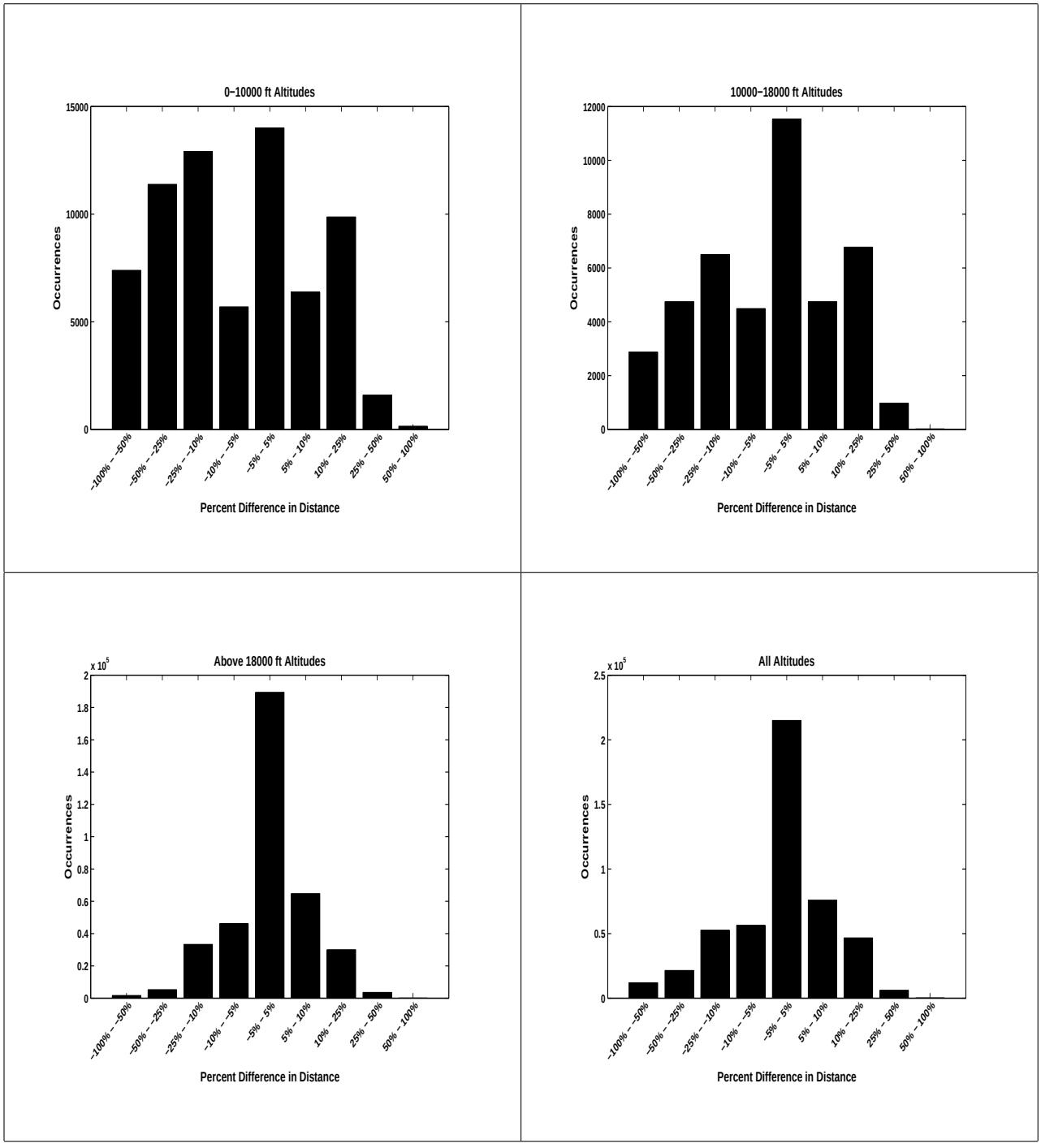

Figure A.73: Fort Campbell, 250 km radius, 1 minute projection, percent difference in distance

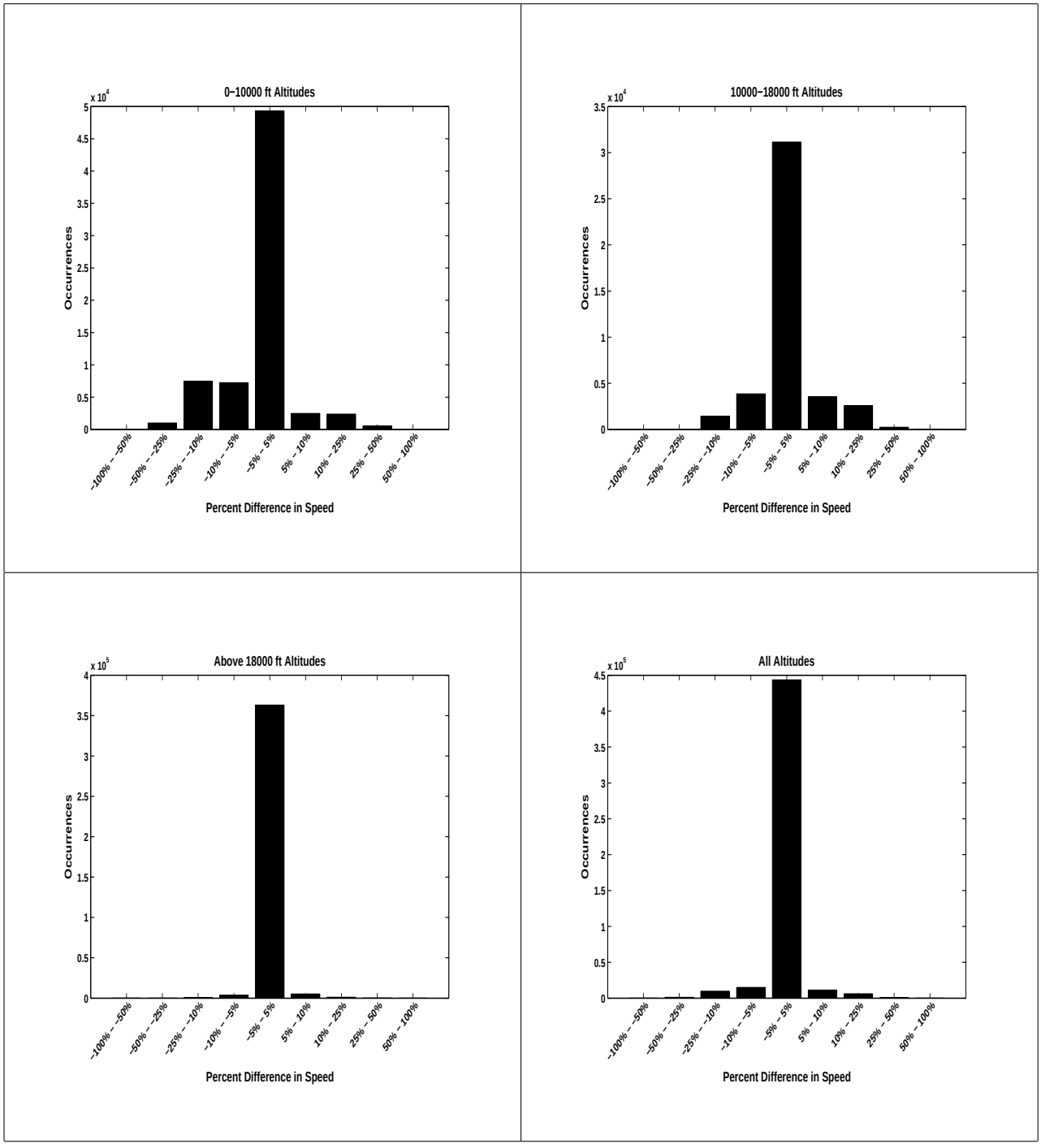

Figure A.74: Fort Campbell, 250 km radius, 1 minute projection, percent difference in speed

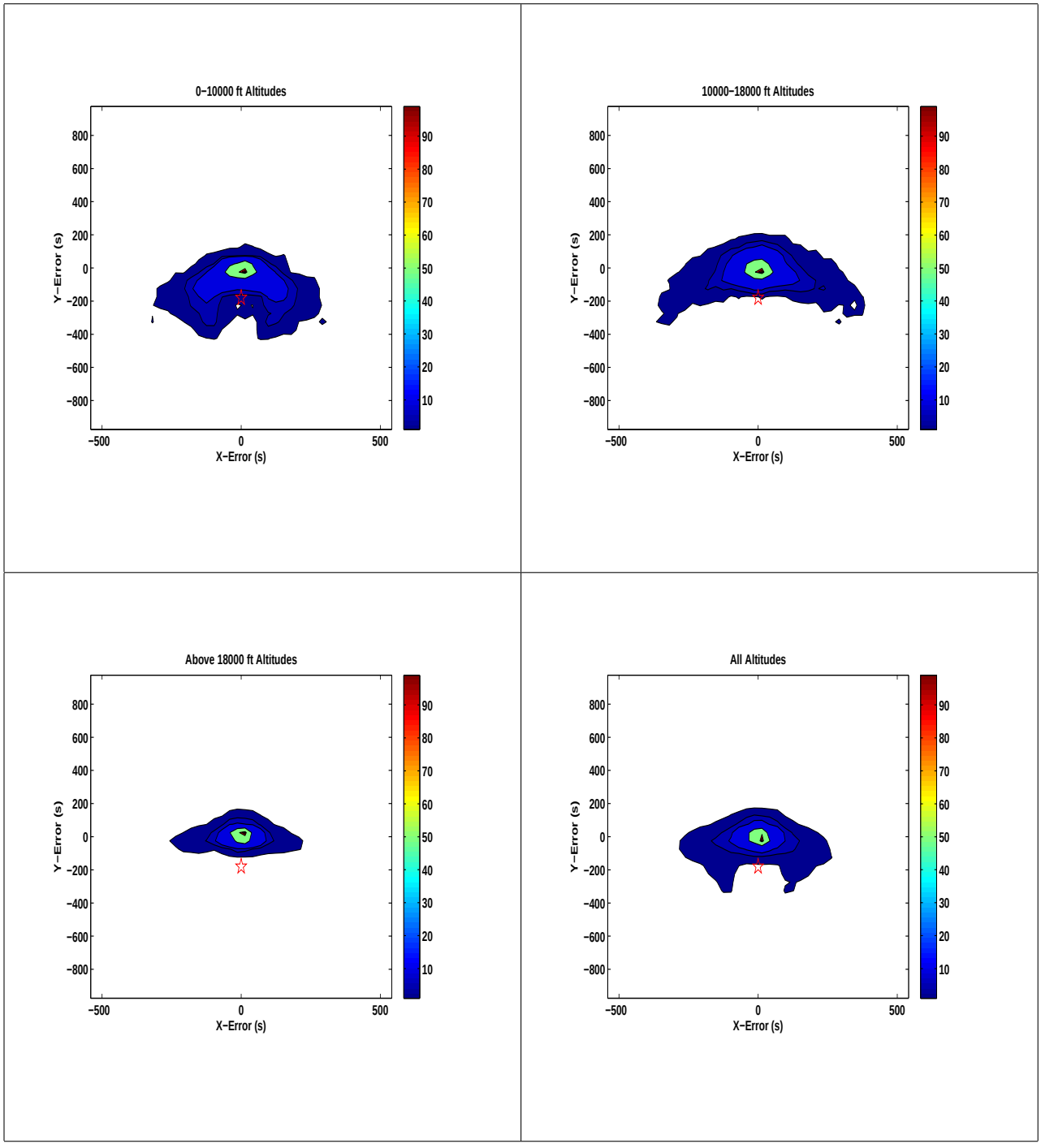

Figure A.75: Fort Campbell, 250 km radius, 3 minute projection, difference in projection to measured histograms

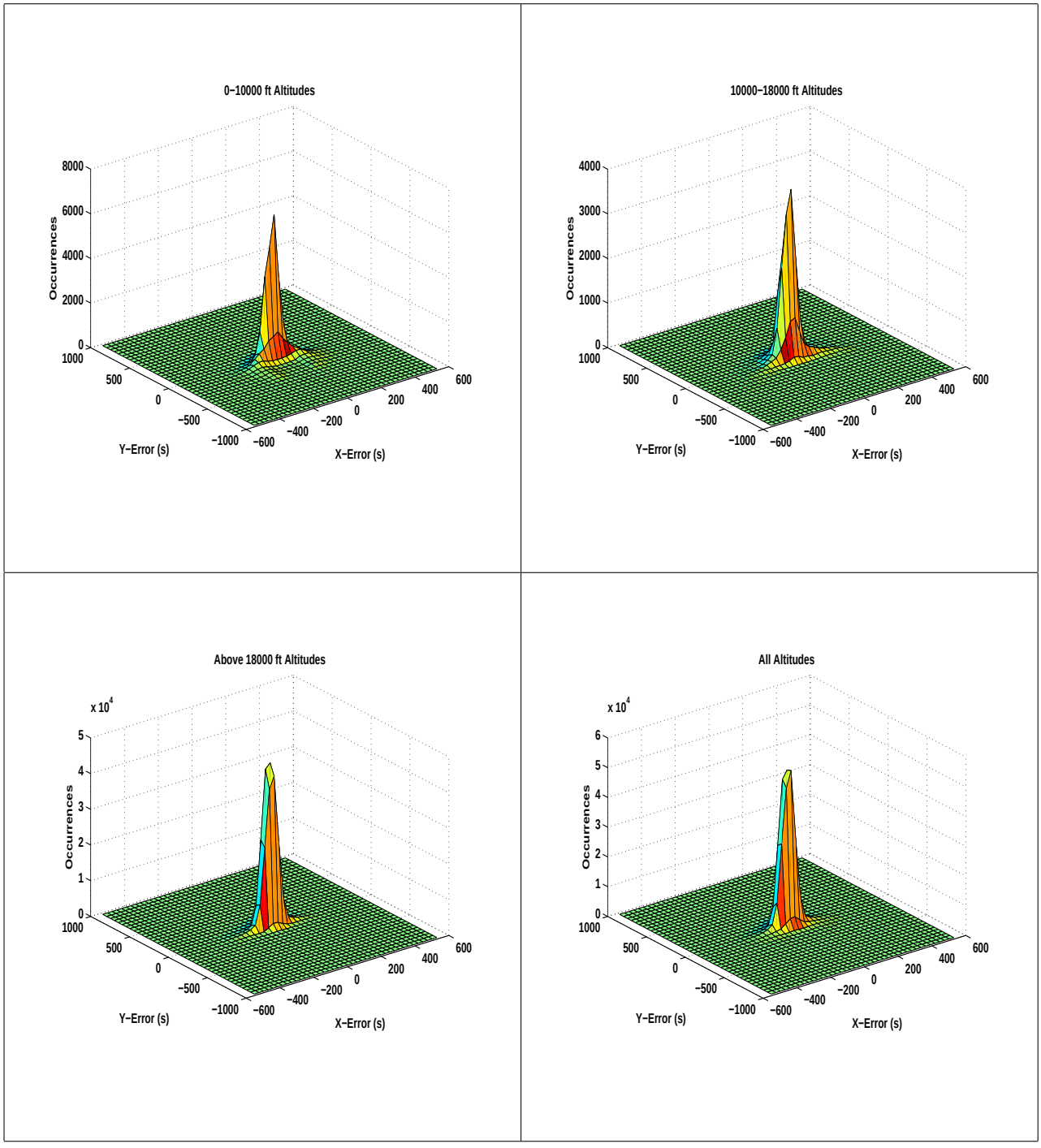

Figure A.76: Fort Campbell, 250 km radius, 3 minute projection, difference in projection to measured three dimensional histograms

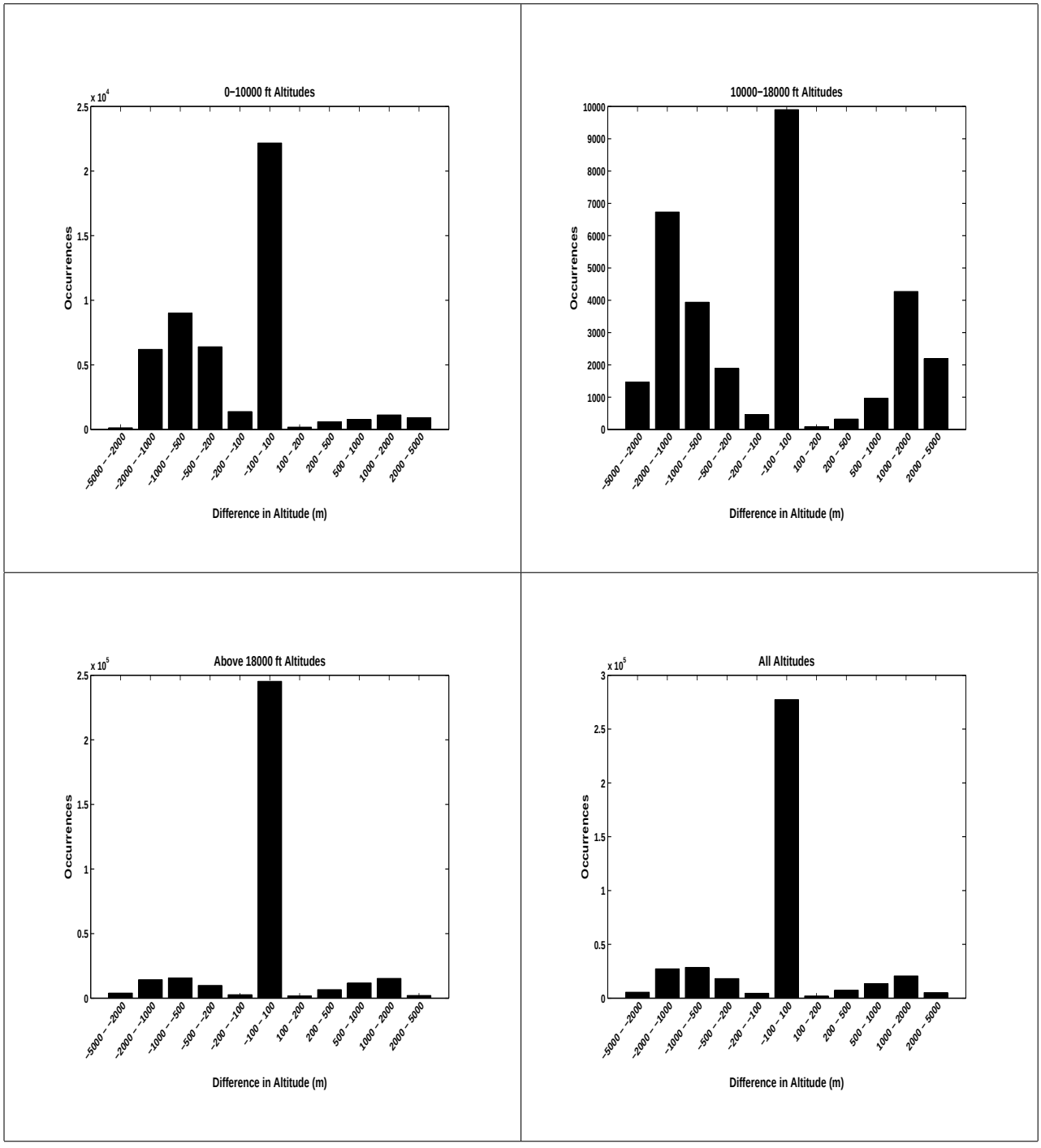

Figure A.77: Fort Campbell, 250 km radius, 3 minute projection, difference in altitude

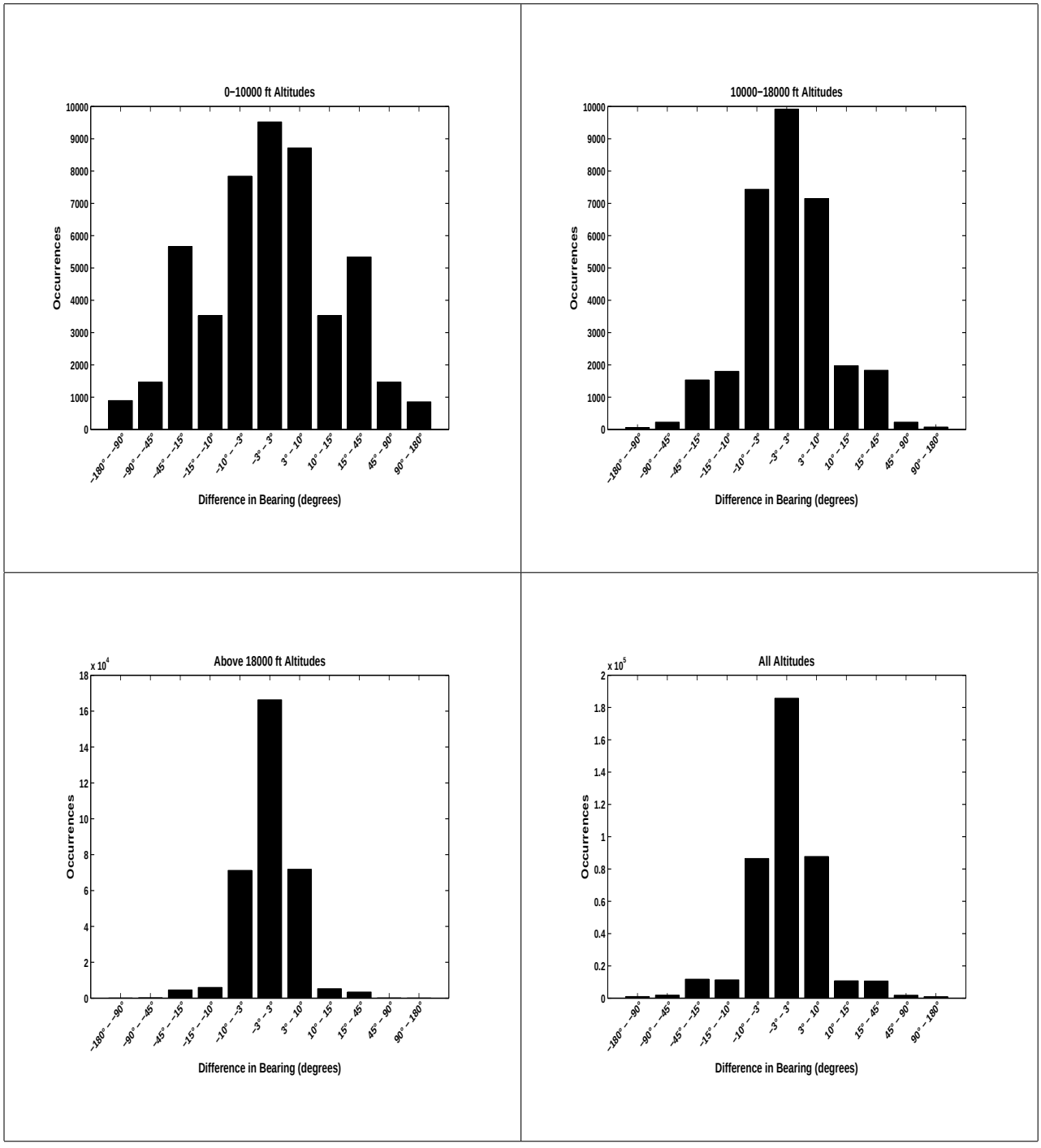

Figure A.78: Fort Campbell, 250 km radius, 3 minute projection, difference in bearing

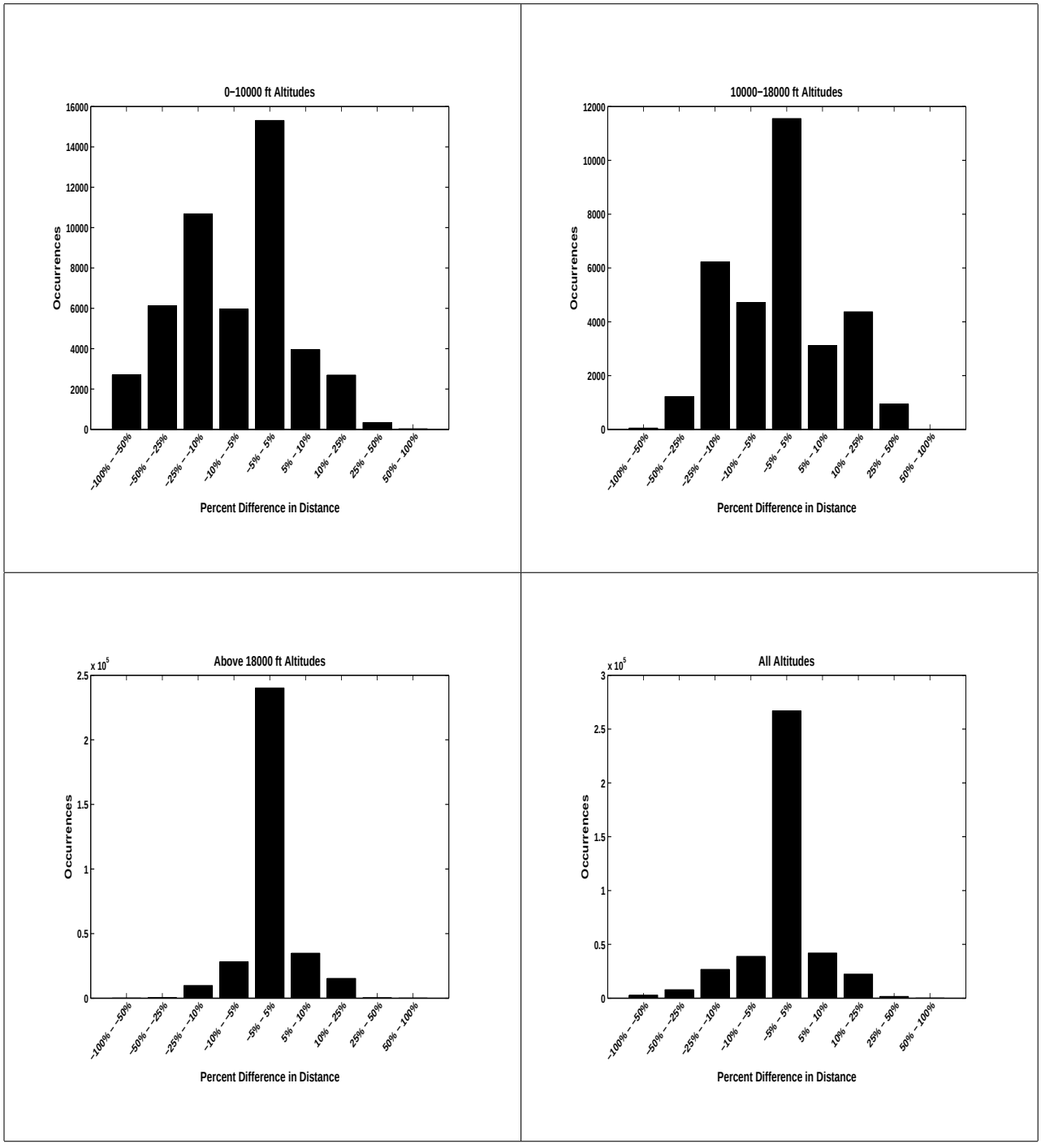

Figure A.79: Fort Campbell, 250 km radius, 3 minute projection, percent difference in distance

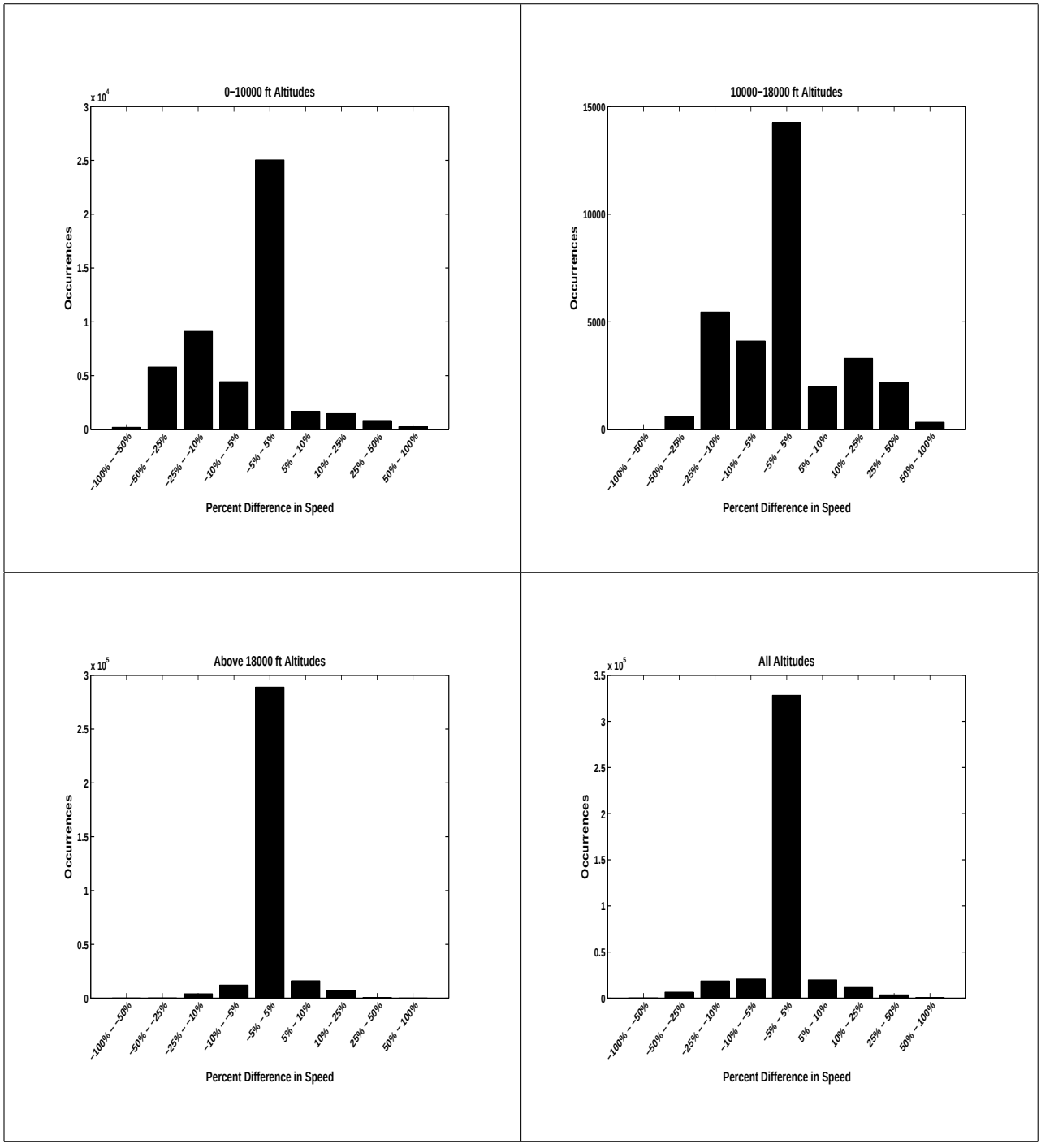

Figure A.80: Fort Campbell, 250 km radius, 3 minute projection, percent difference in speed

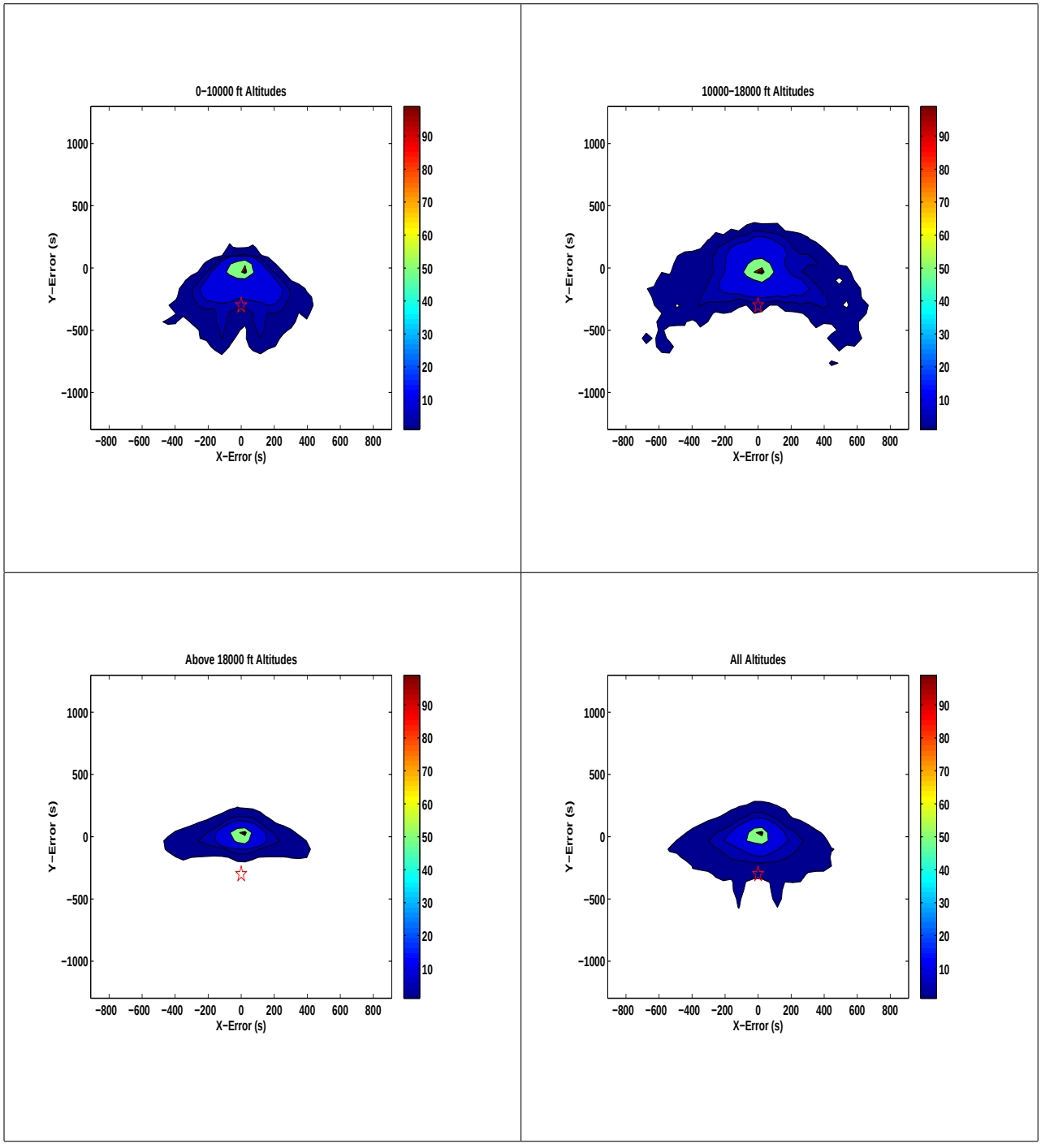

Figure A.81: Fort Campbell, 250 km radius, 5 minute projection, difference in projection to measured histograms

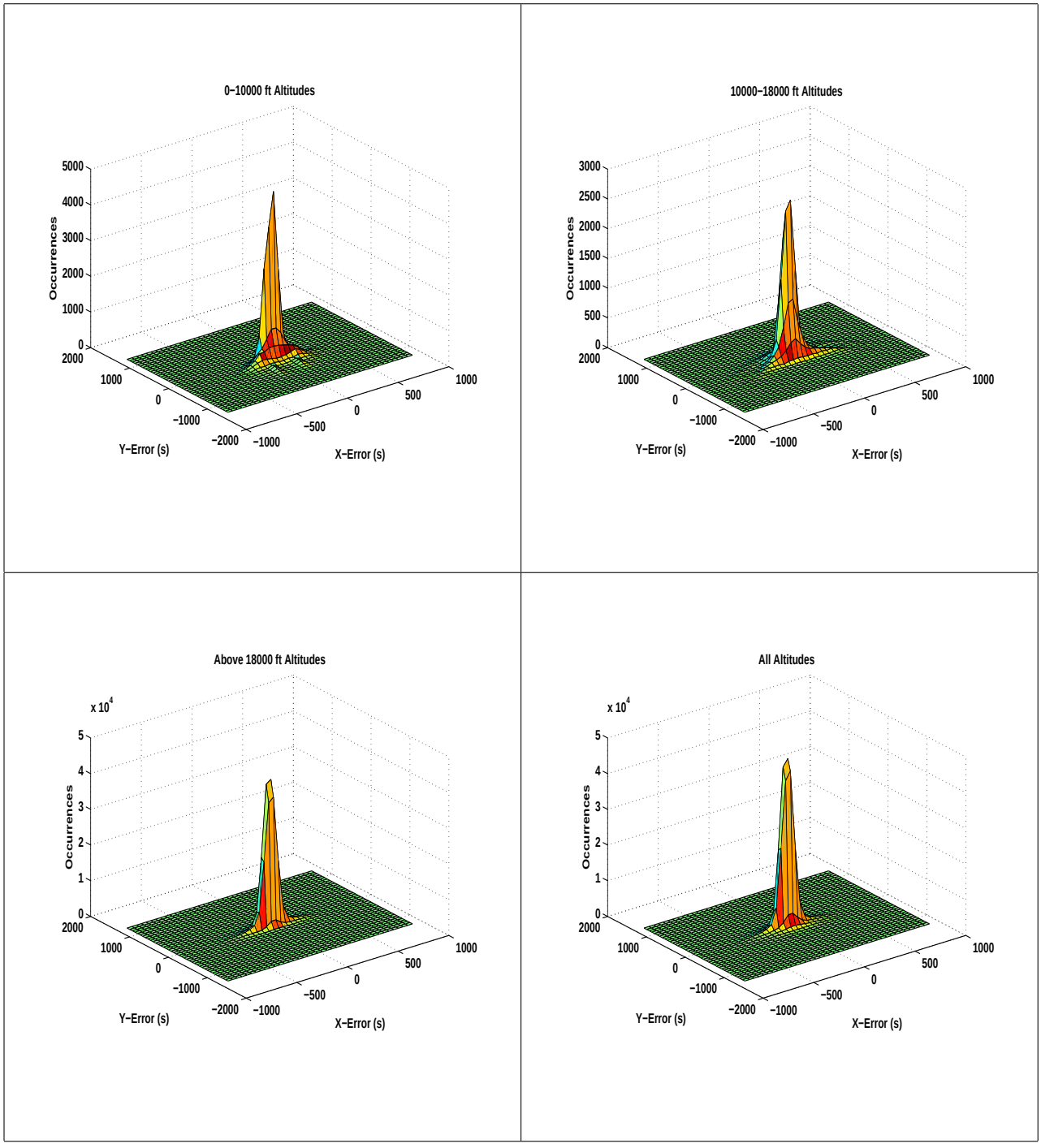

Figure A.82: Fort Campbell, 250 km radius, 5 minute projection, difference in projection to measured three dimensional histograms

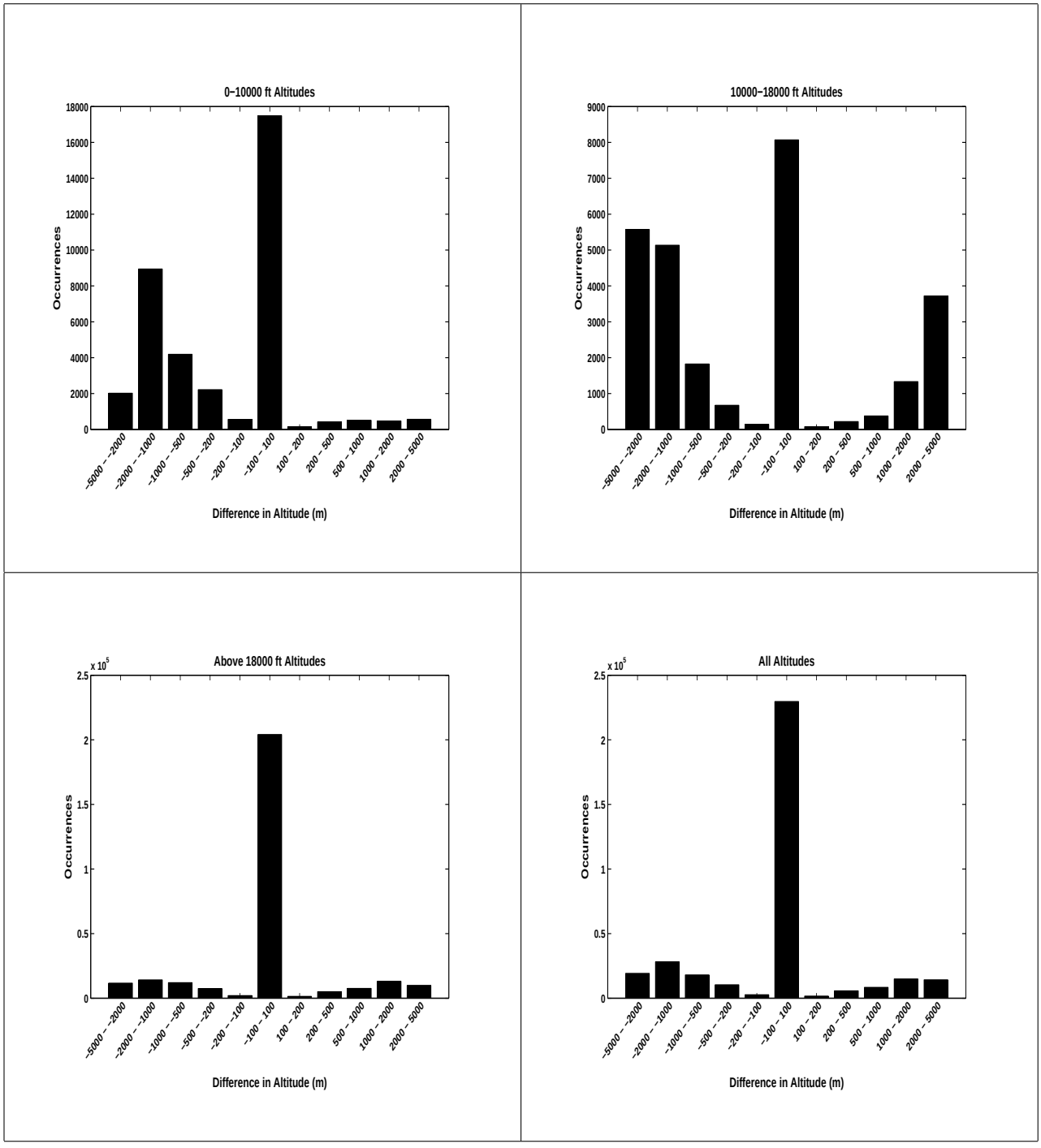

Figure A.83: Fort Campbell, 250 km radius, 5 minute projection, difference in altitude

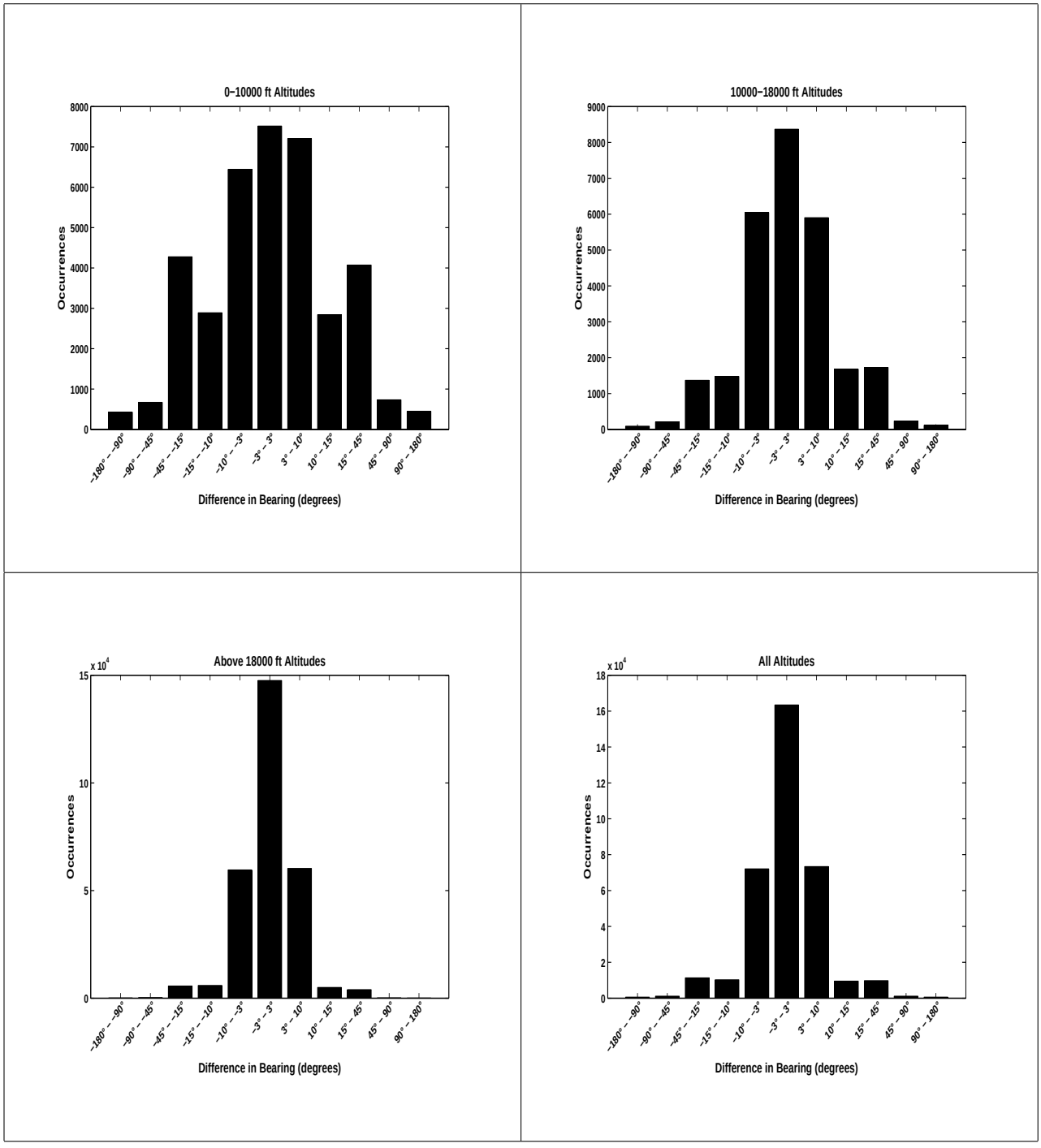

Figure A.84: Fort Campbell, 250 km radius, 5 minute projection, difference in bearing

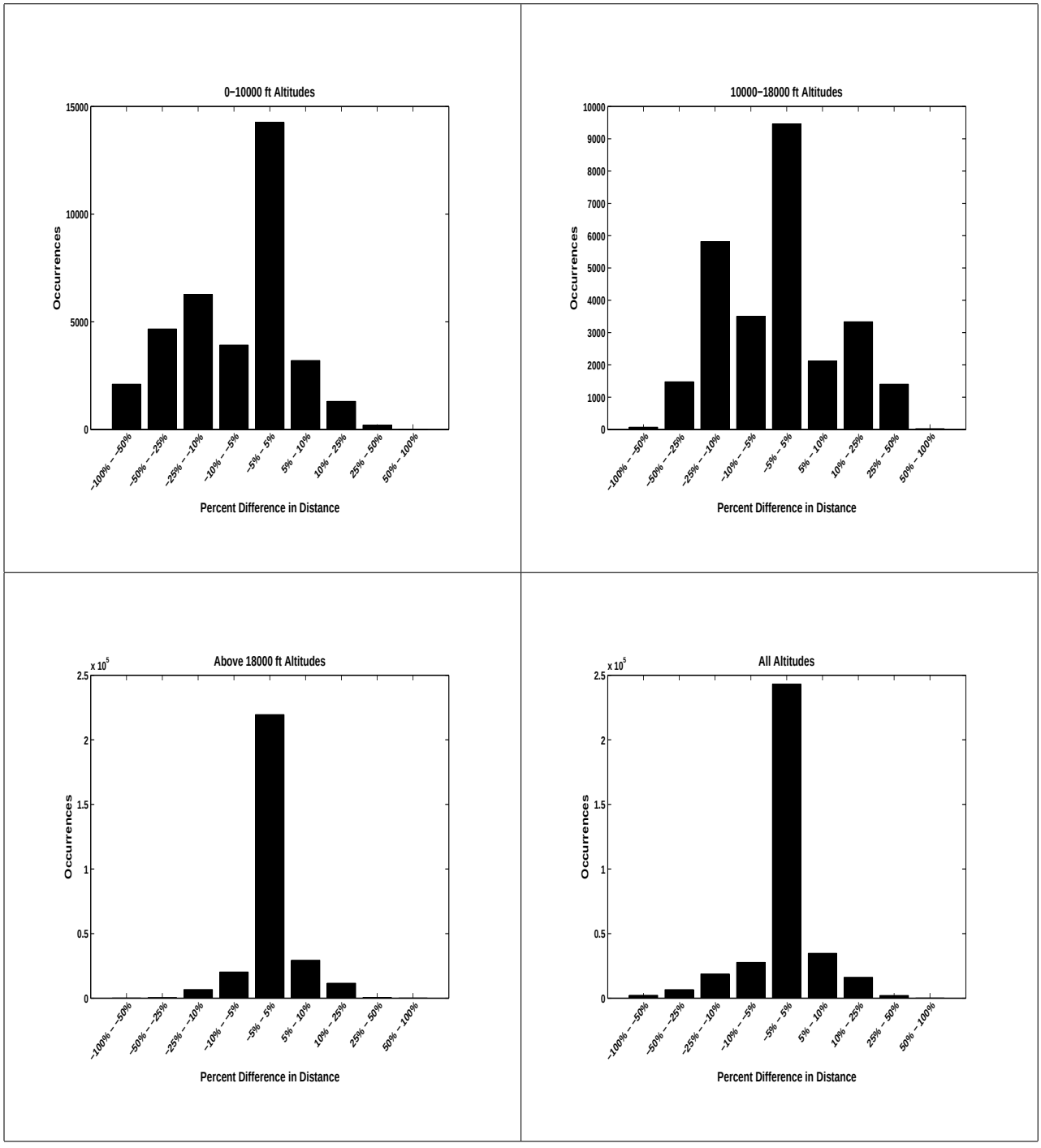

Figure A.85: Fort Campbell, 250 km radius, 5 minute projection, percent difference in distance

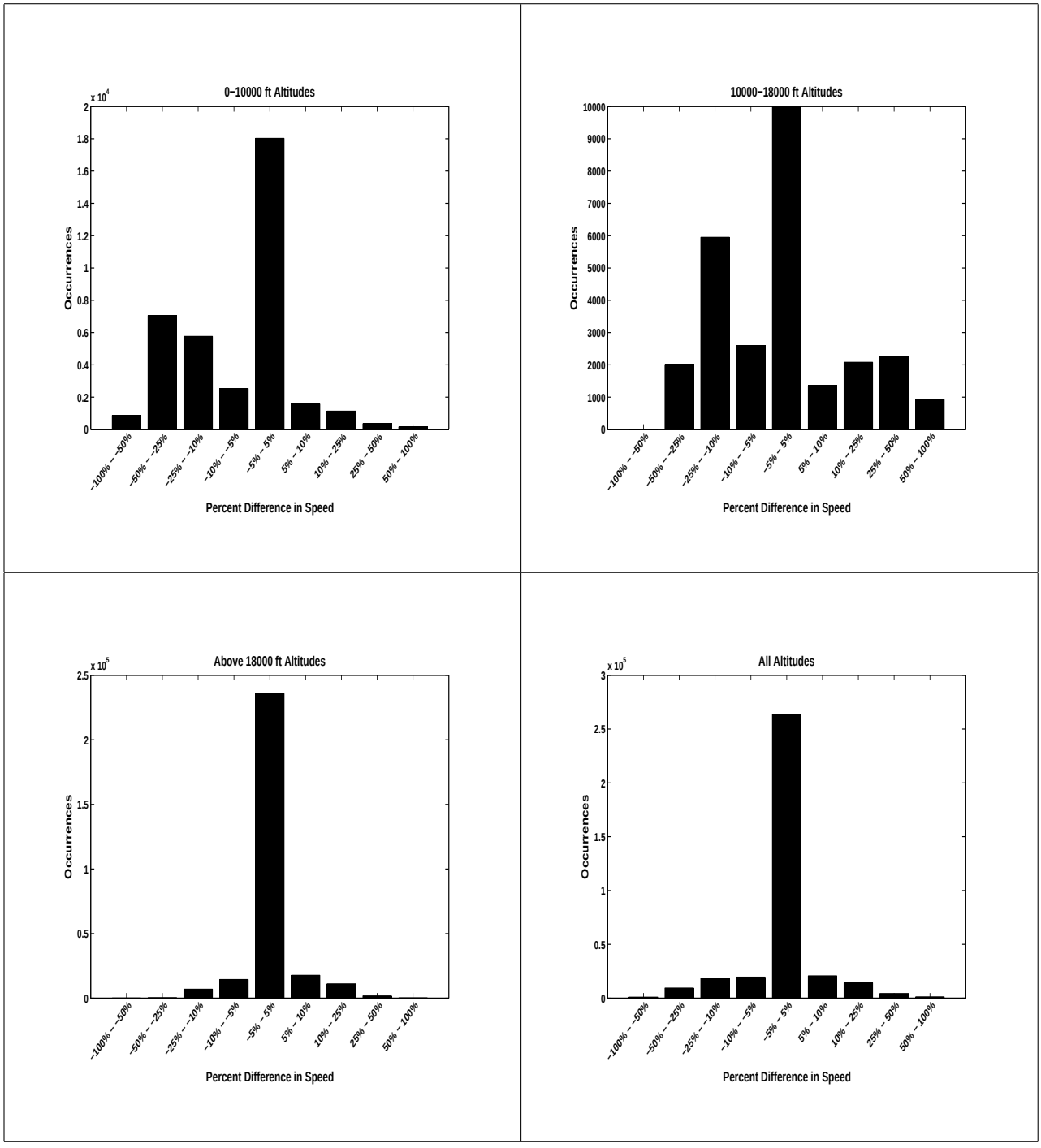

Figure A.86: Fort Campbell, 250 km radius, 5 minute projection, percent difference in speed

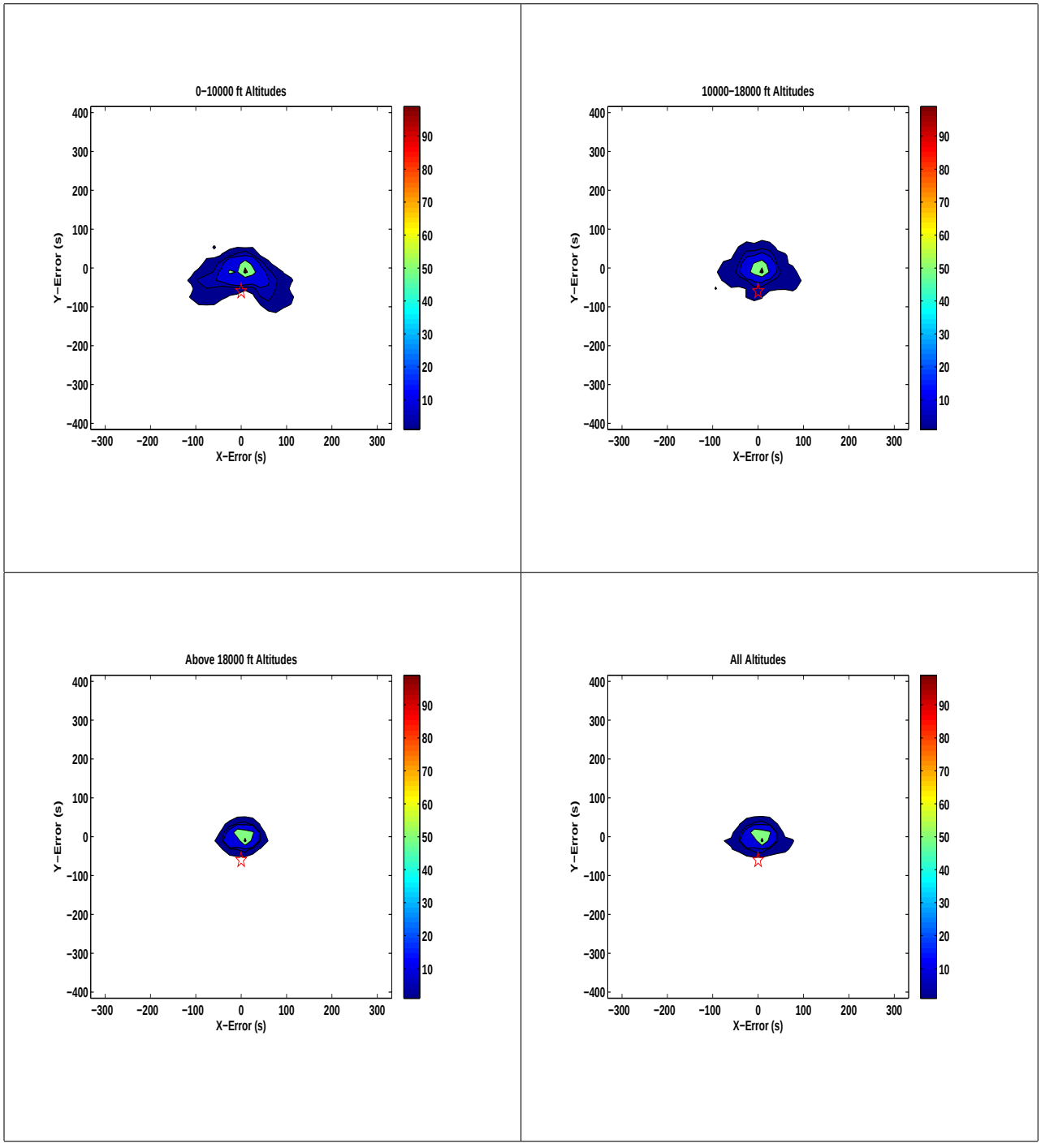

Figure A.87: Las Cruces, 250 km radius, 1 minute projection, difference in projection to measured histograms

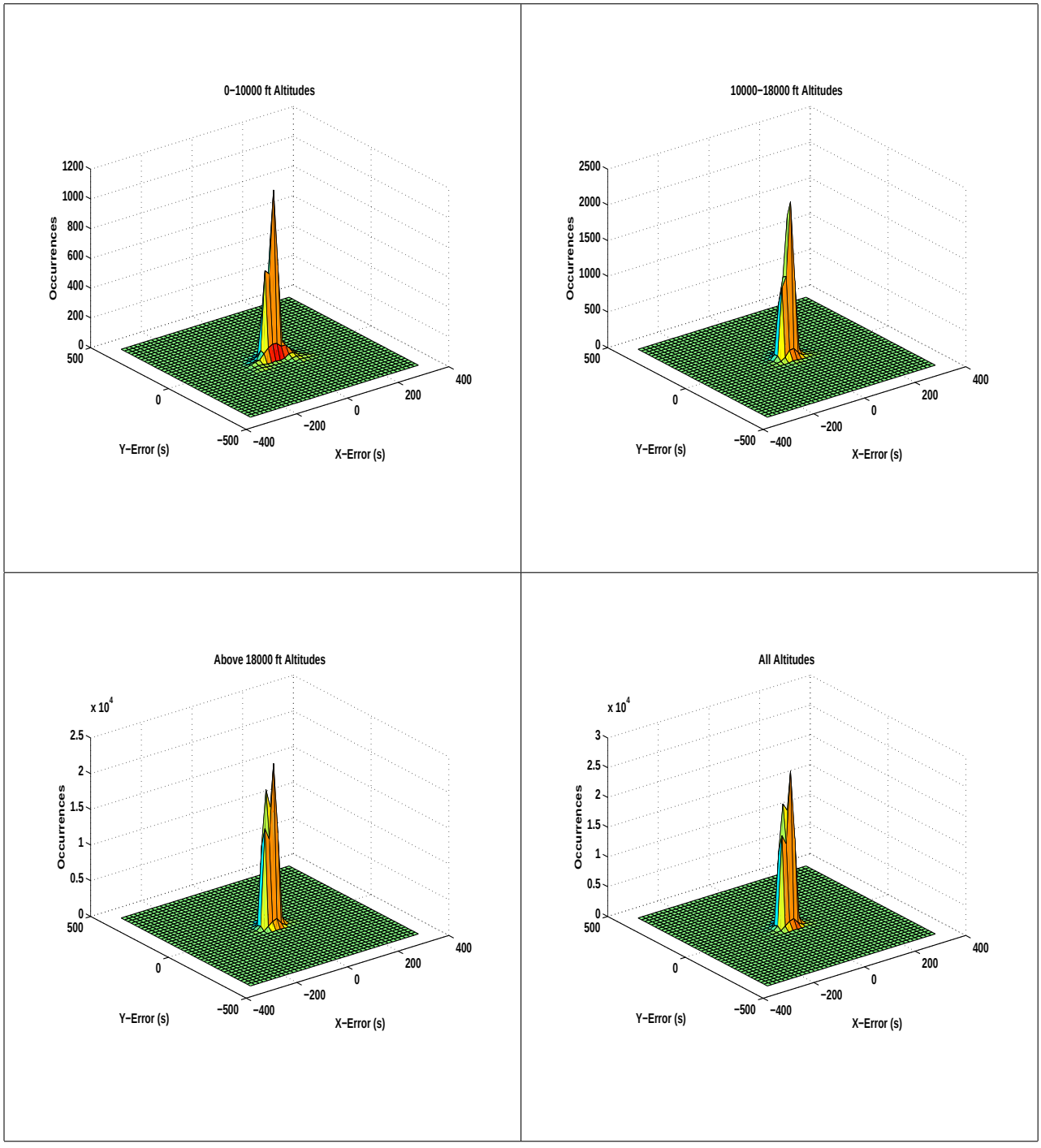

Figure A.88: Las Cruces, 250 km radius, 1 minute projection, difference in projection to measured three dimensional histograms

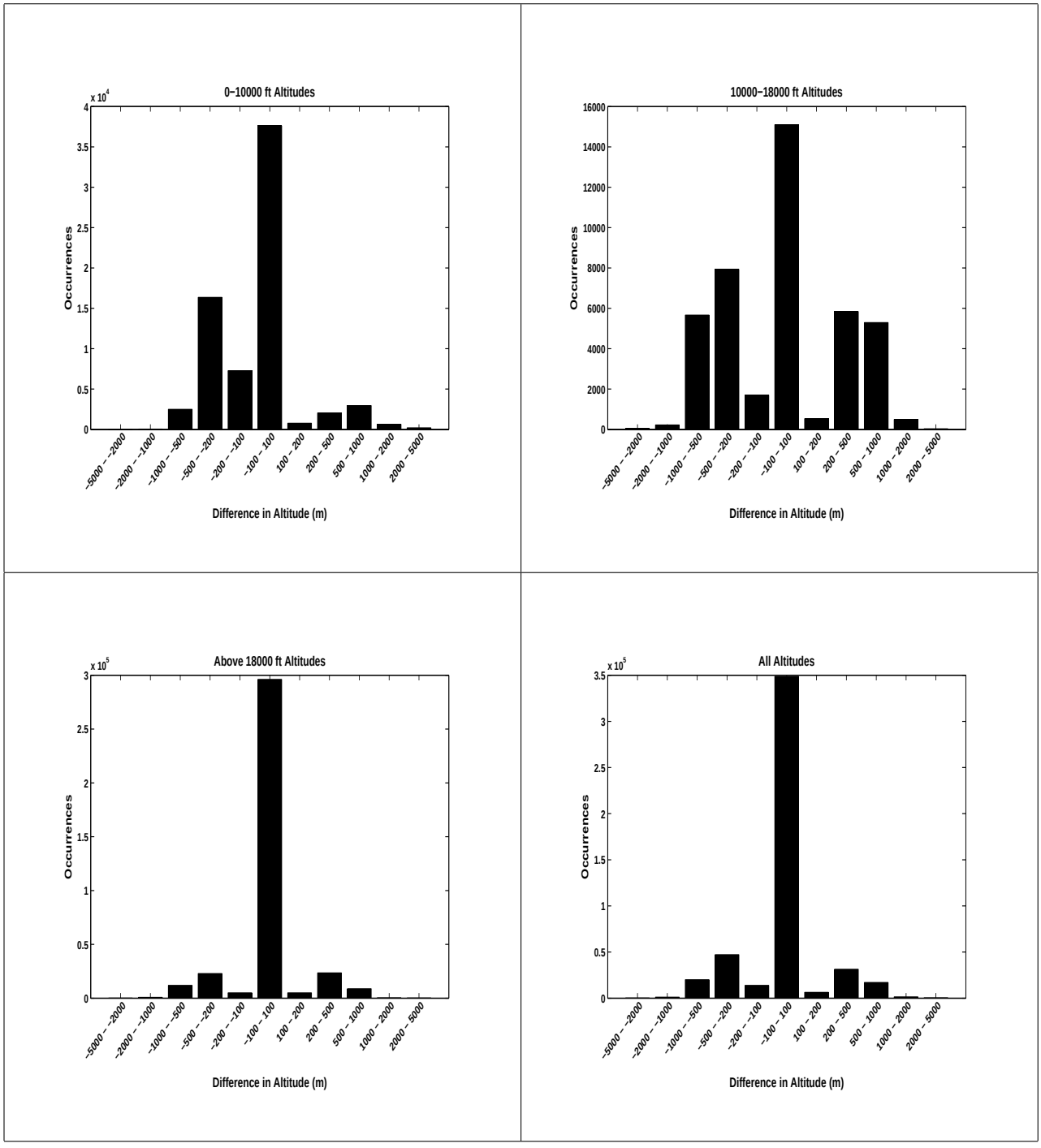

Figure A.89: Las Cruces, 250 km radius, 1 minute projection, difference in altitude

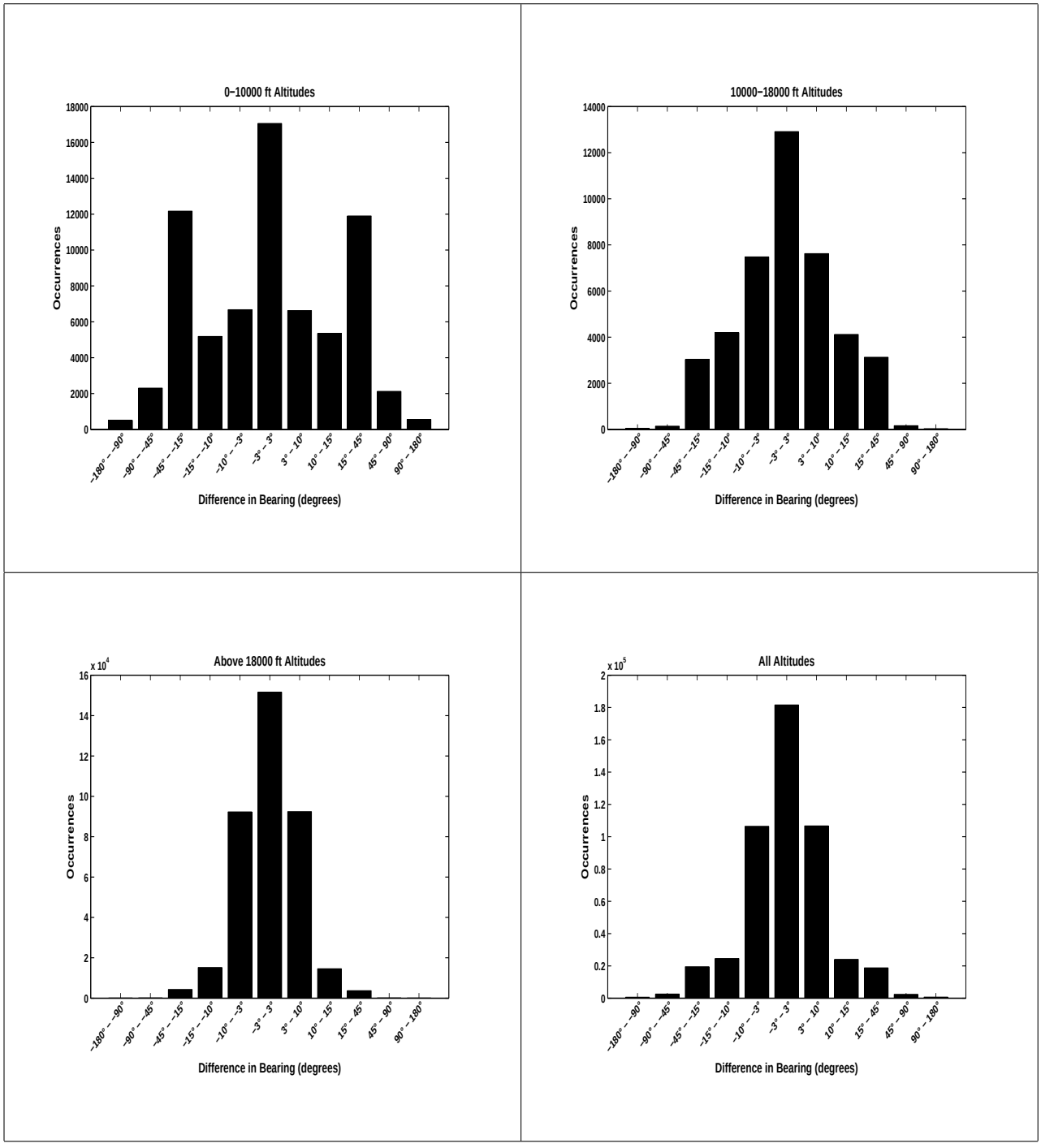

Figure A.90: Las Cruces, 250 km radius, 1 minute projection, difference in bearing

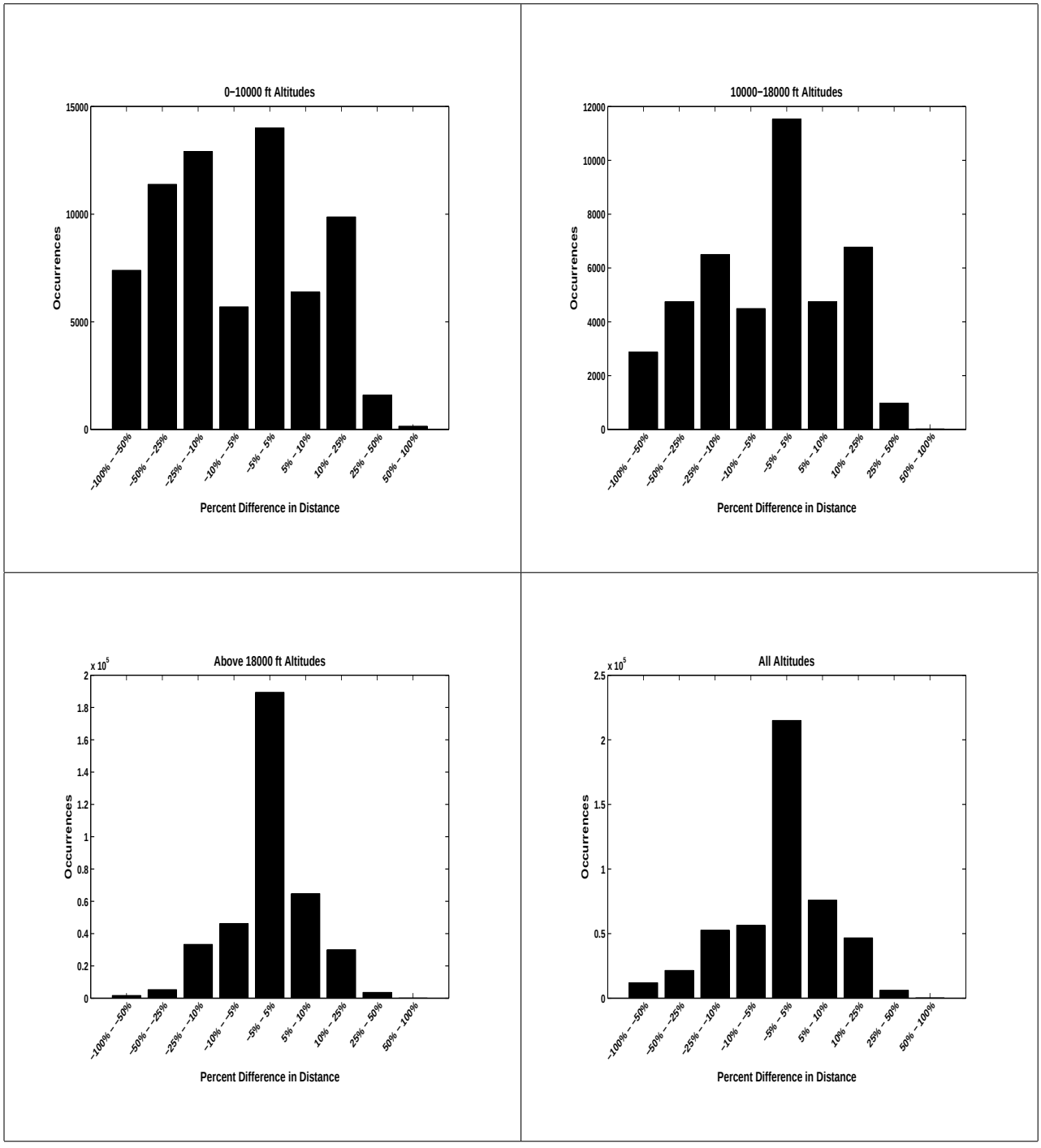

Figure A.91: Las Cruces, 250 km radius, 1 minute projection, percent difference in distance

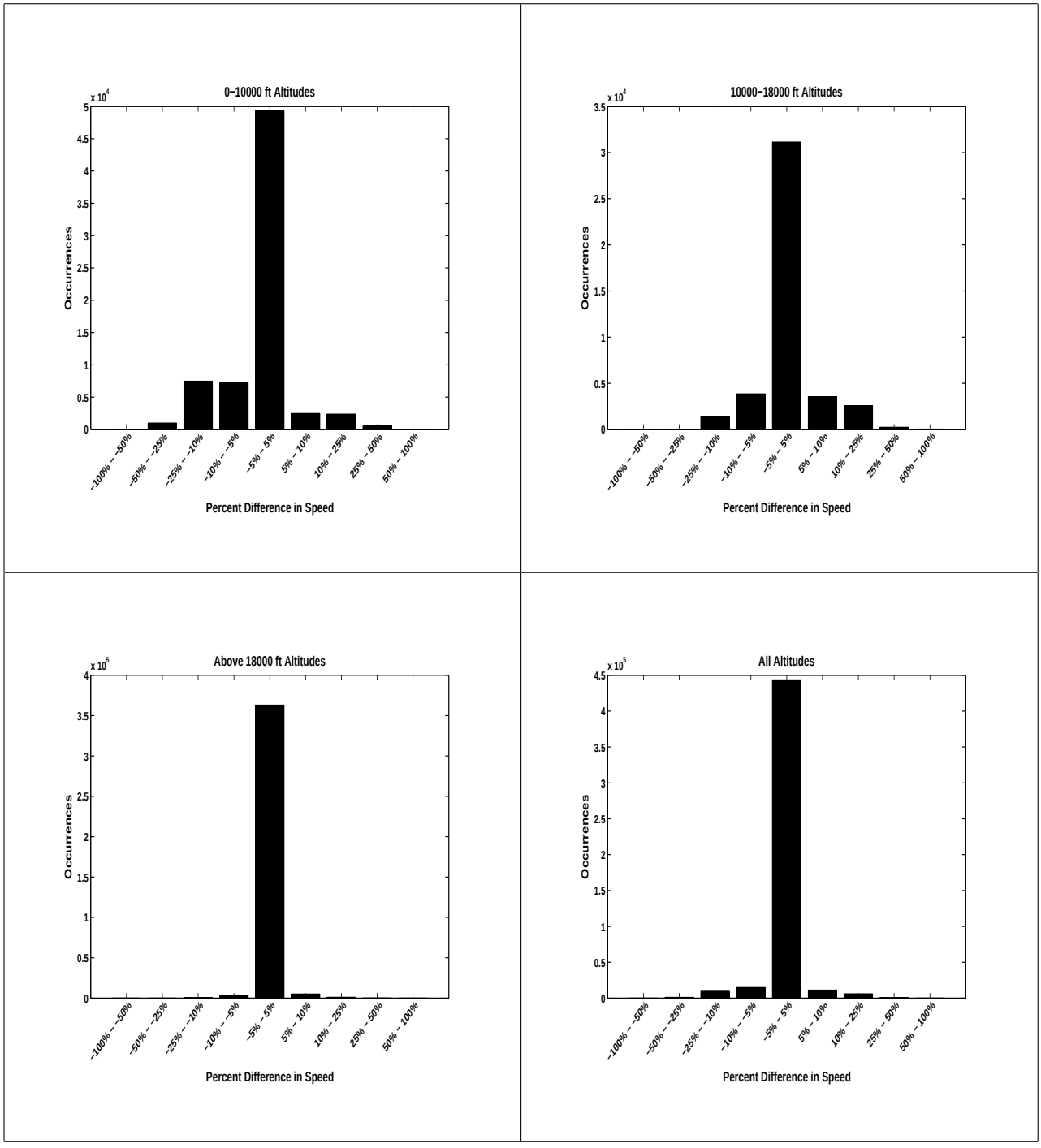

Figure A.92: Las Cruces, 250 km radius, 1 minute projection, percent difference in speed

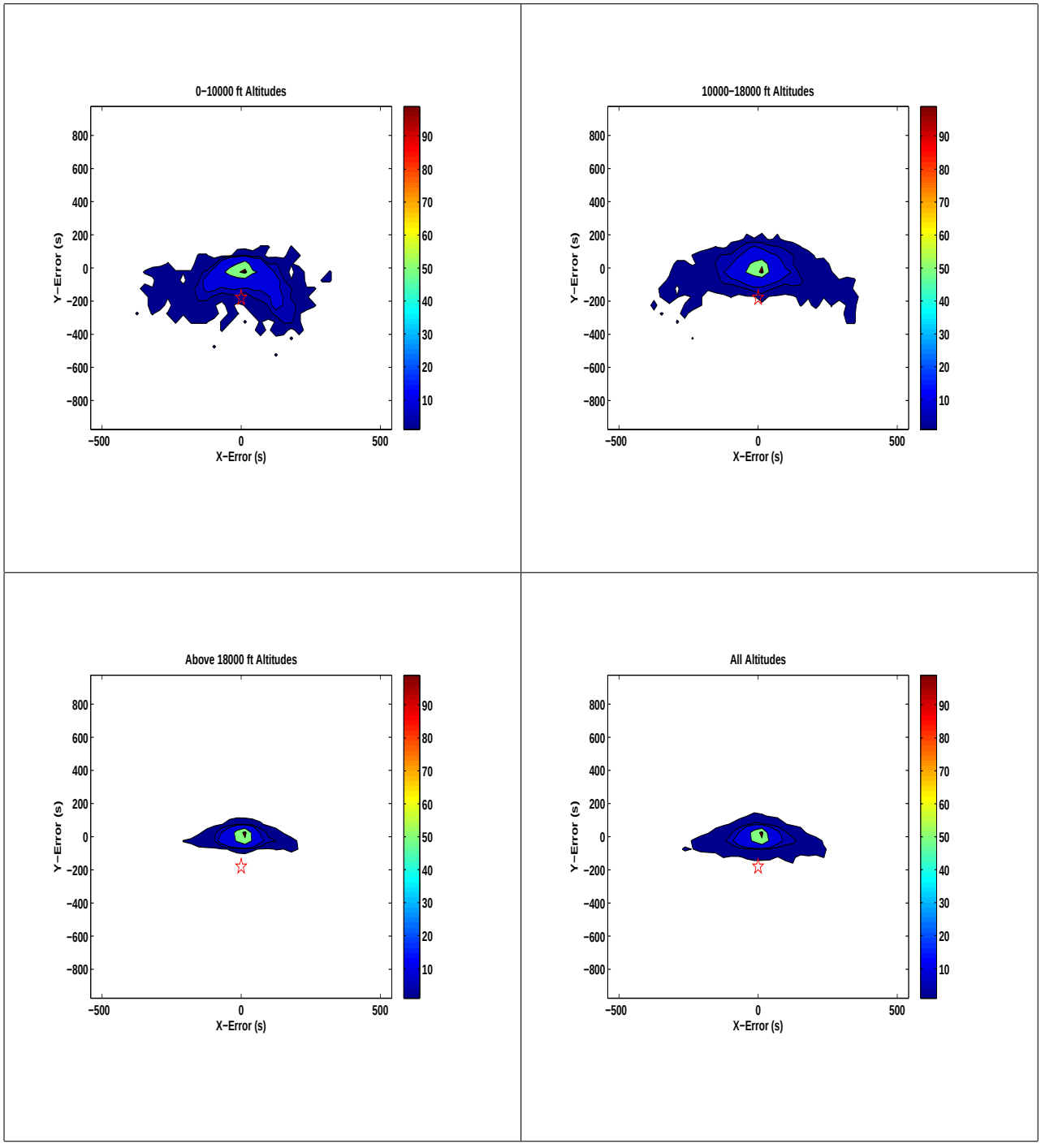

Figure A.93: Las Cruces, 250 km radius, 3 minute projection, difference in projection to measured histograms

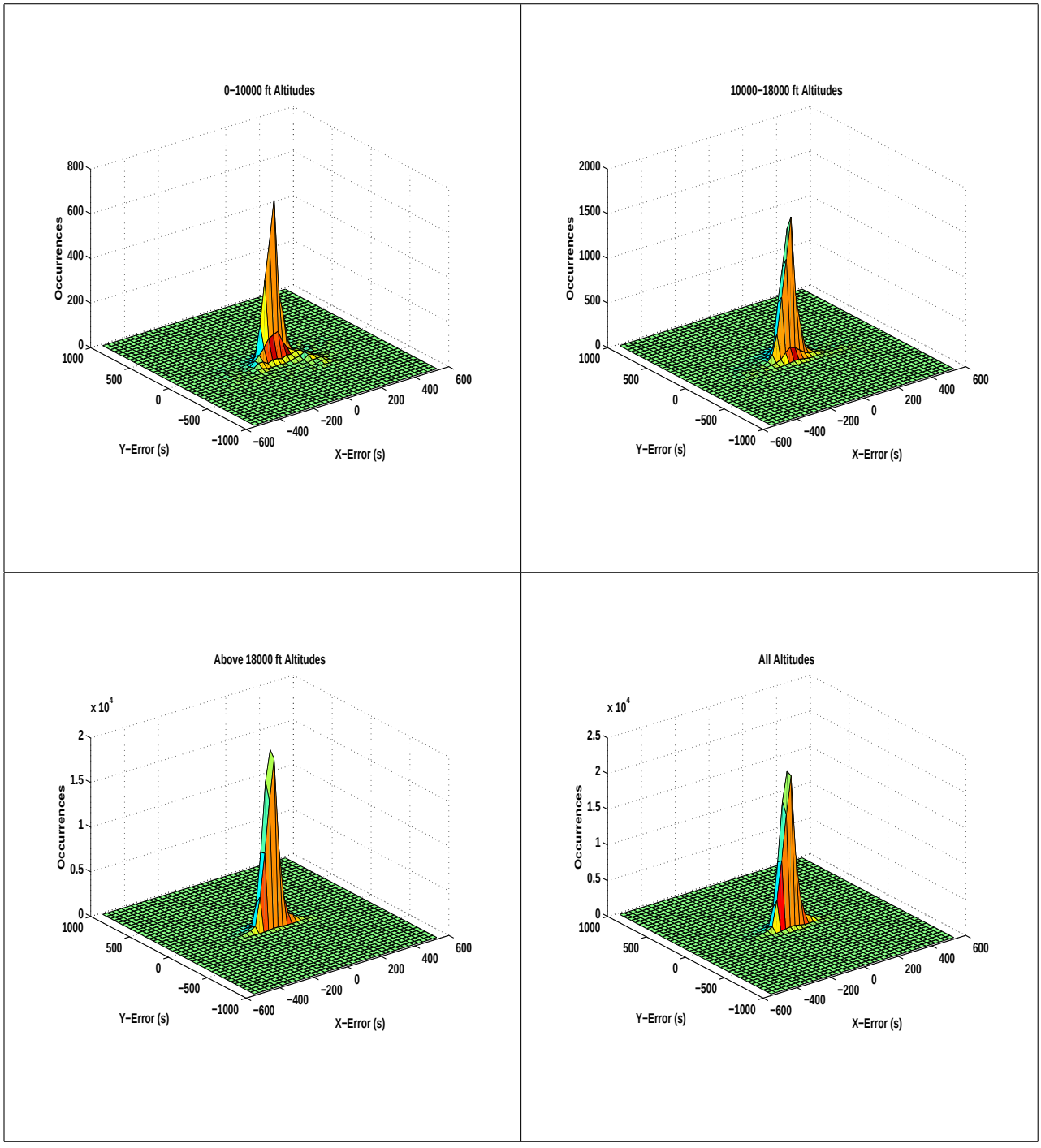

Figure A.94: Las Cruces, 250 km radius, 3 minute projection, difference in projection to measured three dimensional histograms

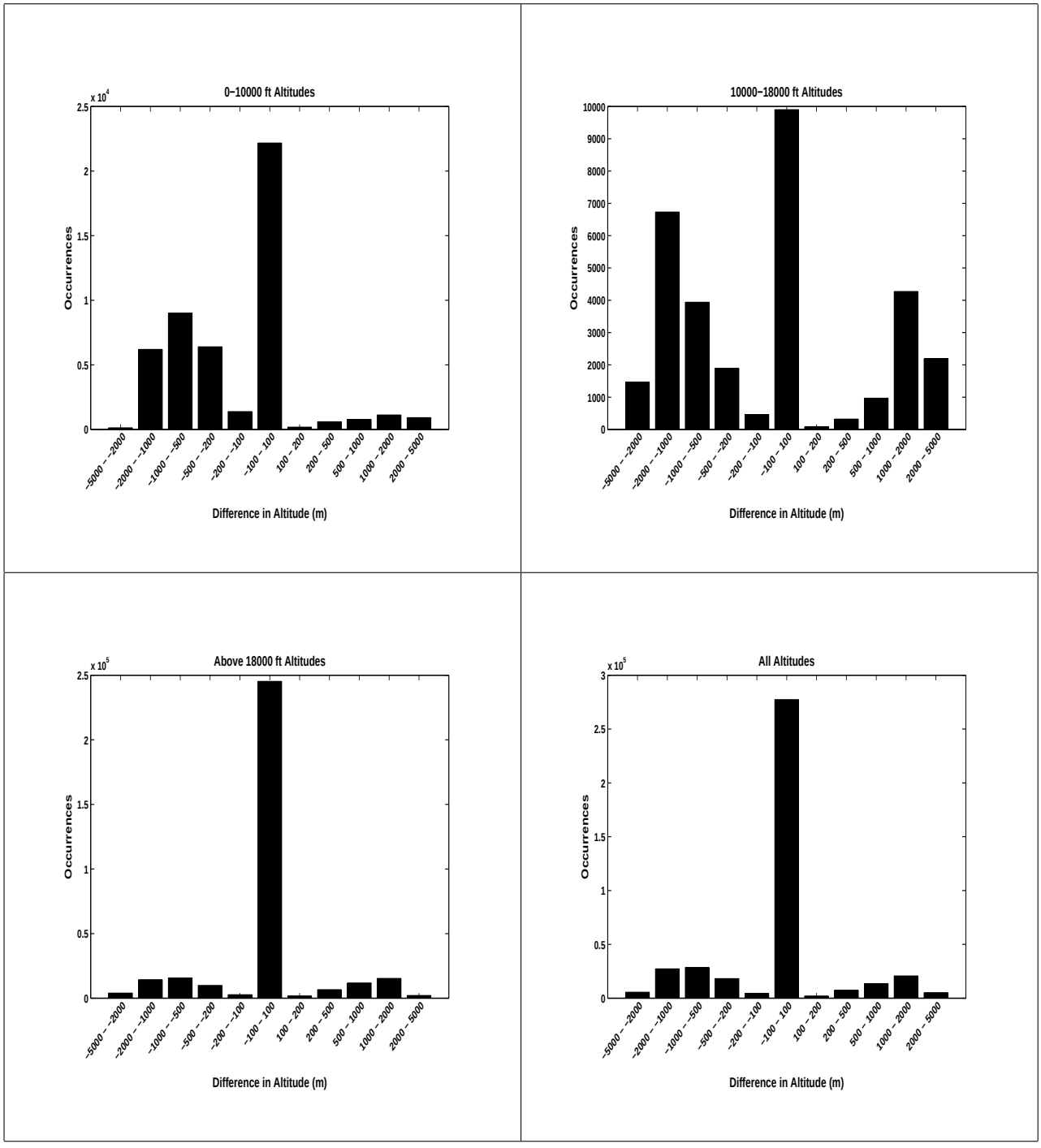

Figure A.95: Las Cruces, 250 km radius, 3 minute projection, difference in altitude

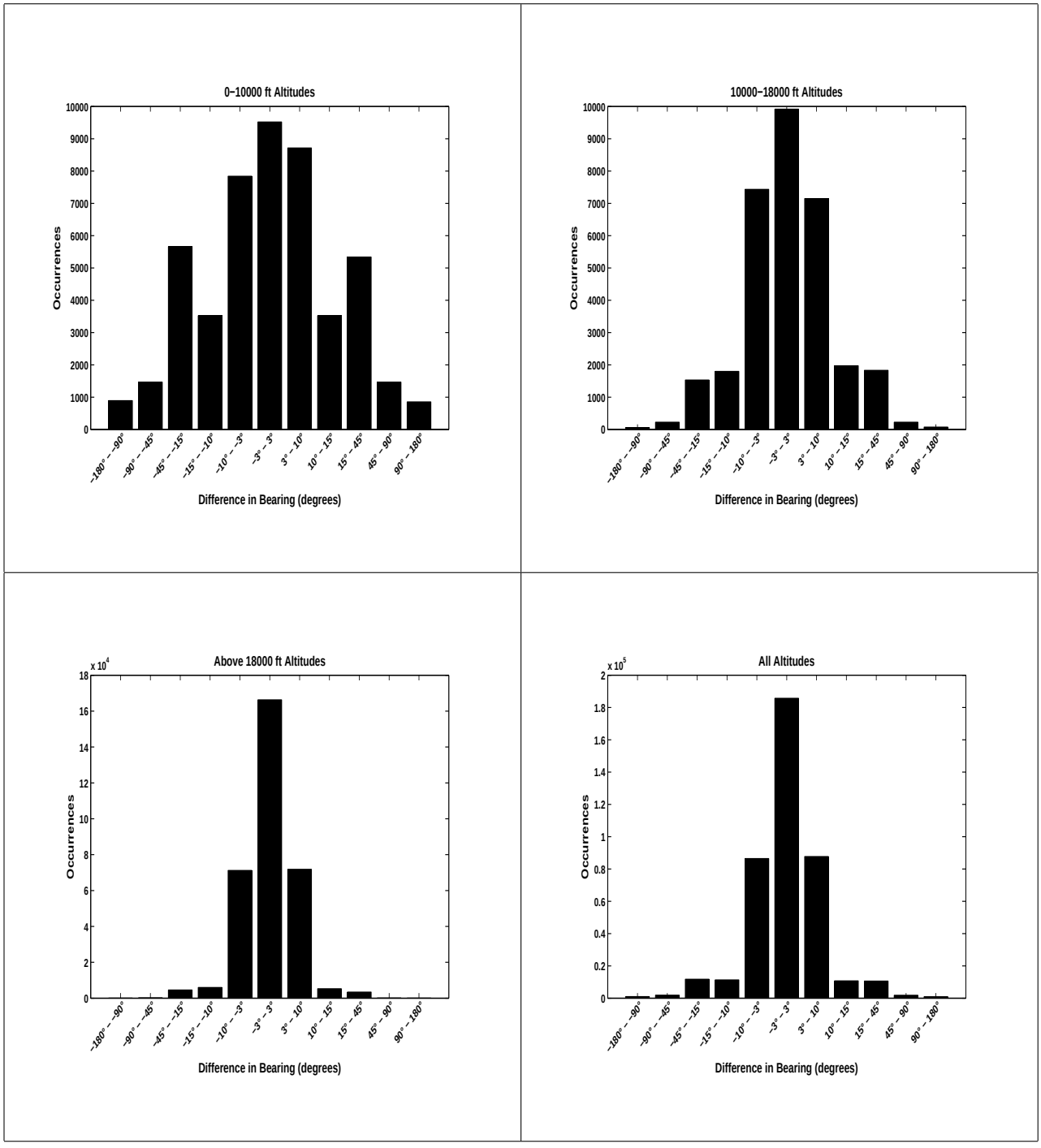

Figure A.96: Las Cruces, 250 km radius, 3 minute projection, difference in bearing

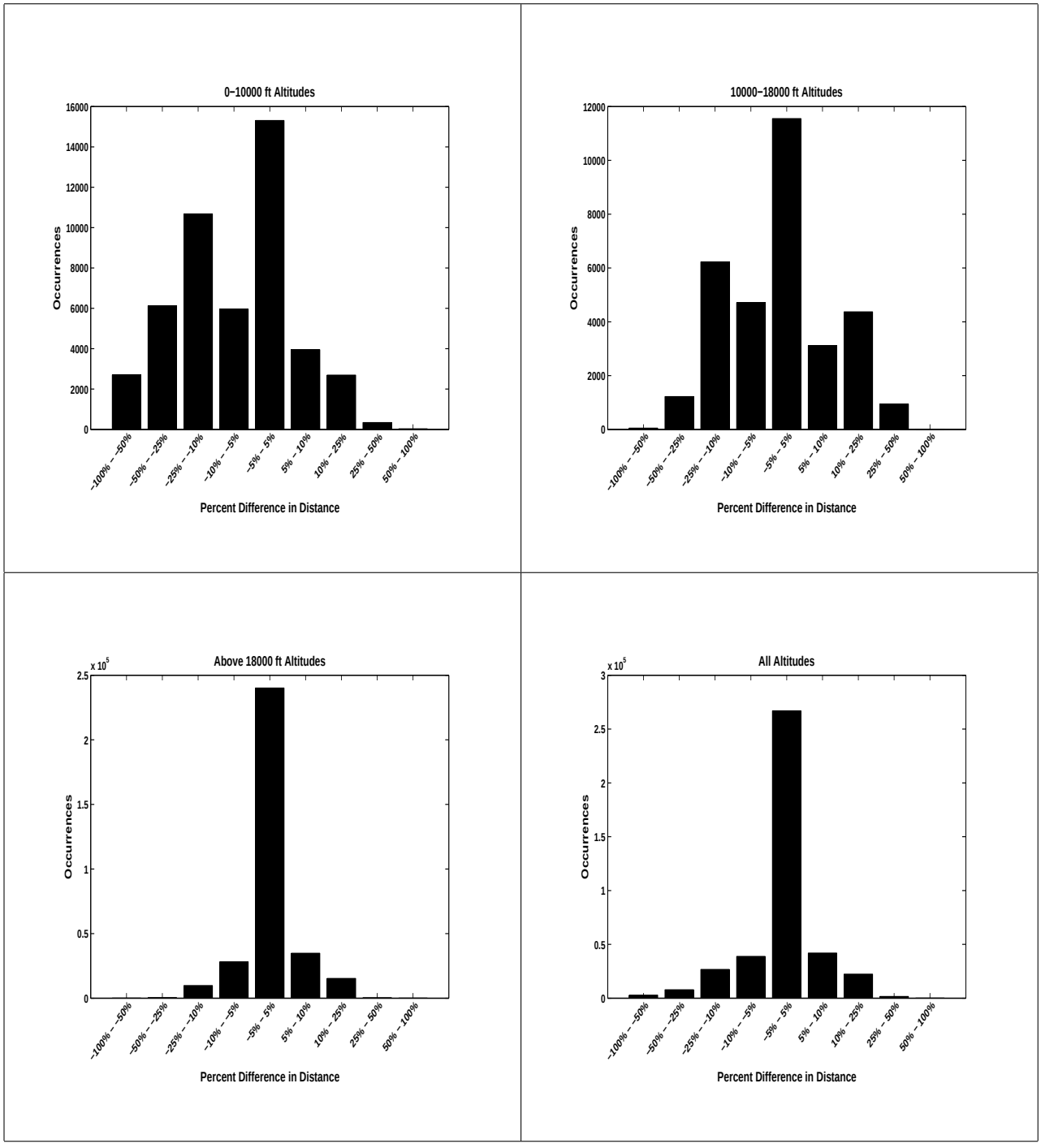

Figure A.97: Las Cruces, 250 km radius, 3 minute projection, percent difference in distance

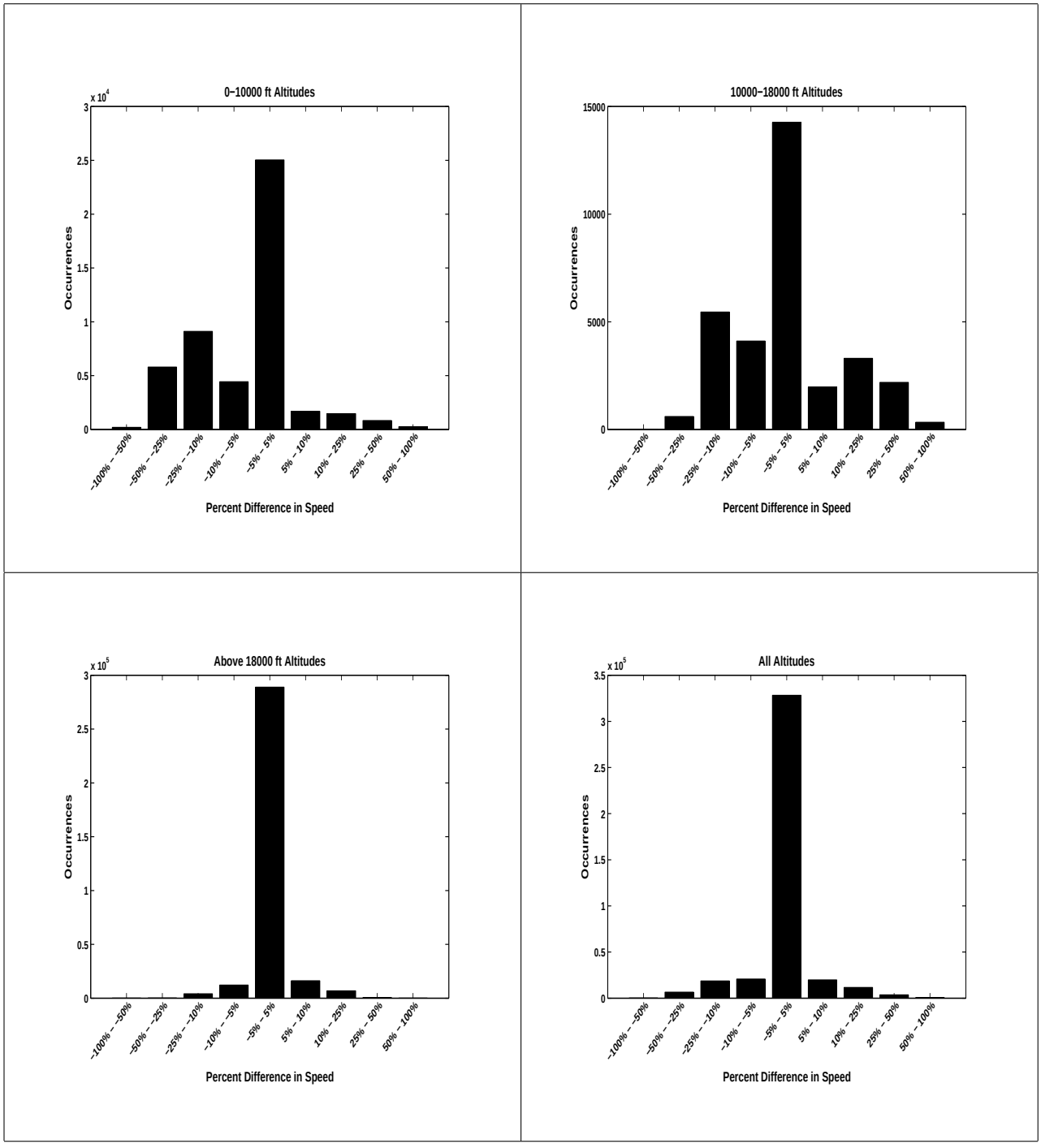

Figure A.98: Las Cruces, 250 km radius, 3 minute projection, percent difference in speed

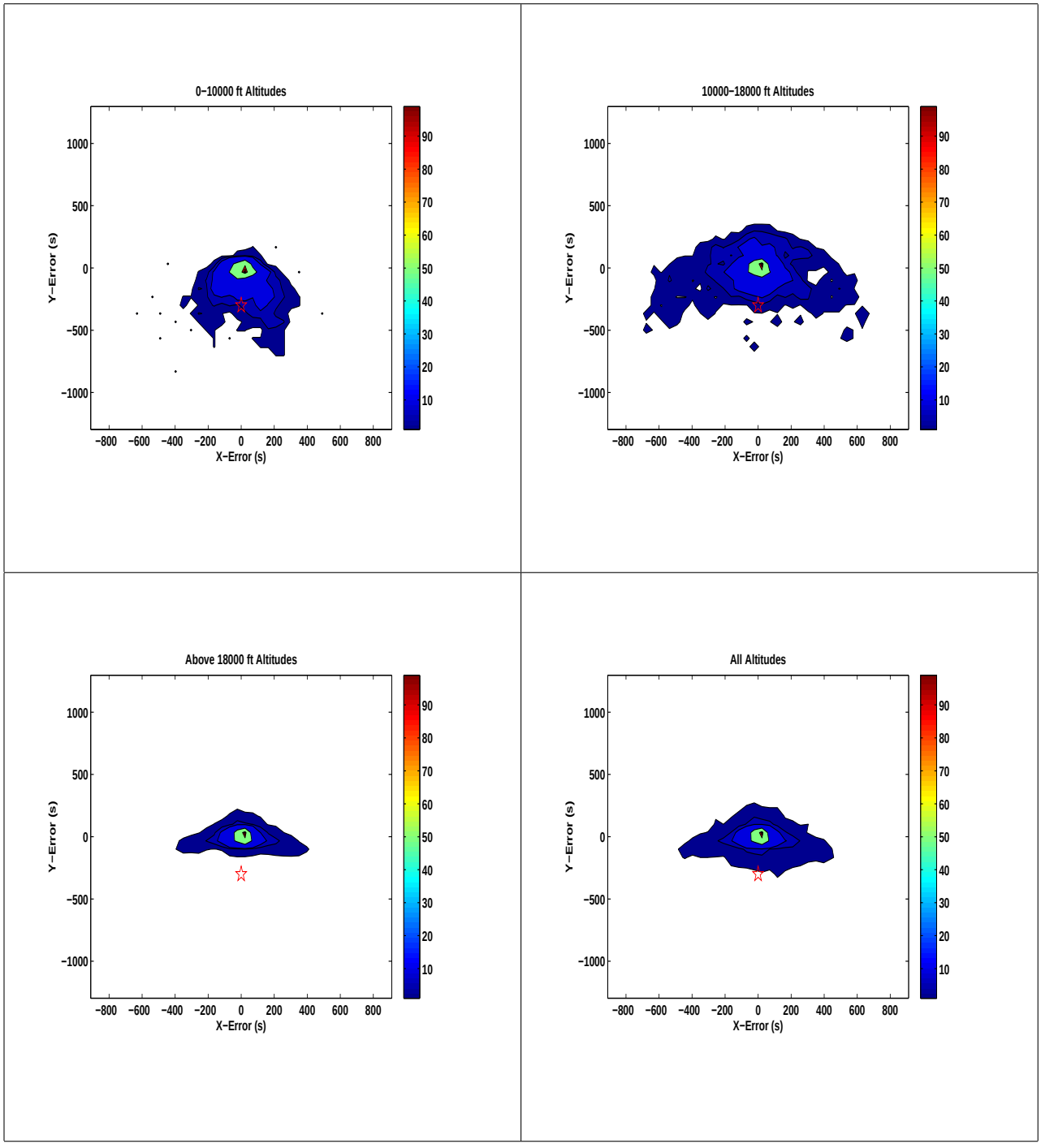

Figure A.99: Las Cruces, 250 km radius, 5 minute projection, difference in projection to measured histograms

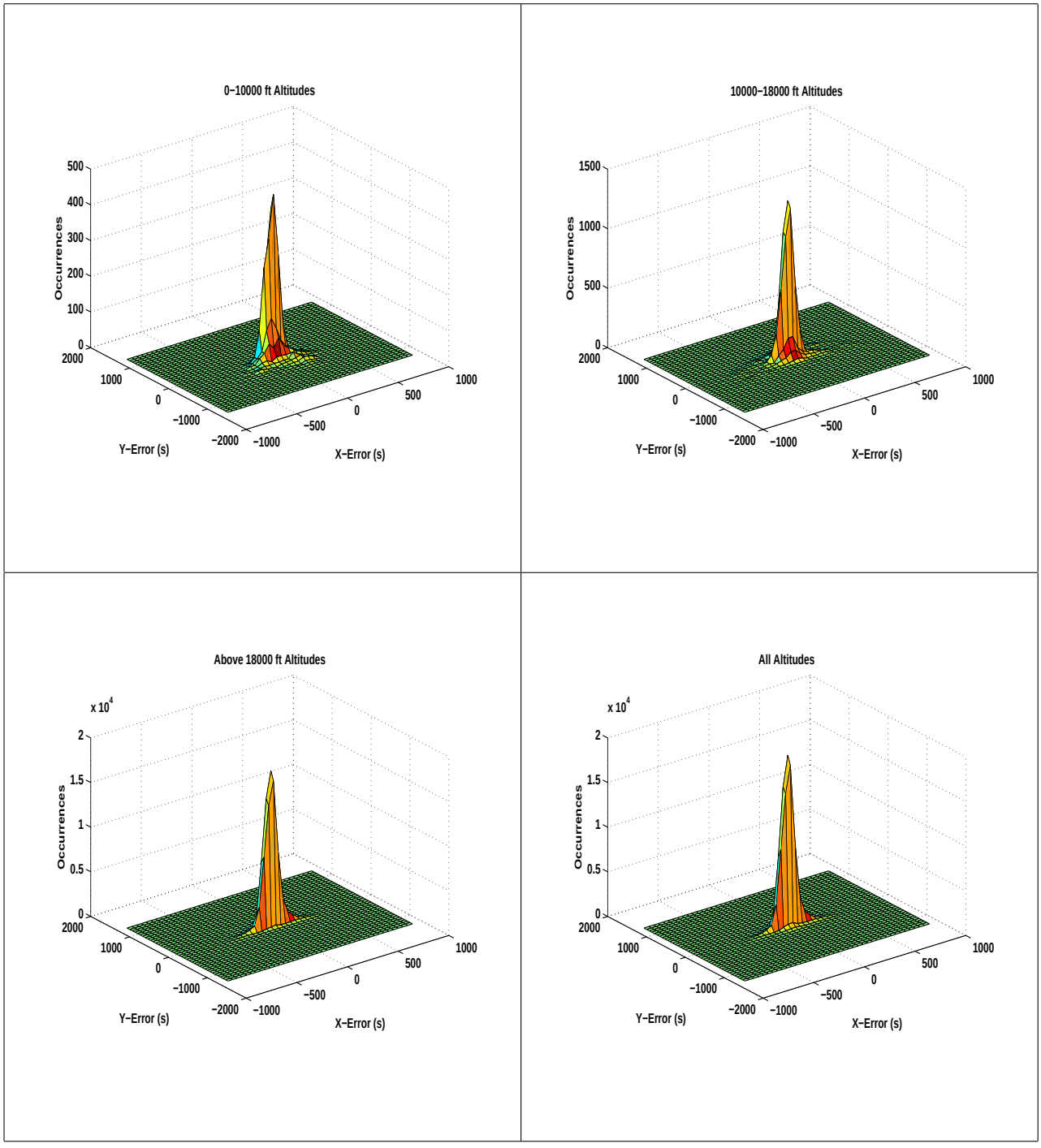

Figure A.100: Las Cruces, 250 km radius, 5 minute projection, difference in projection to measured three dimensional histograms

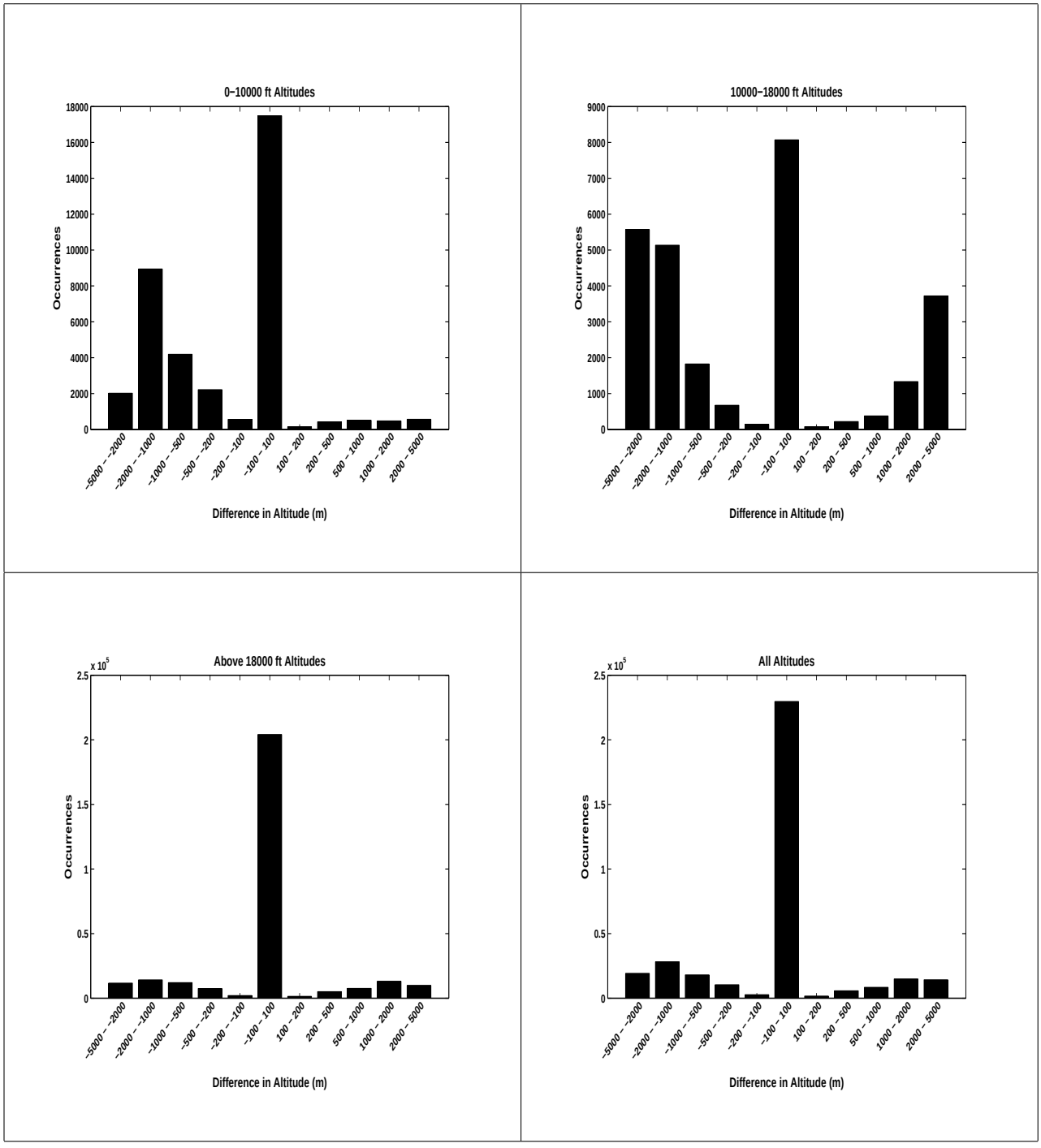

Figure A.101: Las Cruces, 250 km radius, 5 minute projection, difference in altitude

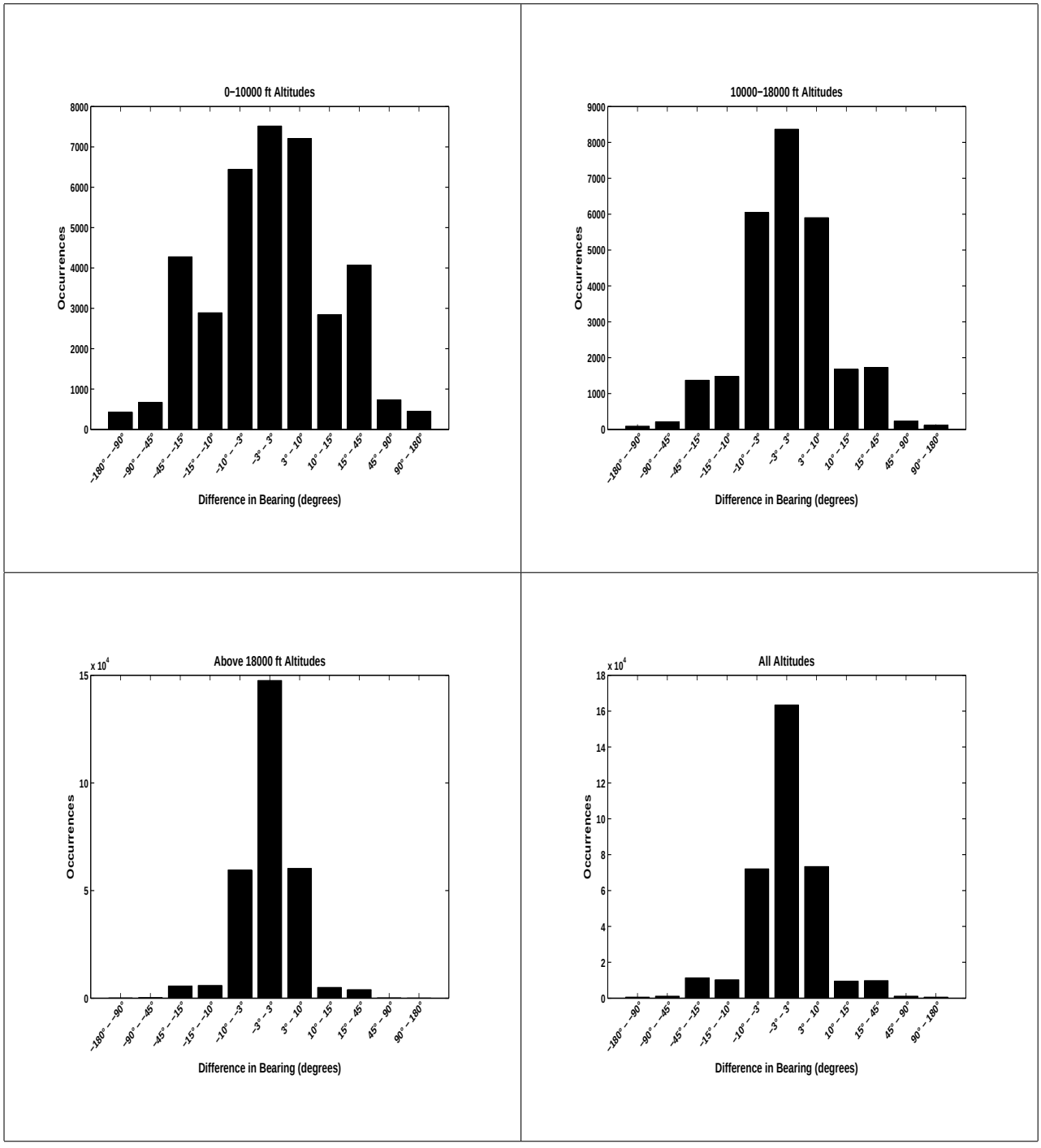

Figure A.102: Las Cruces, 250 km radius, 5 minute projection, difference in bearing

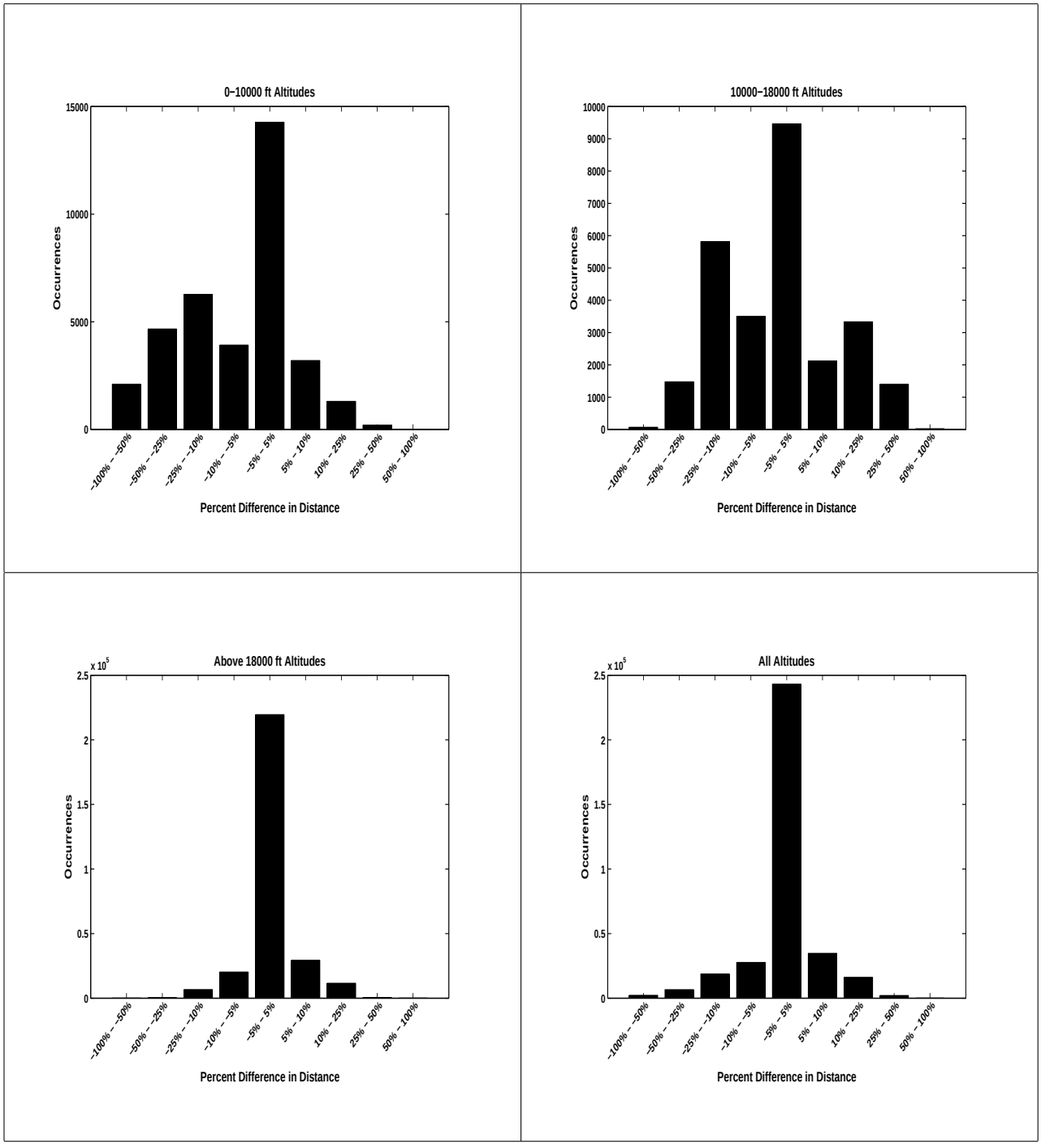

Figure A.103: Las Cruces, 250 km radius, 5 minute projection, percent difference in distance

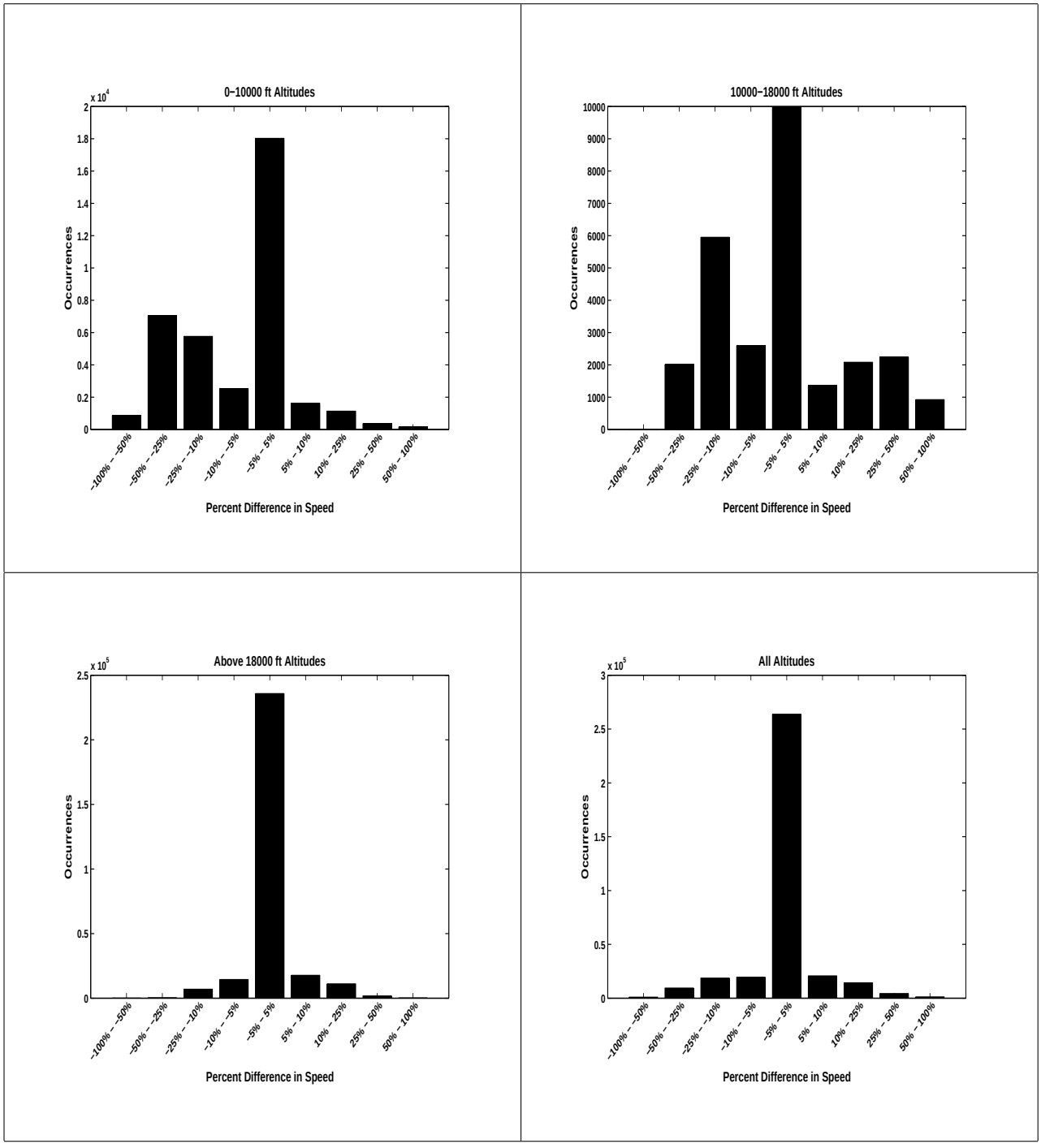

Figure A.104: Las Cruces, 250 km radius, 5 minute projection, percent difference in speed

Table A.1: Altitude Confidence, All Tracks, 0-10000 ft Altitudes

	Confidence (m)			
Projection Time	0.75	0.90	0.95	0.99
1 Minute	335	549	732	1067
3 Minute	914	1341	1737	2438
5 Minute	1433	1920	2286	3139
10 Minute	2499	3292	3749	4602

Table A.2: Altitude Confidence, All Tracks, 10000-18000 ft Altitudes

	Confidence (m)			
Projection Time	0.75	0.90	0.95	0.99
1 Minute	549	732	823	1067
3 Minute	1585	2042	2316	2865
5 Minute	2530	3200	3597	4359
10 Minute	4237	5243	5852	6858

Table A.3: Altitude Confidence, All Tracks, Above 18000 ft Altitudes

	Confidence (m)			
Projection Time	0.75	0.90	0.95	0.99
1 Minute	30	427	610	853
3 Minute	274	1280	1676	2347
5 Minute	610	2042	2682	3658
10 Minute	1219	3749	4877	6431

Table A.4: Altitude Confidence, All Tracks, All Altitudes

	Confidence (m)			
Projection Time	0.75	0.90	0.95	0.99
1 Minute	274	518	671	945
3 Minute	762	1463	1860	2469
5 Minute	1188	2316	2896	3810
10 Minute	2134	4084	4999	6462

Table A.5: Bearing Confidence, All Tracks, 0-10000 ft Altitudes

	Confidence (degrees)			
Projection Time	0.75	0.90	0.95	0.99
1 Minute	22.4	41.9	61.7	96.5
3 Minute	25.1	58.2	88.6	133.2
5 Minute	26.5	58.2	92.2	148.3
10 Minute	21.4	40.7	60.7	141.5

Table A.6: Bearing Confidence, All Tracks, 10000-18000 ft Altitudes

	Confidence (degrees)			
Projection Time	0.75	0.90	0.95	0.99
1 Minute	12.6	21.4	29.8	58.8
3 Minute	12.8	26.3	40.9	94.0
5 Minute	15.1	31.9	52.3	125.2
10 Minute	16.9	34.2	56.8	137.2

Table A.7: Bearing Confidence, All Tracks, Above 18000 ft Altitudes

	Confidence (degrees)			
Projection Time	0.75	0.90	0.95	0.99
1 Minute	7.6	10.3	12.7	21.9
3 Minute	5.5	8.6	11.9	26.1
5 Minute	5.5	9.2	13.8	30.5
10 Minute	6.3	11.9	18.2	41.0

Table A.8: Bearing Confidence, All Tracks, All Altitudes

	Confidence (degrees)			
Projection Time	0.75	0.90	0.95	0.99
1 Minute	9.3	16.8	24.9	62.0
3 Minute	7.2	15.4	27.4	82.2
5 Minute	7.3	16.6	28.8	86.8
10 Minute	8.0	17.3	27.5	70.3

Table A.9: Distance Confidence, All Tracks, 0-10000 ft Altitudes

	Confidence (%)			
Projection Time	0.75	0.90	0.95	0.99
1 Minute	25.6	48.0	64.8	104.6
3 Minute	22.5	42.2	65.4	143.7
5 Minute	29.8	62.9	121.8	305.0
10 Minute	47.2	94.8	166.8	507.5

Table A.10: Distance Confidence, All Tracks, 10000-18000 ft Altitudes

	Confidence (%)			
Projection Time	0.75	0.90	0.95	0.99
1 Minute	18.9	35.8	51.4	82.1
3 Minute	15.8	23.7	29.2	47.1
5 Minute	19.4	27.9	34.2	60.3
10 Minute	27.2	38.3	47.6	118.4

Table A.11: Distance Confidence, All Tracks, Above 18000 ft Altitudes

	Confidence (%)			
Projection Time	0.75	0.90	0.95	0.99
1 Minute	8.9	13.8	18.0	35.8
3 Minute	5.1	8.6	11.6	19.0
5 Minute	4.7	8.6	11.9	20.5
10 Minute	4.9	10.6	16.4	30.7

Table A.12: Distance Confidence, All Tracks, All Altitudes

	Confidence (%)			
Projection Time	0.75	0.90	0.95	0.99
1 Minute	11.7	21.7	34.5	71.2
3 Minute	7.3	15.2	23.0	55.6
5 Minute	7.3	17.1	26.9	84.7
10 Minute	7.7	22.8	35.7	107.2

Table A.13: Speed Confidence, All Tracks, 0-10000 ft Altitudes

	Confidence (%)			
Projection Time	0.75	0.90	0.95	0.99
1 Minute	8.6	16.0	21.1	32.3
3 Minute	20.9	31.9	38.8	52.5
5 Minute	28.7	40.5	47.0	60.2
10 Minute	42.4	53.4	58.3	65.8

Table A.14: Speed Confidence, All Tracks, 10000-18000 ft Altitudes

	Confidence (%)			
Projection Time	0.75	0.90	0.95	0.99
1 Minute	6.4	11.6	15.4	25.3
3 Minute	17.4	27.8	35.3	57.0
5 Minute	26.0	39.3	50.6	81.7
10 Minute	37.7	51.7	67.4	113.3

Table A.15: Speed Confidence, All Tracks, Above 18000 ft Altitudes

	Confidence (%)			
Projection Time	0.75	0.90	0.95	0.99
1 Minute	1.5	2.9	4.3	8.7
3 Minute	2.8	6.4	9.7	18.2
5 Minute	3.9	9.3	14.3	27.2
10 Minute	6.0	15.8	25.2	54.2

Table A.16: Speed Confidence, All Tracks, All Altitudes

	Confidence (%)			
Projection Time	0.75	0.90	0.95	0.99
1 Minute	2.6	6.5	11.1	22.4
3 Minute	5.4	14.9	23.4	40.6
5 Minute	7.5	21.2	31.4	51.2
10 Minute	10.8	32.1	44.4	67.6

Appendix B

Private Personal Aircraft GPS Tracks

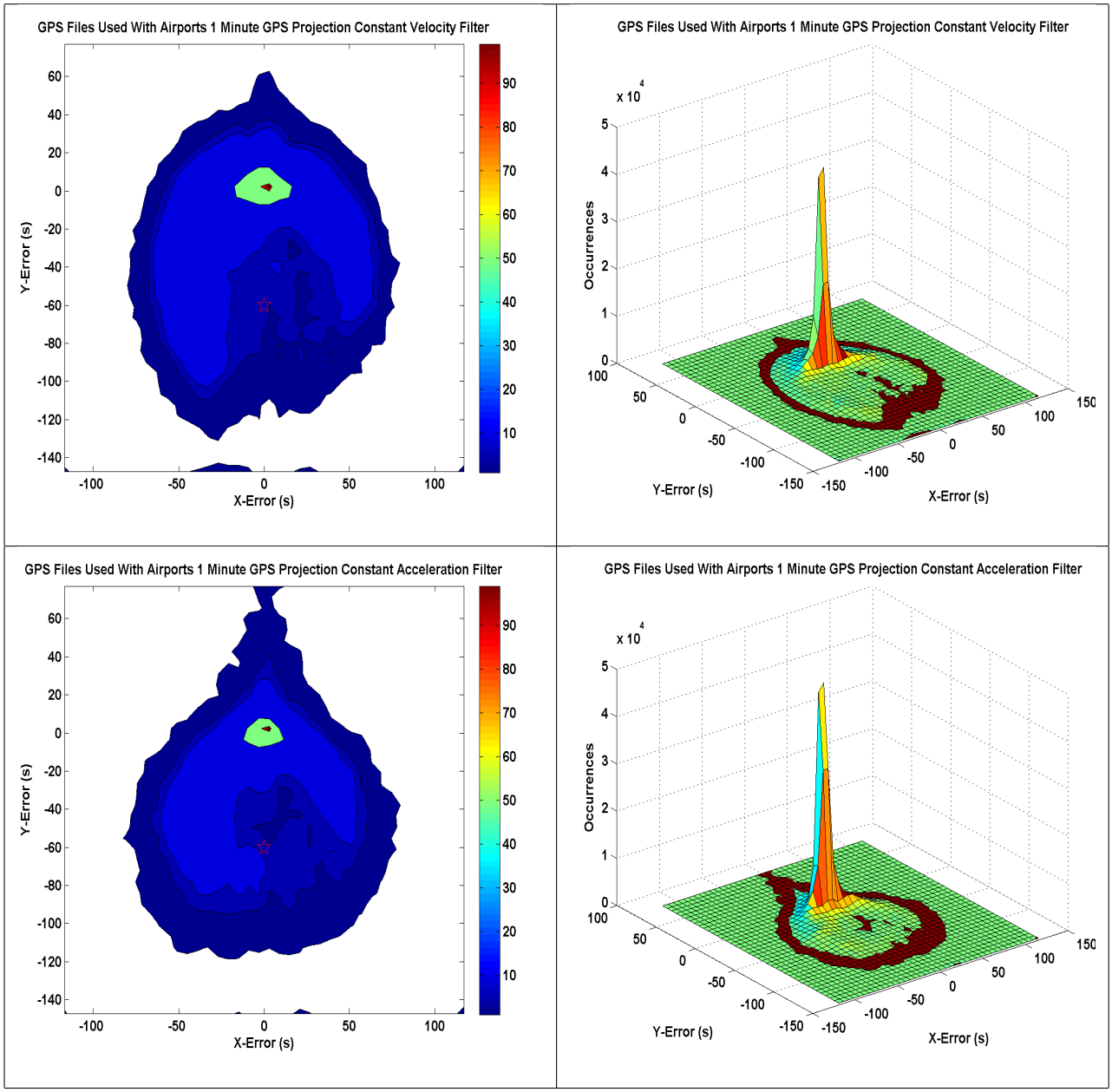

Figure B.1: Constant velocity and constant acceleration filters, all GPS flights with airports, 1 minute time horizon

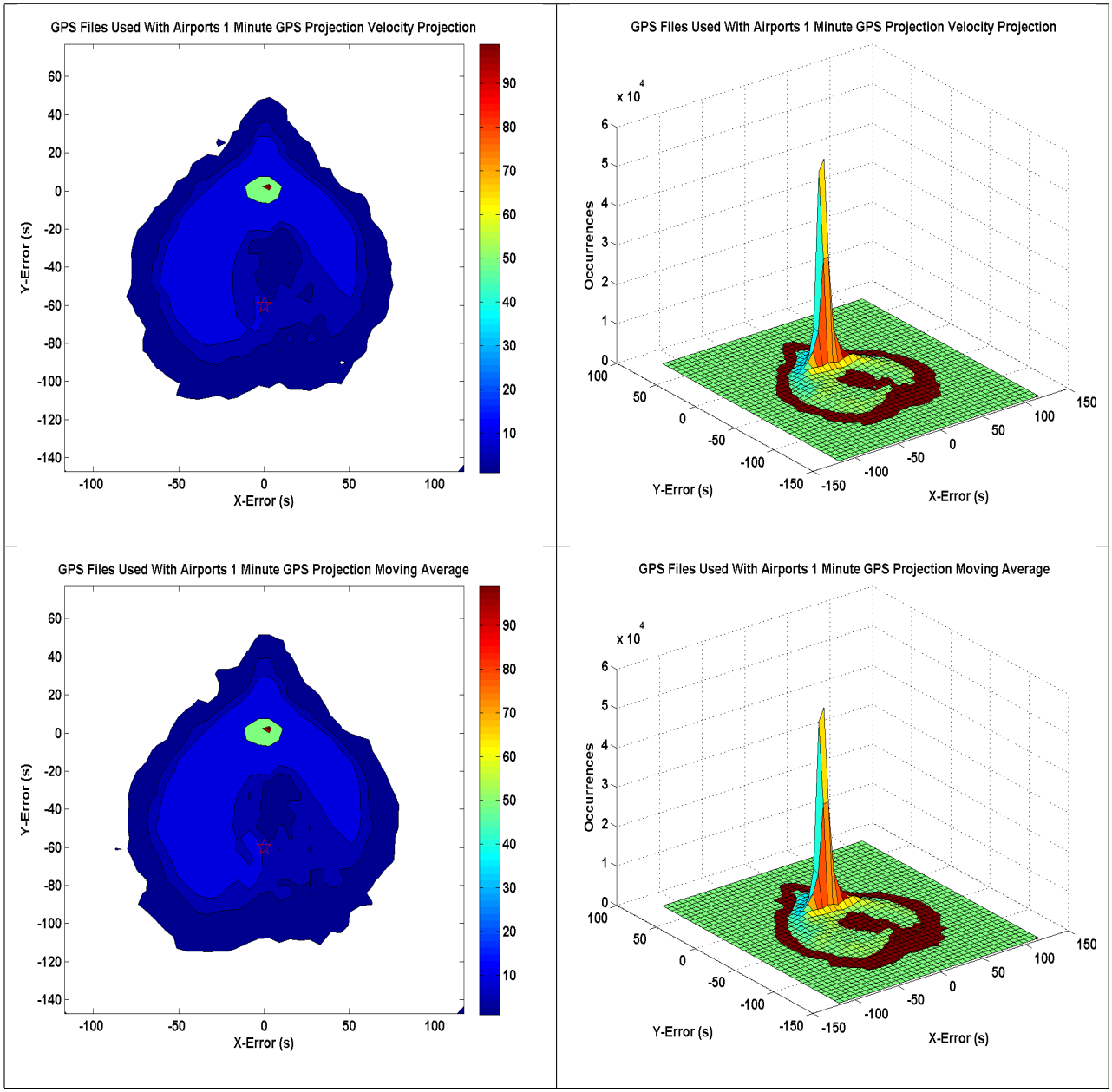

Figure B.2: Straight velocity projection and moving average projection, all GPS flights with airports, 1 minute time horizon

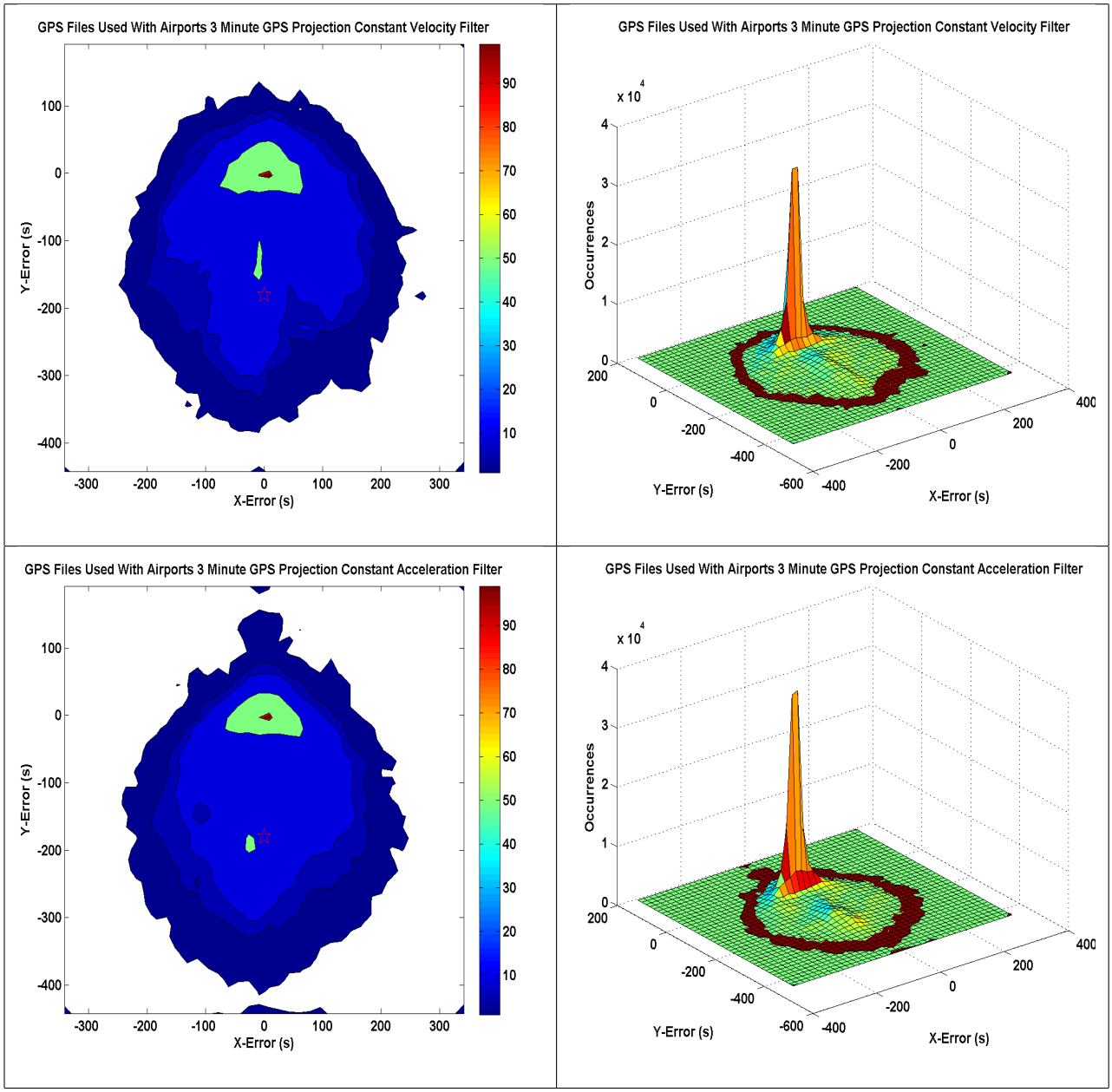

Figure B.3: Constant velocity and constant acceleration filters, all GPS flights with airports, 3 minute time horizon

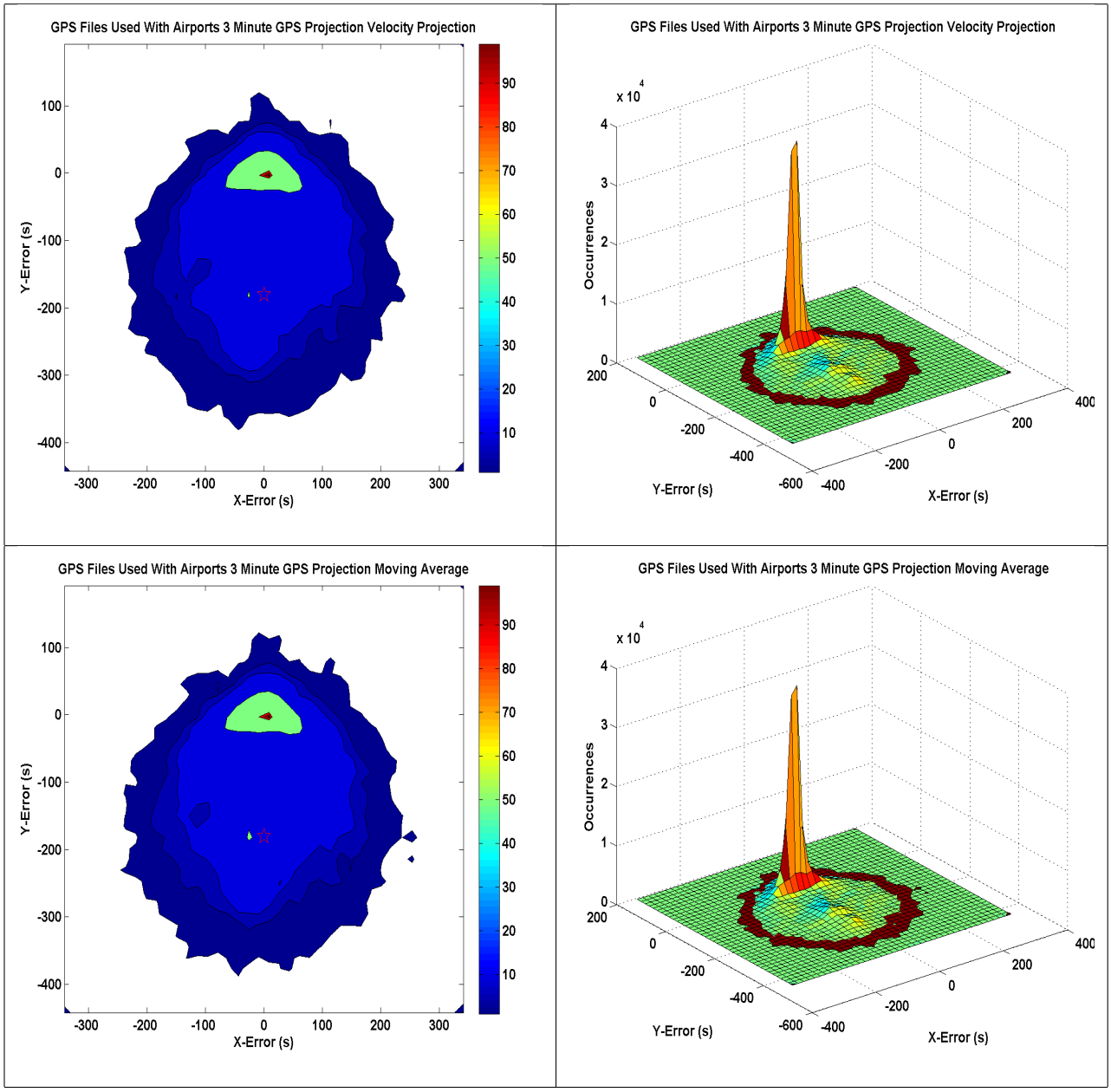

Figure B.4: Straight velocity projection and moving average projection, all GPS flights with airports, 3 minute time horizon

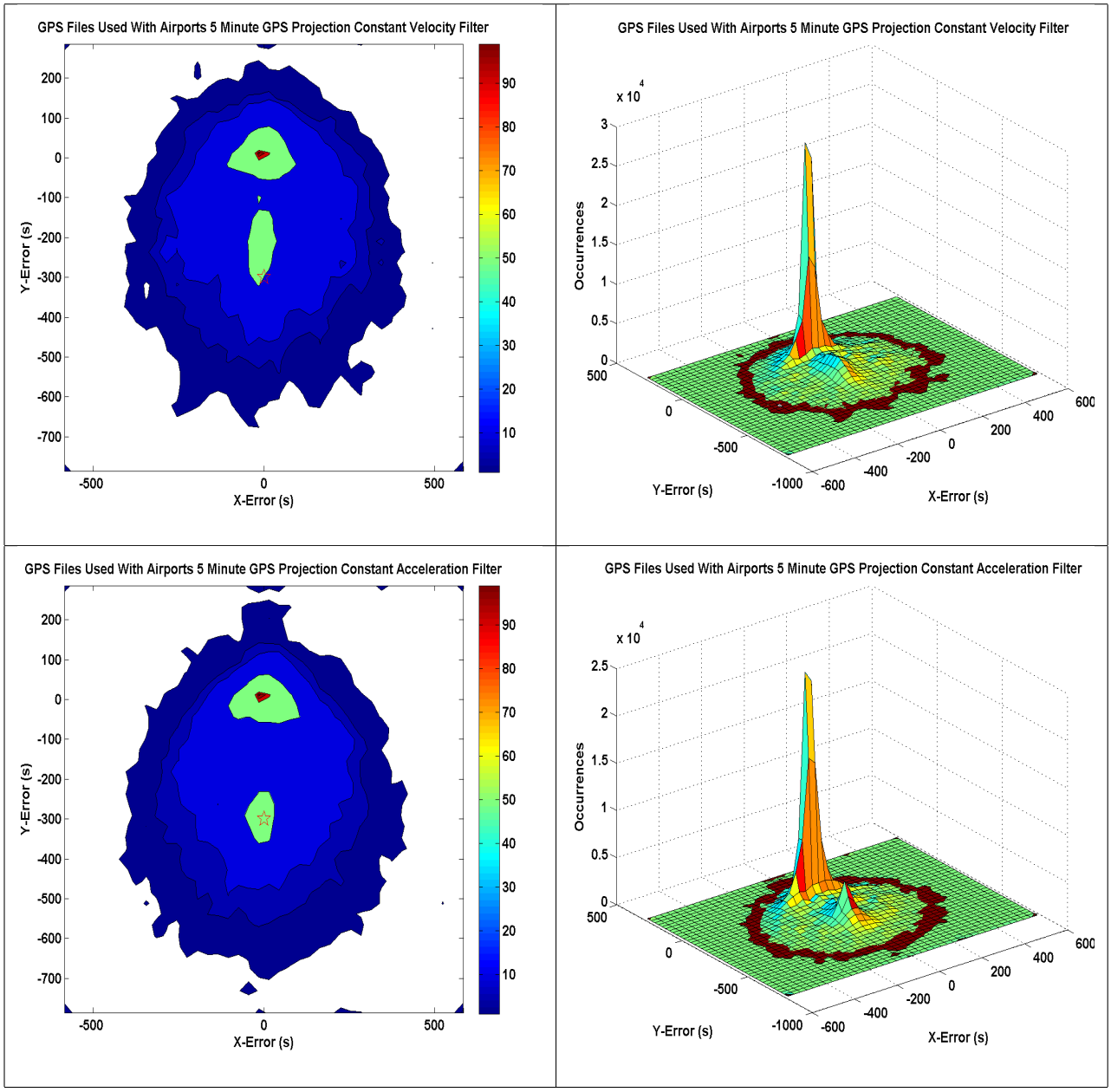

Figure B.5: Constant velocity and constant acceleration filters, all GPS flights with airports, 5 minute time horizon

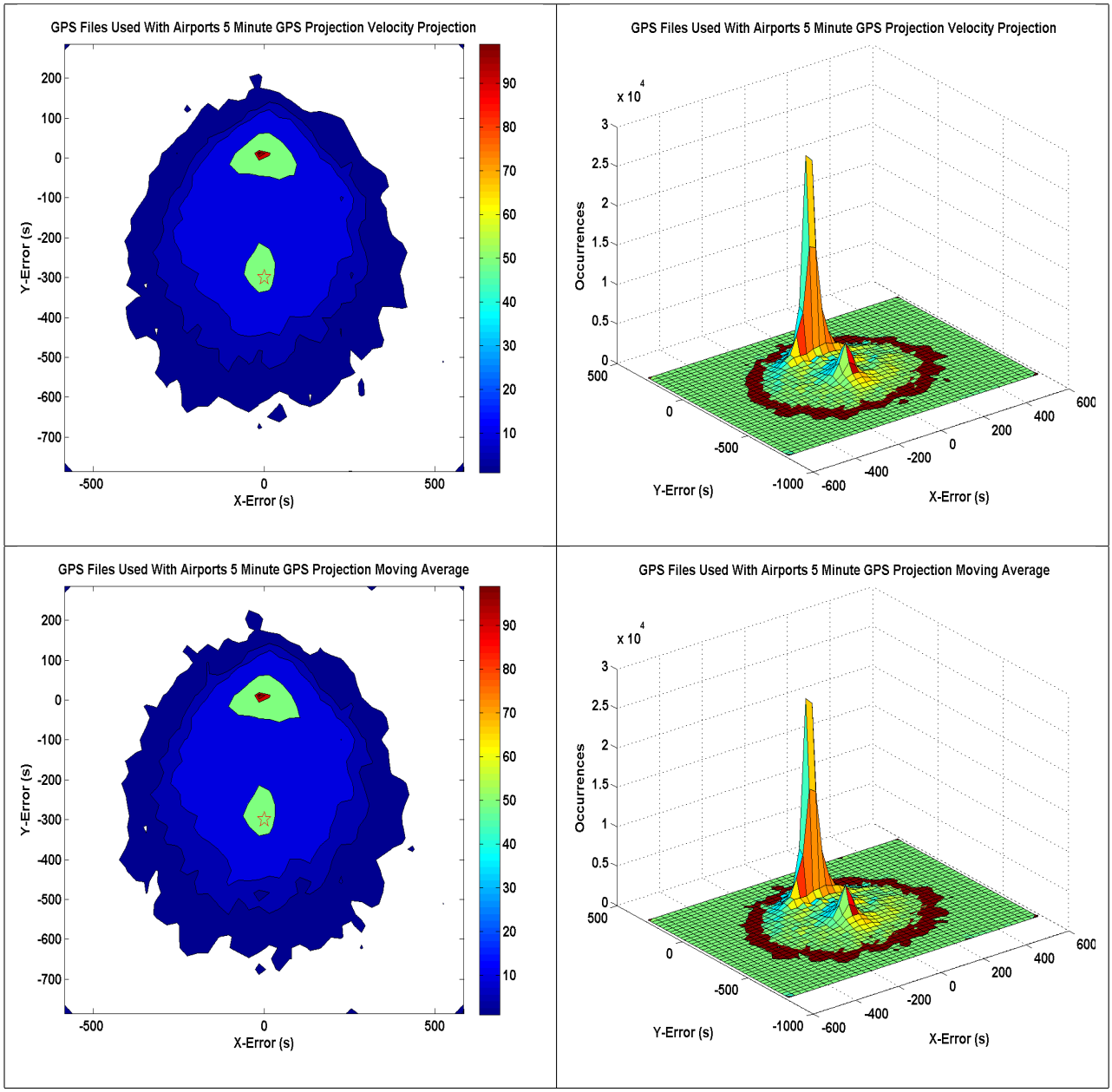

Figure B.6: Straight velocity projection and moving average projection, all GPS flights with airports, 5 minute time horizon

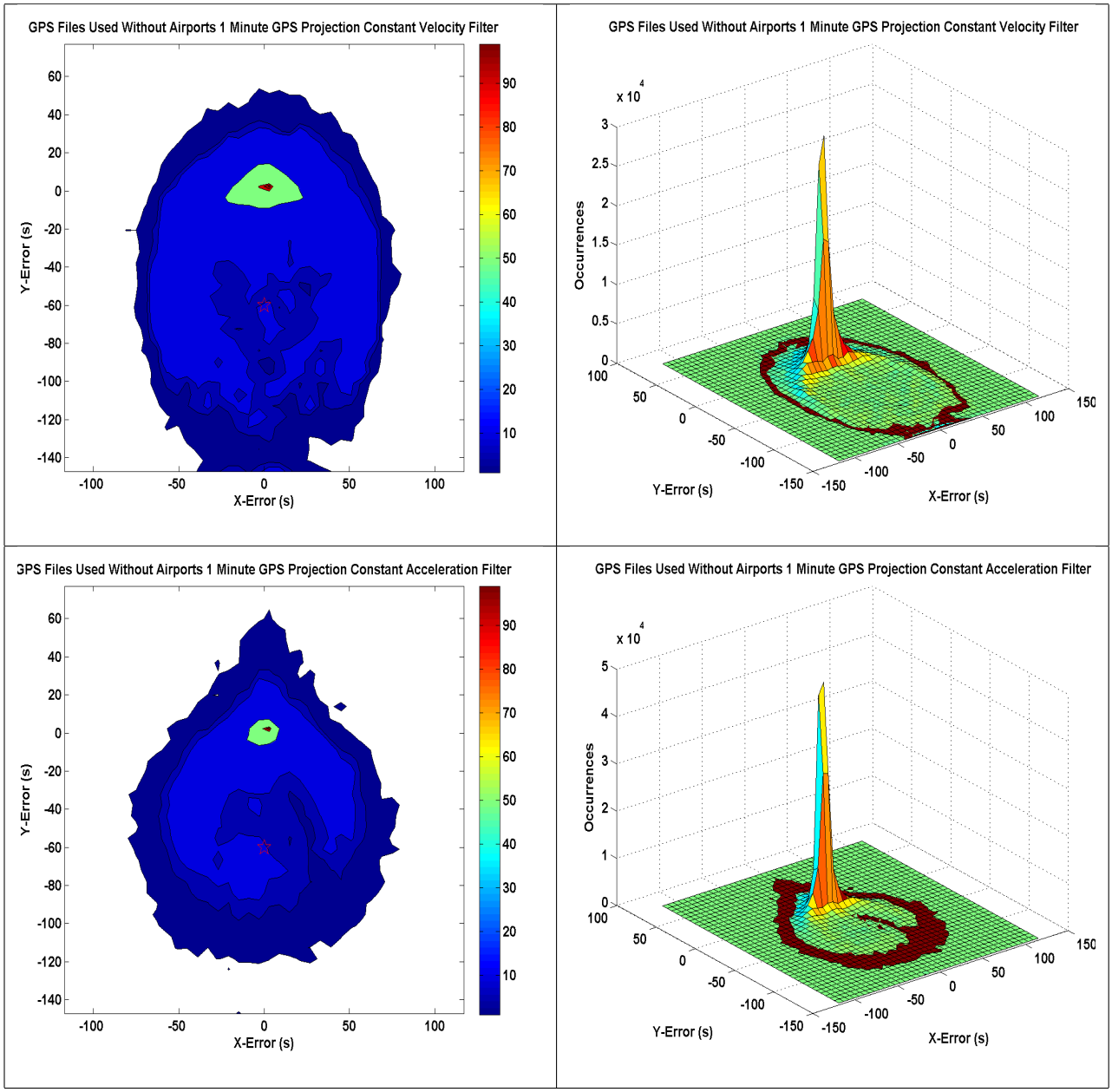

Figure B.7: Constant velocity and constant acceleration filters, all GPS flights without airports, 1 minute time horizon

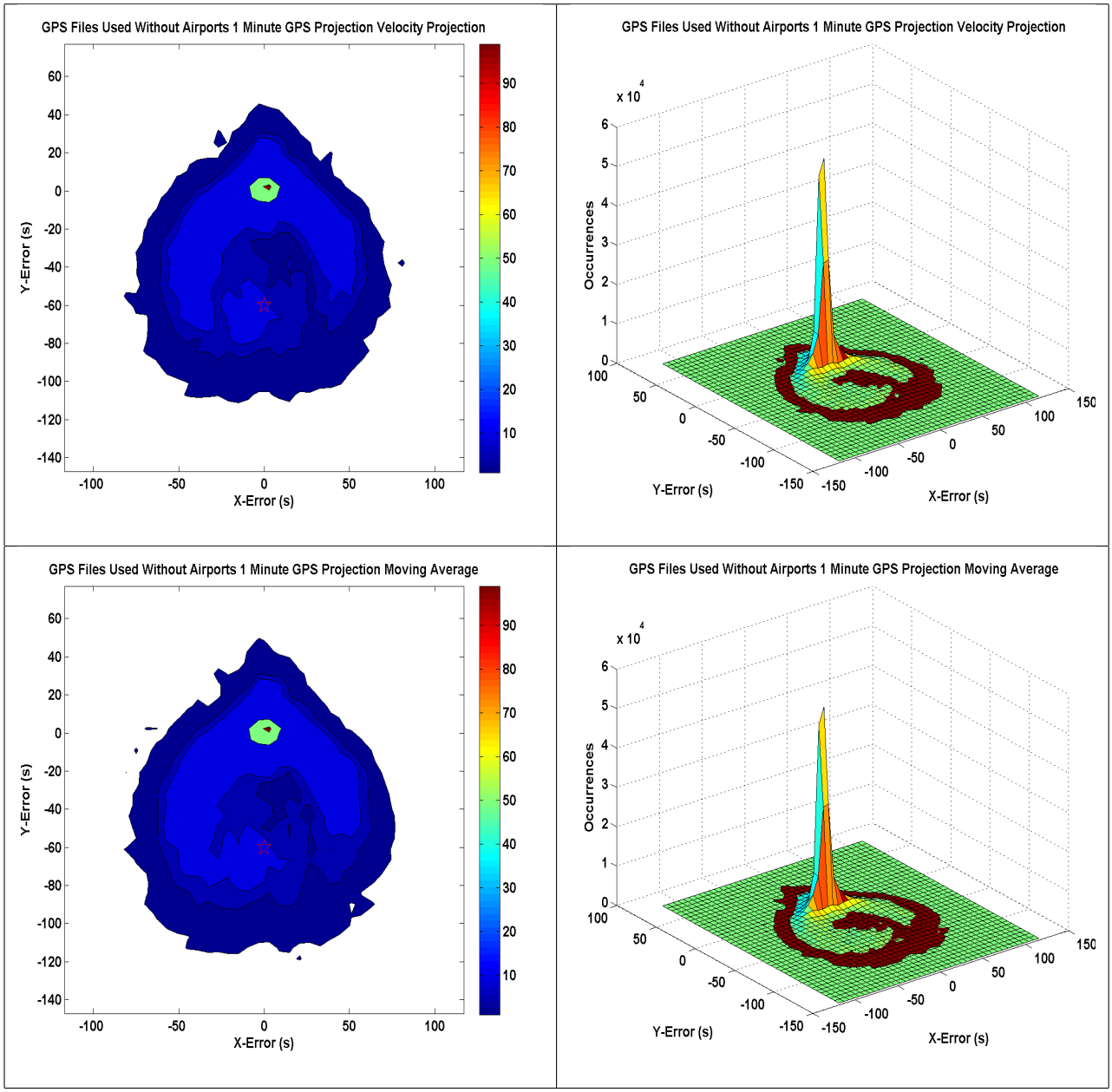

Figure B.8: Straight velocity projection and moving average projection, all GPS flights without airports, 1 minute time horizon

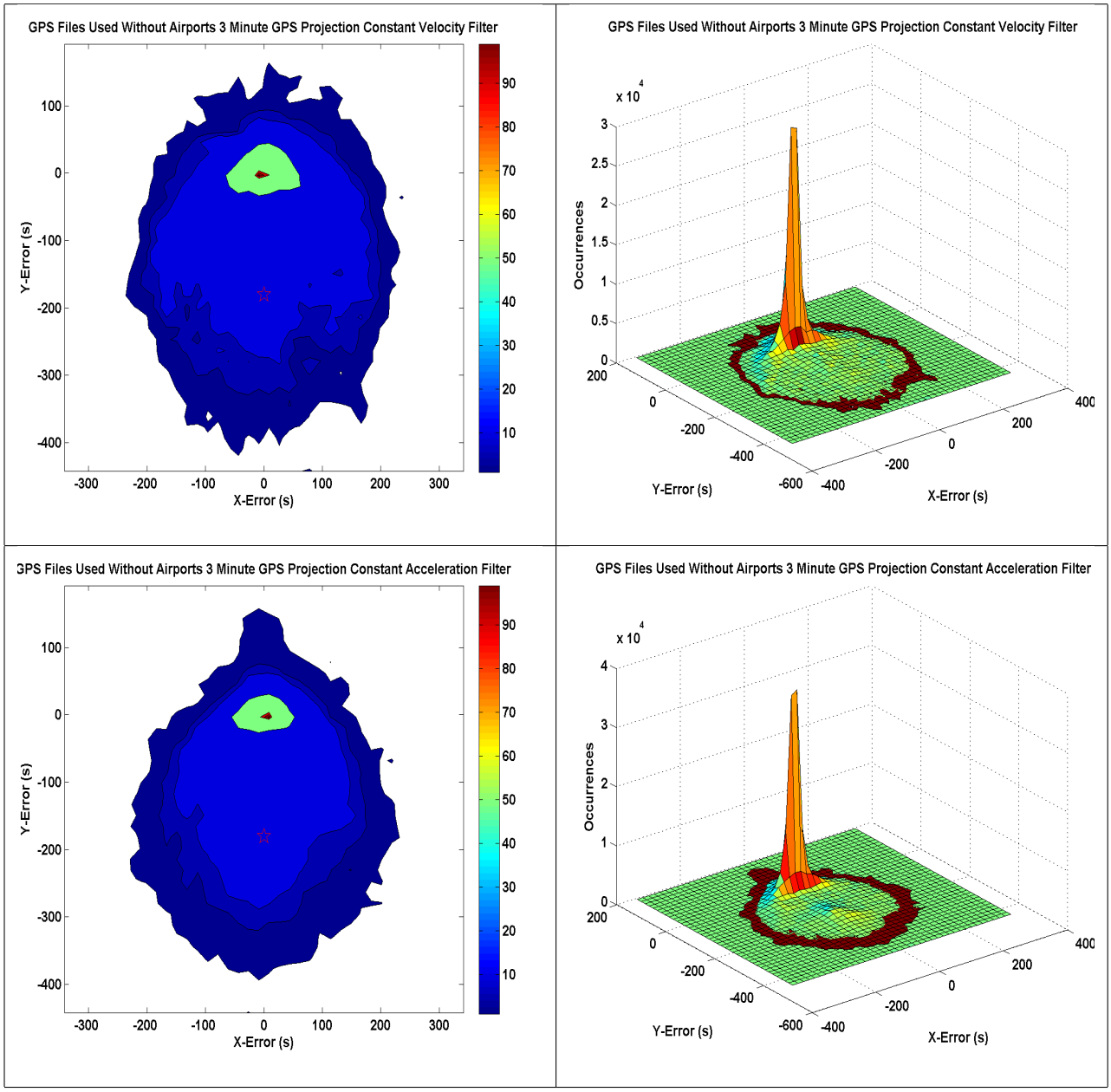

Figure B.9: Constant velocity and constant acceleration filters, all GPS flights without airports, 3 minute time horizon

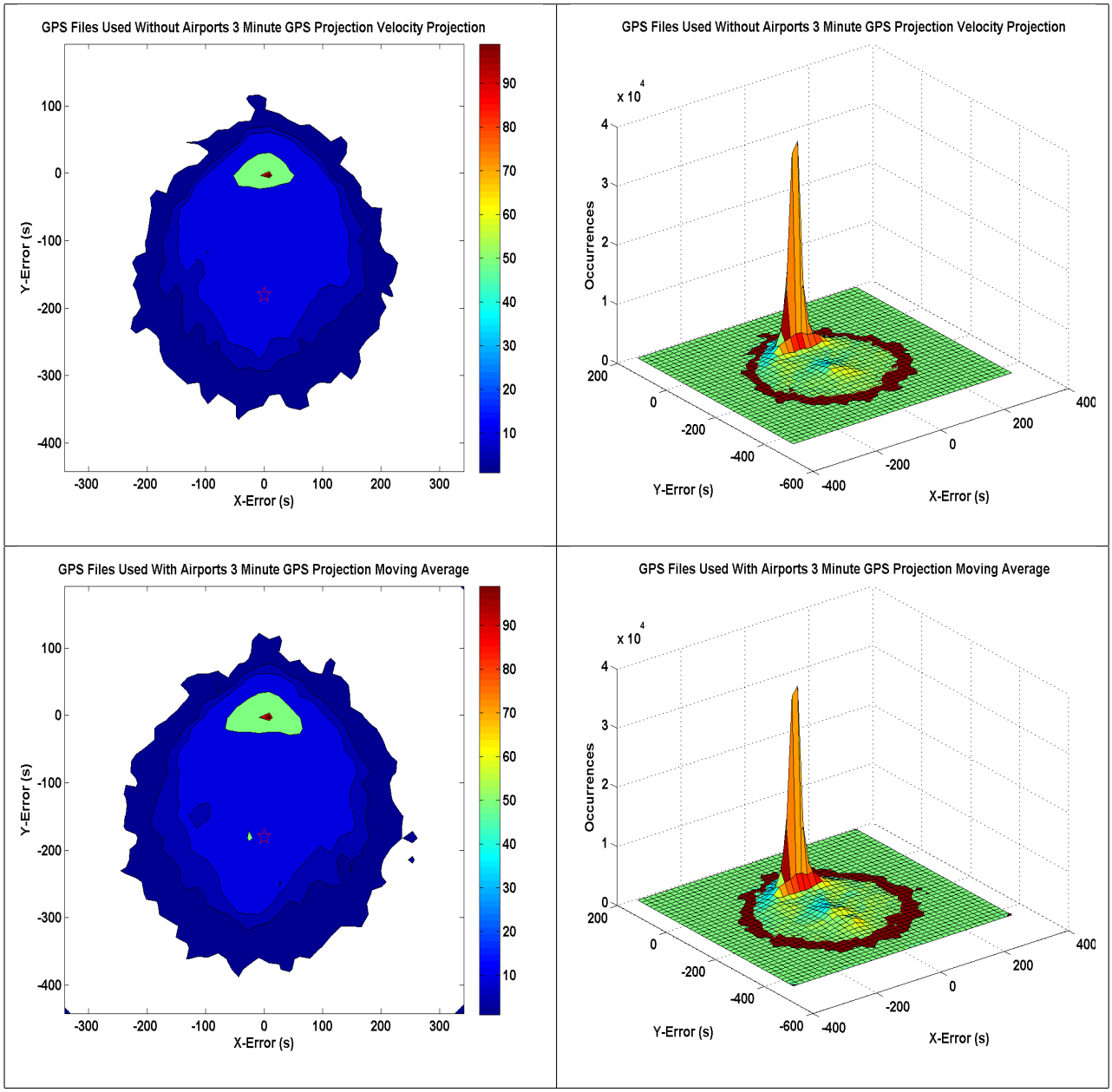

Figure B.10: Straight velocity projection and moving average projection, all GPS flights without airports, 3 minute time horizon

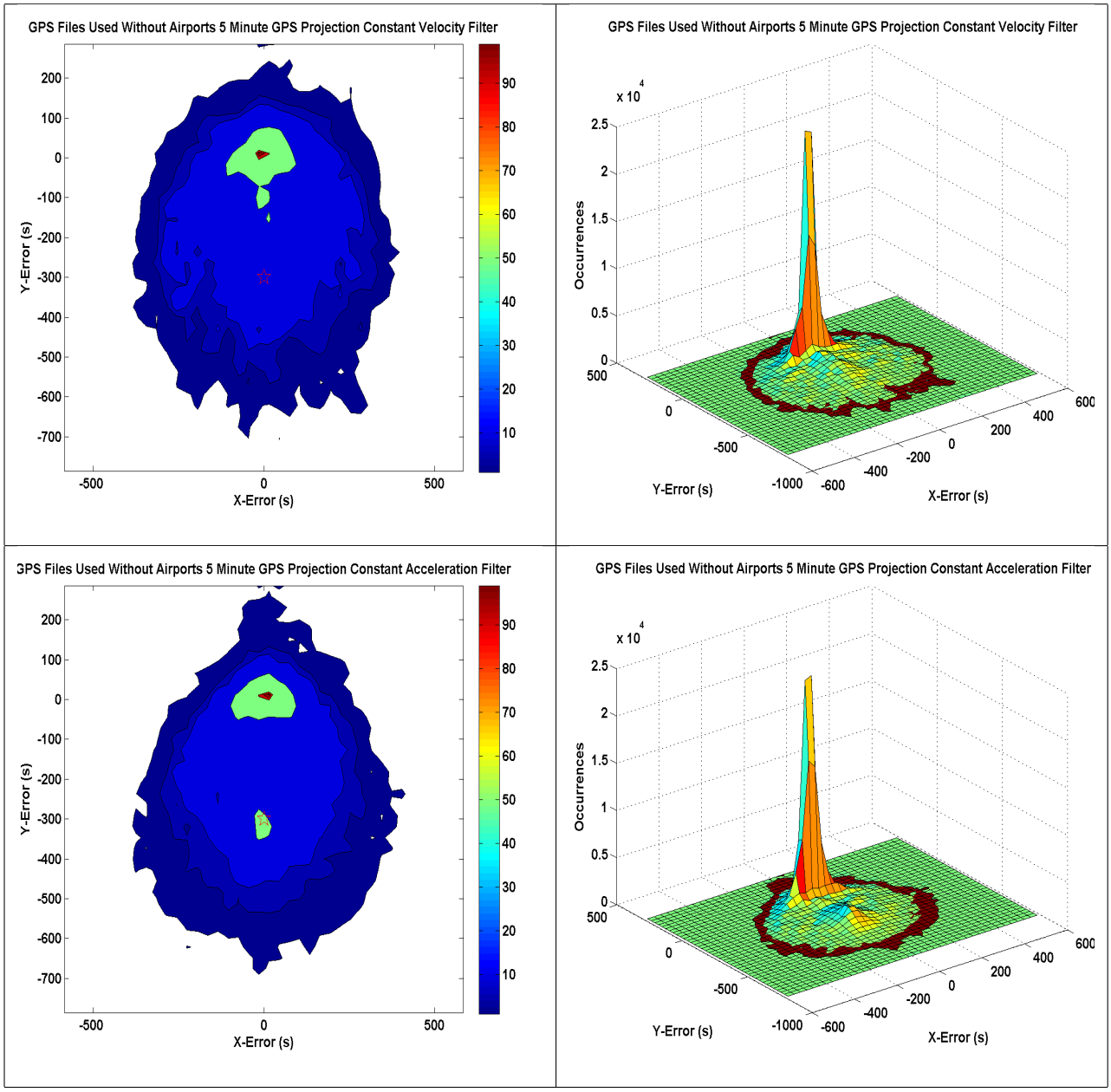

Figure B.11: Constant velocity and constant acceleration filters, all GPS flights without airports, 5 minute time horizon

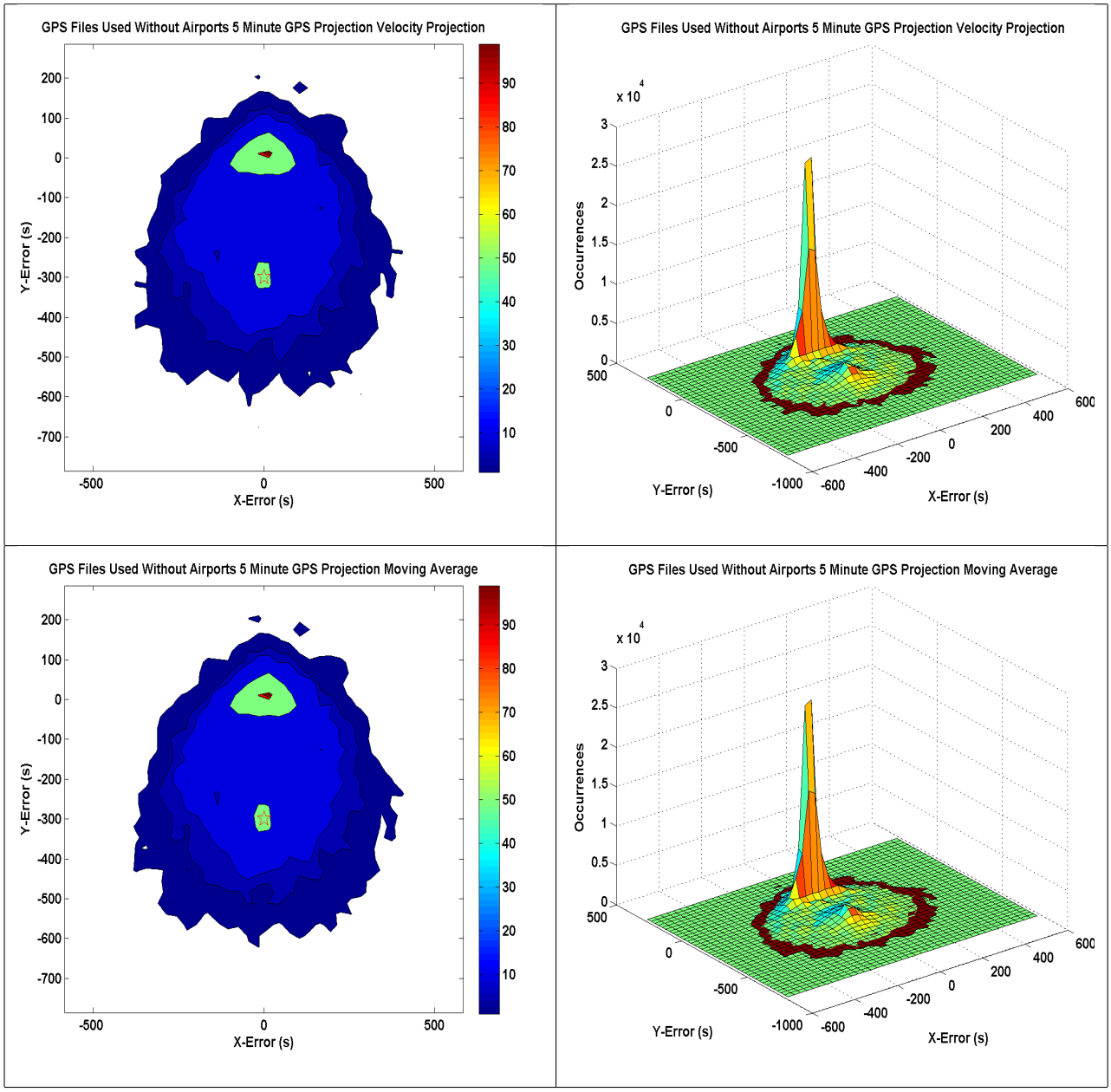

Figure B.12: Straight velocity projection and moving average projection, all GPS flights without airports, 5 minute time horizon

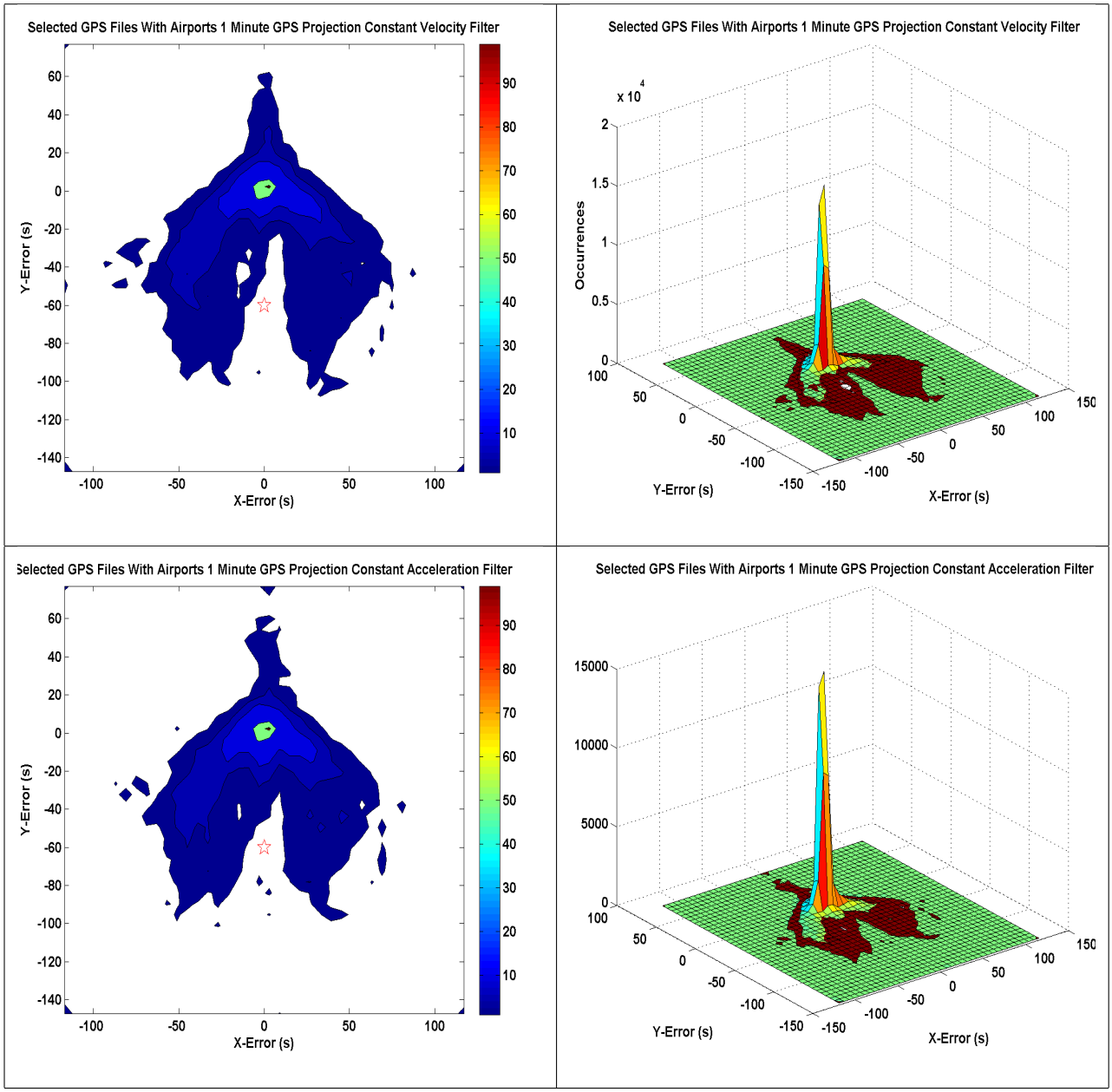

Figure B.13: Constant velocity and constant acceleration filters, selected GPS flights with airports, 1 minute time horizon

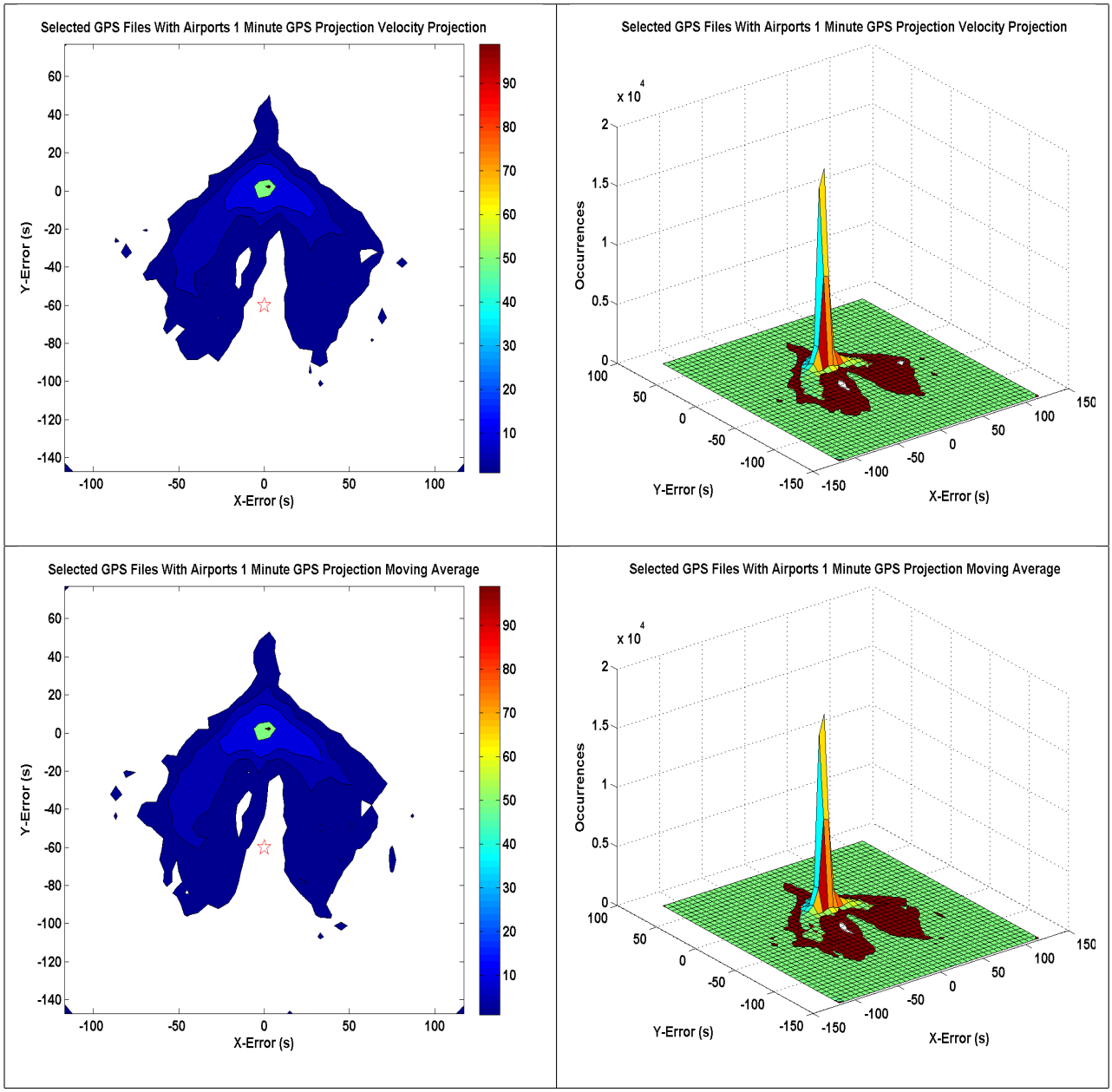

Figure B.14: Straight velocity projection and moving average projection, selected GPS flights with airports, 1 minute time horizon

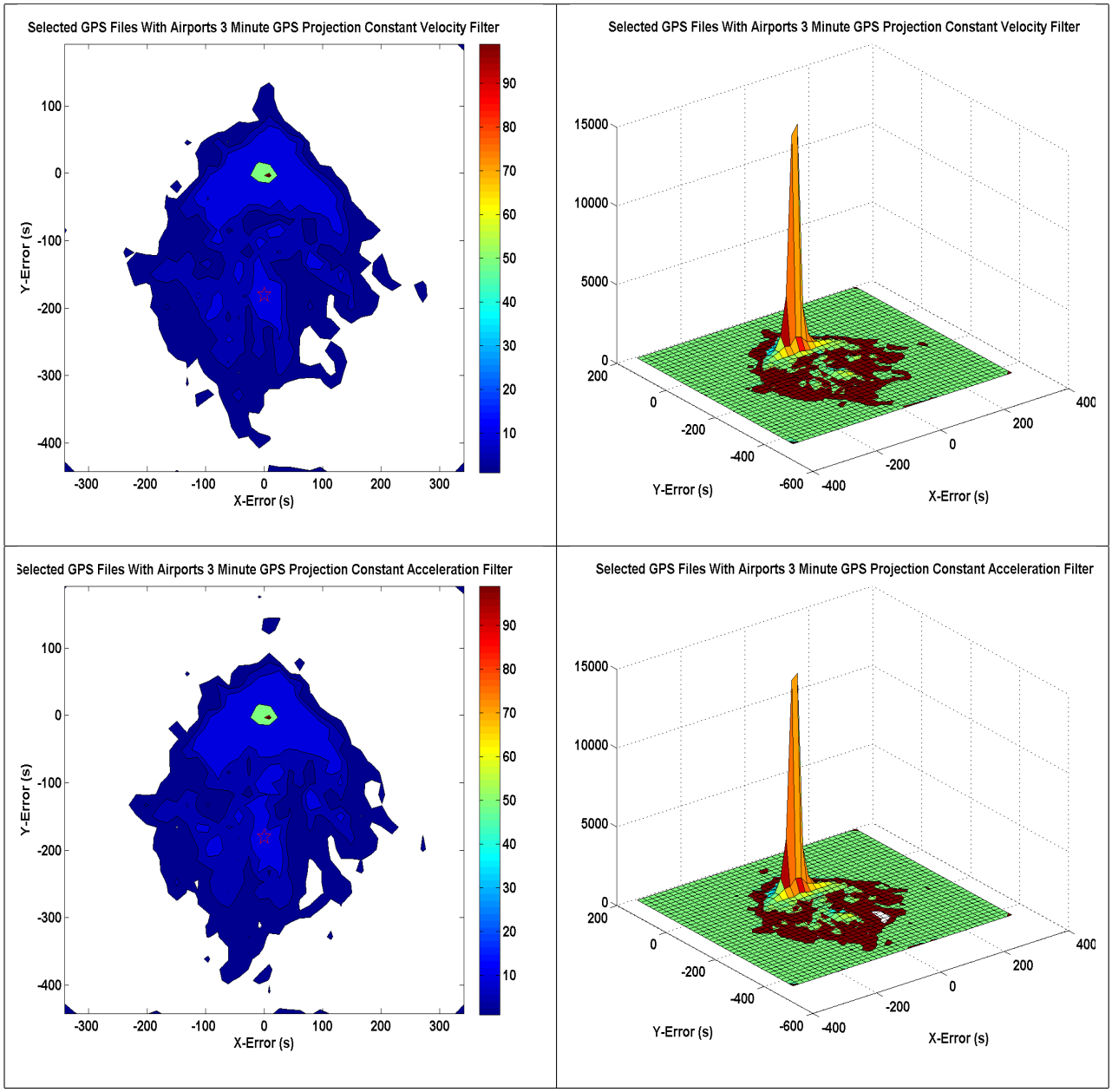

Figure B.15: Constant velocity and constant acceleration filters, selected GPS flights with airports, 3 minute time horizon

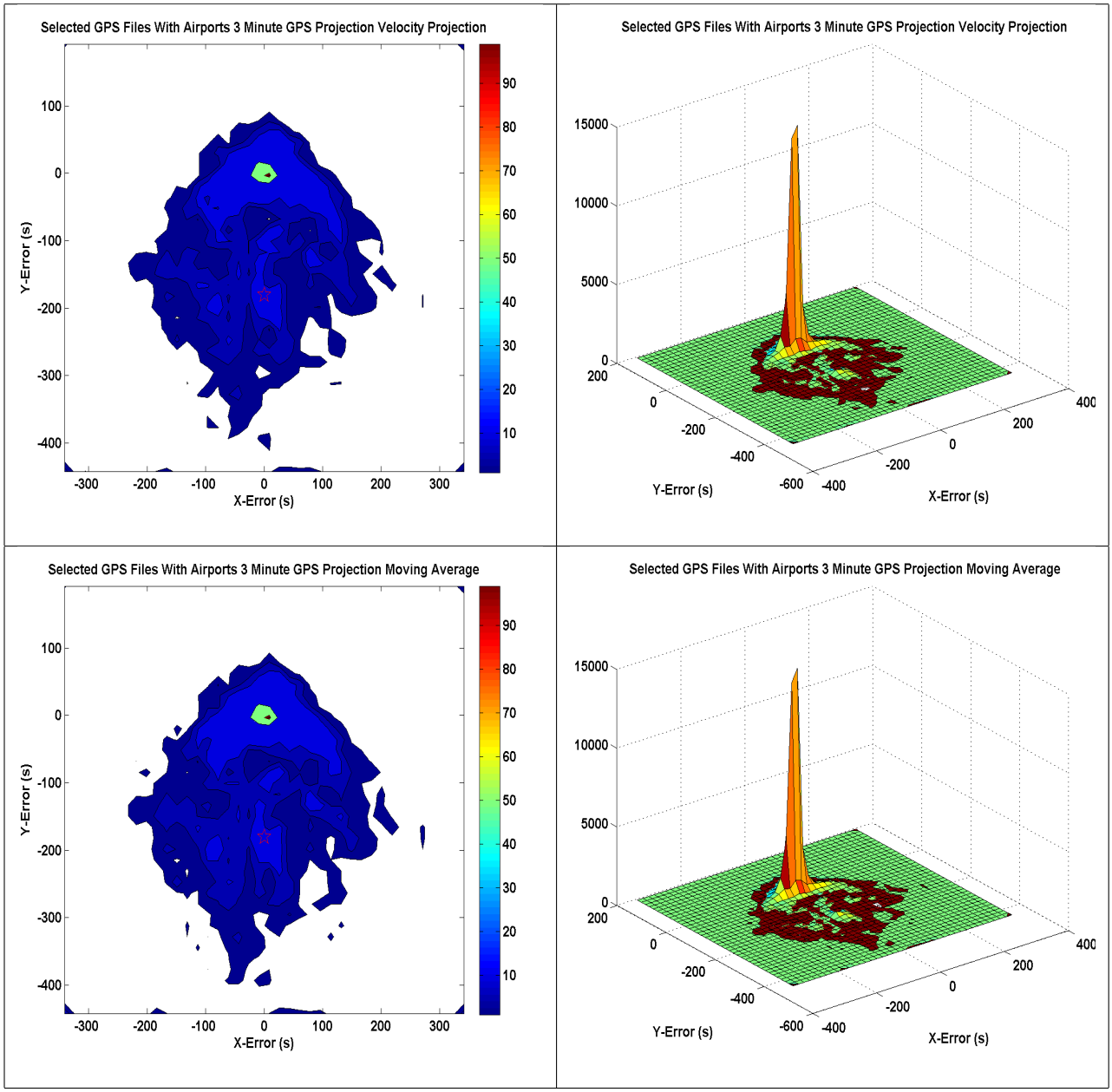

Figure B.16: Straight velocity projection and moving average projection, selected GPS flights with airports, 3 minute time horizon

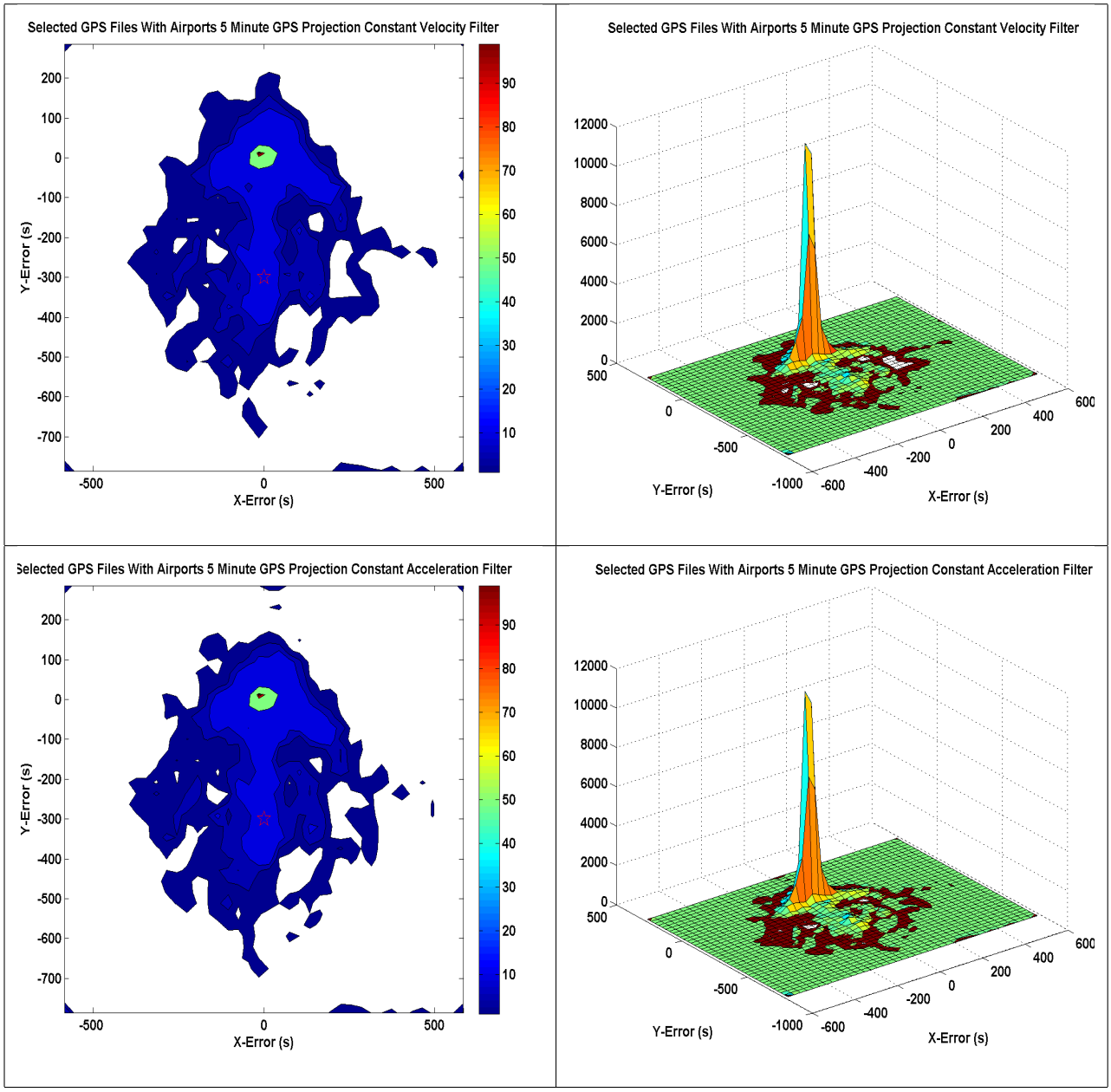

Figure B.17: Constant velocity and constant acceleration filters, selected GPS flights with airports, 5 minute time horizon

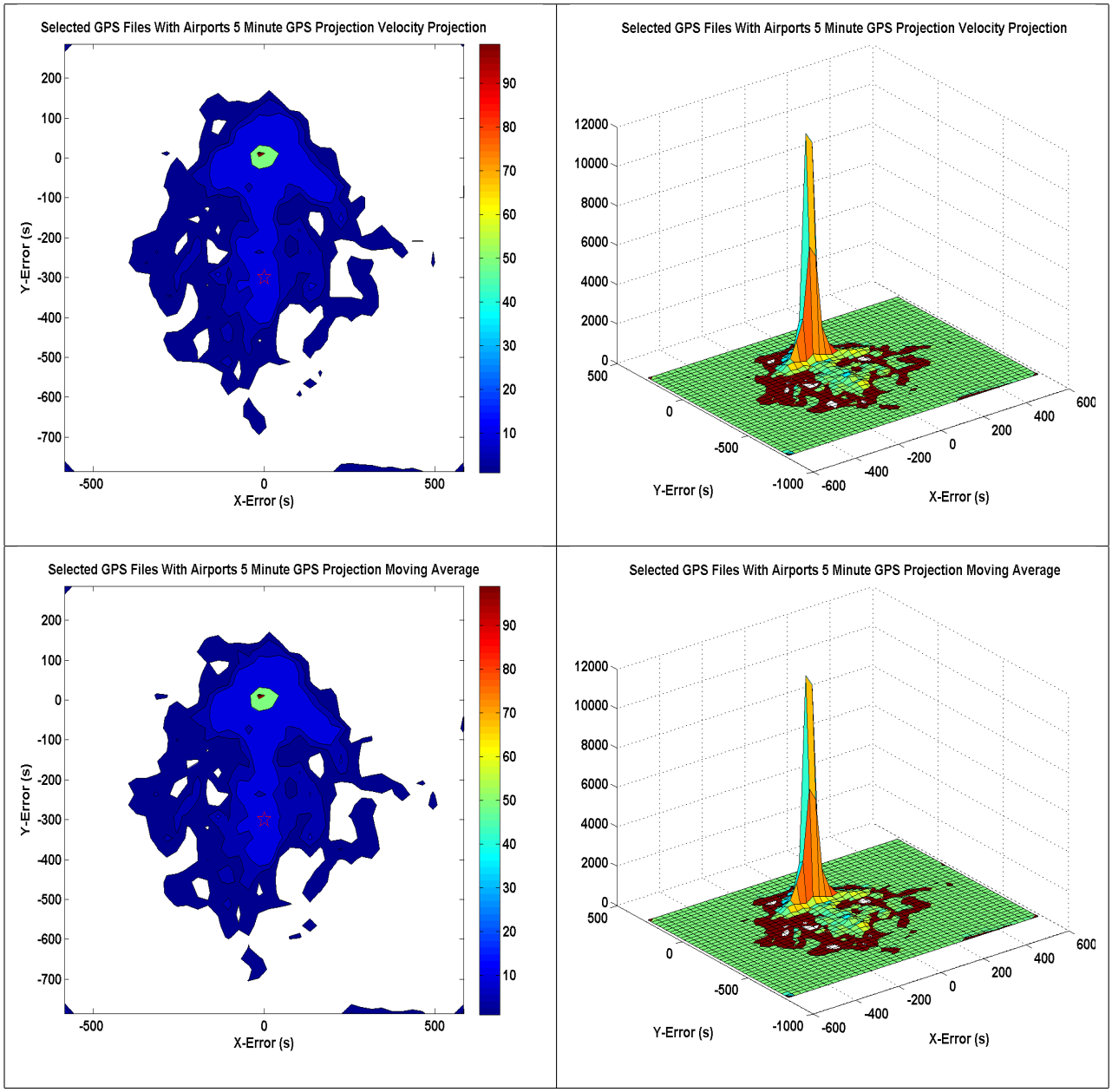

Figure B.18: Straight velocity projection and moving average projection, selected GPS flights with airports, 5 minute time horizon

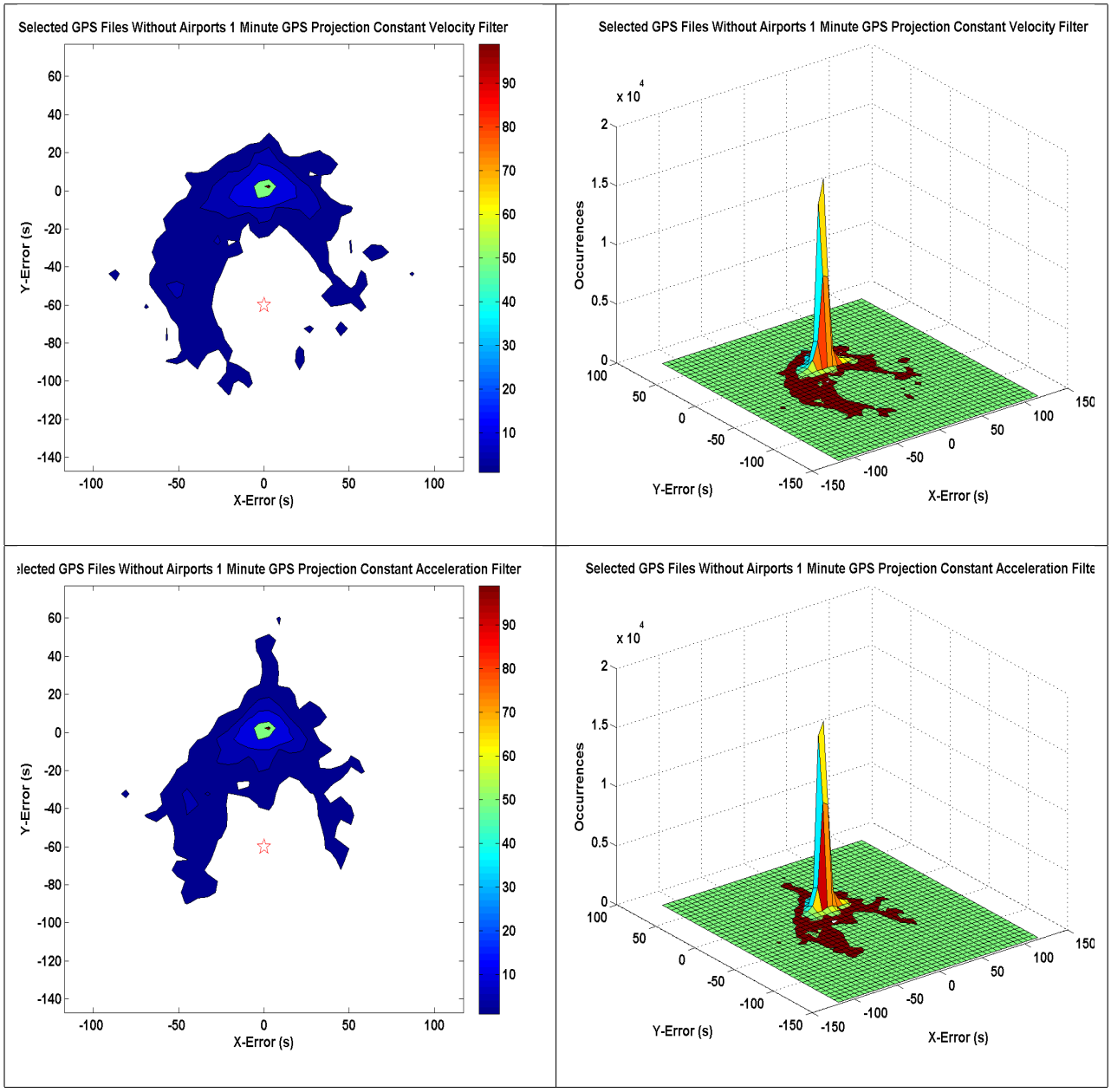

Figure B.19: Constant velocity and constant acceleration filters, selected GPS flights without airports, 1 minute time horizon

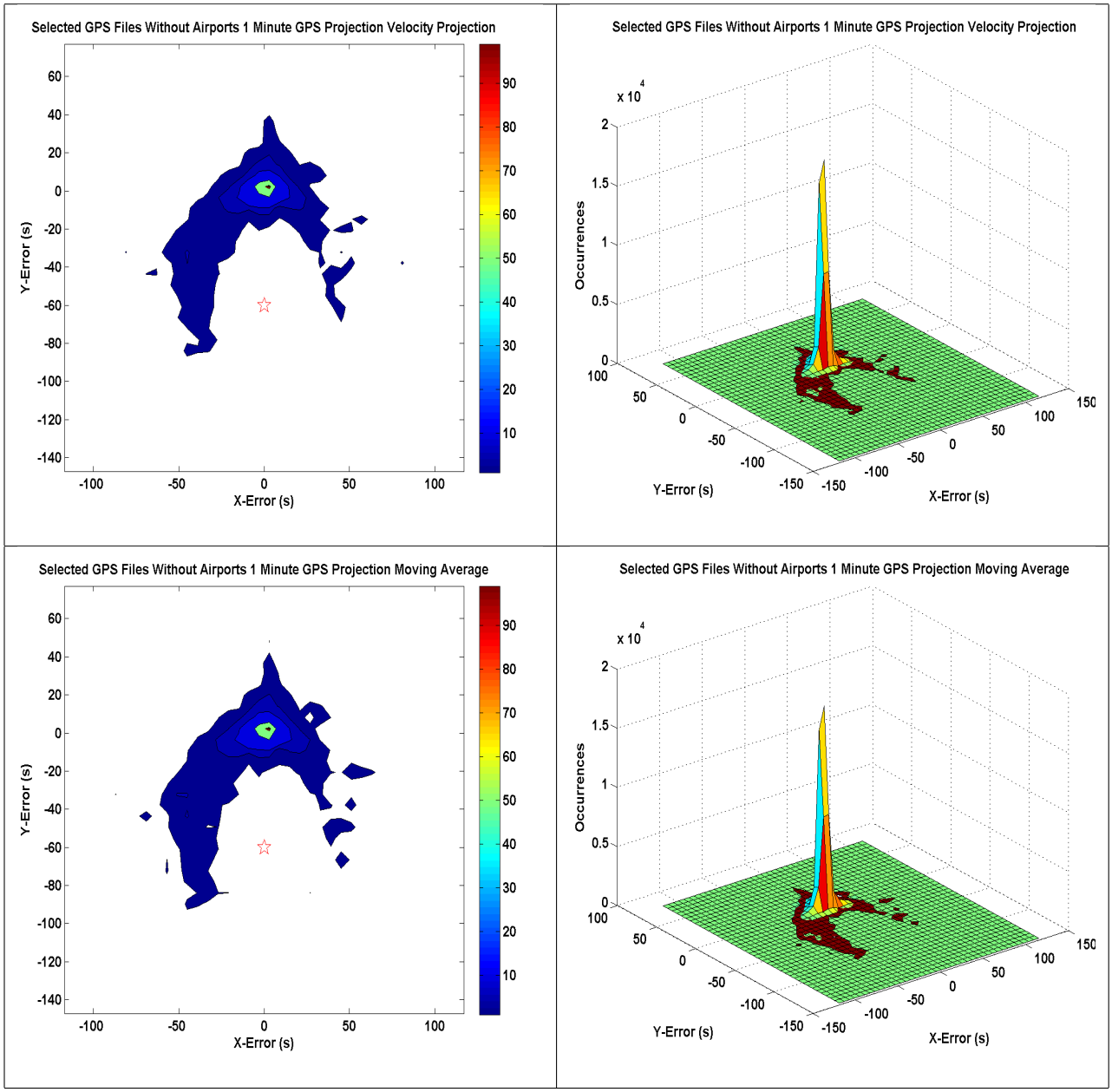

Figure B.20: Straight velocity projection and moving average projection, selected GPS flights without airports, 1 minute time horizon

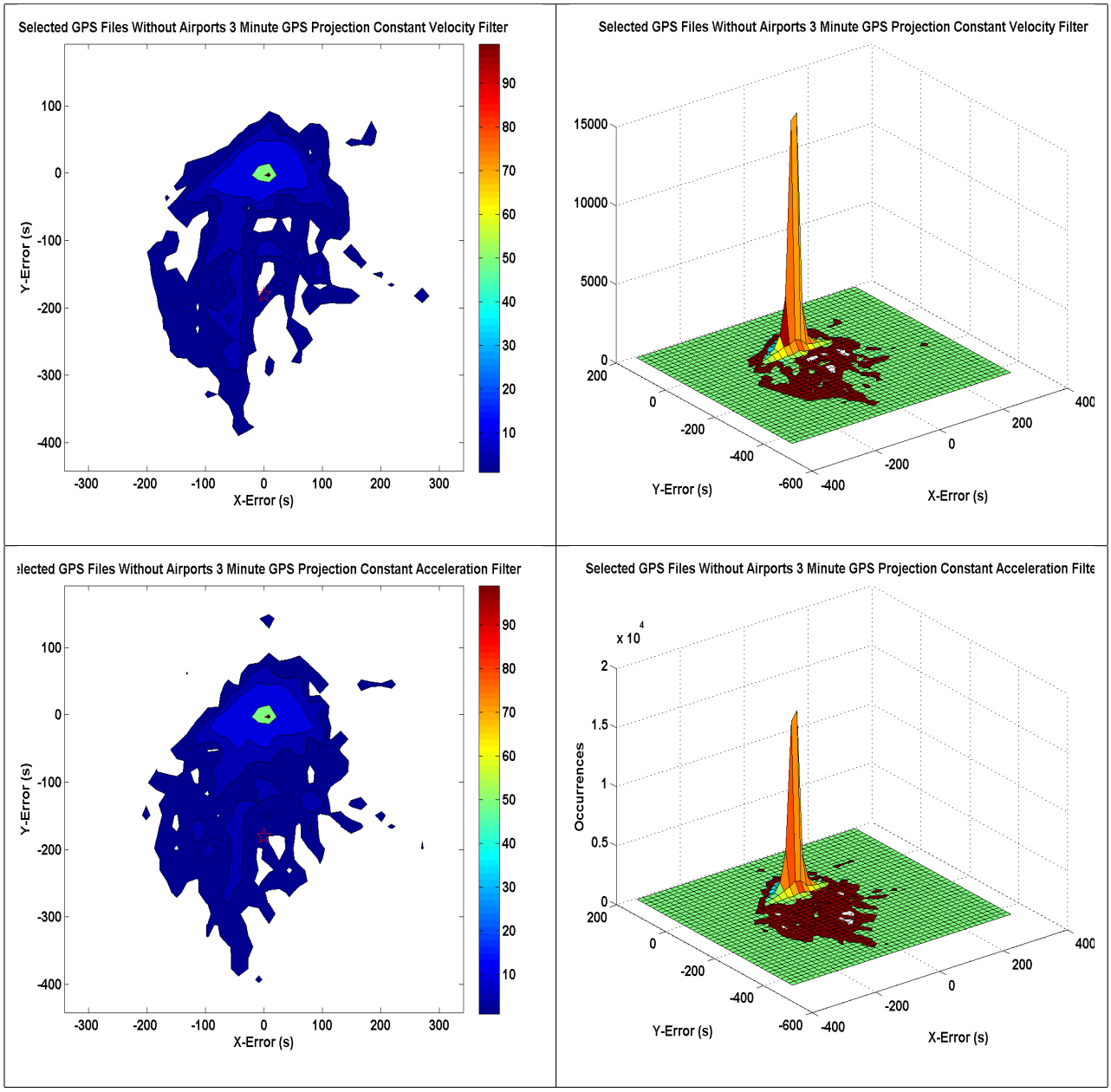

Figure B.21: Constant velocity and constant acceleration filters, selected GPS flights without airports, 3 minute time horizon

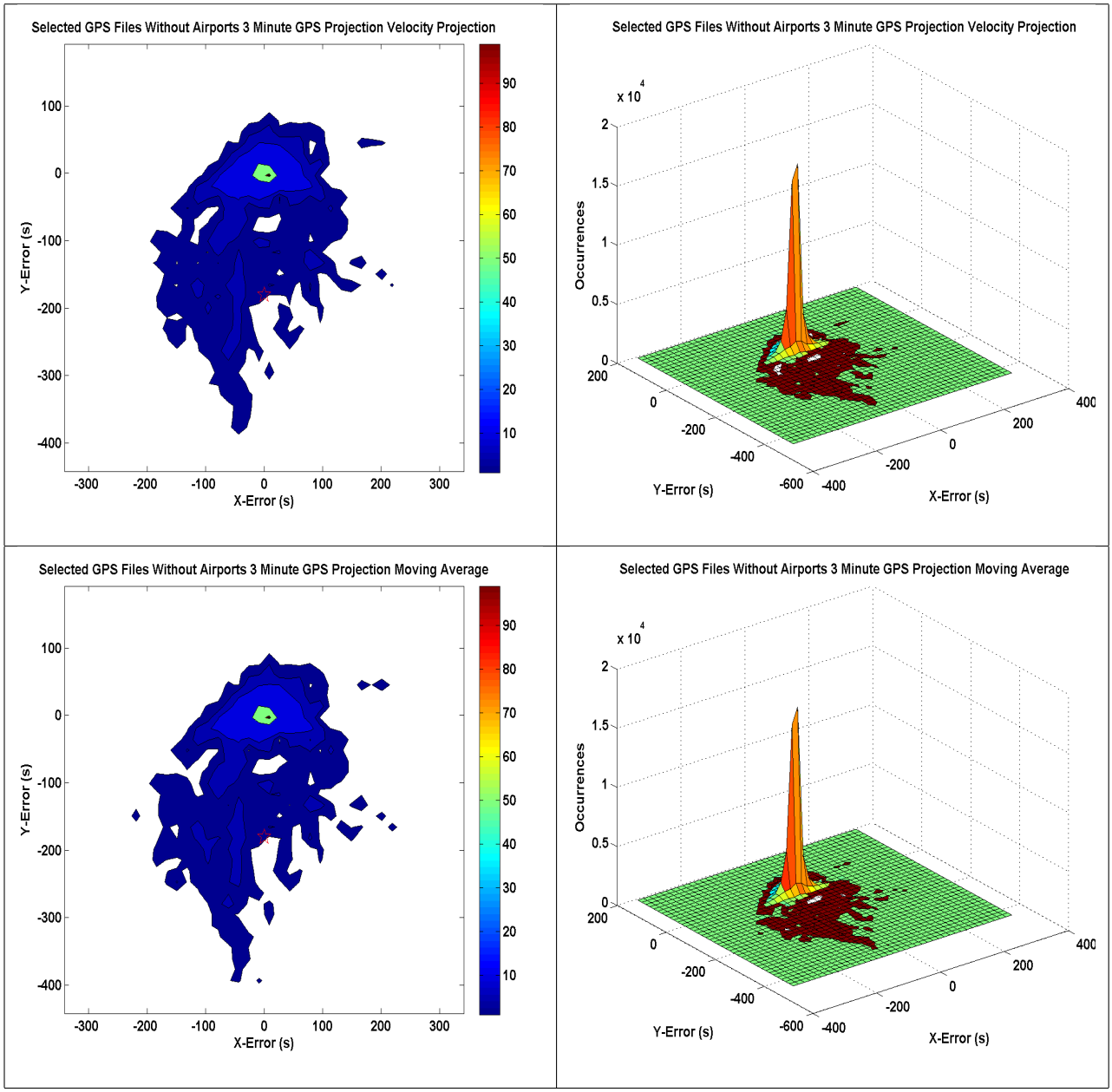

Figure B.22: Straight velocity projection and moving average projection, selected GPS flights without airports, 3 minute time horizon

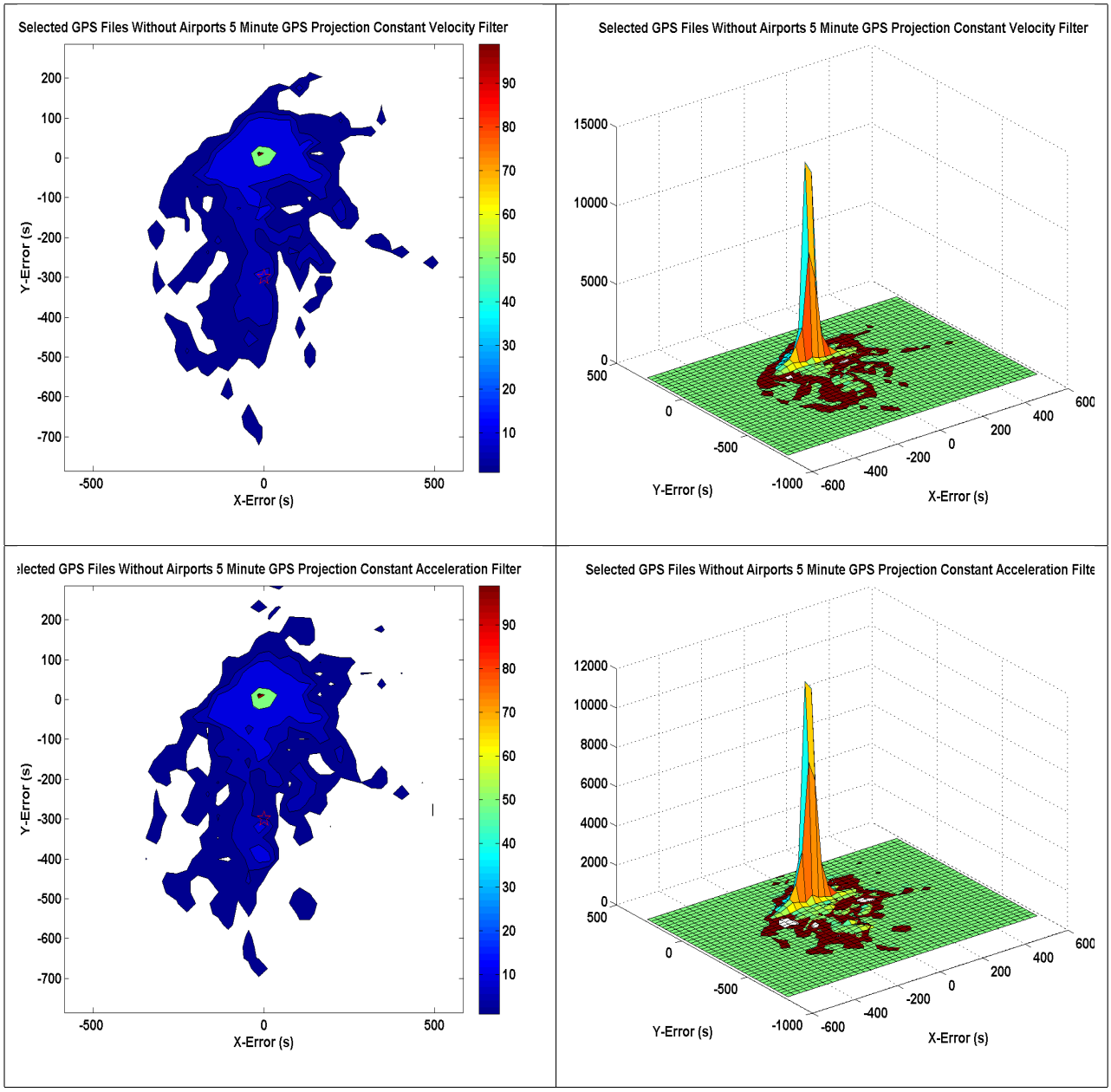

Figure B.23: Constant velocity and constant acceleration filters, selected GPS flights without airports, 5 minute time horizon

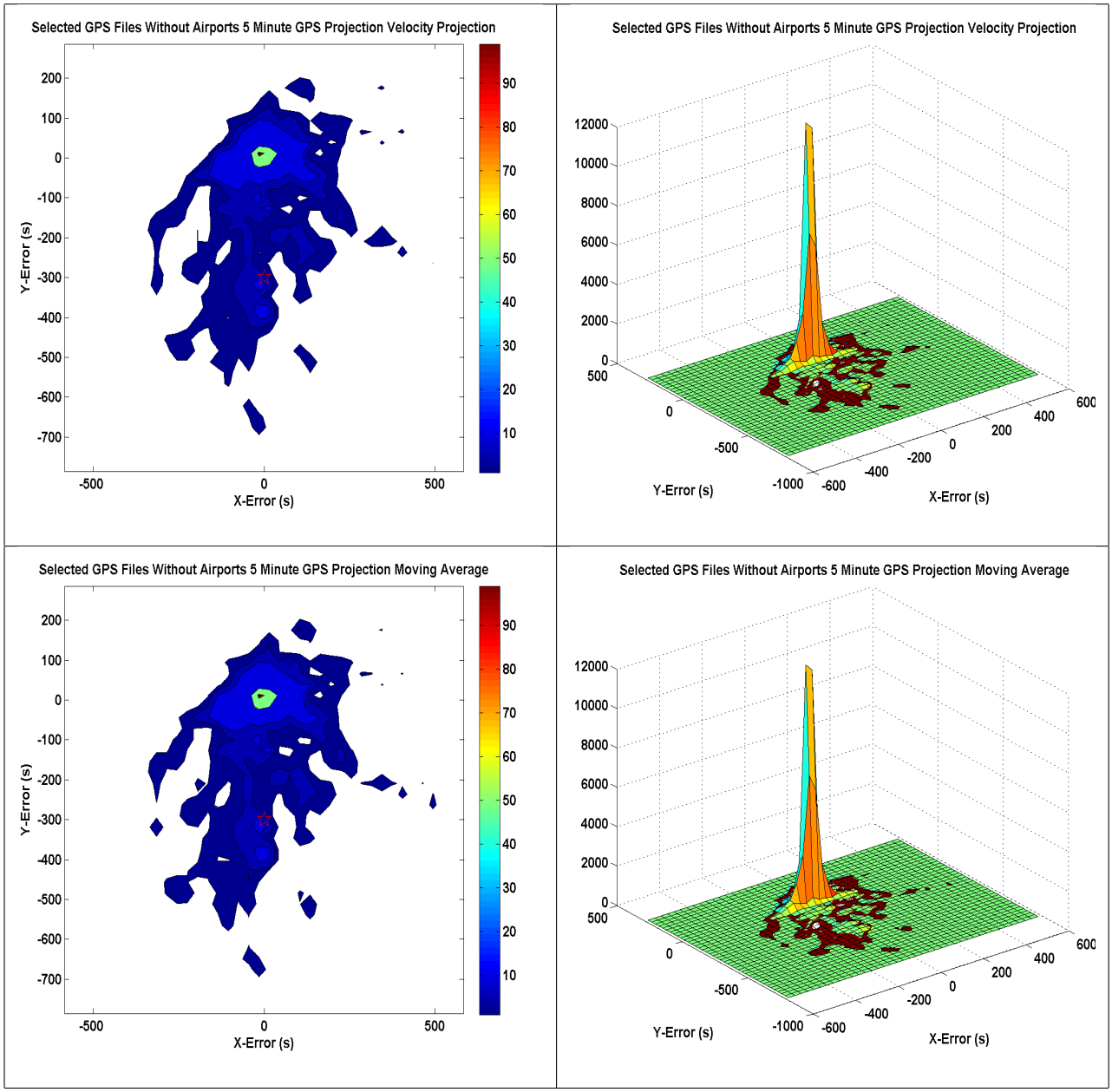

Figure B.24: Straight velocity projection and moving average projection, selected GPS flights without airports, 5 minute time horizon

Appendix C

Rhumb Lines

A rhumb line, or loxodrome, is a line that crosses all meridians of longitude at the same angle. Although great circles provide the shortest distance between two points on a sphere (for navigation, on the Earth), rhumb lines are easier to because of they keep a constant bearing.

Distance Between Two Points

In the error calculations, the bearing and velocity between two points in the track for an aircraft are assumed constant [17]. Therefore, rhumb lines can be used to find the distant and bearing between the two points, as shown below.

Given two geodetic points in radians latitude and longitude (ϕ_1, λ_1) and (ϕ_2, λ_2), respectively. The stretched latitude is defined as follows.

$$\Delta lat = \ln \frac{\tan(\frac{\lambda_2}{2} + \frac{\pi}{4})}{\tan(\frac{\lambda_1}{2} + \frac{\pi}{4})} \tag{C.1}$$

If the stretch latitude, $\Delta\phi$, is zero, i.e. the points share the same parallel,

$$q = \cos(\lambda_1) \tag{C.2}$$

$$\Delta lon = \phi_2 - \phi_1 \tag{C.3}$$

otherwise,

$$q = \frac{\Delta\lambda}{\Delta lat} \tag{C.4}$$

$$distance = \sqrt{\Delta\lambda^2 + q^2\Delta\phi^2}R \tag{C.5}$$

Where R is the radius of the Earth. The constant bearing, θ, is defined as

$$\theta = atan2(\Delta lon, \Delta\phi) \tag{C.6}$$

Destination Given Position, Distance and Bearing

Given the above equations to find the distance between two points, the a priori bearing provided by the measurements gives the bearing to project from the current position to the projected position at the given time horizon. The velocity and time horizon give the desired

distance to project [17].

$$\alpha = \frac{d}{R} \tag{C.7}$$

Where d is the projection distance and R is the radius of the Earth.

$$\phi_2 = \lambda_1 + \alpha \cos(\theta) \tag{C.8}$$

θ is the constant bearing between the current point and the projected point.

$$\Delta lat = \ln \frac{\tan(\frac{\lambda_2}{2} + \frac{\pi}{4})}{\tan(\frac{\lambda_1}{2} + \frac{\pi}{4})} \tag{C.9}$$

If the constant bearing projects the point on the same parallel

$$q = \cos(\lambda_1) \tag{C.10}$$

otherwise,

$$q = \frac{\Delta\lambda}{\Delta lat} \tag{C.11}$$

$$\Delta\phi = \alpha \frac{\sin(\theta)}{q} \tag{C.12}$$

$$\phi_2 = mod(\lambda_1 + \Delta\lambda + \pi, 2\pi) - \pi \tag{C.13}$$